AN EXPERIMENTAL ANALYSIS OF CARRIER LAYER FLOWS

John Bruce Ikin

Submitted in accordance with the requirements for the degree of
Doctor of Philosophy

The University of Leeds
School of Mechanical Engineering

April 2005

The candidate confirms that the work submitted is his own and that appropriate credit has been given where reference has been made to the work of others.

Abstract

This thesis is concerned with flows relating to the continuous coating of multiple layers on moving webs using the slide bead process. The lowermost layer is generally known as a carrier layer when the viscosity and flow rate are both small compared with the corresponding properties of the other layers. This study is predominantly experimental in nature and broad in scope as addressing issues relating to an industrial slide coating process used for the manufacture of photographic products and inkjet media.

Novel specialist pieces of equipment have been designed and built for visualizing such flows as part of this work. The studies have been carried out using a pilot coating machine and ancillary flow control facilities currently owned by HARMAN technology Limited. The new techniques enable fresh insight into the interaction between the carrier layer and the surface properties of the substrate, including roughness, surface free energy, electric charge and porosity - an area of investigation that has hitherto been largely ignored. The behaviour of the bead when coating embossed webs showing a "stippled" finish is of particular interest when compared with apparently equally rough substrates of equivalent surface energy. Increasing slide angle is shown to be advantageous to expanding the coating window for difficult substrates. The results show that the widely perceived criteria for a carrier layer needs to be redefined when coating rough surfaces of low surface energy using this process. Charge assisted coating is shown likely to be superior to conventional slide bead coating for minimising waste due to streaks.

The studies include the visualisation of flows at the slot exit and on the slide. The methods allow the profile of the interface as well as the free surface to be monitored and give new insight into two major unreported effects limiting the use of a thin low viscosity carrier layer. The scope also extends to the study of waves induced in the surface of wet multi-layer coatings when subjected to the impact of air from an impingement dryer – an area of considerable interest to the coating technologist yet largely ignored by the equipment supplier.

To Barbara

Acknowledgements

Firstly I would like to express my sincere thanks to my supervisors Professor Phil Gaskell and Dr. Harvey Thompson for their much valued help and advice during the course of this research. I would also like to extend my thanks to Dr. Nik Kapur for his help and advice with the measurement of rheology and surface roughness, Dr. Mark Wilson and Dr. Cath Noakes for running the numerical models and for the helpful hints when constructing the apparatus for measuring the heat transfer characteristics of dryers and to my external examiner, Professor Terry Blake, for his helpful suggestions in improving the final draft of this thesis.

I would like to express a special thank you to Dr. Trevor Rhodes of HARMAN technology Limited for his continued support and arranging permission to use and exploit the extensive experimental facilities available within the company and for authorising the manufacture of much of the equipment designed specifically for this work. I very much appreciated the willingness of Robert Rayner in undertaking to make the special probe needed for visualising the coating bead. Much of the work would not have been possible without the valuable engineering assistance given by Kevin Dooley and Bob Wotton and the technical assistance with many of the experiments given by David Hook and Andy Cunniffe.

I would also like to extend my thanks to Dr. W. Long and Dr. D. Beveridge for their help in locating patents and other literature, to Roger Brace for forwarding data on his coating experiments, to Gillian Fossdyke in her contribution to the measurement of rheology, surface energy and dynamic contact angle, to Barry Allman for his assistance in the measurement of dynamic surface tension and to Tracy Simcock in preparing the silver based emulsions required for visualising the flows.

I owe a very special thank you to my wife Barbara and daughter Shirley-Rachel for their forebearance and support over the past four years.

Finally, I gratefully acknowledge the financial support provided by the EPSRC for the duration of my studies through Grant reference GR/M93291/01

Contents

List of Figures

List of Tables

Nomenclature

The symbols listed below are those with a common meaning throughout this thesis.

Other symbols are used locally within some of the chapters and are defined at the point of usage.

B	Width of cascade feed slot [m]
g	Gravitational constant [m s^{-1}]
H_G	Coating gap [m]
H_S	Film thickness down inclined slide [m]
H_W	Film thickness at waist in flow down inclined slide [m]
H_∞	Final wet thickness of coated film [m]
m	Index in Sisko equation
n	Power law index
P	Pressure [N m^{-2}]
Q	Volumetric flow rate per unit coated width [m^2 s^{-1}]
S	Coating/web speed [m s^{-1}]
t	Surface age [s]
t*	Parameter defining dynamic surface tension characteristics [s]
U	Velocity in X direction [m s^{-1}]
U_{max}	Surface velocity down slide [m s^{-1}]
X	Coordinate in main flow direction [m]
Y	Coordinate normal to film flow [m]
β	Angle of slide inclination measured from horizontal [deg]
$\dot{\gamma}$	Shear rate [s^{-1}]
λ	Relaxation time [s]
μ	Viscosity of single layer [Pa s]
μ_0	Viscosity of single layer at reference shear rate [Pa s]
μ_∞	Viscosity of single layer at infinite shear rate [Pa s]

ρ	Density of single layer [kg m^{-3}]
σ	Surface tension [N m^{-1}]

Subscripts

F	Denotes flow through the cascade feed slot
G	Denotes flow in the bead forming zone
S	Denotes flow down the inclined slide
W	Denotes flow forming a waist down the slide
1	Denotes lowermost layer
2	Denotes second layer

Chapter I

Introduction

1.1 The Concept of Coating and Drying a Moving Web

Coating processes used throughout industry generally fall into three categories (Apps [2000]:

1. Self-metering coaters, where the film thickness is determined by fluid properties, line speed and coating geometry – for example roll coating processes
2. Pre-metered coaters where all of the solution pumped into the coating applicator is applied to the web. Slot, slide-bead and curtain coating processes fall into this category.
3. Post-metered coaters, where excess fluid is applied to the web and then metered to the correct thickness in a separate operation – for example a knife coating process

In the industrial processes employed in the manufacture of multilayer photographic materials, non-silver imaging products, magnetic storage media and inkjet media, it is common practice to coat one or more liquid layers simultaneously onto a moving web. This naturally constrains the process to the use of pre-metered coating methods. Figure 1.1 shows a simplistic illustration of key features of such a process. The web is transported continuously through the machine from the unwind point to the rewind point. The fluids are applied at a coating applicator and subsequently dried by passing through a dryer usually comprising jets of air that impinge onto the wet coating. Chilling is frequently applied at a stage intermediate between coating and drying – especially where the fluids comprise a significant proportion of gelatin. Roller magazines allow rollers to be changed without stopping the coating process. The process speed is thus constrained to ensure that under all conditions, the coated surface

is completely dry when coming into contact with a web bearing roller or as the web is finally reeled.

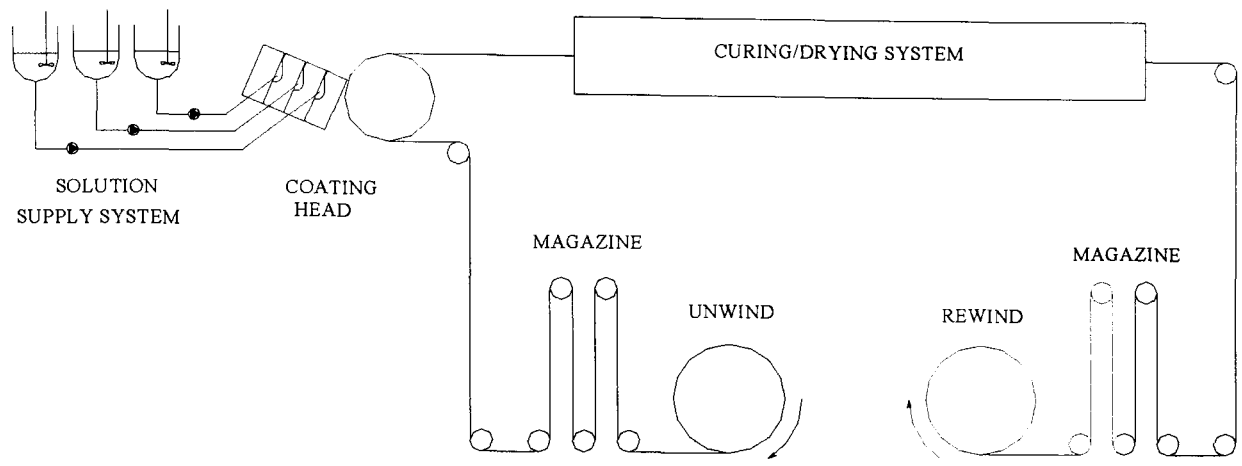

Figure 1.1: Schematic of Industrial Web Coating Plant

The invention of multilayer coating dates back to the early 1950s owing to the need to manufacture colour photographic materials at low cost, see Hens [1996]. Russell [1956] showed how the slot and slide coating methods could be adapted to cater for this purpose. The slide bead process eventually superseded slot coating for the photographic industry as being shown capable of applying any number of layers simultaneously whereas slot coating is limited to two or at the most three such layers. Whereas curtain coating has been used for many years, for example in coating candy cores, Hughes [1970] showed that the process could also be adapted to facilitate multilayer coating.

This thesis is mainly concerned with the application of the slide bead coating process. However comparison is frequently made with the curtain coating process. These two coating methods will now be described in more detail.

1.2 Pre-metered Multilayer Coating Methods

1.2.1 Slide Bead Coating

The slide coating method is shown simplistically in Figure 1.2. The "cascade" coater basically consists of metal blocks clamped together to form cavities and slots through which solutions are pumped to form the individual layers. The number of blocks

varies according to the number of layers required to be coated in a single pass. Up to ten or even eighteen layers can thus be coated simultaneously if so required.

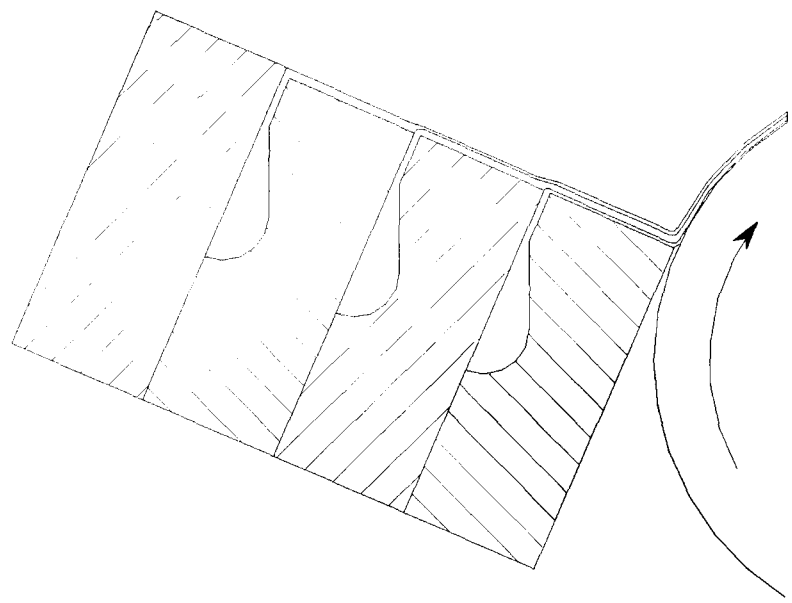

Figure1.2: Slide Bead Coater

When initially starting the coating process, the coater is positioned several centimetres away from the coating roller to ensure the web does not become prematurely fouled while forming a desired flow. The liquids are each pumped up in turn through the slots, commencing with the lower layer. The solution emerging from the upper slot becomes established as a thin uniform flow down the inclined plane or "slide" and merges with the next layer down at the second slot exit. This process is repeated at each subsequent slot exit. The solutions on the slide are bounded at the sides by edge guides. The liquids are maintained as separate layers provided that the surface tension decreases in moving upwards from any one layer to the next - Gutoff [1992].

Once the flow on the slide is established and free of bubbles, the web is set in motion at the required coating speed. The coater is moved towards the coating roller carrying the web until the gap between the end of the slide and the web reduces down to a predetermined value. The mechanical mounting system and machining tolerances are arranged to ensure the gap is accurately parallel and reproducibly controlled to this value, which can typically be in the range of 0.1 to 0.3 mm. This "dipping in" process causes the top layer to initially wet the web. The fluids become rapidly dragged upwards by the shear forces exerted by the substrate and stretch and thin at the terminus of the slide as they accelerate to match the speed of the web. In the final equilibrium state, a bead is formed within the gap while remaining in the form of

discrete layers – as shown in Figure 1.2. The stability of the bead is enhanced by applying a small slightly sub-ambient pressure below the bead. This is enabled by mounting a suction box formed by a lower back bar and side plates. The edges of the back bar and plates are set as close as possible to the coating roller, while ensuring adequate clearance for the moving web.

The coater must be withdrawn from its normal coating position by a small amount to allow each inter-roll splice to pass through without damaging the coating head and then returned. It is important that this "join-withdrawal" operation allows the splice to be overcoated without interruption so as to ensure the laydown of wet fluid on the splice and adjoining web surface is of the same thickness as generally applied over the remainder of the base stock roll. Failure to achieve this can result in fouling of the machine due to inadequate drying of overthick portions of coating. This is because the process is often run to within the limits dictated by the capacity of the drying plant, see Katagiri et al. [2003].

1.2.2 Curtain Coating

Curtain coating has been used for many years, for example in coating candy cores - but more recently developed as a viable method for multilayer coating. The method generally adopted for multilayer coating of photographic materials is to use a slot fed slide (Hughes [1970]). This is extended at the end to form a rounded nose terminating at a vertical edge – Figure 1.3 – thereby allowing the layers to fall freely to impinge as discrete layers onto the web.

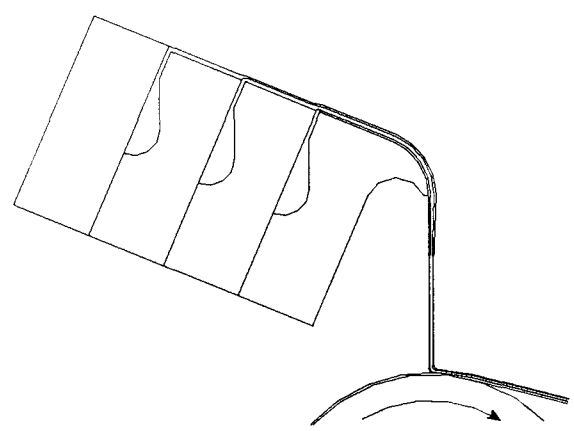

Figure 1.3: Curtain Coater

The main advantages of this system are:

1. The process can generally operate at higher speeds than for slide bead coating owing to the higher impingement velocity which helps to inhibit air-entrainment – see Section 1.3.1 and Blake et al. [1995]
2. It is possible to coat solutions of higher viscosity
3. It is no longer necessary to apply suction to stabilise coating
4. The tolerances for machining and maintaining the straightness of the coater and coating roller can be relaxed owing to the avoidance of very small gaps
5. The large gap also means the coater does not have to be moved to allow splices to pass through (Gutoff [1992])
6. The process does not suffer from streak-lines to the same extent as found with slide coating – see Section 1.3.4

A major limitation of the process is that it is necessary to maintain a minimum flow rate to ensure the falling curtain is sufficiently stable for good coating - Greiller [1976]. Arguments favouring a consequential costly increase in drying capacity when converting from slide bead to curtain coating are in part offset by the ability to coat solutions of higher viscosity and hence less water content.

1.3 The Advantages and Limitations of Slide Bead Coating

The process does not suffer from a constraint on minimum coating speed dictated by flow stability – unlike curtain coating, which requires a minimum flow rate of about 0.5 cm^2s^{-1} (Greiller [1975]).

Earlier work with this process indicated a general belief that the maximum speed of coating is of the order of 150 m/minute as compared with several hundred metres per minute using the curtain process (see for example, Poirier [1966], Booth [1970] and Dragomirescu et al. [2001]). Dittman and Rozzi [1977], however, showed that the coating speed can be enhanced for the multilayer slide bead process to about 210 m/minute using a thin low viscosity bottom layer called a carrier layer – as introduced in detail in Section 1.4. Ishizaki and Fuchigami [1985] were able to demonstrate that

the speed could be further enhanced up to 270 m/minute using water as a carrier layer. Vandaele and Vancoppenolle [1999] demonstrated that the limit for single layer gelatin coatings could be increased to 200 m/minute or more using the method of electrostatic assist – to be discussed in Section 1.5.3. More recently, Clarke et al. [2003] have shown how the method of roughness assist to be discussed in Section 1.5.2 could be combined with electrostatic assist to raise the limit for the process to as high as 540 m/minute under the right conditions.

The slide bead coater, while proven to be a versatile process for manufacturing a wide variety of multilayer based products, suffers from a number of limitations. Some of these will now be described in the following sections.

1.3.1 Ribbing Instability and Rivulets

As suction applied to the lower meniscus is increased, a point is eventually reached where the bead becomes unstable - resulting in a steady regular pattern of lengthwise streaklines, known as ribbing (Hens and Van Abbenyen[1997]) – as shown in Figure 1.4.

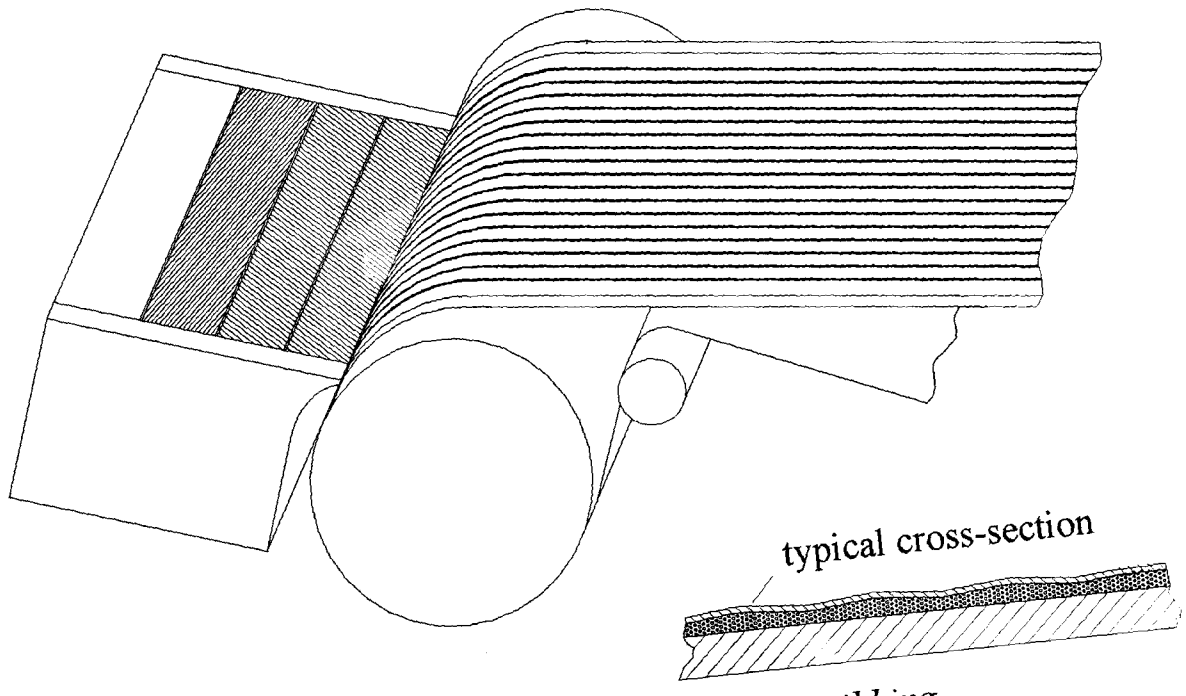

Figure 1.4: Narrow width coating showing ribbing

The wavelength of the ribs is typically a few millimeters. Ikin [1992] observed that for a particular coater geometry investigated, the ribs appear where there is a "hump" in the flow down the slide and appear to originate just upstream of the hump.

Ribbing can vary in amplitude and in the extreme can cause the bead to break up into rivulets with uncoated streaks in between the ribs (Durst and Wagner [1997]). This can occur as the stabilisation suction is further increased (Hens and Van Abbenyen[1997]) or if the mean thickness is low (Schweizer and Rossier [2003]).

Hens and Abbenyen [1997] point out that the exact cause of the ribbing phenomenon is not completely clear. The mechanisms for slide bead coating are thought to be the same as for other coating processes (Schweizer and Rossier [2001]). These occur in the presence of an adverse pressure gradient where the disturbing pressure forces within the coating bead can no longer be balanced by restoring surface tension forces (Ruschak [1985], Hens and Boiy [1986], Coyle et al. [1990], Cohen and Gutoff [1992], Durst and Wagner [1997] and Schweizer and Rossier [2001]) and Schweizer and Rossier [2003]).

Zeldes [1985] conducted a range of experiments, in which he studied the onset of ribbing for solutions containing surfactants and showed the addition of fluorocarbon and a hydrocarbon surfactant enhances the resistance against ribbing. The effect of a surfactant is to cause the surface tension to vary with the elapse of time after the free surface has been rapidly stretched thereby depleting the concentration of surface-active molecules. A full description of the measurement of dynamic surface tension is described in Section 2.2.3. Valentini et al. [1991] and [1996] took as a measure of surface elasticity the time differential of the dynamic surface tension. They found for single layer coatings that ribbing became prevalent as the surface elasticity was low corresponding with the surfactant concentration being high. The sensitivity to ribbing for two layers was determined by the lower of the two surface elasticities. The experiments moreover allowed the bead to be profiled by coating onto a transparent web supported by a curved skid in place of a coating roller. They showed that the maximum suction for no ribbing increased as the curvature of the upper meniscus increased.

Isayama and Takehara [1981] found that ribbing could be reduced by cutting a groove near the end of the slide of depth such as to reduce the height of the hump in the standing wave seen at the terminus of the slide. Schweizer and Rossier [2001] conclude that ribbing is feasible in the flow fields of rapidly thinning films characteristic of slot coating, film splitting flow as in forward roll coating and at the end of the slide in slide bead coating, while explaining why ribbing is not seen in curtain coating where the thinning is more gradual. They carried out a range of experimental trials using a slide coater applying liquid to the surface of a roller. The roller was continually scraped clean to allow continuous observation of the tendency of ribbing as seen by reflected light. Their results showed that the coating speed for no ribbing increases with flow rate per unit width, the sensitivity reducing as suction pressure reduced and as viscosity increased.

1.3.2 Limits to the Minimum Stabilisation Suction

As will be described in greater detail in Section 3.2.2, Cohen and Gutoff [1992] found that the minimum wet laydown H_∞ for a web speed V, viscosity μ, surface tension σ, density ρ and coating gap H_G is given in terms of the suction pressure δP by the expression:

$$H_\infty > \frac{2.19\sigma^{0.25}\mu V^{0.5}}{\rho^{0.25} H_G^{0.25} \delta P} \qquad \text{if } \frac{\delta P}{\rho V^2} < 3.32 \tag{1.1}$$

Cohen and Gutoff [1992] point out that the limits dictating the maximum coating speed for a given coating thickness and those determining the lowest coating thickness at a given coating speed are in fact the same and known as the low flow limits of coatability. Transferring the terms in equation (1.1) gives:

$$\delta P > \frac{2.19\sigma^{0.25}\mu V^{0.5}}{\rho^{0.25} H_G^{0.25} H_\infty} \tag{1.2}$$

It is thus plausible to suggest that the low suction limits are also due the same mechanisms as responsible for the low flow limits when exploring minimum wet laydown at a given suction pressure. In practice, the limits are generally dictated by

the tendency for the bead to become unstable and breaking up to form rivulets. This often starts at the edges (Hens and Van Abbenyen [1997]).

The robustness against this edge break phenomenon can be enhanced by ensuring the coating flow on the slide is uniformly thick across the width. At any given point on the slide, the height of the upper surfaces of the edge guides should ideally match the height of the surface of the liquid flowing down the incline (Barstow [1966]).

1.3.3 Air Entrainment

It is possible within certain limitations to maintain a stable bead and under these conditions, the profiles of the free surfaces and the interface between layers are typically as illustrated in Figure 1.5. During coating, liquid displaces air from the surface of the substrate at the dynamic wetting line where air, solid and liquid meet. The lower interface spans the gap, terminating at the lip of the coater at a line where the liquid is essentially stationary. This line is thus called the static wetting line. When viewed through an optical microscope, the interface is seen to apparently intersect the substrate at a well defined angle. This angle is defined as the dynamic contact angle when measured within the fluid – Figure 1.5.

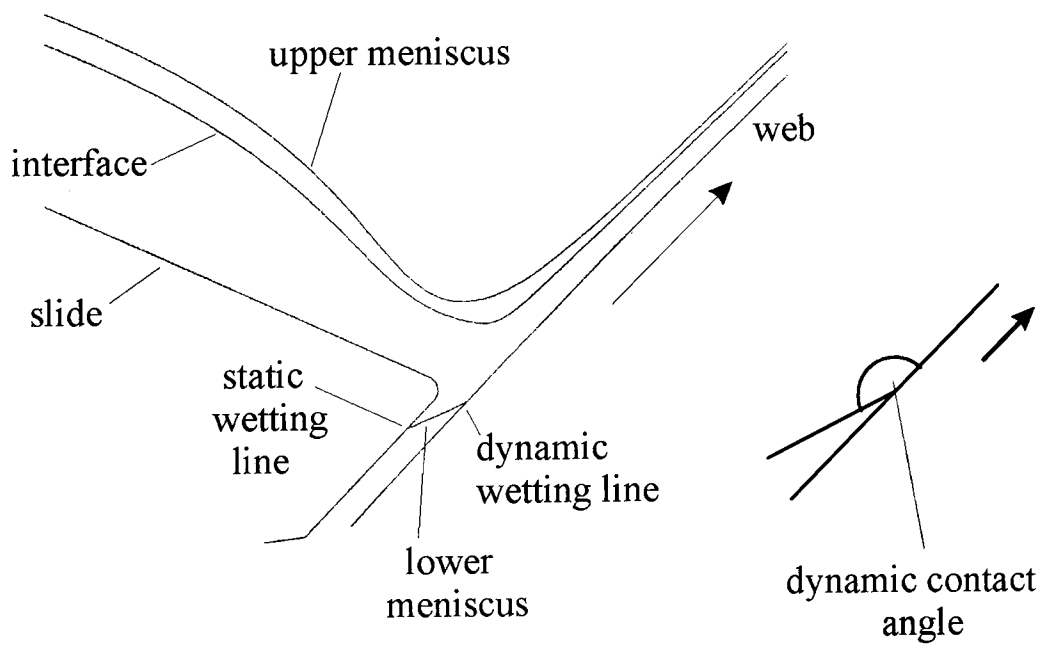

Figure 1.5: The bead forming zone for two layers

At low coating speeds, the dynamic contact angle is the same as the advancing static contact angle. However, as speed is increased, the dynamic contact angle monotonically approaches 180° (Ruschak [1985]).

The key forces (Gutoff [1992], Hens & Van Abbenyen [1997]) acting on the bead are:

1. The upwards viscous drag exerted by the wetted web surface – tending to destabilise the bead

2. The downward force on the lower meniscus due to applied suction — tending to stabilise the bead

3. Inertial forces associated with the momentum of the liquid flowing down the slide and carried off by the moving web

4. An upward acting force due to the momentum of a thin film of air carried along with the moving web surface – tending to destabilise the bead

Increasing viscous drag or reducing the stabilisation suction cause the dynamic contact angle to increase and approach 180° and a point will be reached where air becomes totally entrained and coating fails.

Blake [1993] describes how at values just less than 180°, the dynamic wetting line becomes disrupted to form a sawtooth shape – Figure 1.6. Blake and Ruschak [1979] have shown experimentally that the angle ϕ between the normal to each straight line segment of the sawtooth wetting line and the machine direction is constant and given by:

$$\cos\phi = \frac{s_{180}}{S} \tag{1.3}$$

where s_{180} is the maximum velocity of wetting for a dynamic contact angle of 180° and S is the speed of the substrate. Minute bubbles are seen to become entrained at the leading points of the sawtooth resulting in sporadic patches of defective coating (Blake [1993]).

The appearance of these defects may take on a variety of shapes and features depending on the particular set of pertaining conditions - Figures 1.7 and 1.8. Figure 1.9 serves to illustrate the structure of a bubble cluster and associated coating disturbance at the onset of air entrainment.

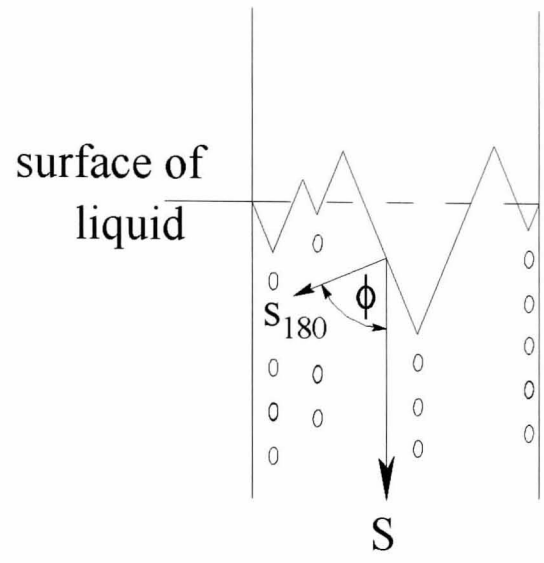

Figure 1.6: Sawtooth waveform as the dynamic contact angle approaches 180° (Blake [1993])

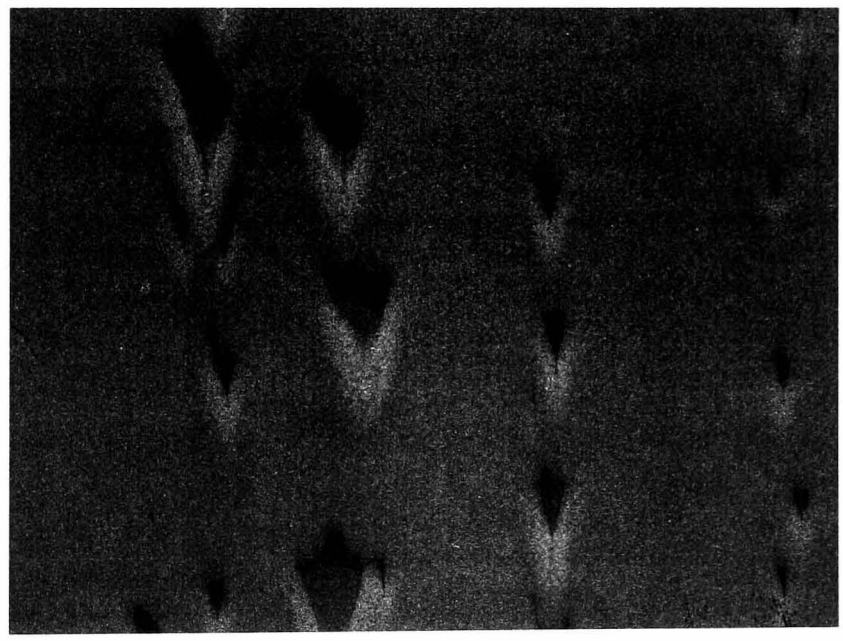

Figure 1.7: Example of coating misses due to air entrainment

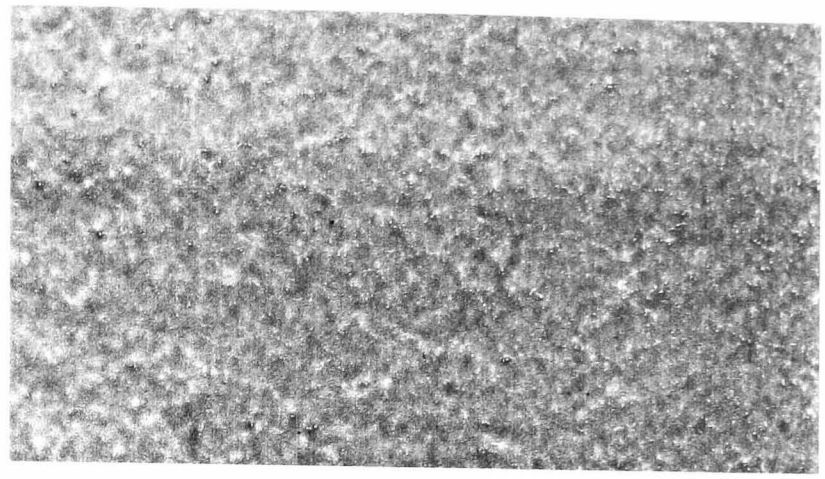

Figure 1.8: Example of minute bubbles due to air entrainment

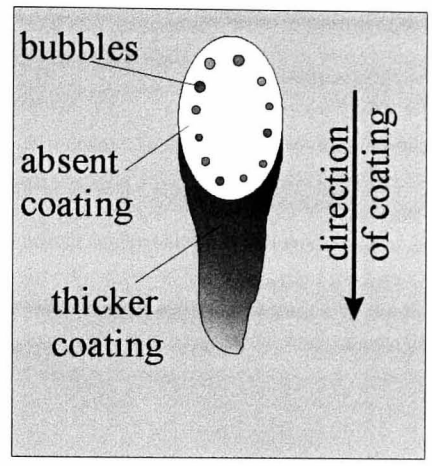

Figure 1.9: Bubble cluster at the onset of air entrainment

The speed at which air becomes entrained for a given coating process is found to be dependent on the properties of the substrate. For example, Goppert-Berarducci and Higgins [2001] have demonstrated using a needle coater that a substrate can be designated with an index value provided the roughness Rz is less than 3 μm. This is given as the ratio of the air entrainment speeds for the sample under test and for a reference substrate comprising ultra-smooth polyethylene terephthalate.

1.3.4 The Coating Window

The operability limits due to ribbing, rivulets, edge failure and air entrainment can be depicted in a number of ways. In principle, the performance can be represented in multidimensional space. It is general practice within the industries using the slide bead coating process to plot the suction pressure as a function of coating speed (Hens and Abbenyen [1997].) Figure 1.10 shows a coating window for a typical gelatin

coating. The diagram shows an additional limit where excess suction pressure can cause the bead to be partially or wholly pulled right through the coating gap to bleed fluid into the suction box.

It will be seen that the lower and upper limits for suction converge at a point representative of the maximum coating speed.

The criteria for good quality can often be more restrictive than those for establishing whether or not the coating is feasible. Coating quality windows can thus be plotted in similar fashion in accordance with acceptance standards that depend on the end use of the coated product (Hens & Abbenyen [1997]).

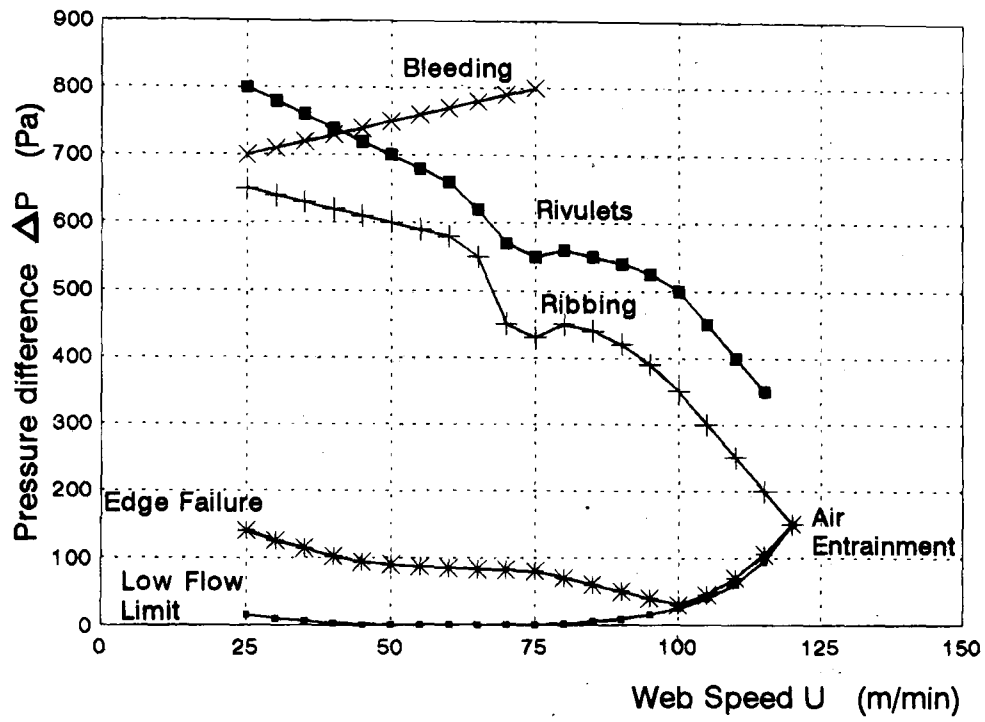

Figure 1.10: Coating window for a typical gelatin coating (Hens & Abbenyen [1997])

1.3.5 Streak-line Defects

The slide coating process is prone to generating streak-lines. In extreme cases, foreign matter can get caught in the nip between the termination of the slide and locally break the bead. In the general case, however, the fluids become disturbed and redistribute by flowing sideways to form regions of non-uniform coating thickness (Apps [2000]). The free surface, when thus disturbed, tends to heal due to the levelling action of surface tension (Orchard [1962]). Healing is minimal at an interface between adjacent

layers, however, due to the lack of interfacial tension (Tricot[1997]). This results in visible defects on the final dried coating. Figure 1.11 illustrates the generation of a single streak-line and the appearance of the free surface and the interlayer interface for a two layer coating before the free surface has fully levelled.

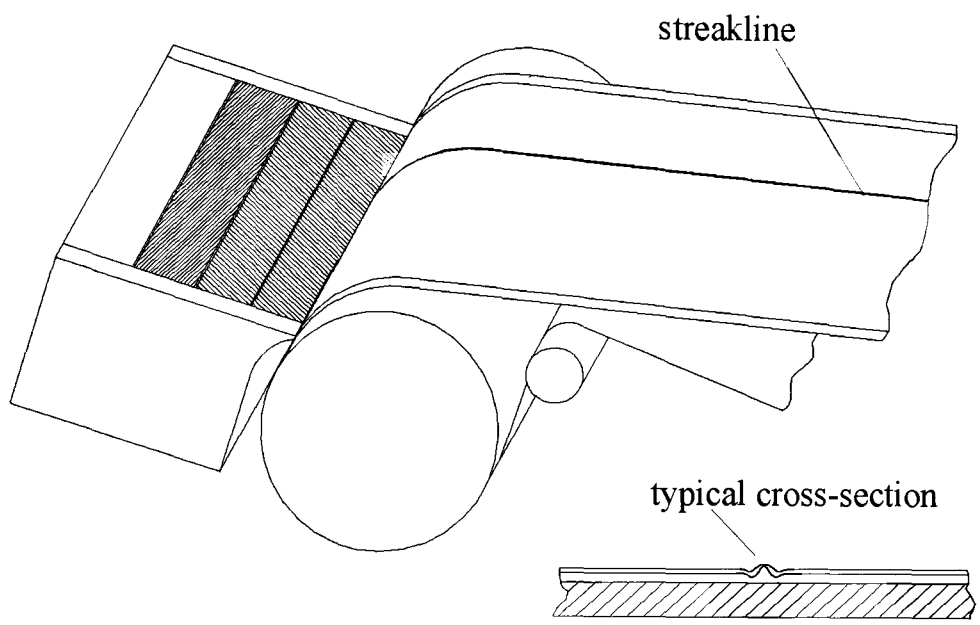

Figure 1.11: Narrow width coating showing a single streak

It is now well established that recirculations in the coating flow are a major cause of streak-line defects (Hens and Van Abbenyen [1997]). The vortices can trap particles or bubbles, which then disturb the flow. Solutions of unstable chemistry will generate solid deposits at the walls due to the long residence time associated with the vortex. Pieces of the solid deposit, being often fragile in nature, can subsequently become dislodged to form a ragged wetting line, which has been shown experimentally to lead to streak-lines. Noakes et al. [2002(1)] showed evidence that the occurrence of streaklines is directly linked to deposit growth, which in turn, closely relates to the strength of the vortex.

Vortices tend to occur where there is a sudden change in direction of the flow. They can thus be found at the exits of the slots or in the bead forming zone (Schweizer [1988], Ikin et al. [1997] and Gaskell et al. [1999]). Figure 1.12 illustrates what happens as suction is increased thereby causing the static wetting line to migrate down the lip face. The illustration shows two of a whole family of counter-rotating vortices as initially described by Moffatt [1964].

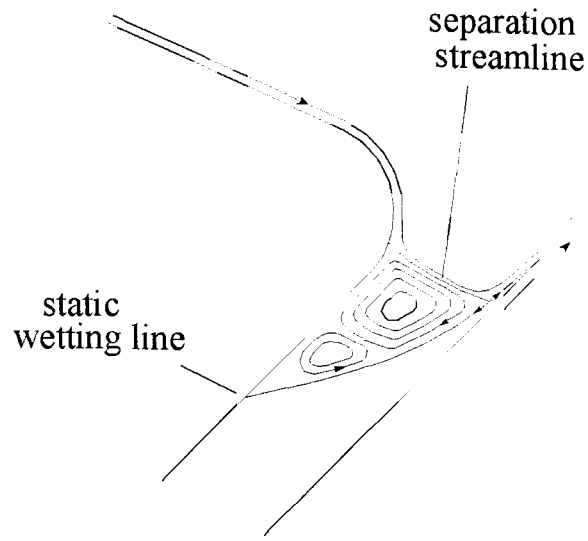

Figure 1.12: Typical counter-rotating vortices in the coating gap

Various methods for inhibiting the migration of the static wetting line away from the lip corner have been investigated. Tobari and Kishido [1998] claim enhanced resistance to streak-lines by applying a hydro-phobic silane material to the lip face. Ikin et al. [2001] showed that the use of a thin low viscosity carrier layer while increasing the average viscosity of the layer assembly is also advantageous – as will be described in more detail in Section 1.4.

Noakes et al. [2002(1)] have shown that lines originating from vortices near the top of the upstream face of the upper slot can be eliminated by ensuring the static wetting line pins to the upstream corner at the slot exit and maintaining the static contact angle close to 90°. They also demonstrated that this could be readily accomplished by applying a silane to the slide face adjoining the backwall of the slot in order to inhibit back-wetting (Schweizer [1997(1)]).

1.3.6 Barring

Barring is a general term for a coating defect caused by an unsteady transfer of fluid onto the web resulting in periodic disturbances in the final thickness of the coating of one or more layers in the machine direction. Oscillations can occur, either spontaneously or excited by external sources within the coating plant (Hens and Van Abbenyen [1997]). Van Abbenyen, Christodoulou and Scriven [1988] showed from

numerical studies of the dynamic response of a two layer coating flow to perturbations that variations in web speed cause a peak response at about 20 Hz, the flow field indicating that this resonance mode was associated with the upper free surface. They moreover found horizontal vibrations of the coating roller to be particularly dangerous at frequencies of the order of several hundred hertz. Pump induced disturbances can become amplified to form waves that grow with time (Conroy and Weinstein [1994]). Instabilities on the slide are further described in Section 1.3.7.

Levarlet et al. [1997] have developed techniques for measuring the dynamic perturbation response using a sensor for detecting coating weight variations while continuously coating. The response to stabilisation suction was examined by exciting the air within the suction box using a loudspeaker. The responses to flow rate and web speed were studied by varying motor current in a periodic manner.

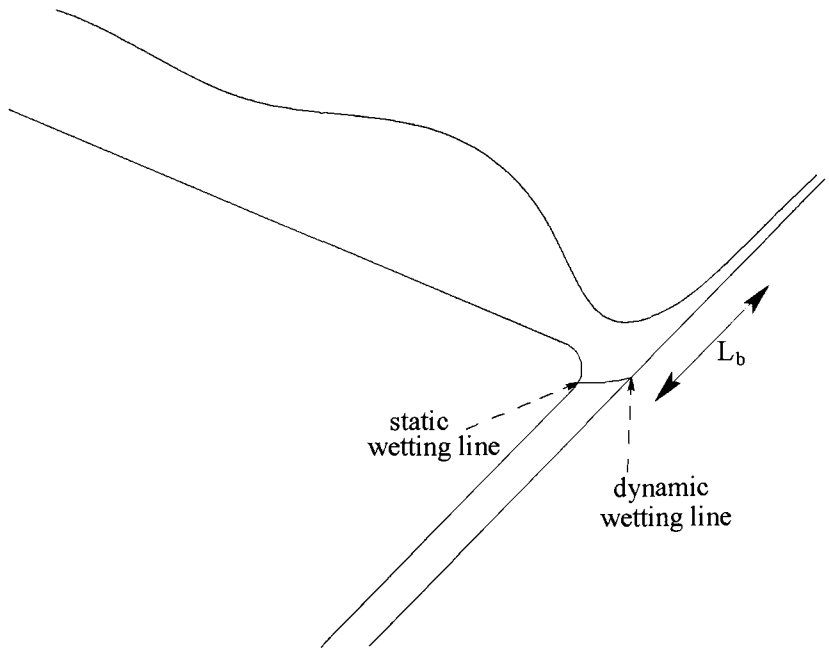

Figure 1.13: Definition of L_b (Hens [1986])

It is well known that the sensitivity to external disturbances increases rapidly as the low flow limit is approached (Hackler et al. [1992]). Hens and Van Abbenyen [1997] suggest that contact bead length L_b provides a good indicator of robustness against perturbations. Here L_b is defined as the distance between the dynamic wetting line and the point at which the free surface is inclined to the web at an angle of 2.86° (Hens and Boiy [1986]) – see Figure 1.13.

1.3.7 Slide Waves

The flow of one or more layers on the slide is prone to instabilities resulting in wavelike perturbations travelling down the inclined plane (Hens and Van Abbenyen [1997]) – see Figure 1.14.

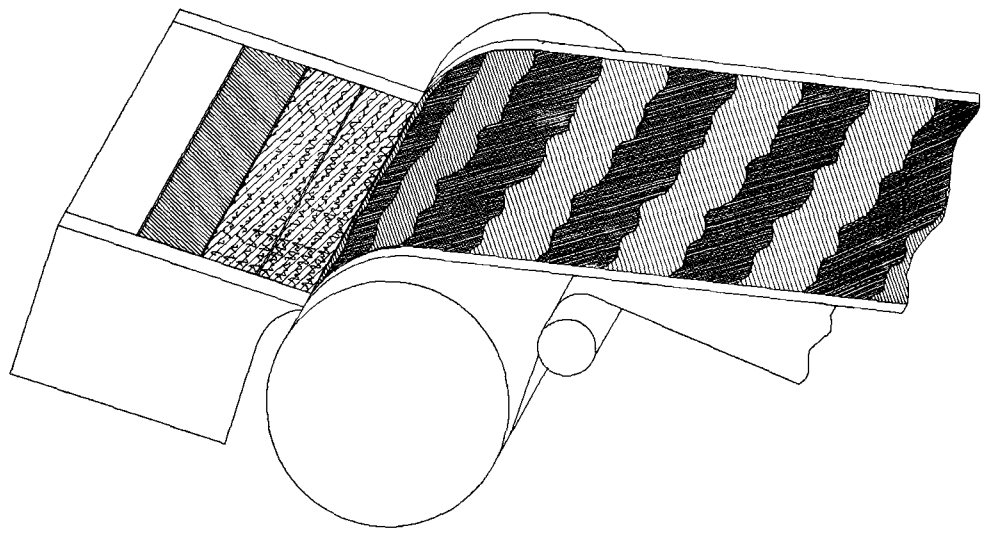

Figure 1.14: Narrow width coating showing slidewaves

The stability analysis of flows on an inclined plane has been undertaken by many workers (for example Yih [1963]; Kao [1965]; Kao [1968]; Weinstein [1990] and Kobayashi [1992].) Yih [1963] determined the stability condition for single layer flows down an incline and concluded that increasing the inclination angle and the coating speed while decreasing the viscosity and the surface tension tended to instability. Weinstein [1990] calculated wave growth factors for multilayer flows and included the effect of shear thinning rheology. He showed that waves associated with the free surface propagate as if they were in a Newtonian system, where the viscosity is an average of the varying viscosities in the shear thinning layer. He also showed that interfacial waves are largely influenced by a local jump in viscosity at the interface. Kobayashi [1992] also solved the Orr-Sommerfeld equations to show that an interfacial mode is always unstable as soon as there is a finite mismatch of viscosity of adjacent layers. He moreover calculated the rate of growth of disturbances as appreciating that from a practical point of view, the slide on a typical coating process is only a few centimetres in length. He also backed up his computations with some

experimental coating trials and obtained good agreement with his predictions on overall defect severity. His results for a typical case study – Figure 1.15 - show that the rate of growth of the interfacial mode exceeds that for surface waves as the viscosity ratio m departs significantly either side of unity. Here m is given by:

$$m = \frac{\mu_2}{\mu_1} \tag{1.4}$$

where μ_1 and μ_2 are the viscosities of the lower and upper layers respectively.

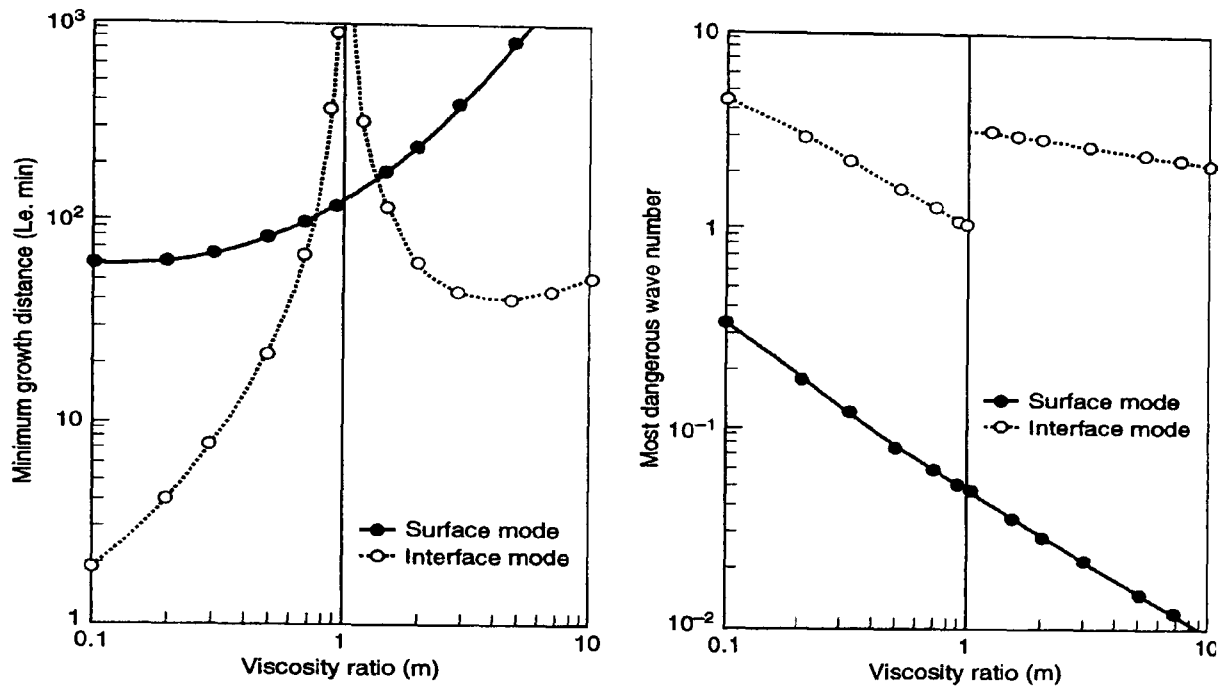

Figure 1.15 Numerical slidewave data of Kobayashi

Conroy and Weinstein [1994] have published a method claiming the advantages of computing the growth of interfacial waves initially triggered from external disturbances. The computations are based on their earlier work on multilayer assemblies (Weinstein [1990]). They show that it is possible to optimise the selection of a layer for dilution with a hardening agent by first computing the wave growth amplification factor. Examples are given which show that the wave amplification factor increases as the layer thickness decreases.

1.3.8 Mottle

Mottle is a general term given to an irregularly patterned defect that can vary from being subtle to gross (Gutoff and Cohen [1995]). Causes vary and include the following:

1. Corona induced patchy surface charge distributions on the surface of the substrate can result in non-uniform coating (Mori et al. [2002]). The distribution may be smoothed and the mottle reduced by firstly flooding the web surface with negative charge and then neutralising with a positive charge (Gibbons et al. [1972], Hartman [1989]).
2. A substrate with a slightly undulating surface can cause a multi-layered coating to subsequently flow from high points to low points under the influence of gravity as governed by the levelling mechanism (Orchard [1962] and Joos [1996]).
3. The generation of surface disturbances due the impingement of air on the wet coating during the early part of drying (Gutoff and Cohen [19995]). This will be considered in more detail in Section 1.6.2.

1.3.9 Join Withdrawal

The interaction of coating flows with a passing join and the general behaviour of the flow as the gap is temporarily opened up has been generally overlooked outside of industry. Katagiri et al. [2003] give special consideration to the overcoating of joins using the curtain process. They conclude that good performance can be obtained by arranging for the viscosity of an intermediate layer to exceed 300 mPa.s, provided that the web tension is sufficient to maintain the join flat when passing over the coating roller. Nakajima [2002] claims that bead break at joins can be prevented for the slide bead process by momentarily increasing the stabilisation suction as the gap is opened out. Yapel et al. [1999] recommend a method whereby the suction box is free to move about a pivot as the gap is opened up to accommodate a passing join. The mechanism is arranged in such a way as to allow the clearances relative to the coating roller as well as the stabilisation suction to be optimised during the short time the join passes through the coating station.

1.3.10 Optimum Coating Geometry

The parameters considered here are the application angle α, the slide inclination angle β and the impingement angle γ shown in Figure 1.16. In specifying these parameters, it is assumed that the slide is inclined at the angle β over its entire length.

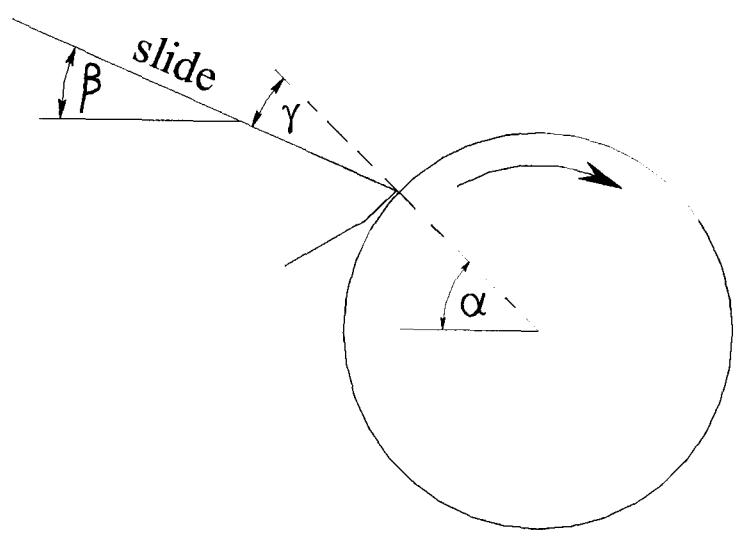

Figure 1.16: Parameters defining coater geometry

From simple geometry,

$$\gamma = \alpha - \beta \tag{1.5}$$

As pointed out by Schweizer et al. [2001], the key parameters of interest to the mechanical design engineer are α and β, whereas the flow field responsible for determining coating performance is essentially determined by the slide inclination angle β and the impingement angle γ.

Burket et al. [1984] showed that the maximum stabilisation suction for which coating remained feasible increased with inclination angle β. The limit on β as dictated by slidewaves was found to be 40°. Having optimised the slide angle, they then varied the application angle and found that the optimum impingement angle was 0°. Katagiri et al. [2001] also state that the preferred inclination angle β is 40° when considering the coating of a multilayer gelatin based assembly constrained by:

$$0.05 < \frac{Q_1}{Q_{total}} < 0.2 \tag{1.6}$$

$$0.2 < \frac{\mu_1}{\mu_2} < 0.67 \tag{1.8}$$

and

$$C_2 - C_1 < 2\% \tag{1.9}$$

where Q_1 and Q_{total} are the flow rates per unit width of the bottom layer and total assembly respectively, μ_1 and μ_2 are the viscosities of the layers and C_1 and C_2 the percentage gelatin concentrations, the suffixes 1 and 2 corresponding to the bottom and adjacent layers respectively. Schweizer and Rossier [2001] found, when fixing β at 23°, that the optimum impingement angle γ is close to 0° for maximum robustness against ribbing. Earlier work by Jackson [1976] and Hirschburg and Christodoulou [1995] showed that where the application angle was constrained to negative values, enhanced coating performance was obtained by remachining the slide to form an upswept lip. Schweizer and Rossier [2001] point out that this modification tends to impose an impingement angle closer to 0°, provided that the length of the upswept lip is at least as long as the characteristic dimension of the bead flow field. Nakajima [2002] claims that the lower practical limit for the slide inclination angle is 10° for achieving adequate flow and the upper limit for no slide waves 30°. He finds that γ should exceed –35° to inhibit ribbing. He additionally claims that the angle of inclination of the lip face to the web surface should not exceed 20° in order to reduce static wetting line migration to acceptable limits.

The general evidence suggests that optimum performance is obtained at higher slide inclination angles while maintaining the slide flow normal to the web at the dynamic wetting line. The explanation for this effect (Hens and Abbenyen [1997]) is founded on the principle of hydrodynamic assist explored by Blake, Clarke and Ruschak [1994] when coating aqueous gelatin onto dry base using a falling curtain. They found that the maximum wetting speed U in units of m/s could be represented by:

$$U = \frac{8.09(V_n \cos\gamma)^{0.81}}{\mu_0^{0.19}} \qquad \text{for } \mu_0 > 14 \text{ mPa.s} \tag{1.10}$$

where V_n is the speed of impingement of the falling curtain in units of m/s, γ the inclination of the web from the horizontal plane at the point of impingement and μ_0 the low shear viscosity in units of mPa.s. They also established that the maximum coating speed was attained when the wetting line was located directly beneath the

falling curtain. Miyamoto and Katagiri [1997] suggest that the capability for high coating speeds using curtain coating is attributed to the localised pressure that results from the high impinging velocity. They argue that the pressure squeezes out the air film that may be entrained between the liquid and the substrate – hence preventing shear-induced instability of the interface at the dynamic wetting line which would otherwise generate catastrophic air entrainment.

1.4 Carrier Layers

1.4.1 The Role of the Lower Layer Viscosity

Air begins to get entrained as the dynamic contact angle approaches 180° - as described in Section 1.3.3. Hoffman [1975] measured the apparent dynamic contact angle θ_D for liquids in capillary tubes. He found his data for liquids fell on a single curve given by $Ca = F(\theta_D)$ for liquids displaying zero static contact angle (Blake and Ruschak [1997]). For liquids with a non zero value of the advancing static contact angle θ_A, he found his data fell on this same curve – Figure 1.17 - if a shift factor was used where:

$$Ca = \frac{\mu U}{\sigma} = F(\theta_D) - F(\theta_A) \tag{1.11}$$

where θ_A is the advancing static contact angle.

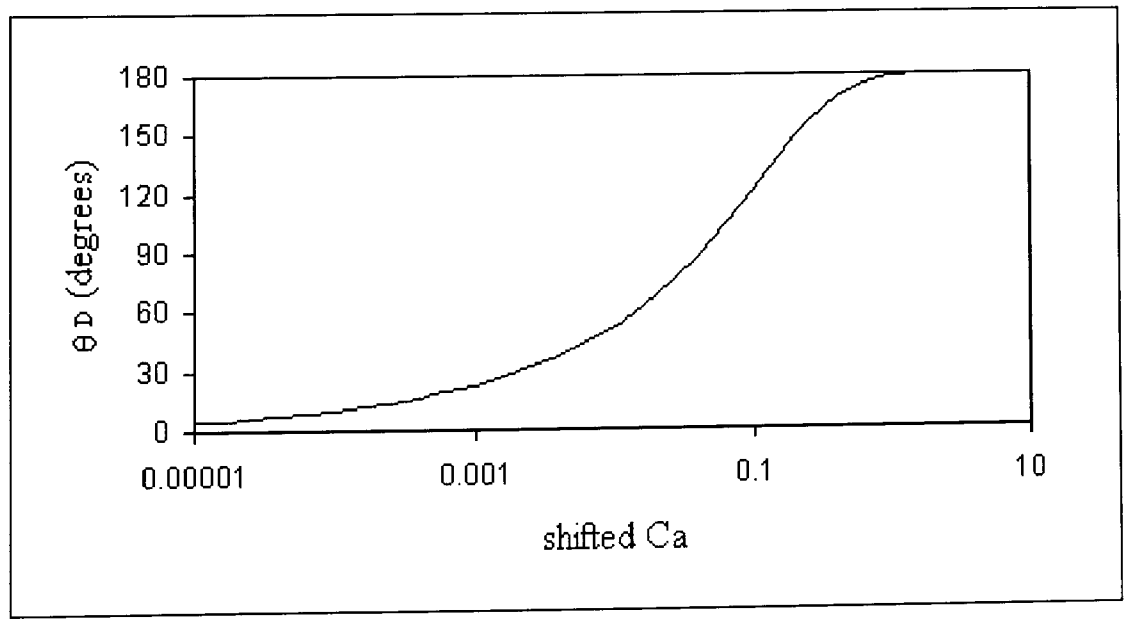

Figure 1.17: Data of Hoffman (Blake and Ruschak [1997])

It is thus plausible to conclude that decreasing the viscosity of the layer responsible for wetting the base will reduce the dynamic contact angle and hence combat the tendency for air entrainment. This concept was initially proposed by Dittman and Rozzi [1977]. They moreover showed that it was still possible to achieve high coating speeds using a thin bottom low viscosity "carrier" layer.

Schweizer and Rossier [2001] concluded from their work on the study of ribbing using a slide bead coater that high coating speeds for a single layer can only be achieved as the viscosity is reduced. They found that implementing the carrier layer concept by combining a thin low viscosity bottom layer with a high viscosity main layer, it was possible to achieve high coating speeds without ribbing.

1.4.2 The Role of the Weighted Mean Viscosity

Dittman and Rozzi [1977] point out that it is advantageous to arrange for the viscosity of layers other than the bottom layer to be substantially higher. A key benefit includes the lower demand for solvent and hence a reduction in drying load (Dittman and Rozzi [1977]).

The upward destabilising force on the lower meniscus predominately comprises viscous drag and air film momentum while the stabilising downward force is largely supplied by suction – Cohen and Gutoff [1972]. As shown in Section 1.3.5 and Figure 1.12, the flow separates at the static wetting line on the lip face to generate counter-rotating vortices in the wedge of fluid between the lip wall and the lower meniscus. Any weakening in the upward force resulting in the static wetting line migrating further down the lip face enlarges the recirculations and hence the propensity for streak-lines. When considering the simplest case of a single layer, it is seen that the liquid delivered to the bead is accelerated by the viscous action of the moving web, as described by Sakiadis [1961] using classical boundary layer theory (Hens and Van Abbenyen [1997]). Fluid is entrained over a length just in excess of L_b (Figure 1.13), thinning down to the final wet layer thickness H_∞. Hens and Van Abbenyen [1997] estimate that the force $F_{v,w}$ exerted by the web on the bead is given by:

$$F_{v,w} \approx \frac{\mu U L_b}{H_\infty} \tag{1.12}$$

The wall shear stress is thus proportional to the product of viscosity and flow rate.

In considering the more general case of n distinct layers, it is clear that all layers contribute to the viscous drag exerted on the bead. It would seem reasonable to assume that the upward force is at least approximately proportional to the weighted mean viscosity given by the expression:

$$\langle\mu\rangle = \frac{\Sigma_{(1..n)}(\mu_i.Q_i)}{\Sigma_{(1..n)}(Q_i)} \tag{1.13}$$

where μ_i and Q_i are the viscosity and flow rate of the i^{th} layer respectively.

As pointed out by Dittman and Rozzi [1977], the optimum solution is obtained from increasing the weighted mean viscosity $\langle\mu\rangle$ while reducing the viscosity μ_1 and wet thickness of the lower layer. This has the additional benefit of a reduced tendency for particles or crystals to be caught on the lip of the coating hopper and it can also be inferred from the above argument and the discussion in Section 1.3.5 that there is consequently a lower propensity for streak-line defects.

1.4.3 The Exploitation of the Carrier Layer Concept

Dittman and Rozzi [1977] claimed that it is possible to achieve speeds up to 300 m/min using a carrier layer of viscosity typically ranging from 3 to 5 mPa.s laid down at a wet thickness between 5 and 10 μm. They stated that the viscosity of the adjacent layer should be in the range 30 to 70 mPa.s and of wet thickness 20 to 35 μm for the reasons already discussed. They pointed out that interlayer mixing effects occur within the coating bead at the interface between the two lowest layers and that this places constraints on the constituents.

Choinski [1978] recommended the use of a shear thinning pseudoplastic carrier layer whereby the viscosity at the high shear rate known to apply near the dynamic wetting line (Muës, Hens and Boiy [1989]) is significantly lower than elsewhere within the flow. This is designed to overcome the tendency for instability of the flow on the slide

associated with a low viscosity liquid (Hens and Van Abbenyen [1997]). He states that the viscosity of the carrier layer should preferably be less than 5 mPa.s when measured at a shear rate of 10^4 s^{-1} and in the range 20 to 200 mPa.s at 100 s^{-1}. Choinski [1978] established improved performance using a power law fluid where the viscosity is given by:

$$\mu = m\dot{\gamma}^{n-1} \tag{1.14}$$

and showed that the consistency m should exceed 50 mPa.s and the flow behaviour index n should ideally be no more than 0.7.

Ishizaki and Fuchigami [1985] recommended that the two lowest layers should differ by no more than 10mPa.s in viscosity when measured at low shear rates to minimise risk of slidewaves and the viscosity of the carrier layer to be less than that of the adjacent layer when measured at a high shear rate. Koepke et al. [1986] advocated that the viscosity of the uppermost layer should be in the range 1 to 10 mPa.s and the wet thickness 5 to 20 μm in order to ensure even drying.

Ishizuka [1989(1)] claimed it is possible to use water as a carrier layer laid down at 2 μm or less. He found that the viscosity of the second layer should exceed that of the carrier layer by at least 15 times and that the lay down be at least five times that of the carrier layer. Ishizuka [1989(2)], when using water as a carrier layer, additionally found that:

1. Extending the length of the bottom slot in the cross-machine direction beyond the others increased the maximum coating speed for achieving stable edge control.

2. Acceptable coating quality could be achieved by ensuring the bead did not droop down into the gap by increasing the coating speed and increasing the viscosity of the second layer to at least 40mPa.s.

3. Reducing the width of the bottom slot from 0.8 mm to 0.4 mm (while maintaining the other slots at 0.8 mm) removed the risk of streakiness under certain conditions.

Howe et al. [1997] show how a carrier layer designed for curtain coating and of wet thickness in the range 2 to 8 μm becomes much more effective in achieving high coating speed by incorporating colloidal silica, which renders the layer shear thinning. Bermel et al. [2003] recommend the use of an organic solvent as a carrier layer to prevent unwanted precipitation on the surfaces of the coater and consequent streak-lines.

These advances generally relate to the coating of smooth well behaved substrates. However, Ikin [1997] found that the ground rules for lower layer viscosity and wet laydown recommended by Dittman and Rozzi [1977] sometimes no longer applied when attempting to coat a variety of paper substrates typically used within industry. In one set of trials, the aim was to coat three layers as shown in Table 1.1, the variable being the viscosity of the carrier layer. The coating speed was set at 100 m/min.

	Viscosity	Wet laydown
Top layer	120 mPa.s	44 μm
Middle layer	90 mPa.s	21 μm
Carrier layer	Variable	6 μm

Table 1.1: Three layer assembly used in coating trial by Ikin [1997]

The results showed there to be a narrow window in viscosity centred about 25 mPa.s outside of which it was found impossible to obtain a stable coating - Table 1.2.

Carrier layer viscosity	5.4 mPa.s	25 mPa.s	>40 mPa.s	>70 mPa.s
Coating performance	Rivulets	Stable	Ribbing	Rivulets

Table 1.2: Response to carrier layer viscosity for assembly shown in Table 1.1

Endoh and Morikawa [2003] attempted to coat an assembly of ten layers onto paper web precoated with polyethylene and having surface irregularities of depth varying between 1 and 4 μm at a characteristic pitch in the range 1 to 4 mm. The viscosity of the bottom layer was varied while that of each of the remaining layers was fixed at 150 mPa.s. The wet thickness of each layer was set at a value between 10 and 15 μm,

the total laydown being 130 μm. The coating speed was 150 m/min. The results are shown in Table 1.3.

Carrier layer viscosity	10 mPa.s	30 mPa.s	50 mPa.s	180 mPa.s
Coating performance	Non-uniform	Good	Good	Poor

Table 1.3: Response to carrier layer viscosity – Endoh et al. [2003]

They concluded from this and other work that the viscosity of the lower layer should be between 15 and 100 mPa.s, while ensuring that each of the other layers achieves a viscosity of at least 30 mPa.s and that the weighted mean viscosity of the remaining layers lies between 60 and 300 mPa.s.

These examples serve to illustrate that the application of the carrier layer concept is by no means as straight forward as would be ascertained from the early patent literature (Dittman and Rozzi [1977], Choinski [1978], Ishizaki and Fuchigami [1985], Ishizuka [1989(1)] and [1989(2)].

In the next section, consideration is given to the surface properties of typical commercially available substrates, with a view to optimising the coating process to suit a wide range of materials.

1.5 The Effect of the Surface Properties of the Substrate

The specific surface properties considered of direct relevance to coating are surface energy, surface roughness, surface charge and porosity. These will now be reviewed in turn.

1.5.1 Surface Energy

It is recognised within industry that a high surface energy is a necessary prerequisite for good adhesion between a fully dried coating and the substrate (Gutoff and Cohen

[1995].) The surface energy of the substrate can be enhanced by subjecting it to corona treatment (Gutoff and Cohen [1995].

There is no direct way of measuring the surface energy of a substrate owing to the fact that the solid does not deform in the same way as a liquid (Woodward [2001]). The solution is to use the Young equation relating the surface energies of the liquid and the solid, the force at the solid/liquid interface and the contact angle – see Section 2.4 for detail. A single measurement using say a drop of pure water yields a nominal value for surface energy using the method of Good [1964]. However, Blake and Morley [1997] have demonstrated for the curtain coating process that it is necessary to decompose the surface energy of the substrate into its dispersive and polar components to enable any meaningful correlation with the critical air entrainment speed. Von Bahr et al. [2004] have shown that the polar component plays a more important role in determining the wettability of AKD-sized papers than the dispersive component. The method used by Blake and Morley [1997] follows on from the work of Fowkes [1962] and extended and applied by Owens and Wendt [1969] and is based on determining the contact angles of drops of two test fluids deposited on the sample. One test fluid is selected as being highly polar, the other non-polar. Care needs to be taken to ensure the liquids do not unduly react with chemicals present on the test surface. Blake and Morley [1997] found that the highest coating speeds for a curtain of 3 cm fall height was obtained for substrates where:

1. The polar component was less than 10 $mN.m^{-1}$
2. The dispersive component was greater than 30 $mN.m^{-1}$
3. The calculated value of the static advancing contact angle for pure water lay between 65° and 100°

1.5.2 Surface Roughness

There are two possible mechanisms for the dynamic wetting of a rough impervious substrate, the first being where the fluid penetrates into the surface cavities and the second where air becomes trapped (Blake and Ruschak [1997]).

The actual wetted area in the first case is significantly larger than the projected area. It therefore follows that the maximum wetting speed is expected to diminish for a rough surface for which this mechanism applies (Blake and Ruschak [1997]).

The trapping of air within the cavities and hollows presented by the surface topography can lead to a composite liquid/solid – liquid/air interface as proposed by Cassie and Baxter [1944] when studying the wetting of fabrics and the feathers of ducks and hens. They found that the apparent advancing contact angle for such surfaces significantly increases as the ratio $\lambda/2r$ increases, where r is the fibre radius and λ is the fibre pitch. Johnson and Dettre [1964] and Dettre and Johnson [1964] showed both theoretically and experimentally that a subtle change in surface structure can cause the wetting mechanism to switch from total liquid penetration to the formation of a composite surface. This switch is accompanied by a dramatic reduction in contact angle hysteresis as determined by differences in the advancing and receding contact angles. Wolfram and Faust [1978] studied the wetting of a plate by a liquid drop as the plate was tilted away from the horizontal. They measured the critical tilt angle at which the drop begins to roll or slide. Contact angle hysterisis was found to diminish with decreasing critical angle. The advancing contact angle thus decreased and the receding contact angle increased, the angles hypothetically converging to a single value as the critical tilt angle reduced to zero. Miwa et al. [2000] used the tilted plate method to show that it is possible to construct a super-hydrophobic surface after experimenting with methods of depositing boehmite particles on a plate and subsequently coating with hydrophobic silane. They found that the critical tilt angle correlated well with the ratio of the true surface area to the projected area (Nakajima [2005]). The lowest achievable angle was 1° for which the surface was seen to have an open spaced needle like structure. In this case, the acceleration of the drop down the 1° incline was determined as being g.sin 1°, thus showing virtually no resistance to motion from the surface. Such needle-like structures having the appearance of a "fakir carpet" are seen on the surfaces of certain types of leaves, which tend to resist water by causing the formation of almost spherical droplets (Bico et al. [1999] and Herminghaus [2000]). Menchaca-Rocha [1992] studied the deceleration of mercury drops on a range of horizontal rough surfaces and found the longest skid length was obtained for a surface showing the least contact angle hysterisis.

Blake and Ruschak [1997] suggested trapped air pockets resulting from a switch to the second mechanism would not necessarily be detectable on a coated film. They argued from the evidence of Menchaca-Rocha [1992], for example, that a composite surface can result in a reduction in the net drag of the substrate on the liquid with a consequential increase in the speed of visible air entrainment. Clarke et al. [2000(1)] showed this indeed to be the case when studying air entrainment speeds for curtain coating. They found for roughness Rz values between 2 and 20 μm that it was possible to achieve a dramatic increase in air entrainment speed on increasing the viscosity of the lower layer above a critical value μ_1 when measured at a shear rate of typically 10^4 s^{-1}. The relationship between μ_1 and Rz, the curtain impingement velocity U, the application angle θ, the total volumetric flow rate Q per unit width, the surface tension σ_1 of the bottom layer and the minimum density ρ of the coating solutions is given by:

$$1818\sigma_1^{1/3}\,Rz\left\{\frac{1}{0.0002}\,\mu_1 U\cos(\theta)\left[1+\Omega\frac{\rho Q}{20\mu_1}\right]\right\} > 1 \qquad (1.15)$$

where

$$\Omega = \frac{25}{25+\left\{\frac{\rho Q}{\mu_1}-8\right\}^2} \qquad (1.16)$$

Clarke et al. [2000(1)] associated this roughness assist phenomenon with the second dynamic wetting mechanism described above. Clarke et al. [2004] additionally showed that the ten point average peak-to-peak roughness Rz alone is insufficient for characterising a surface for roughness assist. The value of Rz produced by a surface composed of beads of equal size remains the same but as the surface density of the beads decreases, the surface tends to behave more like a smooth one and the propensity for generating a composite surface fails.

1.5.3 Surface Charge

The effect of electric charge residing on the surface of the substrate on coating flows is considered here. Charges are of two types, free and bound. Free charges are caused by an excess of electrons or ions at the surface and are free to move under the influence of an electric field (Gutoff and Cohen [1995]). Bound charges comprise dipoles,

which are generally randomly orientated - leaving the surface with no net charge. The dipoles can, however, become orientated under the influence of a strong electric field thereby leaving a net charge on the surface (Gutoff and Cohen [1995]). The decay rate for bound charge can be very long – hours or even days (Gutoff and Cohen [1995]).

The application of electrostatic assist to coating is well established within the coating industry in general – Kisler et al. [1984]. The smoothing of patchy polar charge distributions can be effected by firstly orientating the dipoles in the presence of an electrostatic field to achieve negative charge saturation. The surface charge is then neutralised by subjecting the surface to a reverse electric field – Gibbons et al. [1972]. Increasing the strength of an applied field results in a net charge that can be used to assist dynamic wetting. The patent literature indicates how this can be effected in one of several ways. The method of Gibbons et al. [1972], who set up grid ionisers for assisting slide-bead coating opposite a grounded conducting roller carrying the web has been extended by Hartman [1989] for curtain coating. Kisler et al. [1984] describe techniques for favourably redistributing polar charge by setting up either a bristle brush electrode or a corona discharge opposite a grounded metal roller bearing the web. In another method, a high voltage is applied to the coating roller thereby generating an electrostatic field between the roller and the coating applicator – Quiel et al. [2002].

Clarke et al. [2000 (2)] extended their work on the study of rough substrates (Clarke et al. [2000 (1)]) described earlier in Section 1.5.2 to incorporate the added benefit of charge assist. They show that the level of high-shear viscosity required for roughness assisted coating is then significantly reduced. They found that the conditions expressed in (1.15) can be relaxed to become:

$$1818\sigma_1^{1/3}\,Rz\left\{1/2\varepsilon\varepsilon_0E^2+\frac{1}{0.0002}\,\mu_1 U\cos(\theta)\left[1+\Omega\frac{\rho Q}{20\mu_1}\right]\right\}>1 \qquad (1.17)$$

where ε is the dielectric constant of the ambient air or gas, ε_0 is the permittivity of free space and E is the electrostatic field strength at the lower meniscus. Ω remains as defined in (1.16).

Zvan et al. [1992] used a needle coater to demonstrate how the dynamic contact angle decreases with increasing polar charge for a cylindrical jet of fluid impinging on a substrate. Fermin and Scriven [1999] developed a technique for quantifying the influence of electrostatic fields on a falling curtain by coating onto a scraped hollow glass roller.

Blake et al. [1999] and Blake et al. [2000] explain that the electrostatic field at the dynamic wetting line generates a force which acts normally to the lower free surface where the liquid is conductive. The result is an effective change in local pressure, which enhances wetting by reducing the dynamic contact angle and postpones the onset of air entrainment and can thus lead to an increase in the maximum coating speed. They considered the free energy of the wetting line region - including the work done against pressure - and showed that the static contact angle $\theta_E{}^0$ in the presence of an electric field is related to the value $\theta_0{}^0$ obtainable with no field by the expression:

$$\cos(\theta_E{}^0) = \cos(\theta_0{}^0) + \frac{\varepsilon_0}{4\gamma_{LG}\varepsilon_3 K}(V + V_s)^2 \qquad (1.18)$$

where K is the effective dielectric thickness of the air/base "sandwich" between the coating roller and the liquid, ε_0 is the permittivity of free space, ε_3 is the relative permittivity of the dielectric in contact with the liquid, γ_{LG} is the interfacial tension of the liquid-gas interface and V and V_S are the potentials of the coating roller and substrate surface respectively.

By assuming that the hydrostatic effects could be decoupled from the hydrodynamics, the dynamic contact angle θ_E in the presence of an electric field is related to the value θ_0 in a similar way:

$$\cos(\theta_E) = \cos(\theta_0) + \frac{\varepsilon_0}{4\gamma_{LG}\varepsilon_3 K}(V + V_S)^2 \qquad (1.19)$$

They incorporated the equations (1.18) and (1.19) into the molecular kinetic theory of dynamic wetting (see Blake [1993]), in which a relationship between the wetting line speed U and the static contact angle θ^0 and dynamic contact angle θ are derived:

$$U = 2k^0\lambda \sinh\left\{\frac{\gamma_{LG}}{2nk_BT}[\cos(\theta^0) - \cos(\theta)]\right\} \qquad (1.20)$$

where k^0 and λ are the net frequency and length of molecular displacements at the wetting line for zero wetting speed, n is the number of adsorption sites per unit area of wetting, k_B is Boltzman's constant and T is the absolute temperature. A similar equation is derived for where an electrostatic field is applied:

$$U_E = 2k^0\lambda \sinh\left\{ \frac{\gamma_{LG}}{2nk_BT} [\cos(\theta_E{}^0) - \cos(\theta_E)] \right\} \tag{1.21}$$

Substituting for $\cos(\theta_E{}^0)$ in equation (1.18) into (1.21) yields:

$$U_E = 2k^0\lambda \sinh\left\{ \frac{\gamma_{LG}}{2nk_BT} [\cos(\theta_0{}^0) + \frac{\varepsilon_0}{4\gamma_{LG}\varepsilon_3 K}(V + V_S)^2 - \cos(\theta_E)] \right\} \tag{1.22}$$

Near the limit $U_{max,0}$ for air entrainment in the absence of an electric field, θ in equation (1.20) approaches 180° to yield:

$$U_{max,0} = 2k^0\lambda \sinh\left\{ \frac{\gamma_{LG}}{2nk_BT} [\cos(\theta_0{}^0) + 1] \right\} \tag{1.23}$$

which may be approximated by:

$$U_{max,0} = k^0\lambda \exp\left\{ \frac{\gamma_{LG}}{2nk_BT} [\cos(\theta_0{}^0) + 1] \right\} \tag{1.24}$$

Similarly, near the limit $U_{max,E}$ for air entrainment in the presence of an electric field, θ_E in equation (1.22) also approaches 180° to yield the approximation:

$$U_{max,E} = k^0\lambda \exp\left\{ \frac{\gamma_{LG}}{2nk_BT} [\cos(\theta_0{}^0) + \frac{\varepsilon_0}{4\gamma_{LG}\varepsilon_3 K}(V + V_S)^2 + 1] \right\} \tag{1.25}$$

Substituting for $\cos(\theta_0{}^0) + 1$ from (1.24) into (1.25) finally yields:

$$U_{max,E} = U_{max,0} \exp\left\{ \frac{\varepsilon_0 (V + V_S)^2}{8\varepsilon_3 K n k_B T} \right\} \tag{1.26}$$

Blake et al. [2000], in deriving this expression, point out that the equation contains only one free parameter n, the rest being readily measurable. They used a needle coater following the method of Zvan et al. [1992] to measure dynamic contact angle θ_E as a function of wetting speed U to show that the experimental data closely matched equation (1.22) on assigning unique values for n and k^0. A follow-up experiment using a curtain coater showed excellent agreement between the experimentally determined air entrainment speed and the value as predicted by equation (1.26) on using this value of n for applied potentials ϕ ranging from – 600 volts through 0 volts to + 600 volts.

Zaretsky et al. [2001] point out the necessity of taking into consideration the finite resistivity of the substrate surface when assessing the effective voltage V_s responsible for the force F_x. This is given by:

$$V_s = V_R (1 - e^{-x/\lambda}) \tag{1.27}$$

where V_R is the voltage on the surface well away from the fluid, x is a displacement along the surface away from the dynamic wetting line typically taken to be 50μm and λ is given by:

$$\lambda = \frac{1}{\rho_s CS} \tag{1.28}$$

and termed the "characteristic electrical length". Here ρ_s is the resistivity of the base surface in ohms per square, C the capacitance of the base in $F.m^{-2}$ and S the speed of coating. They claim that λ should not exceed 400 μm – and preferably be less than 100 μm in order to ensure effective charge assist using voltages that are practically achievable and incurring no undue risk of arcing or glow.

Vandaela and Vancoppenolle [1999] and Quiel et al. [2002] have demonstrated that whereas charge assist resists the onset of air entrainment, it also leads to increased susceptibility to ribbing. Vandaela and Vancoppenolle [1999] suggest that the ribbing is induced by an increase in curvature of the upper meniscus while not showing any experimental evidence for this. Quiel et al. [2002] show that combining the addition of a shear thinning thickener to the bottom layer with charge assist tends to resist both ribbing and the onset of air entrainment leading to an overall significant improvement in the coating window.

1.5.4 Porosity

The coating of porous media introduces yet a further degree of complexity. The way a liquid penetrates the pores of a permeable medium full of air depends on how well the liquid wets the walls (Scriven et al. [1993]). A non-wetting liquid must be put under a pressure greater than the "entry capillary pressure" before it can penetrate into the pores. In so doing, the liquid tends to trap air within the pore space. This air can subsequently escape to generate a blowhole in the coating as the pressure is released – Figure 1.18. On the other hand, a liquid that wets well enough to enable a thin film to

precede it by the actions of gas transport and adsorption or condensation is spontaneously imbibed into the pore space by the actions of disjoining pressure and the capillary pressure, which is now negative (Chen and Scriven [1990]; Scriven et al. [1993]). The wettability itself can change locally as the liquid makes contact with the fibres to become absorbed by the structure – resulting in a delay in wetting (Scriven et al. [1993]; von Bahr et al. [2004]).

Once having initially entered the outside of the pore space, the rate of further penetration then becomes governed by Darcy's law expressed by the Richard's equation (von Bahr et al. [2004]):

$$v = \frac{K}{\mu} B(S)[\rho g - \nabla p] \tag{1.29}$$

where v is the velocity of liquid flow into the pores, K is a constant, ρ is the density, μ is the viscosity of the liquid, p is the external pressure field and B(S) the relative permeability of the pore network.

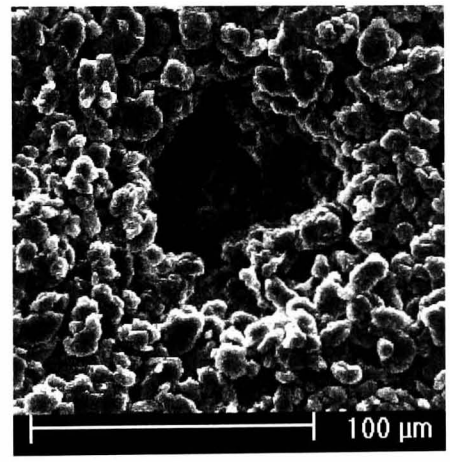

Figure 1.18: Typical blow hole in a coating on a porous substrate

Methods for reducing or eliminating defects due to air escaping from the pores include prewetting the substrate using a spray-bar (Ikin [2000(1)]) or a reverse roll coater (Knight et al. [2002]).

1.6 The Stability of the Coating and Drying Process

Consideration is given to the role of carrier layer flows in determining the stability of two specific areas within a typical multilayer coating process. These concern:

1. The flow behaviour of the two solutions as they merge on the slide

2. The free surface of the coated multilayer assembly when initially subjected to impinging air during the early part of drying

1.6.1 The Merging of Flows on the Slide

A knowledge of the flow structure at the exit of a slot delivering a solution to the slide is of importance to the coating engineer concerned with attaining acceptable coating uniformity. As pointed out in Section 1.3.5, the flow should be free of all recirculations as far as possible in order to reduce the risk of streak line formation. The flows, once established on the slide, should be free from disturbances due to slide waves as they proceed towards the bead forming zone.

Schweizer [1997(1)] set up a flow visualisation experiment in which stream lines within two merging flows were imaged using hydrogen bubble tracers illuminated by a light sheet. The interface was highlighted by injecting a very thin streamer of green dye through the upstream slot wall. The fluids forming the merging layers were identical and of viscosity 18 mPa.s and the flow rates for the lower and upper layers 3.06×10^{-4} and 1.19×10^{-4} m^2/s respectively. The images showed a severe recirculation on the slide just downstream of the exit for a parallel sided slot of width 0.5 mm. Machining back the downstream corner at the slot exit to form a chamfer as recommended by Ade [1978] resulted in only a slight reduction in the strength of the recirculation. Machining both slot walls to form a curved diffuser allowed the flows to merge without any signs of a recirculation – Figure 1.19. Unfortunately, this design is vulnerable to damage owing to the sharp edge left at the upstream corner.

Padday [1961] suggested cutting a step in the slot wall to allow the exit to be opened out as a means of reducing the tendency for recirculations on the slide. Apps [2000] showed results from a computational model which were found to be in good agreement with Schweizer's flow visualisation data. She applied the model to plot the predicted flow for slot exits as recommended by Padday [1961]. She found that

recirculations on the slide were significantly reduced as Padday claimed but that the corners themselves introduced further unwanted vortices.

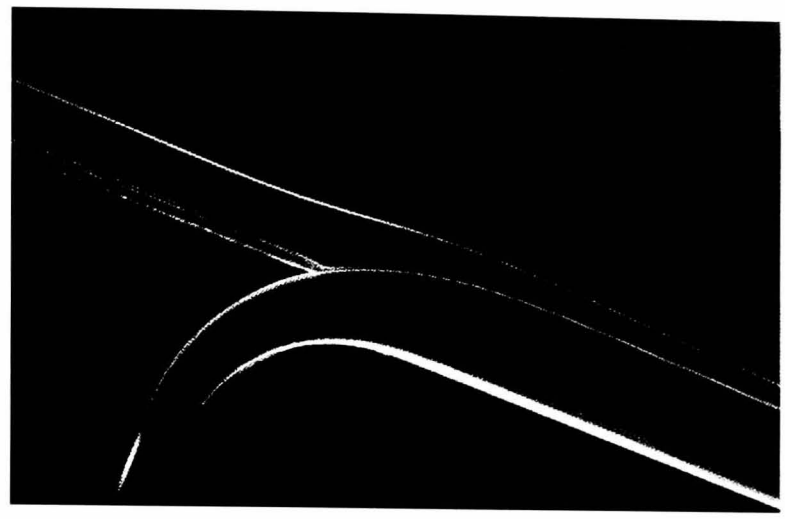

Figure 1.19: Merging flows at a curved diffuser (Schweizer [1997(1)]

Devine [1991] claimed that streaks associated with slot flows can be avoided by ensuring that the slot Reynolds number Re_{slot} does not exceed 10, where:

$$Re_{slot} = \frac{\rho_{slot} Q_{slot}}{\mu_{slot}} \tag{1.30}$$

ρ_{slot}, Q_{slot}, μ_{slot} being the density, flow rate per unit width and viscosity respectively for the solution entering the particular slot. Ruschak et al. [2002] further examined various slot exit design options aimed at preventing unwanted recirculations associated with a "hump" in the flow above the slot exit when pumping the fluid forming the lower layer at relatively high flow rates.

This work was of relevance when considering flows required for the main layers in a multilayer assembly, especially when designing for high speed coating. However, the flows for establishing a thin low viscosity carrier layer can result in non-uniformities for other reasons as will now be described.

1.6.1.1 Carrier Layer Starvation Lines

Behan and Ikin [1998] found, when coating a formulation using a thin carrier layer, that under certain conditions the coating became intolerably uneven due to wandering broad streaks. The defects were traced to the viscosity of the second layer having

been inadvertently increased due to an error in making up the corresponding solution - as seen in Table 1.4 and shown to originate at the carrier layer slot exit – see Figure 1.20.

	Conditions for stable coating		Conditions resulting in carrier layer starvation	
	Viscosity	Flow Rate	Viscosity	Flow Rate
	mPa.s	$m^2.s^{-1}$	mPa.s	$m^2.s^{-1}$
3rd layer	10	3.06×10^{-5}	10	3.06×10^{-5}
2nd layer	47-53	5.96×10^{-5}	67.4	5.96×10^{-5}
Carrier layer	5.6	7.43×10^{-6}	5.6	7.43×10^{-6}

Table 1.4: Conditions for generating unstable coating using a carrier layer

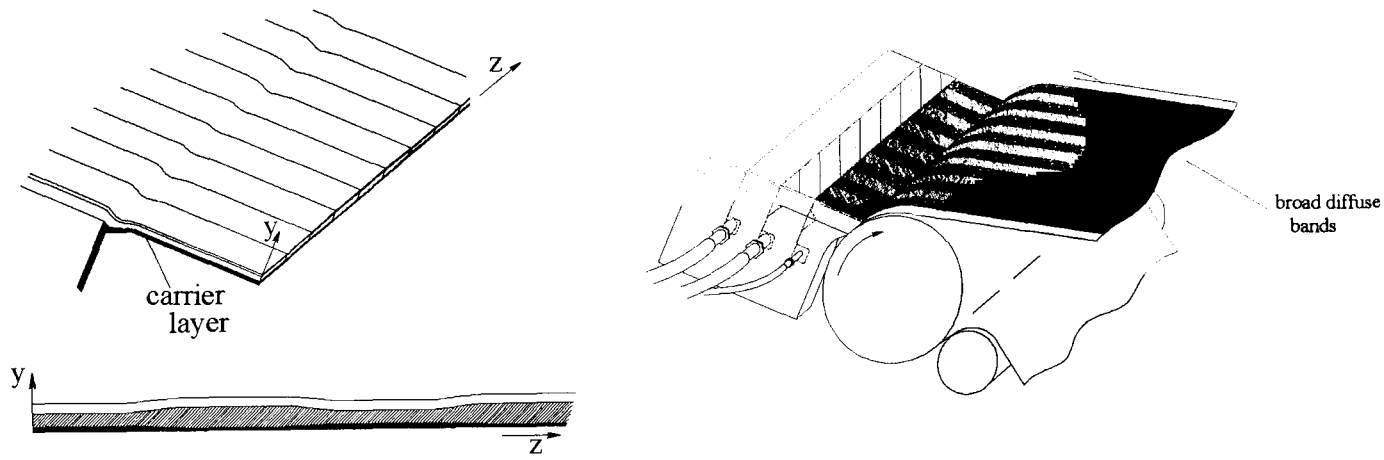

Figure 1.20: Appearance of broad diffuse bands associated with a thin carrier layer.

As shown in Figure 1.21, they moreover found that the tendency for the broad streaks worsened as:

1. The gelatin concentration (and hence viscosity and density) of the carrier layer was reduced

2. The flow rate of the carrier layer was decreased

3. The concentration (and hence viscosity and density) of the second layer was increased

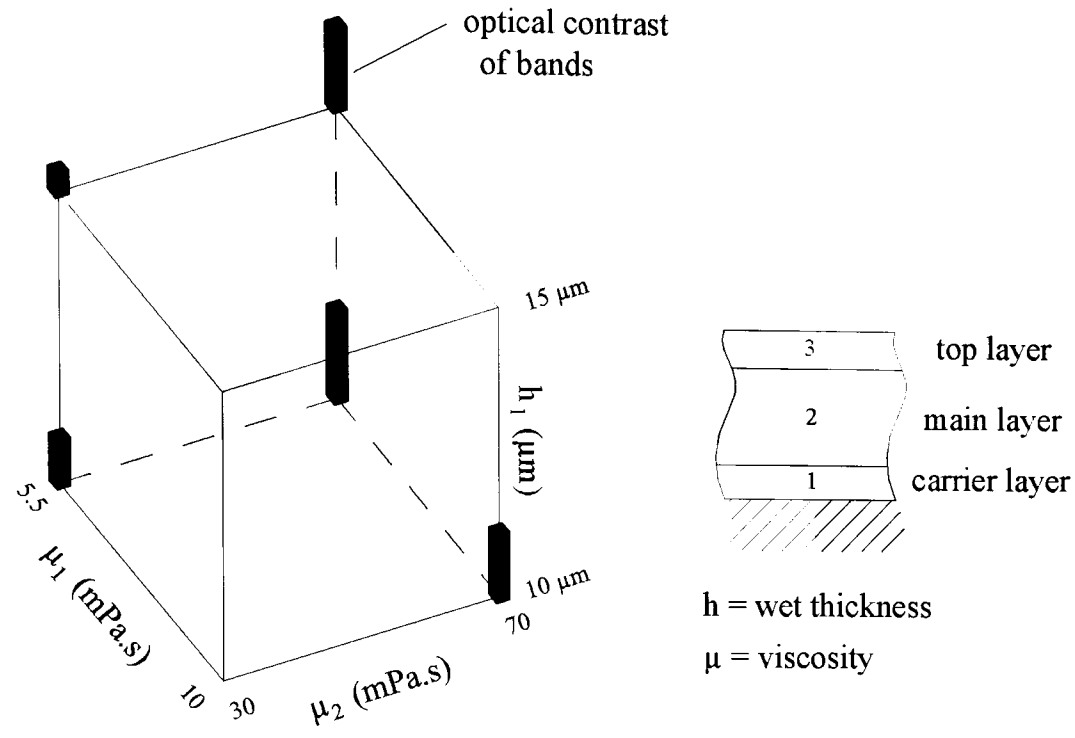

Figure 1.21 - Sensitivity of the bands to viscosity and carrier layer flow rate

Further experiments were run using a cascade fitted with a transparent block forming the upstream slot wall and adding a green dye to the solution forming the upper layer – see Figure 1.22. The results clearly revealed that on reducing the flow rate of the carrier layer forming solution, the upper layer solution was beginning to invade the slot.

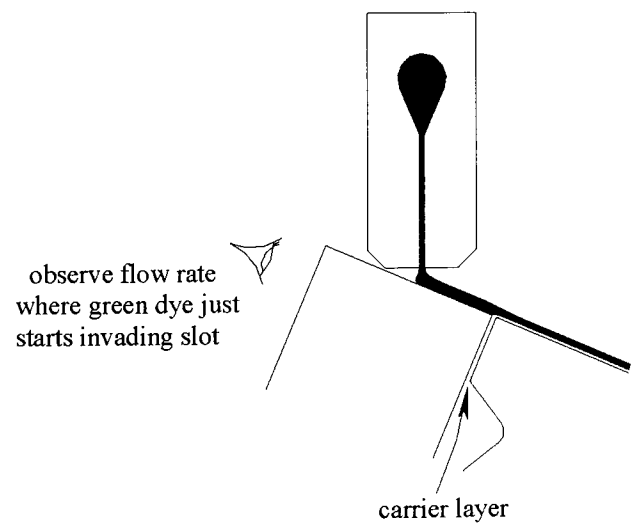

Figure 1.22: Apparatus for visualising the critical carrier layer flow rate

Apps [2000] extended the model described in 1.6.1 to cater for a parallel sided slot of width 1.0 mm. Flow rates for the lower layer ranged from 0.3×10^{-5} m^2/s to 1.0×10^{-5} m^2/s and more typical of thin carrier layer flows. The results indicated a small

recirculation close to the top of the downstream slot wall and it was suggested (Apps [2000]), but not proven, that this may be responsible for the defects reported by Behan and Ikin [1998]. Little is known about the lower viscosity limit for carrier layers and the mechanisms responsible for those limits – especially regarding instabilities in the slot exit and on the slide (Blake [2001]). There is no published literature on the influence of the slot design on the behaviour of carrier layer systems other than a patent recommending a reduction in the width of the carrier layer slot from 0.8 mm to 0.4 mm in order to reduce streakiness (Ishizuka [1989(1)]). Leonard [1996] claimed criteria limiting the width in cm. of the slot B to a maximum value defined by:

$$B < \frac{6.25\mu^2 N_{re}{}^a}{\rho\sigma} \tag{1.31}$$

where μ is the viscosity (poise), ρ is the density ($gm.cm^{-3}$) and

$$N_{re} = \frac{4Q\rho}{\mu} \tag{1.32}$$

where Q is the flow rate ($cm^2.s^{-1}$) and

$$a = 0.981 + 0.3406.\log(N_{re}{}^{0.3406}) \tag{1.33}$$

This work, however, related to single layer flows and took into account pull-in effects at the edges and general stability on the slide rather than the merging of two layers being considered here.

1.6.1.2 Slide Waves

As discussed in Section 1.3.7, there is evidence from the computational analysis of Kobayashi [[1992] that interfacial waves predominate over surface waves for two layer flows and increase in amplitude as $m = \mu_2/\mu_1$ decreases or increases relative to unity. There is thus an increased risk of interfacial slidewaves as the viscosity of the main layer is increased for a two layer coating. It should also be noted that such waves do not heal by levelling owing to the absence of interfacial tension (Hens and Van Abbenyen [1997]). Kobayashi [1992] experienced difficulties in visualising interfacial disturbances on the slide owing to the fact that the layers are thin and the amplitudes of the disturbances small. The validation of numerical predictions of defect severity was thus limited to assessing the quality of final coatings made on a coating machine.

For the case where more than two layers are used, Kobayashi [1992] recommends that viscosities increase from bottom to top and that the viscosity ratio of adjacent layers is smaller than 2 and preferably smaller than 1.5. Weinstein and Kurz [1991], on the other hand maintain that for a three layer flow, the viscosity and density of the middle layer should exceed that of adjacent layers (Hens and Van Abbenyen [1997]). Hens and Van Abbenyen [1997] conclude that despite much work being done to define flows on an inclined plane, the application to multilayer coating is not completely understood.

Blake et al. [1995], in recommending optimum conditions for curtain coating, claim that it is difficult to establish uniform flows on the slide supplying the falling curtain when using a thin low viscosity carrier layer. In addition to reducing slide angle to a minimum and reducing the length of the slide, they propose that the rheology of the bottom layer should be such as to ensure the viscosity is maintained substantially constant and in the range 30 to 200 mPa.s for shear rates less than 1000 s^{-1} to prevent slidewaves. They also point out that the viscosity should ideally be arranged to fall at higher shear rates to be maintained substantially constant at less than 10 mPa.s over the range 10^4 to 10^8 s^{-1} to promote satisfactory dynamic wetting of the substrate without entraining air.

1.6.2 Air Induced Surface Waves during Drying

As discussed in Section 1.3.8, a prime cause of mottle seen on a finally dried multilayer coating is sourced in disturbances to the surface through the impingement of air used for drying (Cohen and Gutoff [1992]). They recommend that such defects can be avoided by reducing the air speed during the early part of drying and increasing the concentration of the solutions. The interest in multilayer coating technology has been largely confined in the past to the photographic industry. Gelatin has been the traditional fluid vehicle for maintaining suspensions of the silver halide crystals responsible for sensitivity to light. This material solidifies at temperatures typically less than 35°C and is therefore supplied and coated at a typical temperature of 40°C. It is readily possible to solidify the coatings in the interval between applying the fluids and drying by reducing the temperature of the substrate and surrounding air. This increases the resistance to mottle due to air impingement within the dryer. The last two

decades, however, have seen an increasing departure from the use of gelatin for multi-layer coating owing to the advent of inkjet printing technology. It is thus no longer so straight forward to ensure robustness against air induced disturbances merely by pre-cooling the coatings. Bell et al. [2000] have demonstrated that mottle can be reduced by redesigning the dryer nozzles to direct the air parallel to the web and matching the air speed to that of the web. Iwado [2003] addresses the problem by designing two dryer stations, the first being less aggressive by limiting the air speed to less than 30 m/s.

Ruschak [1987] has developed a theoretical analysis relating to the flow of a single fluid layer when subjected to a sinusoidal pressure disturbance – see Section 4.4.1 for detail. This gives helpful insight into how a fluid layer flows in response to individual jets of air ejected by an array of holes. There is no corresponding work, however, relating to the effect of air issuing from a parallel array of slots arranged perpendicular to the machine direction. In this case, the flow due to the intermittent shearing action of the impinging air can become unstable. The mechanism involves the inherent instability of the fluid assembly, rather than the response to a sinusoidal air pressure as defined by Ruschak [1987].

The study of air induced instability of single fluid layers is well documented but not for multi-layers. Francis [1954] describes laboratory experiments, in which air is blown over a deep pool of viscous oil in a wind tunnel. He shows that there is a critical air speed of 5 to 5.6 m/s, above which waves grow explosively in about 0.25 s and run down wind. Craik [1966] studied the hydrodynamic stability of thin horizontal water films both theoretically and experimentally. He found two modes of wave propagation, a fast wave and a slow wave. The first is seen with relatively deep films and the second as the depth is reduced. Özgen et al. [2002] describe experiments to study the formation of waves on thin layers of de/anti-icing fluid on the lower wall of a wind tunnel using Newtonian de-icing fluids and non-Newtonian ant-icing fluids. They describe a light absorbing technique for defining the wavelength and wave speed by adding a violet dye that does not adversely affect the rheology. Zuccher and Buchlin [2001] have established an experimental technique for investigating liquid film instability on a rig dedicated to simulate the coating of wires with molten zinc. They used a laser light sheet to determine the mean final thickness and the velocity,

wavelength and amplitude of the waves. They found only one characteristic wavelength for low wire velocities while a progressive wave disappearance occurs for high velocity. Gosset and Buchlin [2003] describe experimental techniques for quantifying waves on a liquid entrained by a rotating cylinder and disturbed by a gas jet. They found that the wave velocity determined by 2-D cross-correlation of successive images recorded by a high speed camera always equalled the substrate velocity for a speed range of 120 to 400 mm/s.

1.7 Scope of this Thesis

This thesis addresses issues concerning carrier layer flows and how these can be used to advantage in industry involved in the coating of multiple layer assemblies in a single pass. Being essentially industrially based, a significant part of the work involves the application of the carrier layer concept to the coating of substrates having a wide range of surface properties. Limitations of the application of the carrier layer technique are also addressed. These aspects have been generally overlooked in the published literature.

In chapter two, experimental methods used and developed for measuring the key properties of the fluids and substrates and for visualising relevant flows are introduced. An area that is overlooked is the fact that the materials of interest to the industrialist are generally very different to those typically used by experimentalists when visualising coating flows. Schweizer [1988] and Chen [1992] both used transparent glycerin at different concentrations as the working fluids and employed a scraped coating roller rather than coat onto a continuously running web. In practice, coating solutions are often opaque and scattering as are the webs on which they are applied. The rheology can be complex. The substrate may be porous and thus involve the additional process of liquid penetrating into the fibres. The surface of the web can vary from being smooth to comparatively rough and can carry an electric charge distribution. It is no longer possible to rely on finding a matching transparent web especially when approaching coating speeds near to the air-entrainment limit. The design and construction of specialist equipment not hitherto available has formed a

very significant part of this work. In addition to detailing the equipment and associated development work, this chapter describes the basic facilities made available by ILFORD Imaging UK Limited and the work undertaken as part of this project to upgrade them.

In chapter three, preliminary experiments are described which serve to address issues presented by the surface properties of the base. Although the concept of the coating window is now recognised as being an important one, there is little published. This is especially true of the slide bead coating process - as pointed out by Schweizer [2001]. Exceptions include the work of Vanadaela and Vancoppenolle [1999] when studying charge assist and the studies of ribbing by Schweizer and Rossier [2001] and Schweizer and Rossier [2003]. Coating windows are presented in this chapter which highlight major differences in coating performance when attempting to coat a given multi-layer assembly. The criteria for acceptable performance include the robustness of the coating process during join withdrawal – an area almost totally overlooked in the literature. Special emphasis is placed on the definition of what is deemed acceptable to the coating technologist within industry when considering the various mechanisms limiting the process. The effect of surface energy is taken first in Section 3.3 because the local contact angle is of importance to the understanding of the role played by surface roughness. This issue and the limitations of applying a carrier layer, are addressed in Section 3.4. Section 3.5 deals with the effects of free surface charge. Section 3.6 describes how the specially developed monitoring equipment has also been exploited to further quantify the influence of bound polar charge on the free surfaces hitherto only studied theoretically. In Section 3.7 a description is given on some preliminary experiments designed to establish the role of the carrier layer in determining the ability to coat porous base and resist the generation of unwanted blow-hole defects.

In chapter four, attention is given to the role of the carrier layer in determining limitations dictated by instabilities. Little is known about the lower viscosity limit for carrier layers and the mechanisms responsible for those limits – especially regarding instabilities in the slot exit and on the slide. There is no published literature on the influence of the slot design on the behaviour of carrier layer systems other than the patent claimed by Ishizuka [1989(1)]. These issues are addressed in Sections 4.2 and

4.3. A model is suggested for explaining the onset of the broad streaklines seen close to the critical limit for establishing a thin low viscosity carrier layer on the slide. In Section 4.4, the benefit of using a carrier layer to enhance the robustness against air induced surface waves is explored – an area hitherto unreported.

Conclusions from the results and recommendations for future work are given in chapter five.

Chapter II

Experimental Methods

2.1 Introduction

The experimental techniques exploited throughout this study to investigate and elucidate flows associated with the use of a carrier layer for the coating and drying of thin multilayer films may conveniently be grouped into six categories:

1. Measurement of key properties of the fluids
2. Measurement of key properties of the substrate
3. Visualisation of flow at the exit slot where the carrier layer merges with the rest of the slide flow
4. Visualisation of instabilities associated with flow down the slide
5. Profiling of the free surfaces in the bead forming region
6. Visualisation of instabilities associated with air directed onto the fluid coating during the early part of drying

Categories 1 and 2 involve use of equipment that is either commercially available or is otherwise a development outside of the scope of this study. Categories 3 and 4 have been developed as part of this work and are novel. The equipment makes use of the facilities available within the flow studies laboratory of HARMAN technology Limited – formerly ILFORD Imaging UK Limited. Categories 5 and 6 are integrated into a pilot coating machine dedicated for development work at HARMAN technology Limited and are again novel and the design, manufacture and commissioning of the experimental apparatus forms a key part of the work.

In addition to detailing the equipment and associated development work, this chapter describes the basic facilities made available by HARMAN technology Limited and the work undertaken as part of this study to upgrade them.

2.2 The Measurement of Key Fluid Properties

2.2.1 Rheology

The study of how the rheological properties affect coating performance for an industrial process is in itself highly complex (Glass and Prud'homme [1997], Schunk and Scriven [1990].) The shear rate within a given flow regime can vary over a wide range over very short time scales – Schunk [1989]. To illustrate this, it was thought helpful to make an estimate of the maximum shear rate at key points within a single layer flow using the following simple analysis based on the parameters shown in Figure 2.1. Newtonian rheology is assumed – again for the sake of simplicity.

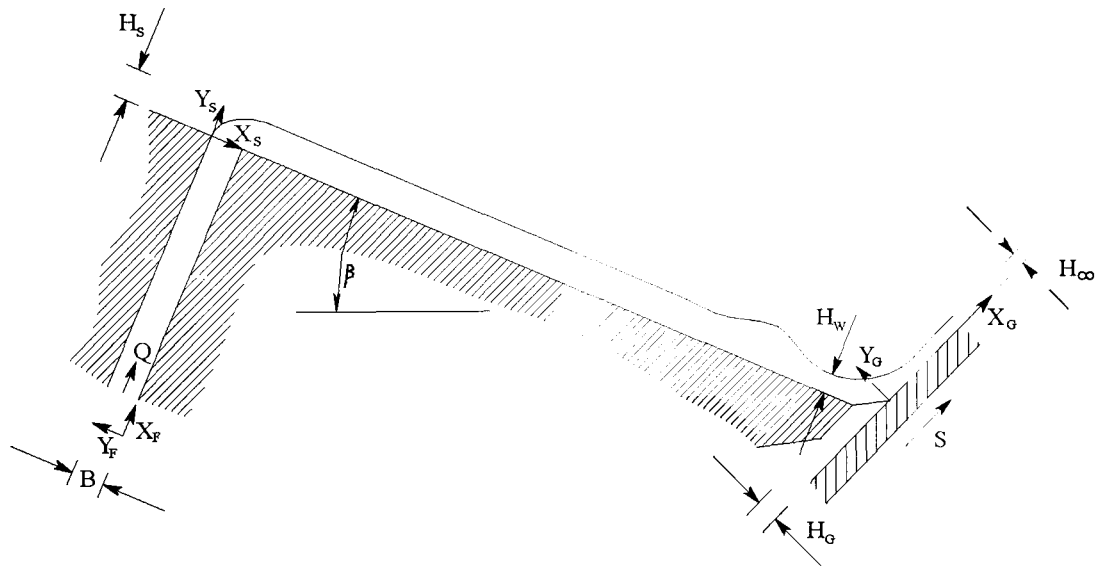

Figure 2.1: Typical flow at key points within the slide bead coating process

2.2.1.1 The Maximum Shear Rate within the Feed Slot

The function of the slot exit and associated cavity just upstream of the feed slot for a typical coating hopper has been reviewed by Weinstein and Palmer [1997]. The aim is to ensure the resistance to flow though the slot is much higher than that for the cavity – thereby ensuring the flow distributes uniformly widthwise within the cavity. This is achieved by making the cross-sectional area of the cavity large, the width of the slot small and the length large – Weinstein and Palmer [1997]. It may therefore be assumed (Weinstein and Palmer [1997]) that the pressure is non-variant widthwise and

the flow thus essentially two dimensional. For a cross-section well away from the cascade side walls and from the entrance and exit regions of the slot, the flow can be considered as equivalent to the ideal case of steady laminar flow between two parallel plates. Here the plates are separated by a distance B and the pressure gradient is dP/dX_F. Massey [1979] shows in this case that $U_F(Y_F)$ is given by:

$$U_F(Y_F) = \frac{1}{2\mu}\frac{dP}{dX_F}(Y_F^2 - BY_F) \tag{2.1}$$

Integrating, an expression is obtained for Q, the flow per unit width:

$$Q = \int U_F(Y_F)dY_F \tag{2.2}$$

$$Q = \frac{-B^3}{12\mu}\frac{dP}{dX_F} \tag{2.3}$$

providing that the width of the coater is sufficiently large that end effects can be neglected - Massey [1979]. Substituting for $\frac{dP}{dX_F}$ from (2.3) in (2.1):

$$U_F(Y_F) = \frac{-6Q}{B^3}(Y_F^2 - BY_F) \tag{2.4}$$

Differentiating:

$$\frac{dU_F}{dY_F} = \frac{-6Q}{B^3}(2Y_F - B) \tag{2.5}$$

The maximum shear rate is thus given by:

$$\dot{\gamma}_F(max) = \frac{6Q}{B^2} \tag{2.6}$$

2.2.1.2 The Maximum Shear Rate for Flow down the Slide

Bird, Stewart and Lightfoot [1960] show that for single layer flow down an inclined plane in a region sufficiently far away from the ends of the slide to ensure the exclusion of entrance and exit disturbances, the flow $U_S(Y_S)$ down the slide is given by:

$$U_S(Y_S) = \frac{\rho g H_s^2}{\mu}\sin\beta\left[\frac{Y_s}{H_S} - \frac{1}{2}\left(\frac{Y_s}{H_S}\right)^2\right] \tag{2.7}$$

Integrating again yields the flow per unit width

$$Q = \frac{\rho g H_s^3 \sin\beta}{3\mu} \tag{2.8}$$

and substituting for $\frac{\rho g \sin\beta}{\mu}$ in (2.8) into (2.7) and differentiating, an expression for the shear rate dU_F/dY_F follows:

$$\frac{dU_s}{dY_s} = \frac{3Q}{H_s^3}[H_s - Y_s] \tag{2.9}$$

The maximum shear rate is thus given by:

$$\dot{\gamma}_S(max) = \frac{3Q}{H_s^2} \tag{2.10}$$

The shear rate near the end of the slide increases at the point where the flow accelerates and thins just upstream of the bead forming zone. The minimum thickness has been defined by Schweizer and Rossier [2003] as the "bead waist" and assigned a value H_W. If it is assumed that the flow is free of recirculations in this region and also characterised by a parabolic velocity profile of form given in (2.7), then an estimate of the maximum shear rate is given by substituting H_W for H_S in (2.10):

$$\dot{\gamma}_W(max) = \frac{3Q}{H_W^2} \tag{2.11}$$

2.2.1.3 The Maximum Shear Rate within the Bead Forming Zone

Gutoff [1992] approximates the shear rate in the bead as given by:

$$\dot{\gamma}_G = \frac{S}{H_G} \tag{2.12}$$

where S is the coating speed and H_G the gap – Figure 2.1

2.2.1.4 Application to a Representative Coating Process

Minimum, maximum and typical values for a representative industrial slide-bead coating process given by S, Q, B, μ, β and H_G as shown in Table 2.1 yield the corresponding values of $\dot{\gamma}_F$, $\dot{\gamma}_S$, $\dot{\gamma}_W$ and $\dot{\gamma}_G$ shown in Table 2.2.

	S ($m.s^{-1}$)	Q (m^2s^{-1})	B (m)	μ (Pa.s)	β (deg)	H_G (m)
minimum	0.83	4.15×10^{-6}	0.5×10^{-3}	0.010	23	100×10^{-6}
maximum	3.33	2.50×10^{-4}	1.0×10^{-3}	0.300	45	510×10^{-6}
typical	2.00	3.57×10^{-5}	0.8×10^{-3}	0.030	23	125×10^{-6}

Table 2.1: Range of values for dimensional parameters S, Q, B, μ, β and B for a representative industrial slide bead coating process.

	$\dot{\gamma}_F$	$\dot{\gamma}_S$	$\dot{\gamma}_W$	$\dot{\gamma}_G$
maximum	9.59×10^3	1.09×10^4	4.37×10^4	3.33×10^4
typical	334	121	481	1.58×10^4

Table 2.2: Maximum and typical shear rates for key regimes within a representative industrial slide bead coating process.

2.2.1.5 The Rheometers used in the Study

It is clear from Table 2.2 that the choice of rheometer is highly dependent on whether or not the particular study includes the flow regime within the bead forming zone – where shear rates can reach 2×10^4 s^{-1} or higher.

A Ferranti viscometer model VL operating over shear rates up to 170 s^{-1} was used to characterise the rheology for flows where limited to the feed slot or on the slide. It was also used when investigating air induced surface waves as described in Section 4.4. The rheometer uses two concentric cylinders, the outer one rotating and the inner one held stationary under the action of a restraining spring generating a maximum torque of 2×10^{-3} kg.m. Calibration was effected by noting spring deflections for each cup speed for Brookfield Viscosity Standard Fluids 5 and 100 – of respective viscosities 4.6 mPa.s and 99.0 mPa.s when measured at 25°C. The measurement precision was of the order of ± 0.1 mPa.s at 10 mPa.s, ± 0.5 mPa.s at 40 mPa.s, ± 1 mPa.s at 75 mPa.s, ± 1.5 mPa.s at 100 mPa.s and ± 4 mPa.s at 200 mPa.s,

A more sophisticated system was required where the study investigated the performance of the coating bead or involved determining the coating window. In addition to the shear rates reaching a very high value, the time of passage through the bead forming zone is very short – being of the order of only a few milliseconds – Schunk [1989]. Ideally, a rheometer should be selected or designed that closely

mimics not only the shear rate but also the same shear history - Cheng [1995]. Capillary viscometers (Bird, Armstrong and Hassager [1987]) lend themselves to this application although care is needed to understand and correct for end effects - Ferguson et al. [1991]. Although not ideal in this respect, a Bohlin CVO Rheometer set up in the laboratories of HARMAN technology Limited and capable of achieving shear rates of the order of 10^4 s^{-1} and higher was used to characterise the rheology of coating solutions for this category. Measurement precision in this case was of the order of 50% of that using the Ferranti viscometer. Care was needed to understand and control unwanted effects as shear rate was increased. Connelly and Greener [1985] describe how they overcame problems due to radial migration of the sample at high shear rates by using two parallel plates and reducing the gap to the order of 50μm. By ramping shear from a starting value to a maximum and back to the starting value over a total period of only 2 seconds, they were able to eliminate errors due to viscous heating and detect unwanted surface fracture effects. They were able to show that errors due to geometric tolerances in the machining of the plates could be determined by calibrating the instrument using two silicone oils known to be Newtonian over a wide range of flow rates. Cohu [2001] used these methods to characterise the rheology of a range of coating solutions up to shear rates of the order of 10^5 s^{-1} when determining the air entrainment speed for curtain coating. In this work, the parallel plate configuration was used, the plate diameter being 55 mm, and the gap set firstly at 1mm and finally at 400 μm. The temperature of the sample was controlled to the value used for the particular coating study. It was found possible to achieve a strain rate of the order of 8000 s^{-1} before there was any indication of radial migration and consequential loss of fluid out of the gap. Rheological parameters were tabled according to which of several available models gave the best match to the data.

2.2.1.6 The choice of a Rheological Model

The fluids studied in this work fall into three classes:

1. Those where the behaviour is mainly dictated by the properties of gelatin.
2. Those having high solids content and based on use of a polymer other than gelatin.
3. Glycerine solutions.

Gelatin is typically used in the manufacture of photographic materials and tends to set and solidify at temperatures below 35°C and is mildly shear thinning. The rheological behaviour of bone gelatin solutions has been studied and defined by Blake, Clarke and Ruschak [1994] following on from earlier work by Connelly, Contestable and Greener [1984]. They show that the apparent viscosity closely follows the Carreau equation (2.13) - (Bird, Armstrong and Hassager [1987] and Carreau [1968]):

$$\frac{\mu - \mu_\infty}{\mu_0 - \mu_\infty} = \frac{1}{[1 + (\lambda\dot{\gamma})^2]^{(1-n)/2}} \qquad (2.13)$$

where μ is the apparent viscosity at shear rate $\dot{\gamma}$ while μ_0 and μ_∞ correspond to zero and infinite shear rates respectively. λ is a characteristic relaxation time and n is the power law index. In practice, μ_∞ is so small that it can be ignored for the solutions considered. It will be seen – Figure 2.2 – that the viscosity is essentially Newtonian over a range of lower shear rates. At shear rates where $\dot{\gamma}$ significantly exceeds $1/\lambda$, (2.13) reverts to a simple power law given by

$$\frac{\mu}{\mu_0} = \frac{1}{(\lambda\dot{\gamma})^{(1-n)}} \qquad (2.14)$$

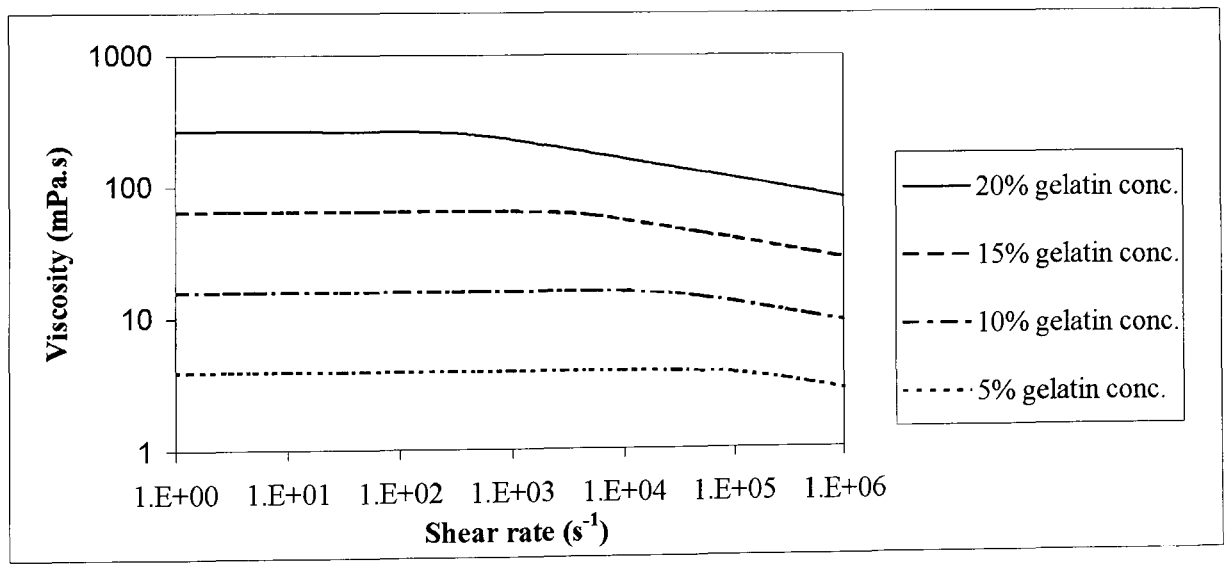

Figure 2.2: Rheology of Bone Gelatin (Blake, Clarke and Ruschak [1994])

The Carreau model, however, is not well suited to the second class of fluids characterised by high solids content. In this case, best fit was obtained using the model

due to Sisko (Sisko [1958]) in which the viscosity is related to shear rate by the expression:

$$\mu = \mu_\infty + k(1/\dot{\gamma})^m \qquad (2.15)$$

where k and m are constants.

The third class of fluids is relatively straight forward as these are essentially Newtonian over the entire range of shear rates of practical interest.

2.2.2 Static Surface Tension

Static surface tension is not necessarily important when considering coability limits as it is seldom reached during the most critical parts of the process (Tricot [1997]) but does affect ultimate coating quality – Valentini et al. [1991]. Values were determined to within ± 0.2 $mN.m^{-1}$ by measuring the adhesion force acting on a platinum ring of circumference 4×10^{-2} m placed at the free surface of the coating solution – after the method of du Nouÿ [1919]. The instrument was a White Torsion Balance for Surface and Interfacial Tension Measurement, calibrated in $N.m^{-1}$ at 20°C. Care was taken to burn off contaminants from the surface of the ring prior to any measurement by firstly cleaning the ring in spirit and subsequently bringing up to red heat in a gas flame.

2.2.3 Dynamic Surface Tension

Dynamic surface tension is the relevant surface tension acting during fast processes such as coating – especially where the use of surfactants is involved – Tricot [1997]. In addition to controlling surface forces in the vicinity of the bead forming region, surfactants play an important role in multi-layer coating in the way the individual layers merge at the slot exit. The surface tension of an upper layer must be lower than that of the next layer down in order to ensure it spreads evenly over the lower layer - Tricot [1997]. Surfactants readily adsorb to the free surface of an aqueous coating solution where the surfactant molecules orientate to present the hydrophylic part towards the bulk and the hydrophobic part outwards (Tricot [1997]). In so doing, the high energy surface water molecules become replaced by the low surface energy surfactant molecules, thereby driving down the surface tension.

The surface tension is at the static value once the surface concentration has achieved equilibrium conditions. When the surface is freshly generated, however, the concentration of surfactant molecules is so low that, for an aqueous solution, the surface tension approaches that of water. Examples include where solution emerges from the upper slot or the lower layer leaves the static wetting line. The time taken by the surfactant molecules to adsorb to the surface is dependent on the bulk surfactant concentration C_0 according to a long-time approximation (Hansen [1960]):

$$\sigma = \sigma_M + \frac{RT\Gamma_0^2}{C_0}\left[\frac{\pi}{kDt}\right]^{1/2} \qquad (2.16)$$

where σ_M is the static surface tension, R the universal gas constant, T the absolute temperature, Γ_0 the equilibrium adsorption density, k a constant depending on whether the surfactant is an anionic or non-ionic, D the diffusion coefficient and t the surface age – Tricot [1997]. In general, the DST (dynamic surface tension) response after a jump in surface area of a surfactant solution is an initial elastic response governed by the dilational surface elasticity |E| - followed by a 'viscous' asymptotic recovery to equilibrium surface tension by diffusion (Tricot [1997]).

The DST of the solution varies throughout the journey of the surface down the slide and through the bead forming region in quite a complex way due to the variety of expansions and compressions – Schunk [1989]. Valentini et al. [1991] used the maximum bubble pressure method (Adamson [1982]) for measuring DST and a modified Langmuir trough operating at 1 cycle per minute (Jiang et al. [1990]) for determining |E|. They found a strong correlation between |E| and the change in DST when measured at surface ages of 0.2 and 2 seconds. They additionally claim that the maximum suction for which a single layer coating is free from ribbing is governed by the value of |E|, whereas, for two layers, the resistance to ribbing is controlled by the layer with the lowest value of |E|. Schunk and Scriven [1997] cast doubt on Valentini's claims by stating that the characteristic time scales of most defect forming phenomena are far less than those over which they measured DST. In this study it was nevertheless decided that measuring DST as a function of surface age over a practically achievable range of 0.13 to 3.5 seconds could give insight into coatability and prove useful when subsequently modelling the flow.

The inclined plane method described by Tricot [1997] was used to determine DST as a function of surface age. The apparatus was as shown in Figure 2.3.

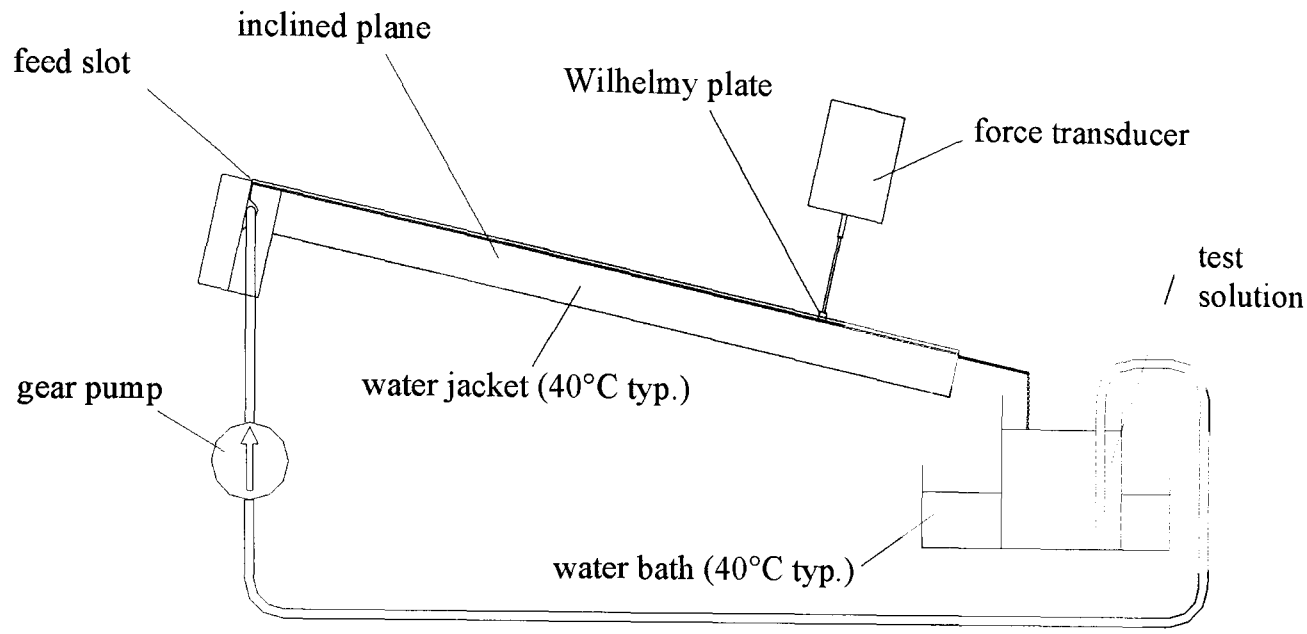

Figure 2.3: Inclined plane apparatus for measuring dynamic surface tension

The solution was fed to the distribution chamber of a miniature cascade using a miniature gear pump (Michael Smith) capable of delivering 2.8 litres/min. and allowed to flow down an inclined plane of length 455 mm to be collected back in the supply container. The container sat in a water bath maintained at 40°C and the temperature of the inclined plane and cascade was controlled to 40°C by circulating water through an in-built water jacket. Surface tension was determined to within ± 1 $mN.m^{-1}$ by measuring the force exerted on a Wilhelmy plate of length 5 mm using a force transducer of ±5 g capacity (Hottinger Baldwin Messtechnik). The force transducer was moved to various positions down the inclined plane and a spot check made of the force reading at each point. As for static surface tension, care was taken to burn off contaminants from the surface of the Wilhelmy plate prior to any measurement by firstly cleaning the plate in spirit and subsequently bringing up to red heat in a gas flame.

Substituting H_s for Y_s in (2.7), an expression for the surface velocity U_{max} down the slide is obtained:

$$U_{max} = \frac{\rho g H_s^2}{2\mu} \sin\beta \tag{2.17}$$

Substituting for H_s from (2.17) in (2.8):

$$U_{max} = \frac{3}{2}\left[\frac{Q^2 \rho g \sin\beta}{3\mu}\right]^{1/3} \tag{2.18}$$

Thus, to a first approximation, U_{max} is constant down the slide, enabling the calculation of surface age t in terms of distance X_s down the slide by the expression

$$t = \frac{X_s}{U_{max}} \tag{2.19}$$

For the sake of simplicity, any corrections (Tricot [1997]) to the predicted value for t in the immediate vicinity of the exit slot have been neglected in this study. The method suggested by Tricot [1997] has been adopted for characterising dynamic surface tension as a function of surface age using a four parameter equation (Hua and Rosen [1998]):

$$\sigma = \sigma_M + \frac{\sigma_0 - \sigma_M}{1 + (t/t^*)^n} \tag{2.20}$$

where σ_M is the static surface tension, σ_0 is the surface tension extrapolated back to zero surface age and t* and n are constants dictating the shape of the curve of best fit.

2.3 Off-line Measurement of Substrate Topography

2.3.1 Surface Roughness

Whereas the study of static wetting of rough surfaces has been extensively studied (Dettre and Johnson [1964], Menchaca-Rocha [1992], Zhou and Th.M. [1995], Rolley et al. [1998] and Miwa et al. [2000]), there is relatively little published on the important role played by roughness when attempting to coat at high speeds (Hartman et al. [1987] and Clarke [2002]). Buonopane et al. [1986] showed that the critical air entrainment speed for a variety of web surfaces in a series of plunging tape experiments generally increases with surface roughness. Suga et al. [1993] studied the wetting of a variety of substrates using the curtain process and showed it is possible to attain higher coating speeds for a given impingement velocity as the surface roughness

exceeds 0.3 μm. They moreover found an advantage in increasing the viscosity of the bottom layer and the weighted average viscosity of all layers beyond 90 mPa.s and 80 mPa.s respectively when coating rougher substrates. Clarke et al. [2001(1)] and Clarke [2002] extended this work significantly by showing that above a threshold roughness Rz of 2.5 μm and also above a threshold viscosity of typically 80 mPa.s the speed of coating limited by air entrainment increases as $Rz^{1/2}$ when coating single layers using the curtain method. They conclude there is a second wetting mechanism coming into play above these threshold values whereby the liquid skips from peak to peak rather than the wetting line moving up and down the peaks and valleys. The case for slide bead coating is, however, different in that a textured or matt substrate becomes much more difficult to coat at high speeds compared with a smooth one - Hartman [1989].

The method for characterising roughness in this work was essentially the same as that used by Clarke [2002]. A Wyko NT3300 optical profiler owned by the School of Mechanical Engineering was used in this study.

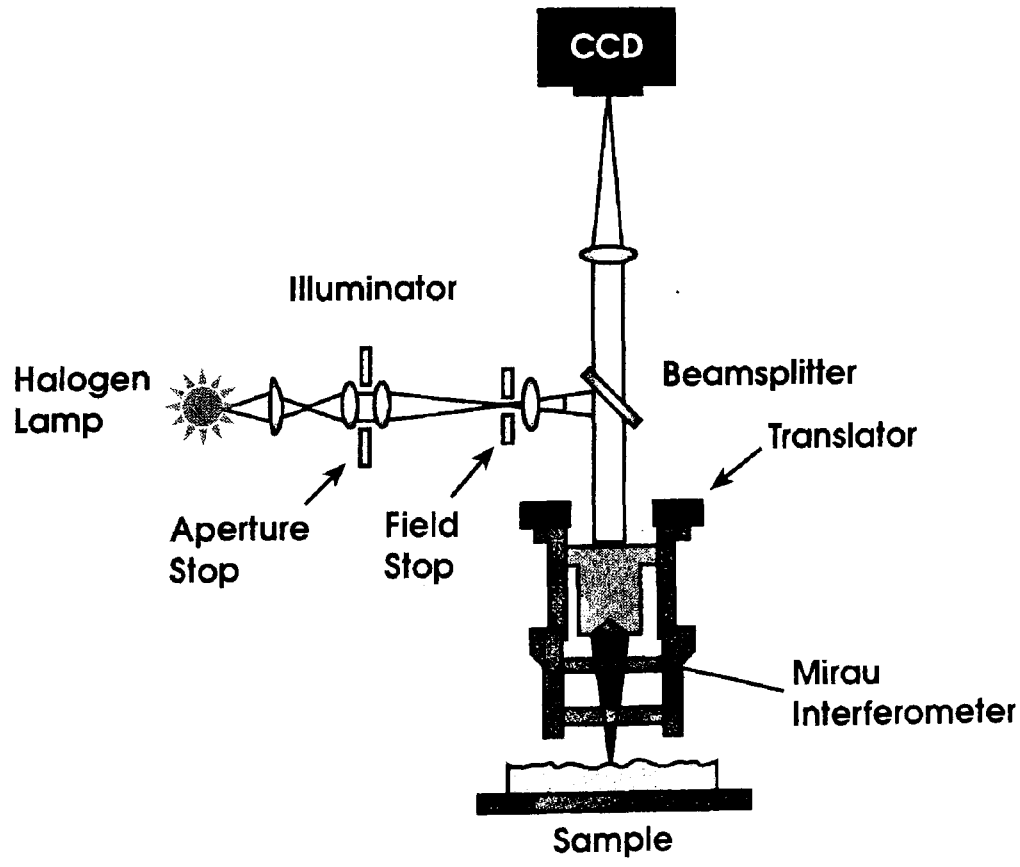

Figure 2.4: Principles of operation of a white light optical profiler (Reproduced by Permission from Veeco Metrology Group)

The profiler comprises a white light interferometer operating in vertical scanning mode – Larkin [1996]. The illumination is split within the objective, with part of the beam going to the test surface and part to a reference surface. Fringes formed as the beams are recombined go in and out of focus as the objective stage is scanned up and down in a direction orthogonal to the sample plane. The instantaneous height of any given element on the sample surface is determined by the point of sharpest focus. The manufacturers - Veeco Metrology Group - Tucson – claim that the profiler is capable of mapping up to a 10 mm wide area with sub-nanometer resolution and that it is ideally suited to quantifying surface roughness – Olszak et al. [2001].

Three parameters available within the topographical analysis software were investigated for possible correlation with coating performance:

$$R_a = \frac{1}{MN}\sum_{i=1}^{M}\sum_{j=1}^{N}|Z_{ji}| \tag{2.21}$$

and

$$R_z = \frac{1}{10}\left[\sum_{i=1}^{10} H_i - \sum_{j=1}^{10} L_j\right] \tag{2.22}$$

where R_a in (2.21) is the mean height stated in microns as calculated over the entire measured length or height, M and N being the number of data points in the machine direction X and cross-width direction Y respectively and Z the surface height relative to the mean plane. R_z in (2.22) is the average maximum profile of the ten greatest peak-to-valley separations in the evaluation area and again stated in microns. The third parameter was the surface index computed as the ratio of the actual surface area taking into account the hills and valleys to the projected area of the sampled portion. The evaluation area was 238 μm x 181μm and the sampling interval 324 nm. Measurement precision was of the order of ± 3% for Ra and Rz and ± 0.1 for surface index.

2.3.2 Dynamic Absorption

A technique was required to quantify the rate of water inbibition into the surface of a porous substrate in order to study how porosity influences the coating window. Von

Bahr et al. [2004] show that the volume V_a of liquid absorbed by paper over a contact area A varies with time t approximately according to the expression:

$$V_a = A\left\{\frac{2\varepsilon K p t}{\mu}\right\}^{1/2} \tag{2.23}$$

where ε is the porosity defined as pore volume per unit volume of the media, K is a constant, p the capillary pressure and μ the viscosity.

Bristow [1967] set up a method for measuring inbibition rate which has since become widely accepted as standard throughout the paper making industry. He constructed a wheel and arranged to pull the sample attached to the periphery past a slot applicator fed with ink supplied from a small reservoir via a restrictor. Here, contact time t is given in terms of slot length s_B and substrate speed u_B by:

$$t = \frac{s_B}{u_B} \tag{2.24}$$

Bristow [1967] found that the volume transferred per unit length was proportional to $t^{1/2}$ provide that t exceeded a critical value relating to the delay in wetting the surface.

Enomae et al. [1999] point out that Bristow's method is less than ideal as the residual liquid left in the reservoir decreases with transfer resulting in the transferred volume tailing off at the end of the ink trace. They overcame this difficulty by setting up a needle coater supplied with a constant head of fluid by arranging the capillary to be horizontal at the upper end. The liquid head was set to counter-balance the surface tension force exerted on the free meniscus in order to attain zero pressure at the coater orifice. Water transfer was measured by tracking the free meniscus using a specially constructed optical sensor. They used the device to quantify variations in dynamic absorption across the surface of paper known to exhibit a mottled appearance during printing caused by non-uniform ink take-up. Sensitivity to the changes in porosity was achieved only by reducing scan speeds to 20 mm/minute – equivalent to a contact time of the order of 3 seconds when taking into account the aperture diameter, which was 1 mm.

The apparatus built for this project is a simplified version of that used by Enomae et al. [1999]. The aim was to provide a low cost system capable of quantifying

differences in the dynamic absorption properties of samples of length limited to 100 mm – and thus smaller than could be accommodated on a conventional Bristow wheel system. This provision was made to enable a study of how defects due to outgassing as described in Section 3.7.2.1 and Figure 3.47 related to drying rate by including samples that had been dried using the rotary dryer described in Section 2.14.2. The sample was taped to a metal drum driven and transported past the orifice of a needle of 0.70 mm bore as shown in Figure 2.5. The needle was supplied with an aqueous pigmented dye held in a glass capillary tube of internal bore 0.37 mm. and marked with graduations calibrated in microlitres. The drum was driven by a variable speed motor and gear box so selected to achieve a sample speed of 14 mm/minute to ensure a contact time of approximately 3 seconds as determined by the orifice width of 0.7 mm. – in accordance with the findings of Enomae et al. [1999].

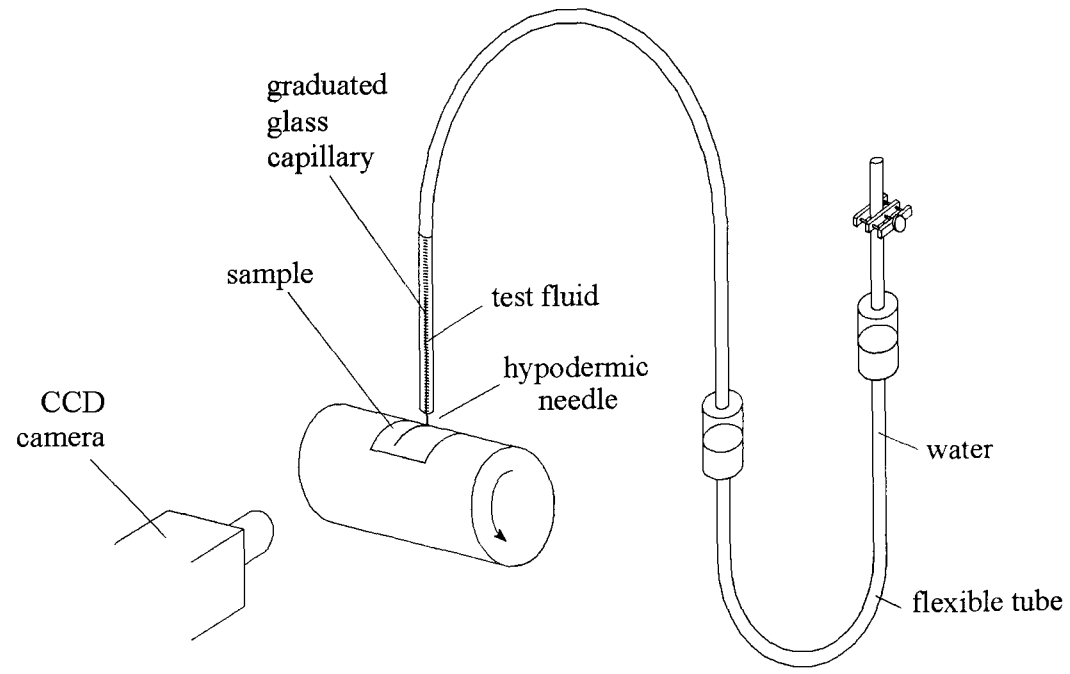

Figure 2.5: Apparatus for measuring dynamic absorption of porous media

The needle was first filled with the dye by drawing the fluid upwards through the capillary using an aspirator. The device was then lowered until the gap between the tip of the needle and the sample was about 125μm and the aspirator released to the atmosphere. The drum was set in motion and the descent of the meniscus within the capillary recorded on video using a CCD camera. A magenta pigment of particle size ~ 130 nm was used for dyeing the test fluid, the density ρ being 1030 $kg.m^{-3}$, viscosity 2.35 mPa.s and surface tension σ = 46.3 $mN.m^{-1}$ - measured as described in Section

2.2.2. The pressure P within the bead formed between the needle orifice and substrate varies with height h of the meniscus within the capillary of internal diameter D – Figure 2.6 - according to the expression:

$$P = \rho gh - \frac{4\sigma}{D} \tag{2.25}$$

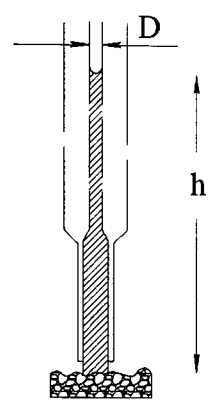

Figure 2.6: Meniscus and bead forming zone – absorption meter

In order to achieve zero driving pressure – as achieved by Enomae et [1999], the height h is then given by:

$$h = \frac{4\sigma}{\rho gD} \tag{2.26}$$

or 49.8 mm. The dynamic absorption of a given sample was accordingly cited in terms of fluid transfer rate in ml per mm scan length – measured at the point at which the meniscus fell to the height of 49.8 mm above the needle orifice.

2.4 Measurement of the Surface Energy of the Substrate

When considering the wetting of a solid surface by a drop of liquid, Young [1805] showed that the static contact angle θ shown in Figure 2.7 is given by:

$$\sigma_L \cos\theta = (\sigma_S - \pi_e) - \sigma_{SL} \tag{2.27}$$

where σ_L is the interfacial tension for the liquid-gas interface, σ_S is the intrinsic interfacial tension of the pure solid, π_S is the two dimensional film pressure exerted by the adsorbed gas on the solid and σ_{SL} is the interfacial tension for the solid-gas interface – Tricot [1997].

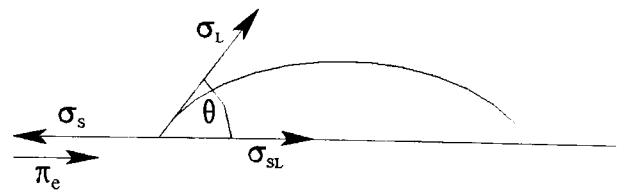

Figure 2.7: Forces acting on a drop of liquid in equilibrium with a solid surface

When the liquid drop spreads completely, the contact angle θ reduces to 0° and (2.27) becomes:

$$\sigma_L < (\sigma_S - \pi_e) - \sigma_{SL} \qquad (2.28)$$

Hence wetting is enabled by increasing the surface energy of the substrate above a threshold value dependent on the properties of the fluid.

Whereas the surface energy may be defined for a solid, there is unfortunately no direct way of measuring it as the solid will not deform in the same way as a liquid will – Woodward [2001]. The methods generally used comprise two stages - Woodward [2001]. In the first stage, the contact angle is determined for drops formed with test fluids of known static surface tension, hence enabling the terms on the left hand side of (2.27) to be quantified. In the second stage, a suitable model is employed allowing the separation of the terms on the right side of (2.27) to finally extract a measure of the surface energy of the substrate σ_S.

The apparatus shown in Figure 2.8 and associated software was used for carrying out both procedural stages in this work. (The figure was drawn by the author using AutoCAD.) The system is owned by HARMAN technology Limited and supplied by First Ten Ångstroms of Portsmouth, VA.

The equipment essentially comprises a syringe pump driven by a stepper motor and terminating in a needle of bore ~ 0.1 mm. This allows individual 30 μl drops of a test liquid of known surface tension to be individually positioned onto the substrate sample fixed down onto a stage in order to present a flat surface. A silhouette image of the drop is obtained via a monozoom optic and camera and analysed using an edge finder algorithm and curve fitting program to calculate the contact angle.

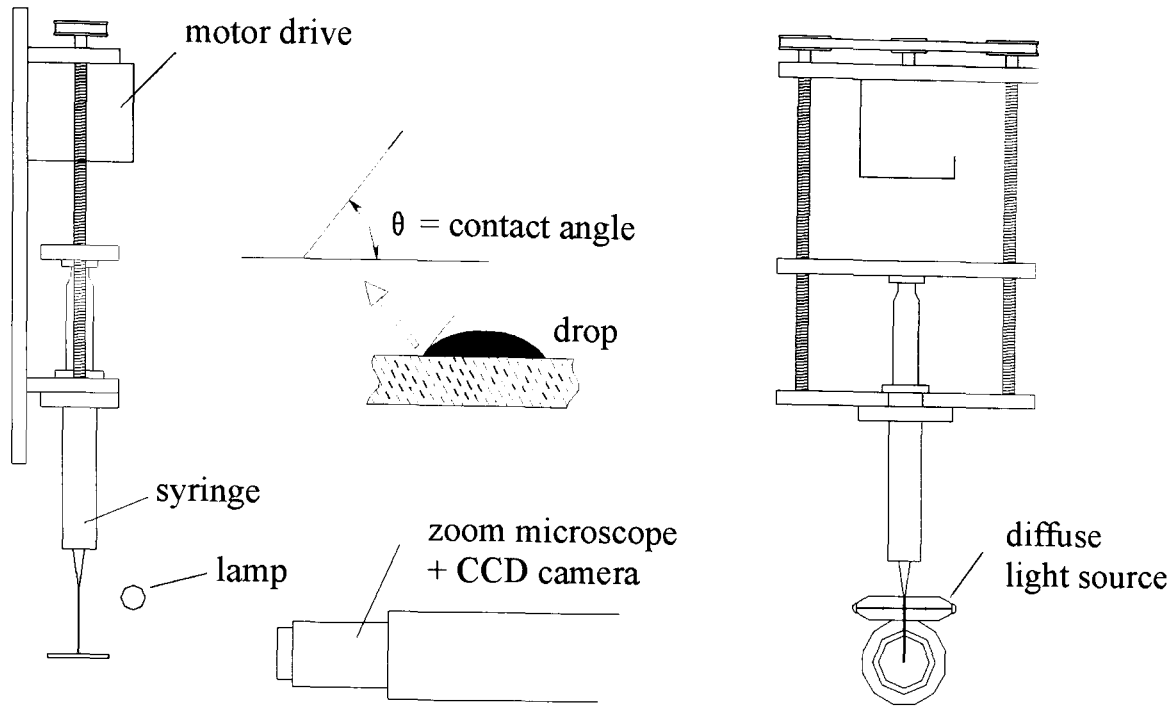

Figure 2.8: FTÅ200 Dynamic Contact Angle System

Before running measurements, a choice must first be made on which of several models to employ. In this work, two models were examined. The first was that originally due to Girifalco and Good [1957] and developed by Good [1964] for single test fluids who showed that:

$$\sigma_S = \frac{\sigma_L (1+\cos\theta)^2}{4\phi^2} \tag{2.29}$$

where ϕ is a function calculated from the molar volumes, polarisabilities, dipole moments and ionisation energies of the liquid and solid. The value of ϕ is generally taken to be unity (Woodward [2001]), but only truly applicable where there is a similarity between the molecules in the solid and liquid - Good [1964]. Whereas water is sometimes recommended as a test fluid for the sake of experimental simplicity, this is not ideal, as it is highly polar and does not usually give a value of ϕ equal to unity – Blake [2005].

The second model was that used by Owens and Wendt [1969], following on from the work of Fowkes [1962], who considered the effects of the intermolecular forces responsible for surface tension. These forces always include long range dispersive van der Walls forces, which are the only ones to operate across phase boundaries and are thus responsible for the work of adhesion – Tricot [1997]. Short-range forces present

include polar interactions such as hydrogen bonds – Blake and Ruschak [1997]. Fowkes [1962] proposed that the attractive forces responsible for surface tensions are additive and concluded that if the liquid and solid interact by dispersive forces only, then:

$$\sigma_{SL} = \sigma_L + \sigma_S - 2\sqrt{\sigma_L^d \sigma_S^d} \tag{2.30}$$

where σ_L^d and σ_S^d are the dispersive components of the surface energies of the liquid and solid respectively, and substituting into (2.27) after neglecting π_e, obtained:

$$\cos\theta = -1 + 2\sqrt{\sigma_S^d}\,\frac{\sqrt{\sigma_L^d}}{\sigma_L} \tag{2.31}$$

Owens and Wendt [1969] extended the assumptions of Fowkes [1962] by proposing a model for where both dispersive and polar forces operate at the liquid-solid interface and obtained a more general form of (2.31) as shown in (2.32):

$$\cos\theta = -1 + 2\sqrt{\sigma_S^d}\,\frac{\sqrt{\sigma_L^d}}{\sigma_L} + 2\sqrt{\sigma_S^h}\,\frac{\sqrt{\sigma_L^h}}{\sigma_L} \tag{2.32}$$

where σ_L^h and σ_S^h are the polar components of the surface energies of the liquid and solid respectively. They measured θ for two test fluids of known and widely differing dispersive and polar surface tensions and solved the two simultaneous equations resulting from substituting the two values of θ and the known values for σ_L, σ_L^d and σ_L^h into (2.32) to obtain σ_S^d and σ_S^h. The choice of test fluids should be such as to ensure that the liquid drops do not react unduly with the surfactants likely to be present within the surface of the substrate being evaluated. The same test fluids as employed by Blake and Morley [1997] were used for this work – namely 1-bromonaphthalene and 2,2'-thiodiethanol. These are essentially non polar and polar and have surface tensions as shown in Table 2.3:

Test Liquid	σ_L^d ($mN.m^{-1}$)	σ_L^h ($mN.m^{-1}$)	σ_L ($mN.m^{-1}$)
1-bromonaphthalene	43.7	0.9	44.6
2,2'-thiodiethanol	33.6	20.4	54.0

Table 2.3:Surface tension components for 1-bromonaphthalene and 2,2'-thiodiethanol

Blake and Morley [1997] applied the method of Owens and Wendt [1969] to the study of how surface properties dictate coating performance using a falling curtain. They found that it was important to correlate the maximum coating speed with a calculated rather than measured value of static contact angle for water to avoid problems associated with the leaching of surfactant into the test fluid. They calculated the predicted value for θ assuming the surface tensions of pure water to be as shown in Table 2.4. They found that the highest coating speeds for a curtain of 3 cm fall height was obtained for substrates where $\sigma_S^h < 10$ mN.m^{-1} and $\sigma_S^d > 30$ mN.m^{-1} and where the calculated value of the static advancing contact angle for pure water lay between 65° and 100°. These findings were used as a guide to interpreting the data obtained in this work – as described in detail in Section 3.3.

Test Liquid	σ_L^d (mN.m^{-1})	σ_L^h (mN.m^{-1})	σ_L (mN.m^{-1})
Water	21.8	51.0	72.8

Table 2.4: Surface tension components for water

2.5 Key Facilities for studying Coating and Drying

2.5.1 Pilot Coating Machine – Key Components

Extensive use was made of the M22 pilot coating facility set up in the Test Coating wing at the HARMAN technology site in Mobberley Cheshire. This section describes features of the machine existing at the commencement of the project. Section 2.5.2 goes on to define work done to improve the facilities either directly in support of the project or as part of an ongoing development to improve the application of drying to ILFORD Photo products.

The pilot coating machine - Figure 2.9 - was originally designed to coat small samples of photographic film and paper.

The machine is housed in a dedicated laboratory. Views from the coating head and rewind ends of the machine are shown in Figures 2.10 and 2.11 respectively.

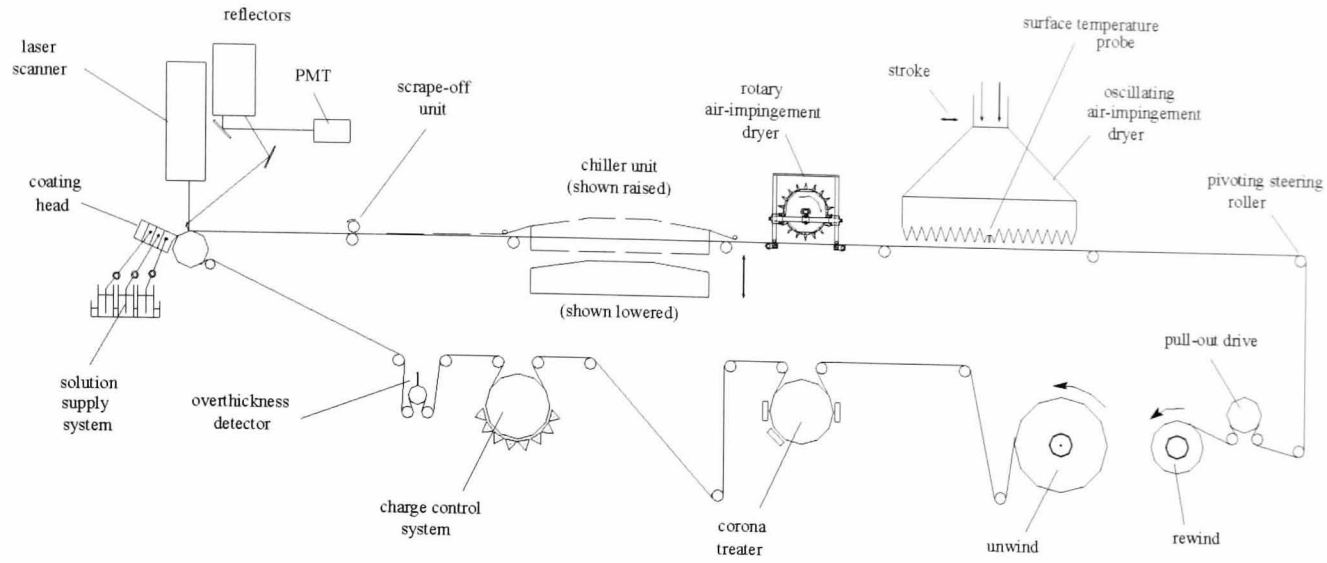

Figure 2.9: M22 pilot coating machine before upgrading in support of project

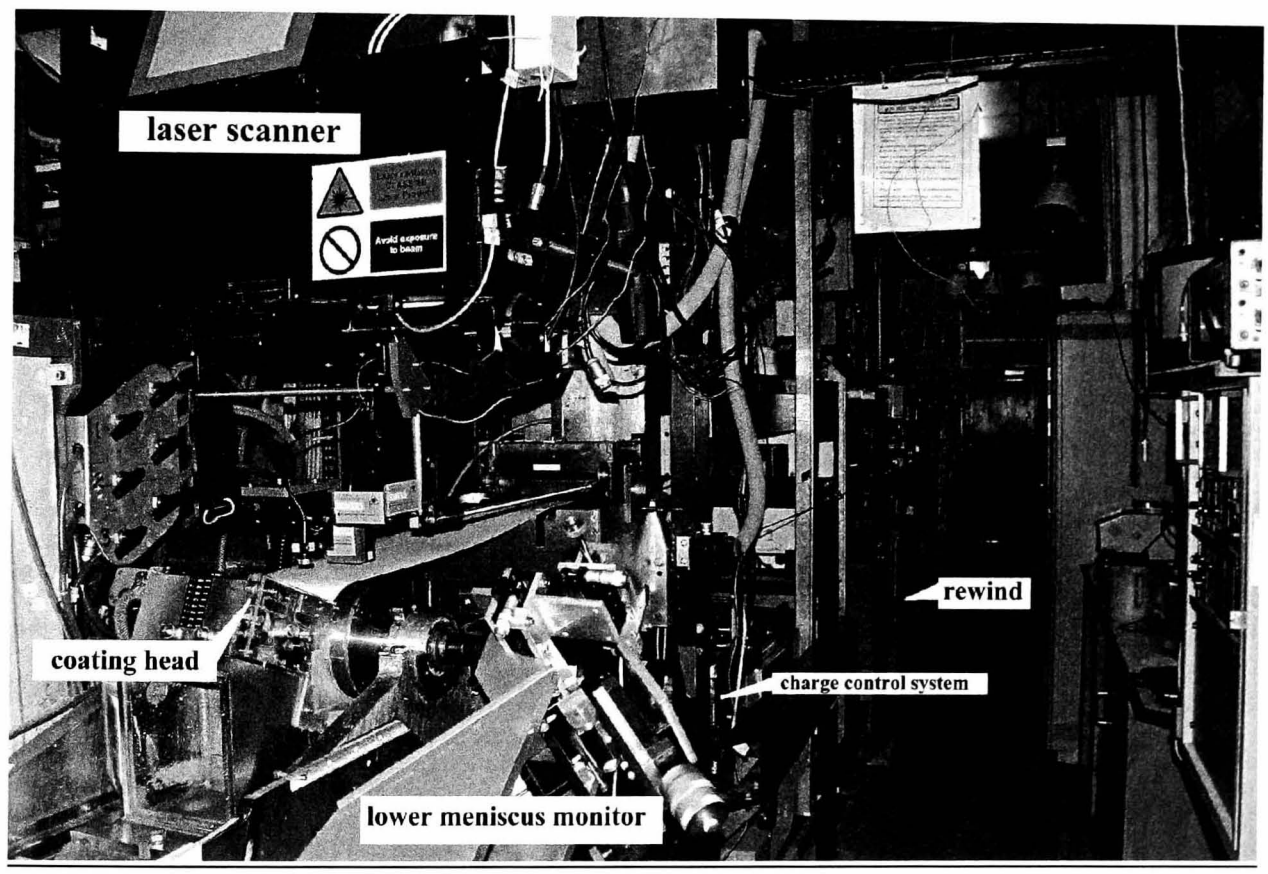

Figure 2.10: View of pilot coating machine from coating head end

The coating fluids traditionally comprise gelatin as a key ingredient, which has a transition temperature of about 32°C and is typically coated at about 40°C. The paper or plastic web to be coated leaves the unwind point and is transported through a corona treatment station, a system for controlling surface electric charge and an over-thickness detector before passing round the coating roller. The web path continues beneath a laser scanner system – to be described more fully in section 2.11.2 – under a

scrape-off roller, over a chill bed and under two experimental dryers to terminate at the rewind.

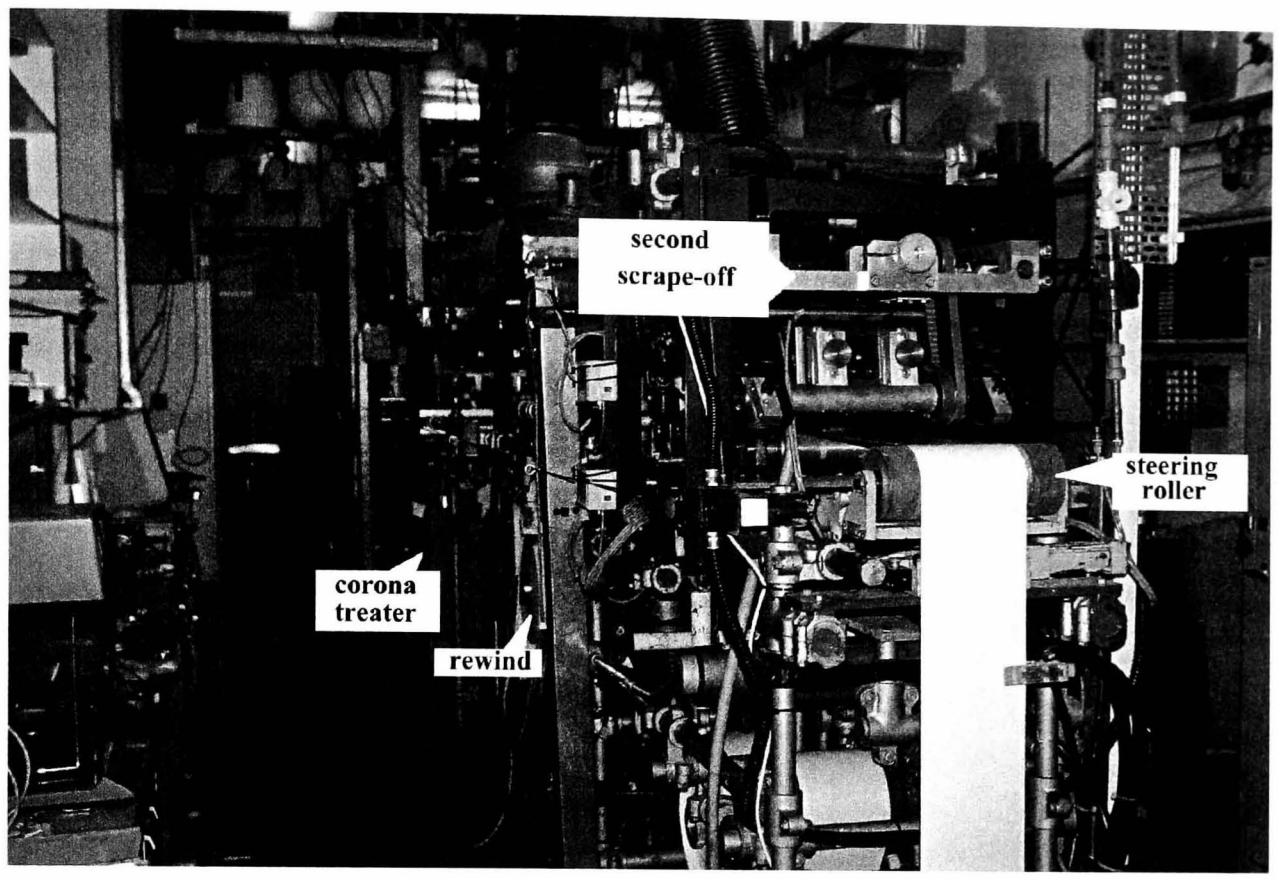

Figure 2.11: View of pilot coating machine from rewind end

The machine may be operated to either a) enable continuous coating as dictated by the size of the stock roll or b) allow samples to be extracted for visual inspection of coating quality or further testing. The scrape-off system serves to remove the wet material from the web surface in order to minimise fouling of the machine at the wind-up end when continuously coating. Sampling is enabled by initiating a sequence commencing with disengaging the scrape-off system and bringing the leading edge of the unscraped coating to a stop at the end of the chill bed section. The chill bed comprises a curved platten that can be raised or lowered by pneumatic cylinders and is maintained at typically 2°C by circulating a water-glycerol mixture round an external loop. The platten is raised to make contact with the underside of the coated sample to enable heat to be transferred out of the coating in order to solidify the material prior to final drying – as is commonly practised within the photo-industry - Gutoff and Cohen [1995]. The final part of the process involves transporting the web to bring the sample under one of the experimental air impingement dryers to remove residual moisture

prior to final cutting and extraction at a point near the rewind end of the machine. The key components of the machine will now be described in more detail.

2.5.1.1 Web Tension Control and Tracking

In order to ensure optimum speed uniformity at coating, the coating roller acts as master drive and tension is roughly balanced either side so as to minimise slip. "Pre-coat" tension is adjusted by varying the unwind motor torque in accordance with the position of a follower arm tracking the diameter of the stock roll. "Post-coat" tension is controlled through the use of a motorised rubber roller – or pull-out drive. Tension at the final reeling point is adjusted by varying the corresponding motor torque in accordance with the position of a follower arm tracking the diameter of the roll of collected material. Improvements made during the course of the work to enable higher coating speeds will be described in 2.5.2.

Web tracking is controlled by two steering mechanisms, one allowing the stock roll to be moved to and fro in the cross-machine direction to allow one edge to be aligned with a datum. A second device comprises a pivoted roller mounted at the end of the horizontal web path as shown in Figure 2.9 and corrects for any drift in position of the same edge relative to datum.

2.5.1.2 Corona Treatment

The corona treatment unit comprises an earthed metal roller carrying the web - with the surface to be coated facing outwards. Three electrode assemblies are mounted in close proximity to the web surface and connected to high-voltage power supplies operating at high frequency. The system is designed to generate a corona discharge at each electrode and associated breaking down of the resistance of the air to produce reactive ionized oxygen, which oxygenates the surface thereby increasing its surface energy - Gutoff and Cohen [1995]. The main benefit is a significant improvement in adhesion between the coated layers and the base surface – especially post-drying – Gutoff & Cohen [1995]. Gutoff & Cohen [1995] suggest that surface treatment including the use of corona is often used to improve wettability as well as adhesion. Whereas it is clear that corona treatment does increase the equilibrium wettability of

the substrate and through this the adhesion, it should not necessarily be assumed that dynamic wettability is thereby enhanced.

2.5.1.3 Charge Control System

It is well known that a typical corona treatment system can also generate a polar charge distribution on the web surface that is highly non-uniform – Nakajima et al. [1993]. This can be readily revealed by taking a sample and sprinkling xerox powder onto the surface and observing the resulting particle distribution. Nadeau [1960] pointed out that variations in surface charge result in corresponding non-uniformities in the coating. The charge control system on M22 was originally built to smooth out these non-uniformities using the method of Gibbons et al. [1972], who showed that it is possible to reduce the effect by first charging the web to one potential and then charging with an opposite potential. This is effected using an array of grid ionisers or screen-controlled corona charging devices – Figure 2.12 – similar to those originally developed at the Batelle Memorial Institute by Walkup [1957], described by Vyverberg [1965] and more recently adapted by Hartman [1989] for high speed curtain coating.

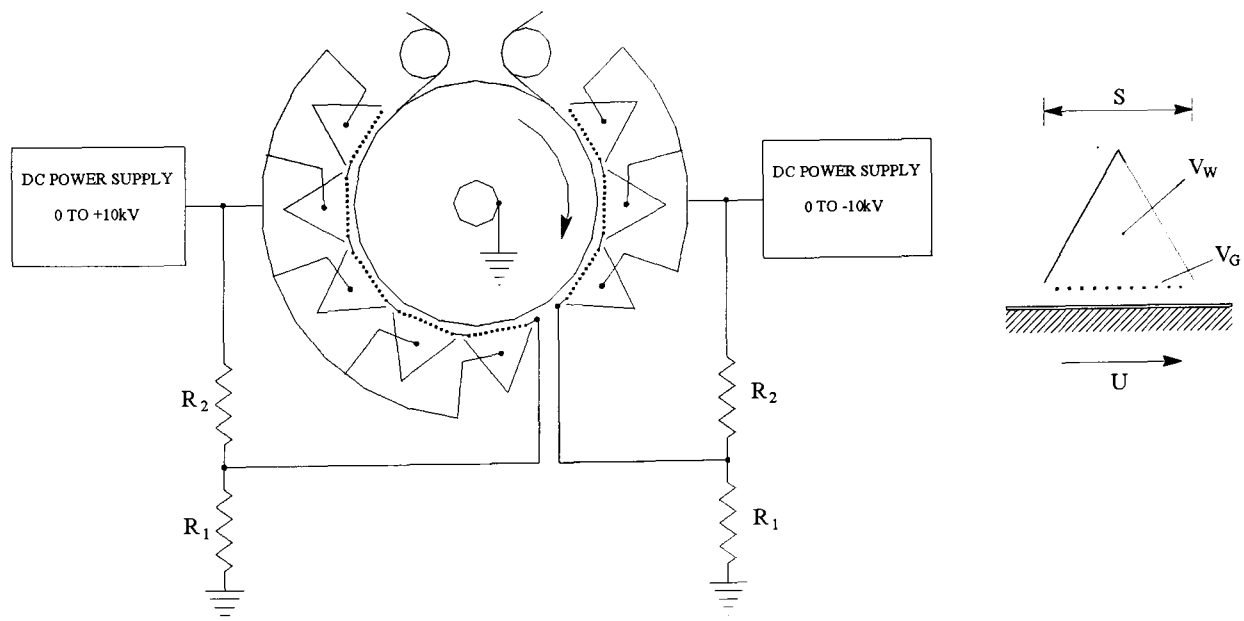

Figure 2.12: Charge control system

Each charging device comprises an earthed electrode of width S at the centre of which is suspended a thin tungsten wire connected to a DC power source supplying a potential V_W – typically a few thousand volts. The electrode is mounted close to an earthed roller carrying the web – where the surface to be coated again faces outwards. A grid or screen of closely spaced wires is mounted in close proximity to the web as shown and maintained at a potential V_G approximately given by

$$V_G = rV_W \tag{2.33}$$

where

$$r = \frac{R_1}{(R_1 + R_2)} \tag{2.34}$$

While planning studies undertaken in this work to determine the effect of varying charge level on coatability, the following analysis was made in order to establish how web charge relates to the control voltage for a range of web speeds U. It is well known (Vyverberg [1965]) that the corona current I_W emitted by a fine wire in close proximity to a conducting plate is related to the potential difference V_W measured between the wire and the plate by the expression:

$$I_W = a_0 + a_1V_W + a_2V_W^2 \quad \text{for when } V_W > V_T \tag{2.35}$$

where a_0, a_1 and a_2 are empirically determined constants and V_T is the threshold voltage for corona discharge. It is also established (Vyverberg [1965]) that for a screen controlled collecting plate, the current I collected by the plate is related to the plate potential V by the capacitance per unit area C according to the equation:

$$I = C\frac{dV}{dt} \tag{2.36}$$

The system under consideration here comprises a moving web instead of a stationary plate. For any single electrode, the current emitted by the central fine wire is collected by the outer electrode, a further part by the grid and the rest by the web surface. The current I(t) collected by the web is proportional to the potential difference across the gap between the grid and web surface and is given by:

$$I(t) = kI_W[V_G - V(t)] \tag{2.37}$$

where V(t) is the web surface potential at time t and k is a constant.

V(t) is given by substituting for I(t) from (2.36) into (2.37) and integrating:

$$V(t) = V_G - (V_G - V_0)\exp\left[\frac{-kI_Wt}{C}\right] \tag{2.38}$$

where V_0 is the potential of the incoming web surface. For where N electrodes are used in sequence, the total web exposure time T is given in terms of web speed U by:

$$T = \frac{NS}{U} \tag{2.39}$$

Hence, substituting T for t in (2.38) and using (2.33) and (2.35)

$$V = V_G - (V_G - V_0)\exp\left[\frac{-kNSf(V_G)}{CU}\right] \tag{2.40}$$

where $f(V_G) = a_0 + a_1(V_G/r) + a_2(V_G/r)^2$ for when $V_G > rV_T$ (2.41)

Figure 2.13 shows experimentally determined web potentials and the predicted response on trimming values of a_0, a_1, a_2 and k for best fit when using three grid ionisers after initally neutralising V_0 to zero using an array of negative grid ionisers.

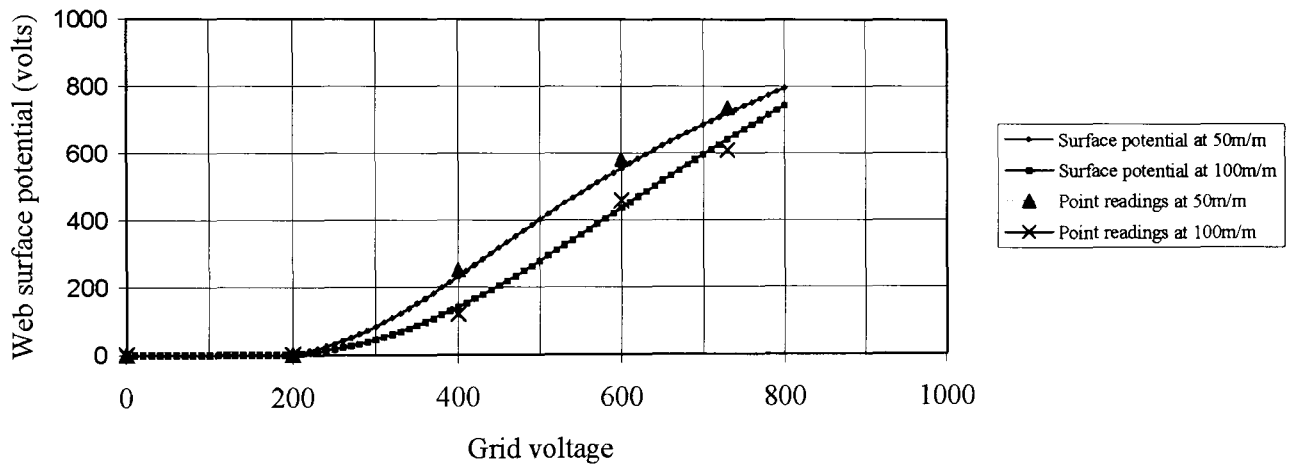

Figure 2.13: Web potential vs grid voltage for three positive grid ionisers

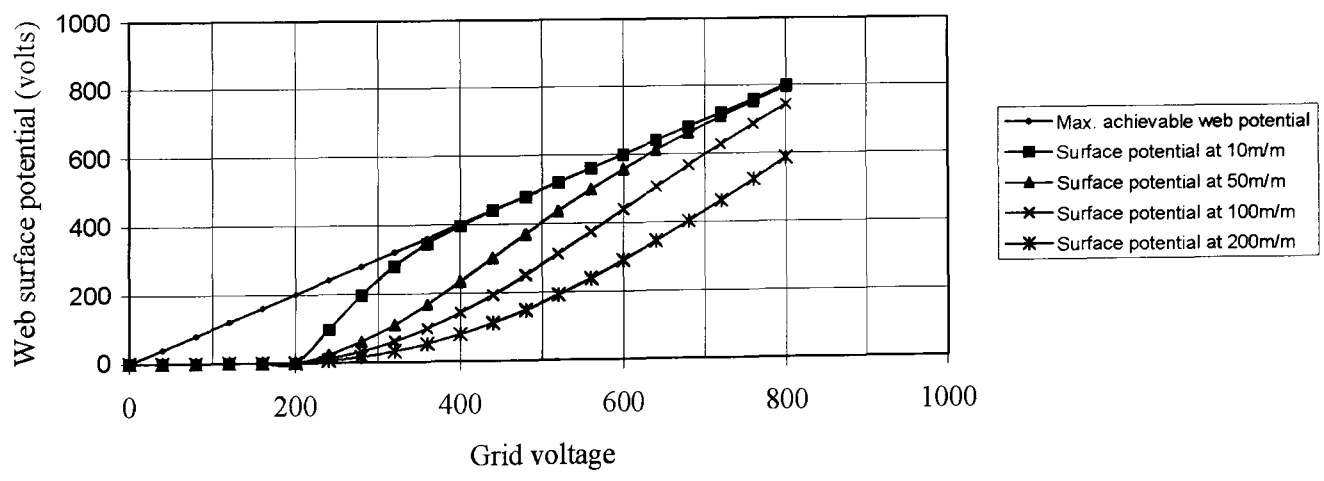

Figure 2.14: Predicted response of positive grid ionisers for four different web speeds

Figure 2.14 shows by extension, the predicted response for four different web speeds. It can thus be seen that that the potential acquired by the web continuously traversing

under N electrodes at speed U asymptotically approaches V_G at a rate that increases with N but decreases as U increases - all provided that $V_G > rV_T$, or in this case about 200 volts. In addition to smoothing charge – as revealed, for example, using the xerox powder test - the use of the system can be extended to exploring the effect of charge assisted coating by adjusting the ratio of positive to negative charging currents to leave the web surface with a net polar charge.

2.5.1.4 Over-Thickness Detector

The detector - Figure 2.15 - serves to generate a signal as a lump on the base above a predetermined height, or in the more general case, an inter-roll join approaches the coating head. Pneumatic cylinders are activated to open up the gap at the coating head to let through the protrusion or splice by an amount to prevent damage to the lip face while hopefully not breaking the coating bead.

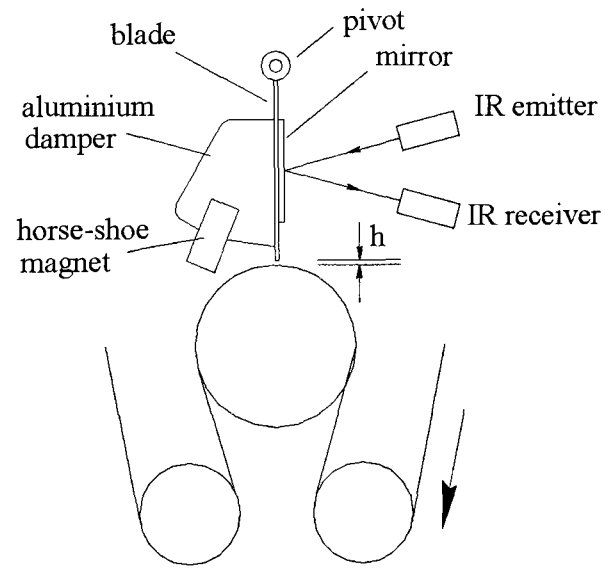

Figure 2.15: Over-thickness detector

The module comprises a stainless steel blade free to swing about a horizontal pivot bar and set above a precisely ground roller to leave a gap h set to equate to the coating gap. The blade carries a plane mirror which reflects an infra beam from an emitter into the entrance aperture of an infra-red receiver unit. Improvements made in support of this study include the fitting of an aluminium damper blade and magnet designed to speed up the return of the blade when triggered by a join. This was considered important when coating at higher speeds as observations show the static wetting line to take a finite time to migrate down the lip face after opening up the gap.

2.5.1.5 Coating Head and Solution Supply

The coating head is as shown in Figure 2.16 and essentially comprises a number of precisely machined blocks of equal height and clamped together to form a cascade using bolts of the same material. Each block is machined at one of the mating faces to leave a slot and cavities into which the solutions are pumped at a predetermined rate. The cavities and slots are otherwise sealed at the ends by side plates. The blocks carry water ways used for maintaining the assembly at typically 40°C for the reasons already described. Outer side plates constructed of transparent Perspex extend to almost touch the coating roller. The cavity formed between the coating head and roller is partially sealed at the bottom with a suction box designed to maintain a pressure difference of a few hundred Pa between the upper and lower free surfaces of the coating bead in order to stabilise against air entrainment – Beguin [1954]. The head is mounted on a rugged bridge carried by a translating table free to move in a horizontal direction for controlling the coating gap. The head can be moved back from the roller by a distance of about 130 mm enabling solutions to be pumped through the slots and uniform slide flow established without fouling the roller or web before attempting to make the bead. A wash-up tray serves as barrier between the head and the translation table. The suction box carries a drainage system fitted with a trap designed to conserve suction pressure.

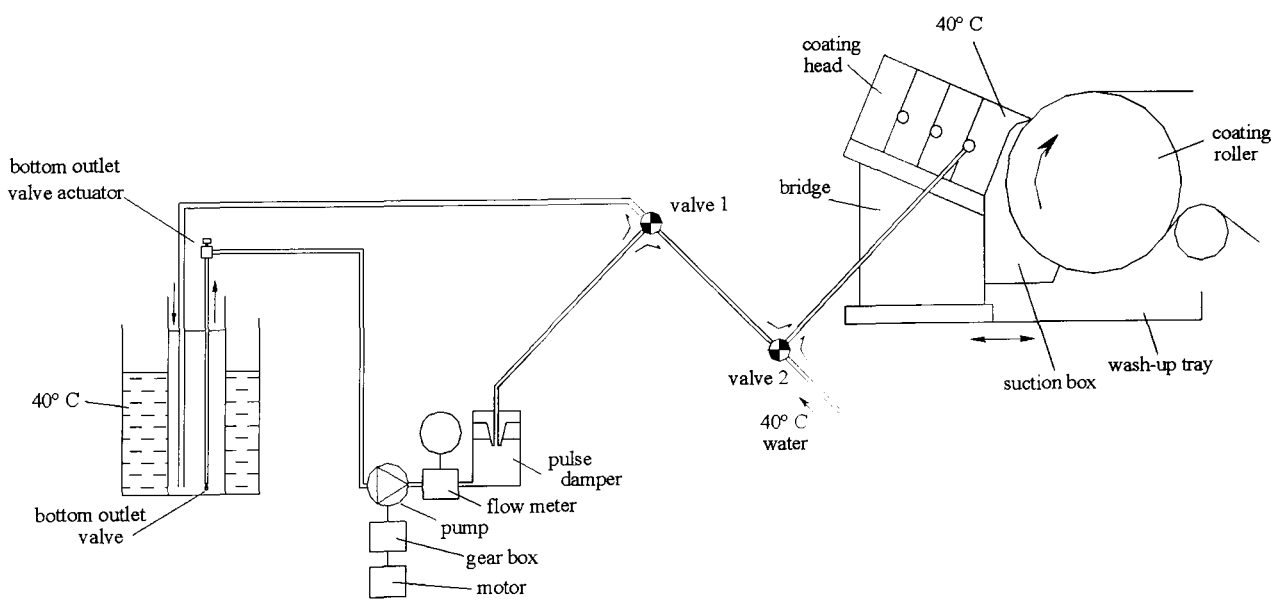

Figure 2.16: Coating head and bottom layer solution supply in original form

Individual solutions are fed from stainless steel containers seated in a water bath controlled to typically 40°C using three separate supply systems, one of which is shown in Figure 2.16. They are initially circulated round a loop at a flow rate exceeding that required for coating in order to remove bubbles adhering to the walls of the pipes – Schweizer [1992]. To coat, the valves are switched to divert the solutions to the coating head and diverted back to the loop at the end of coating. Flow is energised by Liquiflow gear pumps capable of delivering up to 1.5 litres/minute and controlled to ± 1% of set-point using electromagnetic flowmeters. Pump induced pulsations are reduced by trapping air in a cavity in a specially designed miniature pulse-damper of the air-spring type - Schweizer [1992]. Water maintained at 40°C is fed to the cascade ports when not coating in order to wash the lines, cavity walls and slots.

2.5.1.6 Scrape-Off Device

The scrape-off assembly comprises a well polished accurately machined stainless steel roller. This is motorised and caused to make contact with the wet coating so as to exert a drag force in the direction opposite to the web motion - resulting in the majority of the fluid becoming transferred to the roller. The roller is scraped clean by a water flushed doctor blade mounted at top-dead centre and the assembly provided with a collector tray mounted beneath the blade for drainage. The assembly can rotate about a horizontal pivot in such a way that the roller can be lifted clear of the web under the action of an electromagnetic solenoid when a sample is required. Sample length is typically 1 m.

2.5.1.7 Air Impingement Dryers

Two dryers are incorporated into the machine. The first is a novel system designed and installed just prior to the commencement of this study – Ikin [2000]. This comprises eighteen equispaced air impingement jets mounted on the periphery of a circular drum free to rotate about the drum axis. The drum is driven by a variable speed motor capable of achieving peripheral speeds matching those studied during this project.

The system and the work done during this study to enable the simulation of continuous web movement over protracted periods is more fully described in Section 2.14.2.

The second dryer is a linear array of eighteen air impingement jets of slot width 1.5 mm spaced 75 mm apart. The array forms the lower part of a jet box. The height of the jets above the web can be varied over a range of 10 to 40 mm. The air entering the jet box is supplied by a fan and is initially drawn through a dehumidifier unit designed to control dew point to typically −12°C. The air supply incorporates a chiller designed to control the incoming air to 20°C. A fast response electric heater is installed just upstream of the jet box. This allows the dry bulb temperature of the air issuing out of the jets to be varied with time from the moment the sample is stopped under the dryer - for a period equivalent to the drying time used in a typical production set-up for a given coating speed. The temperature 'profile' is designed to match that typically used for drying the product being studied. A steam injector is mounted between the heater and jet box and similarly used for varying dew point. A drying model is used for estimating the dew point at the surface of the partially dried coating for a typical full-scale set-up and for assigning an appropriate profile for controlling steam injection. The jet box was initially mounted on rails via linear bearings and caused to oscillate back and forth in the machine direction under the action of pneumatic cylinders. The original aim was to minimise local disturbances to the wet coating immediately below each jet.

2.5.1.8 Sampling

Sampling is very crude and effected by transporting the dried coating to a point near the end of the machine between the last dryer and pivoting steering roller, releasing the tension and cutting either side with scissors or scalpel blade.

2.5.2 Work done to Upgrade the Machine

2.5.2.1 Objectives and Justification

Three projects were undertaken in which the specification of requirements, design, installation and commissioning were carried out in direct support of this work – with no support from ILFORD Imaging UK Ltd. other than resourcing the manufacture of

parts and providing technician resource as required. These projects are described in detail in Sections 2.5.2.2, 2.5.2.3 and 2.5.2.4 and addressed the following issues:

1. Solutions were being delivered at the head at a variable temperature and hence variable viscosity.

2. Scrape-off was inadequate when continuously coating at speeds exceeding 130 m/minute - resulting in excessive fouling of the machine at the rewind end, premature slip at the pull-out drive and consequent failure of the web tension control.

3. The charge control system was limited to setting constant charge levels, whereas a need arose to study the response of the coating bead to a sinusoidal variation in surface charge.

Two major projects were additionally set up. These were resourced by ILFORD Imaging UK Limited in order to meet the requirements for a stable experimental system to study methods for increasing drying capacity – while recognising commitment to the needs of this study. These activities are described in more detail in Sections 2.5.2.5 and 2.5.2.6. A user requirement specification was written – Ikin [2003] – which not only catered for ILFORD Imaging's requirements but also took into account the following additional issues of direct relevance to the work described in this thesis:

1. The poor reliability of the machine drive often necessitated time consuming and expensive remake of solutions as these rapidly deteriorate when held at elevated temperatures.

2. The machine speed was limited to a nominal maximum of 150 m/minute – in practice only 120 m/minute with any degree of reliability.

3. Sample control dynamics was very unreliable owing to the tendency for the web to slip forwards or backwards over the coating roller when decelerating the web to rest

4. Setting drying profiles for quantifying air induced disturbances while drying the wet coating was extremely laborious – moreover the equipment was old and unreliable.

Whereas the major engineering work involved in these two projects was directed and resourced by the company, the ensuing programme for commissioning the refurbished machine of necessity became a key part of the work supporting this study.

2.5.2.2 Improvements to the Control of Solution Temperature carried out in direct support of this study

Gelatin solution - as used throughout the photographic industry as the main vehicle for holding light sensitive crystals in suspension - gels when the temperature falls below 40°C – and the relationship between viscosity, concentration by volume and temperature is typically as shown in Figure 2.17 – Schweizer [1992].

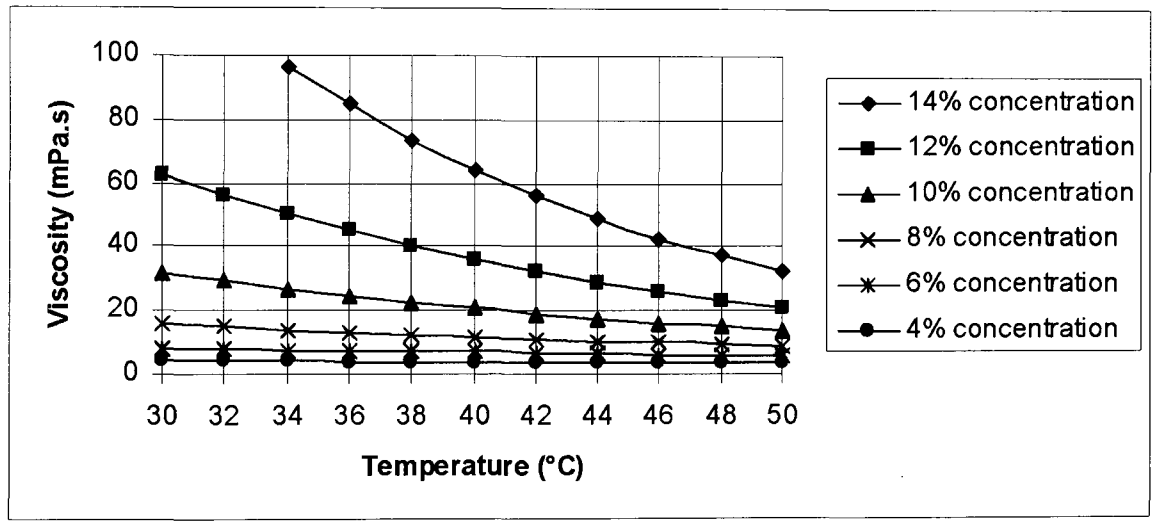

Figure 2.17: Viscosity vs concentration and temperature for a typical gelatin solution

It can be seen from Figure 2.17 that the temperature of solution entering the cascade must be controlled to better than ±1°C if viscosity is to be maintained to the order of ±5% of the required value. Measurements using the system shown in Figure 2.16 showed that the temperature fell from 40°C to typically 35°C after about 30 minutes. Thus was found to be due to evaporation losses at the free surface within the reservoirs and cooling within the pumps, flow meters and pulse dampers as well as the long pipes leading up to the three way valves. It was found that the desired tolerance could readily be achieved after designing and installing hinged lids, heated pipe jackets and enclosing the key components in a box maintained at 40°C as shown in Figure 2.18.

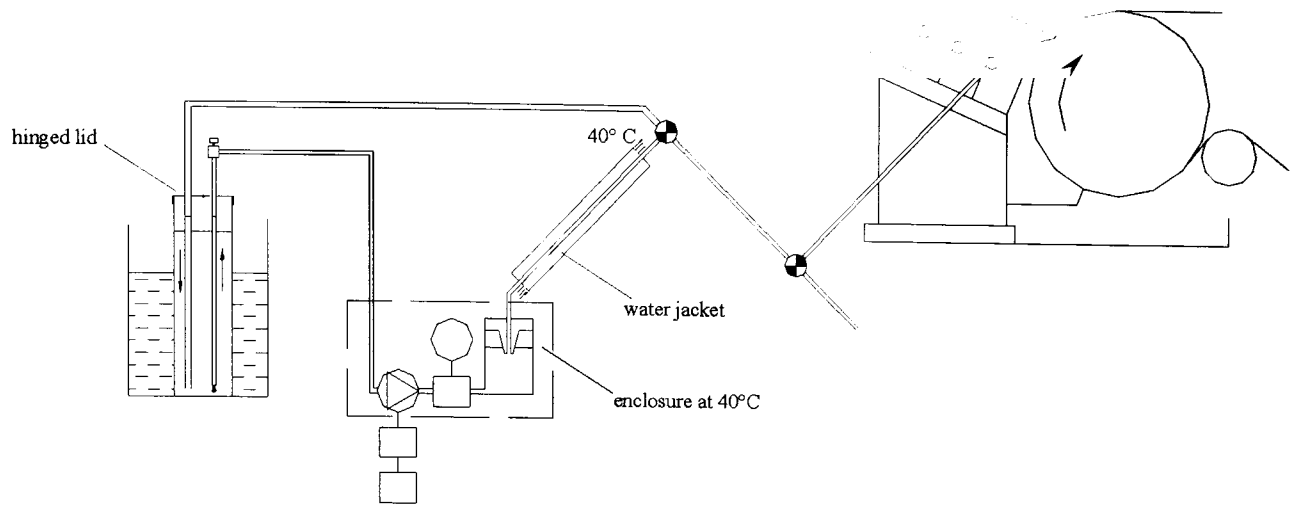

Figure 2.18: Modified bottom layer solution supply

2.5.2.3 Improvements to the Scrape-Off System carried out in direct support of this study

An additional scrape-off unit – originally designed as a prototype for the production plant – was taken out of storage and mounted at the end of the machine – as shown in Figure 2.20. This operates on a similar principle to the first scrape-off installed near the coating head. It uses a larger roller and a precision engineered flushed doctor blade unit. It is capable of removing the majority of the wet deposit on the web when continuously coating at speeds up to 200 m/minute and thus saves undue fouling of the face-on rollers at the rewind end of the machine – especially at speeds exceeding 130 m/minute.

2.5.2.4 Modifications to the Charge Control System carried out in direct support of this study

A small modification has been made to the charge control system for varying polar charge sinusoidally with time – to enable studies on the dynamic response of the coating bead. The potentiometric control of the high voltage power supply feeding electrodes 4 to 7 has been replaced by a variable voltage source comprising an auxiliary variable DC power supply and an oscillator – as shown in Figure 2.19.

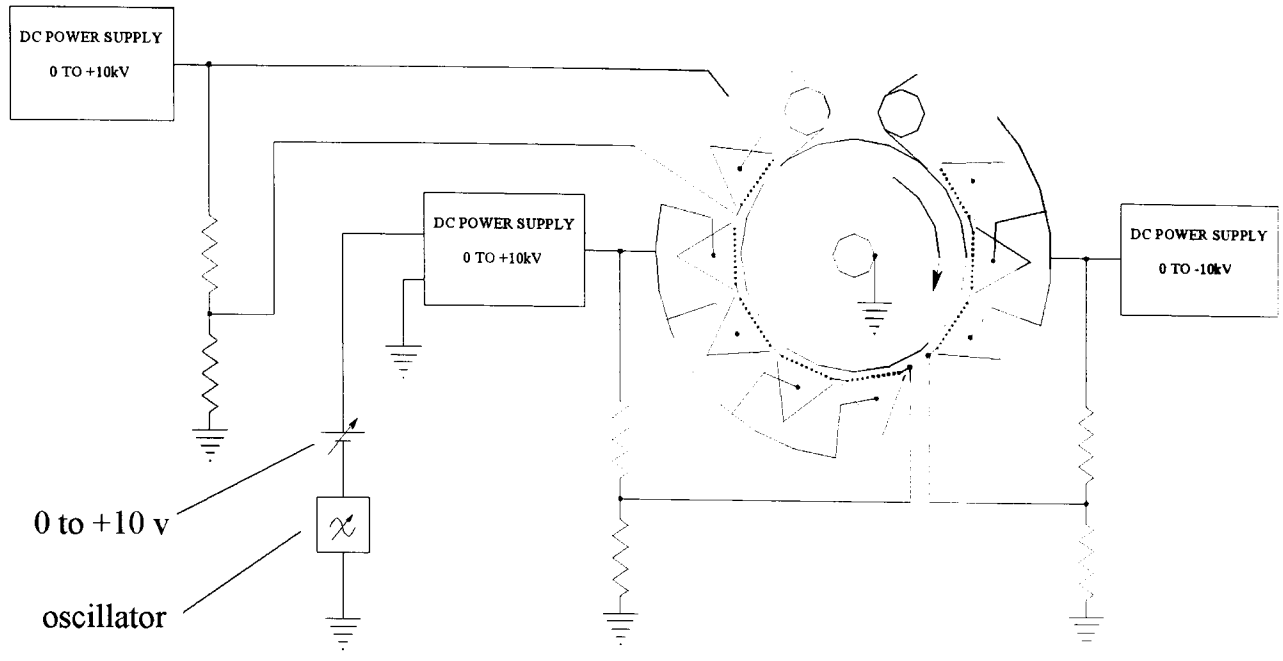

Figure 2.19: Modifications to charge control system

The oscillator output amplitude is variable, the instrument being operated with the minimum of each cycle clamped at zero volts. The DC offset is first adjusted to ensure each electrode wire is always operating above the emission threshold. The oscillation amplitude is varied to ensure the maximum of each cycle is at a level as to yield maximum swing in polar charge without driving into positive saturation.

2.5.2.5 Improvements to the Machine Control System in partial support of this study

The main control cabinet was completely replaced and all wiring renewed as part of the effort to improve machine reliability. A new programmable logic controller and computer interface were installed in order to address the above issues. This has enabled an operator to now load a new drying profile in a few minutes instead of typically several hours. A pressure sensor mounted in the duct supplying air to the linear air impingement jet array enables precise profiling of air pressure throughout drying to within ± 5 % – a feature essential to the study of limits due to air induced surface waves.

2.5.2.6 Improvements to the Web Transport System and Sampling Dynamics in partial support of this study

"Dancing" roller systems have been added at the unwind and pull-out drive sections as shown in Figure 2.20. These enable precise control of tension either side of the coating roller for web speeds up to 200 m/minute independent of the diameters of the stock roll and scrap roll at the reeler.

Problems due to slip at the coating roller were overcome by installing a rubber tracking wheel near to the charge control system which is used to feed pulses relating to actual web position in the machine direction to the new computer for control purposes.

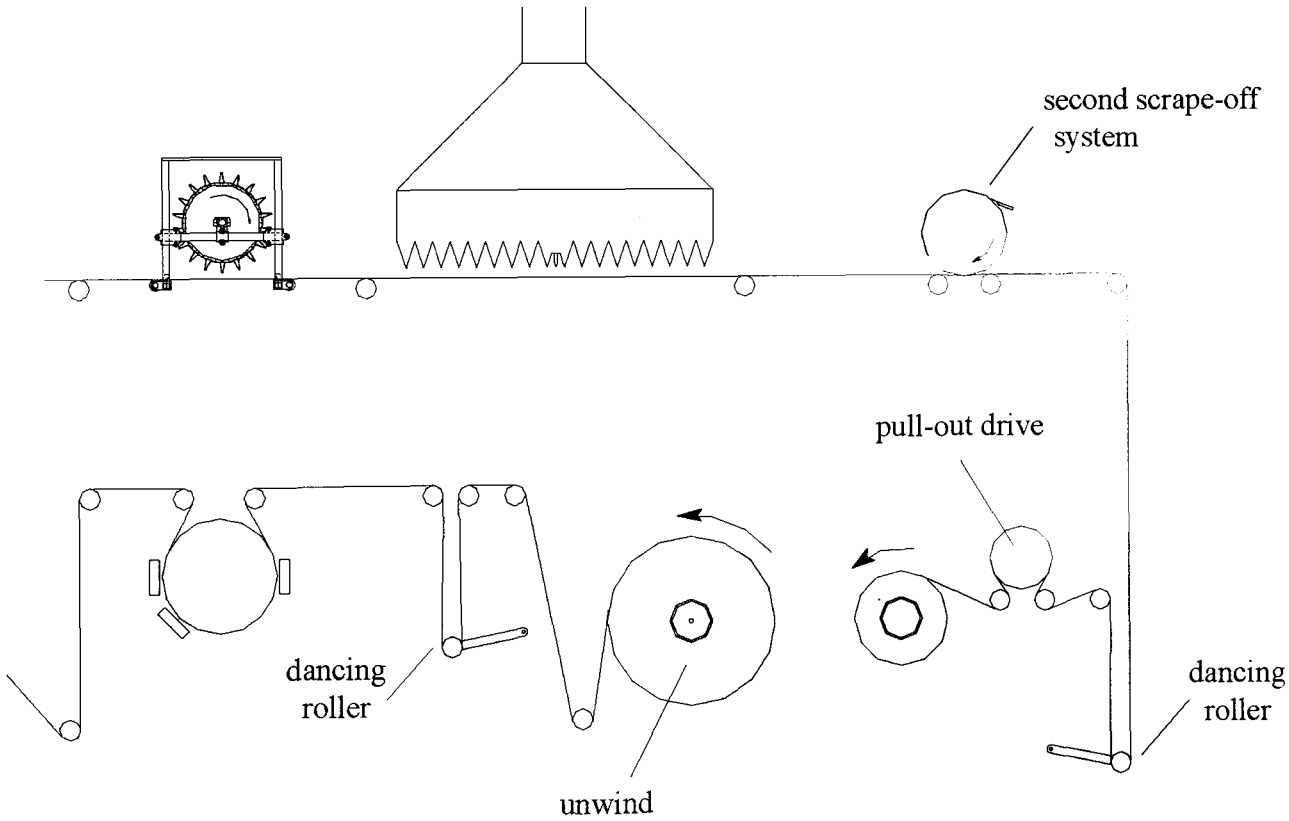

Figure 2.20: Improvements to web transport system and scrape-off facilities

The overall effect of these improvements is that it is now possible to attain a steady maximum speed of 200 m/minute for all stages during the unwinding of a stock roll of diameter up to 0.4 m – provided that the diameter of the scrap roll is kept below defined limits. It is moreover now possible to direct a sample to any pre-defined point

on the machine to a precision of ±5 mm irrespective of slip at the coating roller for any web speed up to 200 m/minute.

2.5.3 Off-Line Flow Rig

The second main facility provided by ILFORD Imaging UK Limited for the purposes of this study was the so called Solution Supply Rig set up within a Chemical Engineering Laboratory. This rig comprises an enclosure 2.45 m long by 2.0 m wide and of height 2.47 m. The panels are supported on a welded frame constructed of 40 mm x 40 mm square cross-section tubes. The enclosure is bunded to allow drainage to central points within the laboratory to enable all systems mounted within it to be freely hosed down for cleaning at the end of a run. The Philips VBS (Variable Building System) comprising a variety of components readily clamped onto 25 mm stainless steel tubes forms the basis for mounting experimental systems off the internal framework. Wherever possible, all optics and electrical connections are assembled outside of the enclosure to ensure delicate items remain undamaged and the system safe during use and subsequent wash-down.

2.6 Off-Line Perspex Cascade

An initiative was taken to design a special cascade for mounting within the Solution Supply Rig - to address an evident need to visualise flows in the regions where layers merge on the slide and to record instabilities in slide flow. The idea was to construct the main blocks and side plates of transparent Perspex – a brand name for polymethylmethacrylate – to enable visual access to the flow. The fact that the surface energy and hence the wetting properties of the material differ from that of the metal alloys used for production cascades was considered not to be an issue as the study was aimed at the merging of flows that were already established. Support was given by ILFORD Imaging UK Limited for funding the manufacture of the cascade using the specialist skills of engineers familiar with the machining of this material. Care was taken to avoid setting up thermally induced internal stresses by firstly normalising the Perspex, significantly reducing cutting speed and using sufficient lubricant.

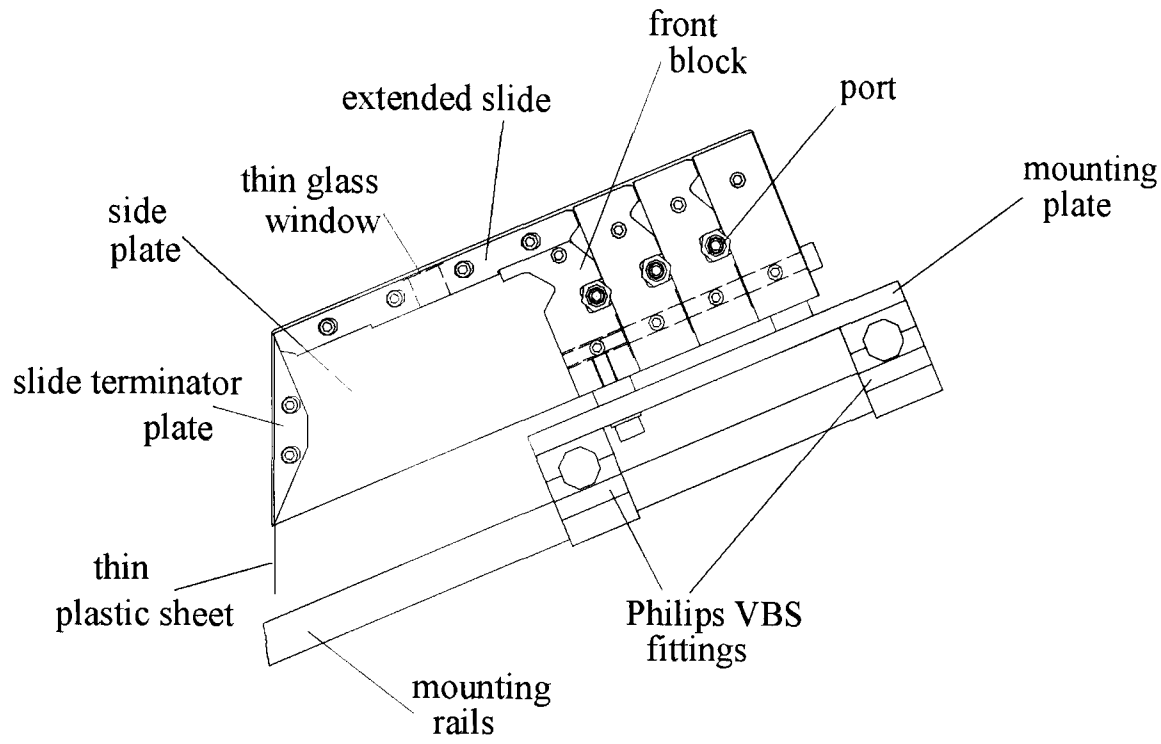

Figure 2.21: Off-line Perspex cascade and mountings

The completed cascade and its mounting system are shown in Figure 2.21. The front block is machined at a lower height than the rest of the blocks to allow an extension of the slide to be bolted to its upper surface. The slide extension can be turned end-for-end and remounted on the front block – the aim being to provide facilities for studying two different slot exit geometries, one chamfered and the other non-chamfered – as described by Apps [2000]. Moreover the fixing holes are slotted to enable the width of the bottom exit slot to be varied between 0 to 1.45 mm – well in excess of the range considered for industrial use. A terminator plate is mounted vertically to ease transfer of fluid from the slide to waste via a thin plastic sheet. The front block has a cavity machined in its external face to accommodate a laser diode module. This is used for illuminating the lower slot exit to facilitate the visualisation of merging flows in this region – as described in Section 2.7. Special care has been taken to ensure the critical regions used for transmitting light in and out of the slot region are as flat and as well polished as possible to reduce losses in intensity due to scatter and distortion due to refraction. The slide extension is fitted with a thin glass window to enable disturbances in the slide flow to be accurately monitored – as described in more detail in Section 2.8.

2.7 Methods for Studying the Flows at the Carrier Layer Slot Exit

2.7.1 Principles of the Methods

The experiments were confined to the study of the merging of two layers at the exit of the lower slot. The test fluids generally comprised PVOH (polyvinyl alcohol) at various concentrations and supplied at room temperature. The fluid forming the upper layer contained scattering agent while that forming the lower carrier layer was left transparent. Silver halide has been found suitable as a scattering agent elsewhere – Valentini et al. [1996]. Silver chloro-bromide photographic emulsion prepared by a controlled crystal growth technique proved a useful additive in this case, the particle size being typically 350 nm. This enabled the profile of the interlayer interface and the free surface to be imaged by illuminating the slot with a knife of light from beneath and viewing from one side in directions as close to horizontal as possible – Figure 2.22.

The fact that the main layer was opaque also provided a basis for determining the optical density profile of the flow downstream of the lower slot and measured in the crosswise direction, from which coating uniformity could be calculated.

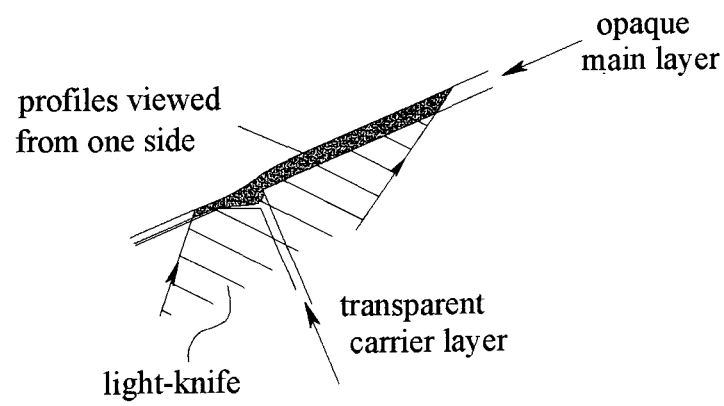

Figure 2.22: Principle of method to visualise flows at the carrier layer slot exit

2.7.2 The Experimental System

The solutions were supplied from two reservoirs via the pumps and flow meters already installed within the Solution Supply Rig – Figure 2.23. Special care was taken

to minimise disturbances to the flow profile due to bubble entrapment within the slots and cavities of the cascade and to conserve expensive solution as much as possible. This was achieved by arranging the delivery system to ensure fluids moved continually upwards from the bottom outlets of the reservoirs. Inherent difficulties associated with priming the pumps were overcome by temporarily coupling each supply outlet to an evacuated chamber specially set up for this purpose. A secondary supply system was installed to allow the cascade to be washed up independent of the supply systems in order to minimise solution wastage.

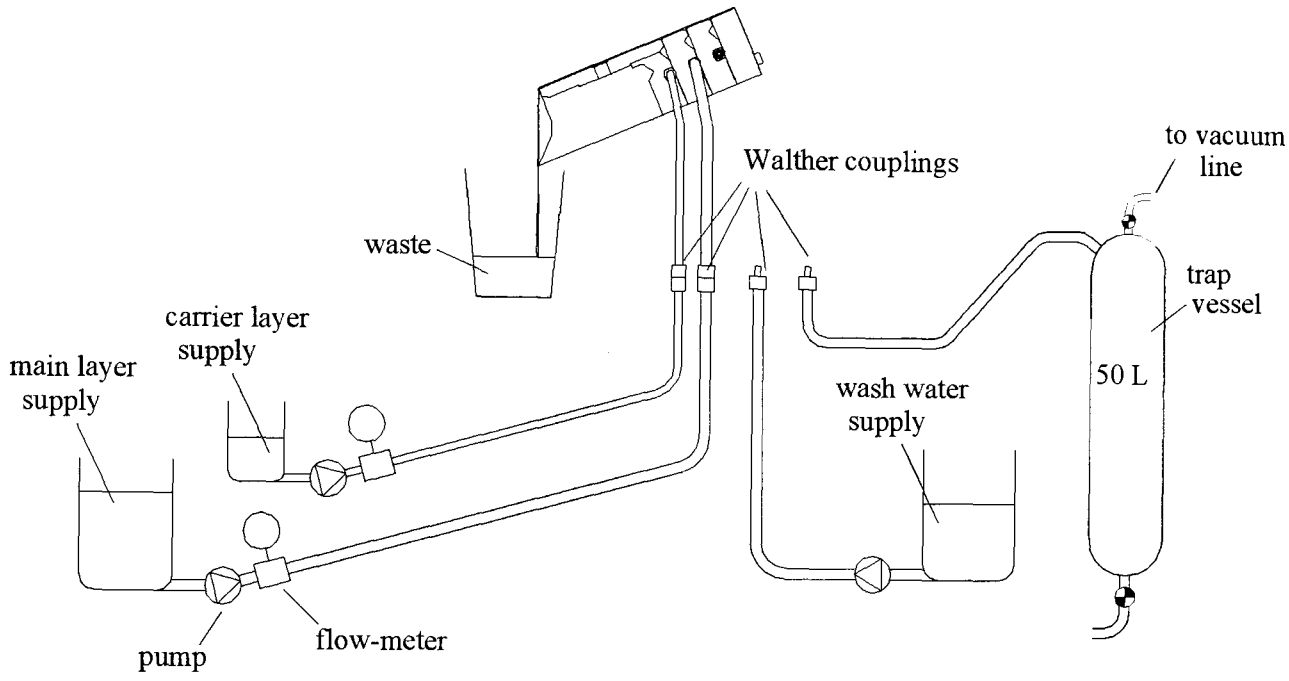

Figure 2.23: Solution supply system used for visualising slot exit flows

The light knife was supplied by a 3.0 mW laser diode module operating at a wavelength of 670 nm and manufactured by Vector Technology – Figure 2.24. The laser was fitted with a singlet lens and a cylindrical lens to convert the beam to a fan of light of total angle 16° and capable of being focused to a line of width typically 100μm at a distance of about 25 mm from the exit aperture. The laser was mounted just outside the front block and arranged so that the light knife was in a vertical plane and focused at the exit region of the lower slot. The illuminated region was at a distance of 20 mm from the edge of the slide to ensure freedom from edge effects – Schweizer [1988]. Care was taken to minimise reflection losses at the interface between the Perspex slide and Perspex front block by introducing a drop of pure

glycerol and allowing it to spread and dispel the intervening air film in the vicinity of the laser beam path. Also shown in Figure 2.24 is a pointer carrying a "bull's eye" pattern and illuminated by a fibre-optic white-light source. This served as optical reference when fixing profiles relative to the slot exit geometry.

Observations with a hand held low power microscope showed that it was necessary to view the profiles of the free surface and interface from slightly different directions – one above and the other below the horizontal. This requirement has been accommodated using a beam splitting device specially designed by the author - Figure 2.25.

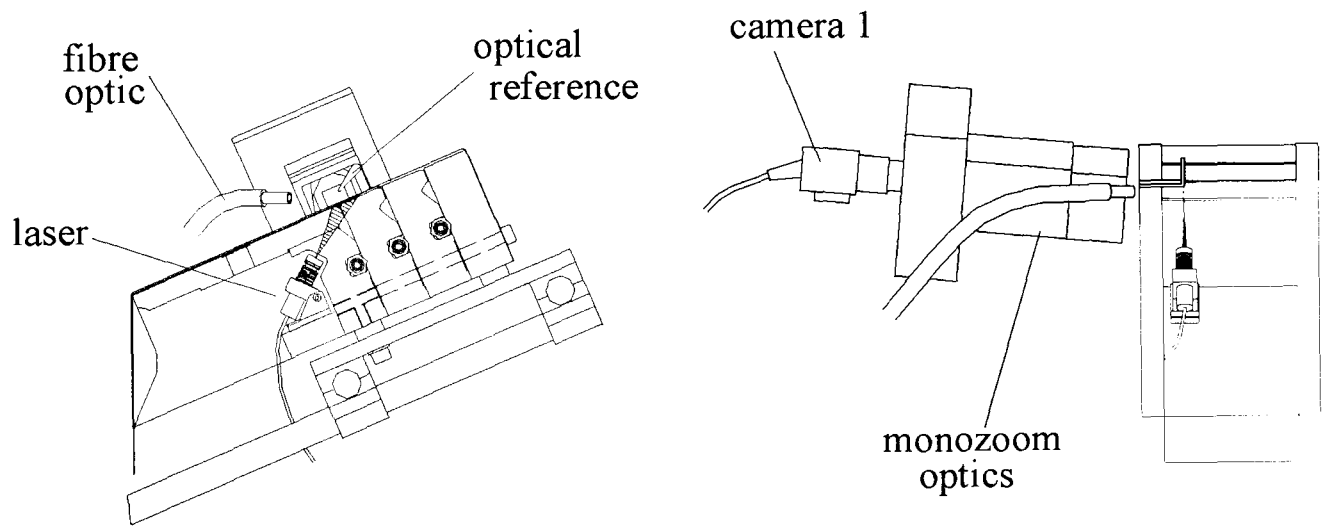

Figure 2.24: Optical components for visualising slot exit flows

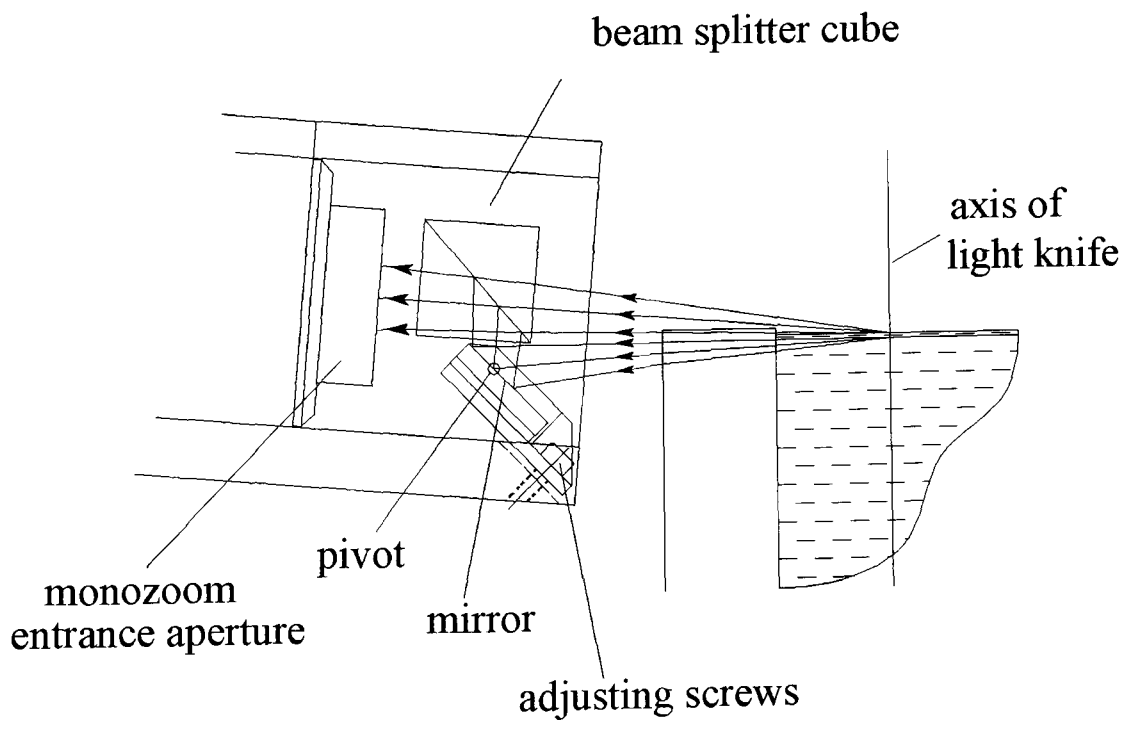

Figure 2.25: Beam splitting optics for profiling the free surface and interface

The optics allowed the two images to be recorded simultaneously using a single Cohu model 6712 monochrome camera fitted with Monozoom-7E optics manufactured by Bausch and Lomb. The camera operates at ½" format, has selectable automatic gain control allowing sensitivity to 0.005 lux and is capable of resolving 4×10^5 pixels. The monozoom assembly is fitted with a 0.75X objective. The working distance measured from the collection aperture is of the order of 80 mm. The minimum and maximum magnifications are 13.4 and 93.6 respectively for which the corresponding field diameters are 26.6 mm and 3.81 mm.

Scaling was achieved by pre-recording the image of a graticule set up on the dry slide prior to recording the flows. The positions and orientations of the beam splitter cube, mirror and camera aperture have been adjusted to ensure the focus for either received beam coincides with the illuminated section of the flow for when the monozoom is operated at minimum magnification. The calculations took into account refraction as the received beam passes through the beam splitter cube, which is constructed of BK7 glass of refractive index 1.52. Allowance was similarly made for refraction at the boundaries of the Perspex side wall, the refractive indices for the material and for water being 1.49 and 1.33 respectively – all indices being taken for the laser wavelength.

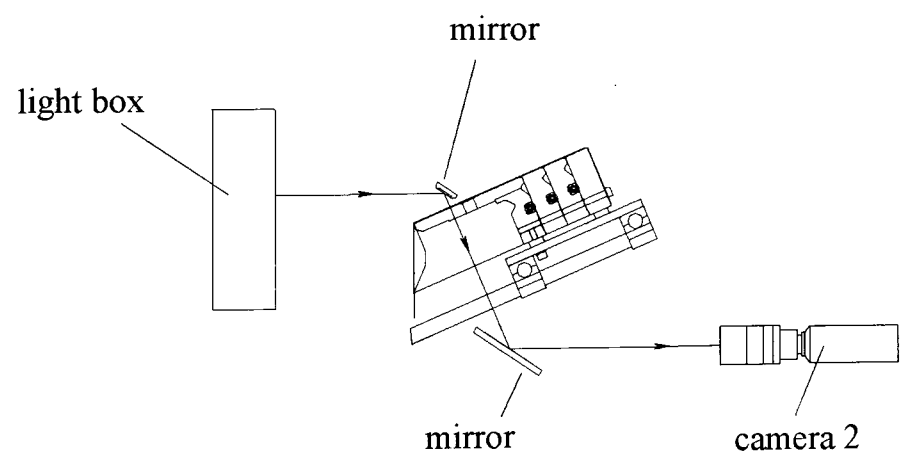

Figure 2.26: System for recording cross-width uniformity of the slide flow

Care was taken in designing the optics for recording slide flow to ensure good access to the slide for clearing bubbles lodged in the slots. A single bubble in the line of sight into the lower slot can seriously disturb or even destroy any image generated by the interface. The system used is shown in Figure 2.26. A second camera was set up to

record the view of the slide from beneath via a lower folding mirror. The slide was illuminated via an upper folding mirror by a light box housing fluorescent tubes mounted behind a diffusing screen.

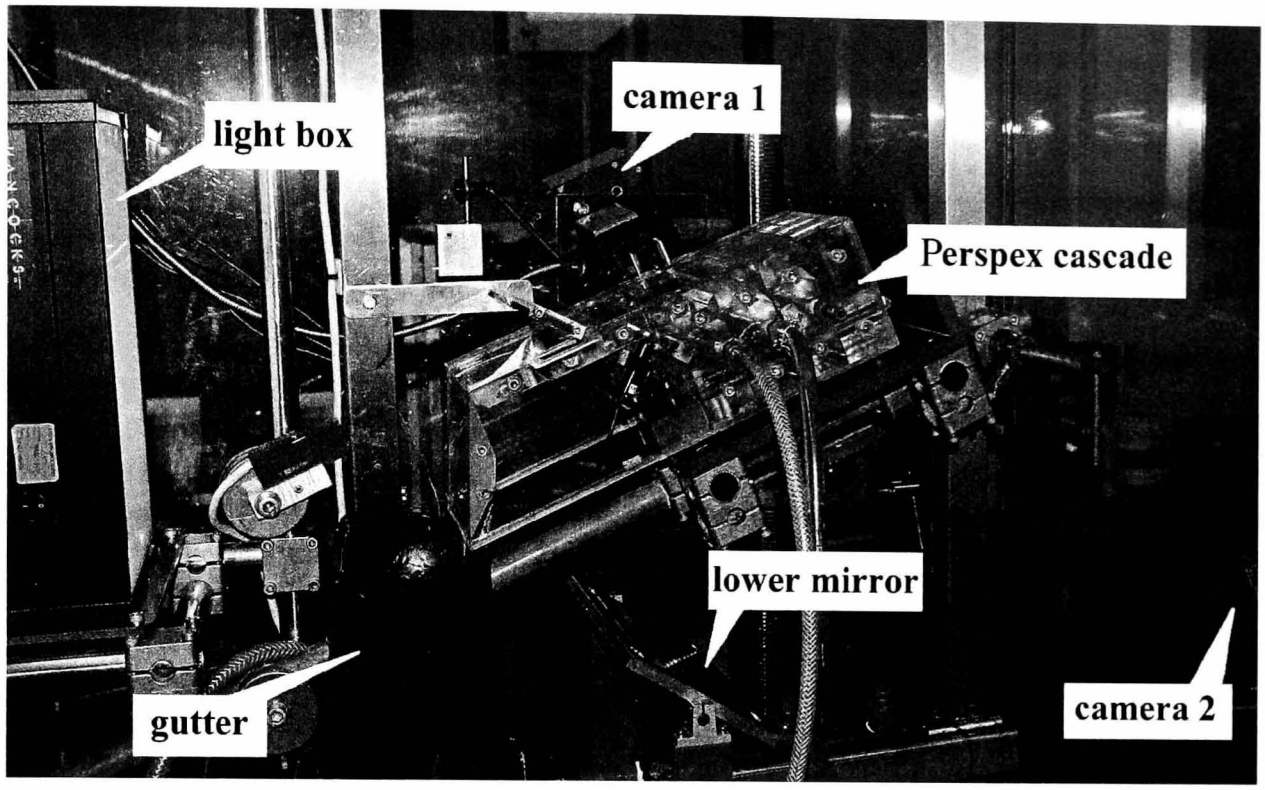

Figure 2.27: General view of equipment for studying slot exit flows

The outputs from the two cameras – Figure 2.27 - were recorded on a single video-tape using a Norbain Gem 2 Multiplexer and Panasonic NV-D48B video recorder. The system was pre-programmed to allow the images to be viewed simultaneously on a single monitor screen in quadrature format. The images of the profiles of the free surface and interface were digitised using the OPTIMAS image analysis software produced by Bioscan Incorporated to generate a table of coordinates. The individual points were then superimposed onto a drawing in AutoCAD LT after suitable allowance for scaling and a curve drawn using cubic spline interpolation built into the software. The images of the flow down the slide were analysed by taking a luminance profile of a single line scan and converting to optical density according to the expression:

$$D_i = \log\left[\frac{Ldry_i - L0}{Lcoat_i - L0}\right] \tag{2.42}$$

where Ldry and Lcoat are the luminances for the clean dry slide and for the flow respectively, L0 is the luminance at an area of a recorded image corresponding to where an opaque strip is laid down on the dry slide and i is the i^{th} element in an array

spanning the width of the slide image. By recording a sequence where the flow rate was stepped through four changes, it was then possible to relate mean density to flow rate down the slide. Solving the equations for fully established flow of two layers down an inclined plane – Appendix I – yields a value for thickness of the main layer downstream of the carrier layer slot, for each flow rate in turn – thus enabling optical density to be directly correlated with thickness.

2.8 Methods for Recording Instabilities of Two Layer Slide Flows

2.8.1 Principles of the Methods

This work addresses a clear need to establish a viable method for experimentally quantifying the interfacial instability mode for two layer flows on an inclined plane – Hens [1996]. Numerical models based on solving the Orr-Sommerfeld equation were initially limited by the assumptions that instabilities are characterised by long wavelengths – for example Kao [1965], Kao [1968], Akhtaruzzaman et al. [1978] and Wang et al. [1978]. These have been shown to be misleading – Kobayashi et al. [1986] and Kobayashi [1992]. Very little work has been done to experimentally validate these models. Kobayashi [1992] was able to distinguish between surface and interfacial waves by coating layers containing coloured dyes and taking thin cross-sections of the dried samples. Van Abbenyen et al. [1992] investigated the mechanism for some unexpected interfacial instability by profiling the velocity profiles down a long inclined glass plate using a Laser-Doppler apparatus.

The work exploited the unique properties of the laser triangulation technique – generally applied to profiling a diffuse solid surface. Limitations presented by liquid polymers as pointed out by Ikin [1995] and Schweizer [1997(1)] were addressed in the method. It was expedient to reveal the interface by adding a scattering agent to the fluid forming the upper layer while leaving the lower layer transparent – as for the study of flows at the slot exit. Viewing the flow from above and beneath the extended transparent slide provided with the Perspex cascade gives opportunity to monitor the displacement of the upper and lower boundaries of the upper layer at given points using the laser based triangulation devices shown in Figure 2.28.

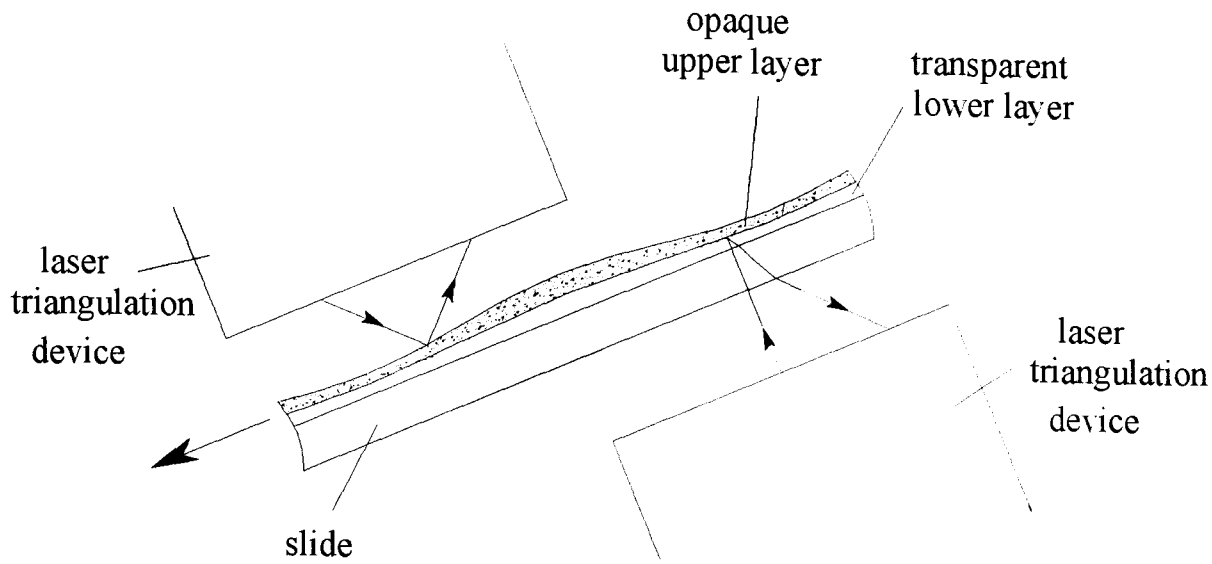

Figure 2.28: Principle used for measuring displacements due to slidewaves

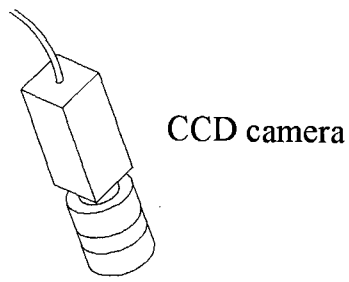

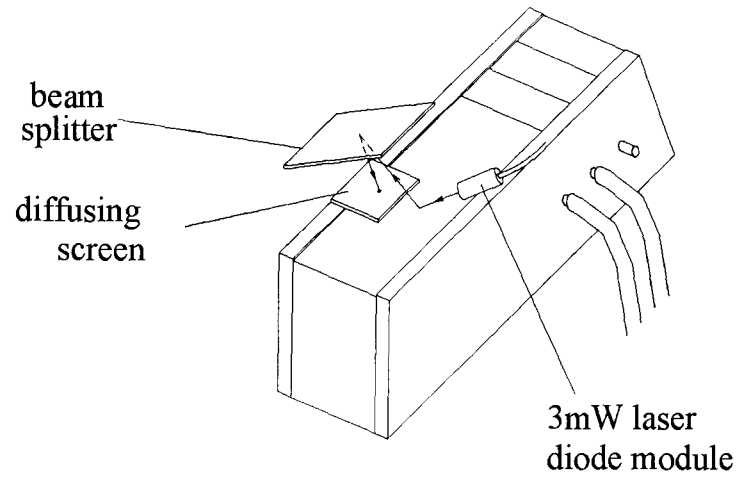

Figure 2.29: Method for monitoring slide-wave induced surface disturbances in 2-D

The instantaneous slope of the surface as affected by slide waves was tracked in two dimensions by directing a third laser beam at the slide by adapting a method reported elsewhere – Baumlin [1990]. The reflected beam was intercepted by a beam splitting plate to be again reflected to finally impinge on a white diffusing surface to generate

an intense spot of light. The movement of the light spot was monitored using a CCD camera as shown in Figure 2.29.

2.8.2 The Experimental System

The off-line Perspex cascade described in Section 2.6 was used for this work. The fluids studied were gelatin based and thus required to be maintained at about 40°C.

Special care was taken in setting up the solution supply to remove key sources of disturbance to save any ambiguities in determining inherent instabilities in the slide flow itself. The gear pumps were quickly abandoned in favour of a specially designed pressurised supply comprising three aluminium paint spray applicator cans purchased from Machine Mart and installed specifically for this work. The upper two layers were supplied from two 12.6 litre capacity vessels of type CPP12 and the carrier layer from a 2 litre capacity vessel type CPP2 – Figure 2.30.

Potential corrosion problems due to silver bearing gelatinous fluids coming into contact with the aluminium were overcome by installing stainless steel liners within the cans. The liners, being well polished, also provided surfaces that could be readily cleaned at the conclusion of each experimental trial. The intervening gaps were filled with water to effect thermal transfer for maintaining the solutions at the required temperature. Restrictors were inserted into each supply line of internal bore so designed to achieve the desired flow rates at flow meters F when the pressures P were adjusted by regulators R to be of the order of 0.7 bars. The three vessels were partly immersed in a water bath, the temperature of the bath being controlled to a value depending on the final application required. The three solutions were fed via narrow bore pipes passing through a water jacket controlled to the same temperature as the water bath.

Two laser triangulation devices were already available for use. A Keyence laser displacement meter model LC-2100 owned by ILFORD Imaging UK Limited was set up for monitoring interfacial waves. An Anritsu displacement meter fitted with a KL132A sensor head and owned by the School of Mechanical Engineering was

employed for the surface. The operational principles of these two devices are slightly different and will be now be described in more detail.

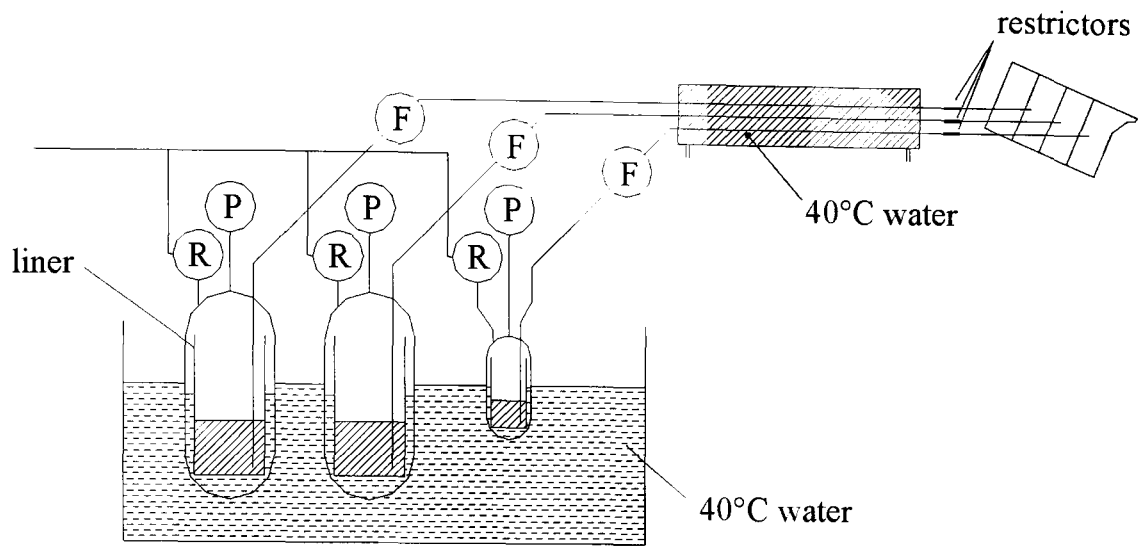

Figure 2.30: Solution supply system for studying slide-waves

2.8.2.1 Keyence Laser Displacement Meter

The Keyence LC-2220 head used in this system incorporates a 1.9mW laser diode emitting red light of 670nm wavelength and focused as a spot onto the target surface at point A – Figure 2.31. The unit depends on the surface or interface being measured scattering light back into the receiver aperture – hence the need for including scattering particles within the layer of interest. Part of the back-scatter centered about a line inclined to the surface at typically 45° enters a lens to be refocused to a point B on a CCD sensor array. Where the target moves in an upward direction, the incident spot $A^{/}$ then becomes imaged as $B^{/}$ on the sensor array. The internal digital circuitry is arranged to output a signal that represents the instantaneous displacement of the target surface and is designed to sample at a frequency of 40 kHz. The overall response extends to a frequency of 16 kHz and the device is capable of resolving displacement to 0.2 μm.

The liquid from which back-scatter is received must contain sufficient scattering agent per unit volume to enable the unit to function as required. A given particle

concentration generates a hemispherical source of back-scattered light – as shown in Figure 2.32. The finite limiting radius is indicative of the degree of uncertainty as to the true position of the interface at the point of measurement and is itself a function of the coefficient of absorption of the liquid for the wavelength of the laser. This presents potential error where the radius (or penetration depth) exceeds the thickness of the scattering layer.

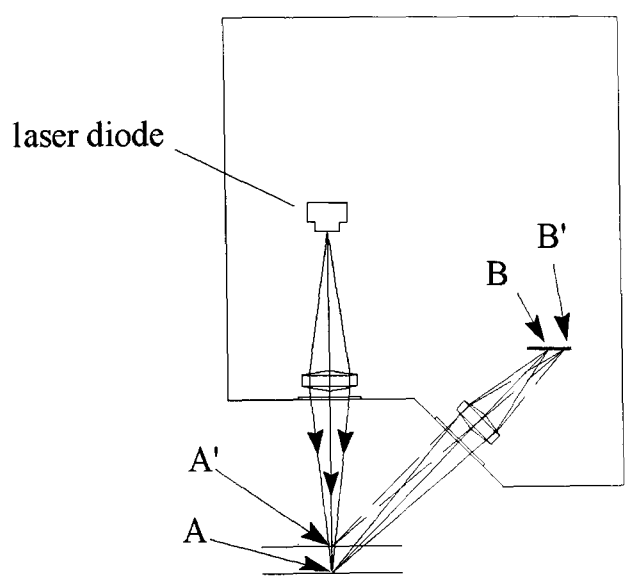

Figure 2.31: Operational principles of the Keyence laser displacement meter

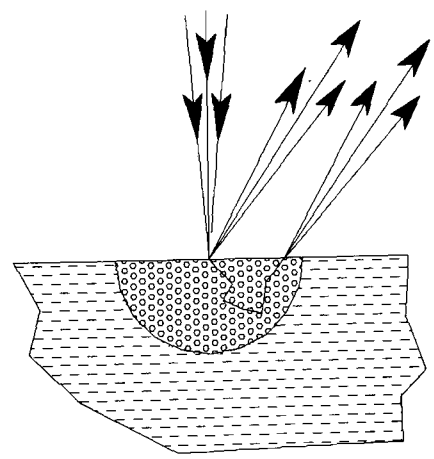

Figure 2.32: The effect of finite penetration depth of laser light

A simple test is to make use of the capability of the meter to display the intensity of the received beam and compare this with the intensity of back-scatter received from the surface of liquid contained in a beaker and hence presenting significantly higher

depth. A lower reading indicates that the layer depth is less than the penetration depth and hence the need to increase particle concentration.

In applying the device to monitor the interface from beneath, care has been taken to reduce the thickness of transparent solid material lying in the optical paths. This was achieved by machining an aperture in the Perspex slide to take a 1mm thick glass window – comprising a standard microscope slide. The recess was such as to ensure the top face of the window was coplanar with the slide. Adhesive was applied as edge sealant and smoothed flush to minimise any disturbance to the flow.

Allowance was made for refractive effects when interpreting a signal waveform. A ray path passing though the centre of the receiving lens will be deviated at the interface between the lower layer and glass window and again at the glass-air interface as shown in Figure 2.33.

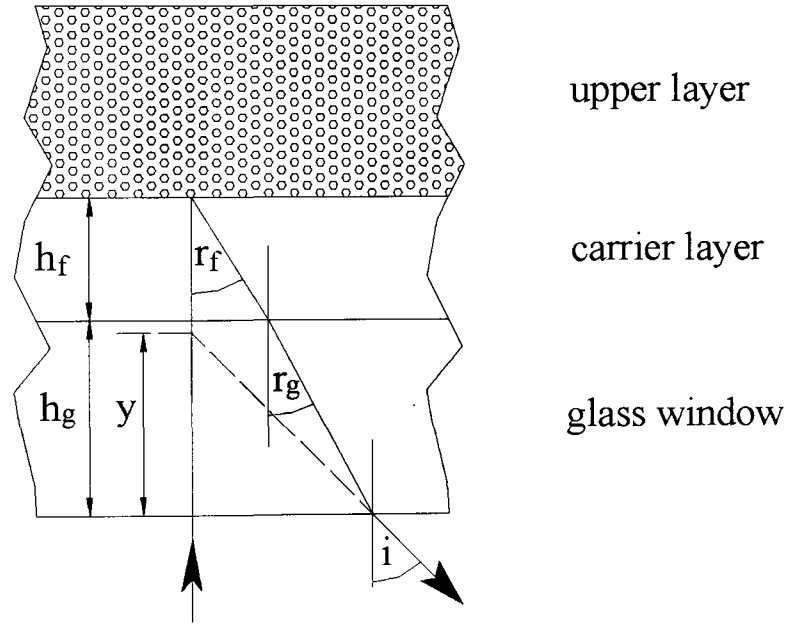

Figure 2.33: Ray path through centre of Keyence receiver lens

The apparent depth y of the lower layer looking from below is given by the expression:

$$y.\tan i = h_f.\tan r_f + h_g.\tan r_g \qquad (2.43)$$

where r_f and r_g are given from Snell's law by:

$$\sin r_f = (1/n_f).\sin i \qquad (2.44)$$

and

$$\sin r_g = (1/n_g).\sin i \tag{2.45}$$

n_f and n_g being the refractive indices for the bottom layer fluid and glass window respectively – measured at the laser emission wavelength.

For a small change in depth δh_f, the corresponding apparent depth of the lower layer (looking from below) is then given by:

$$(y + \delta y).\tan i = (h_f + \delta h_f).\tan r_f + h_g.\tan r_g \tag{2.46}$$

and from (2.43):

$$\delta h_f = \delta y.\ (\tan i)/\tan r_f) \tag{2.47}$$

2.8.2.2 Anritsu KL130 Laser Displacement Meter

The system incorporates a triangulation device which operates in a similar way excepting that the laser emits in the infra-red and the optics are designed to receive specular reflections instead of back-scattered light - Figure 2.34.

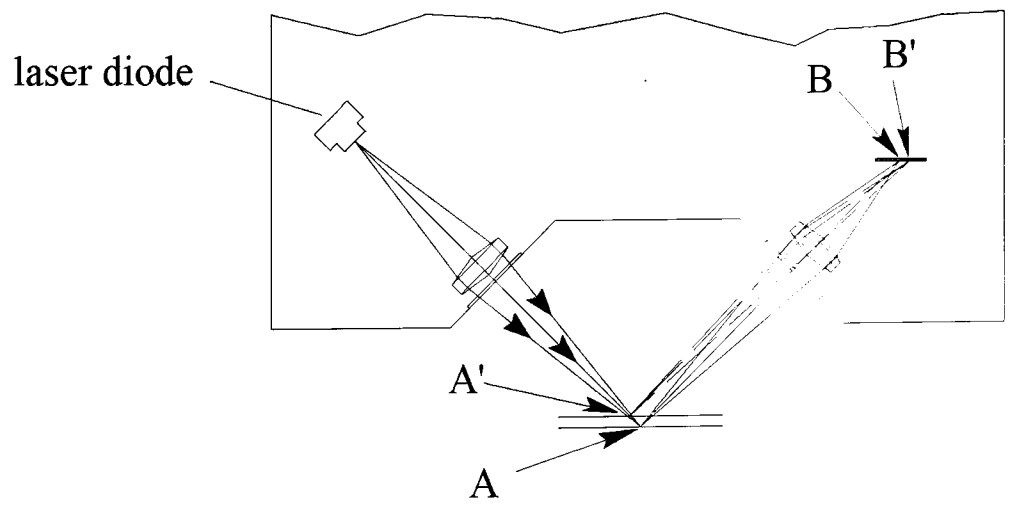

Figure 2.34: Operational principles of the Anritsu laser displacement meter

The system is intended for determining the displacement of well polished solid targets. The operating range is 1.6 mm and the frequency response bandwidth 4 kHz at –3dB.

It is thus well suited to the task of profiling surface waves in the slide flow and is not affected by issues concerning penetration depth as for the Keyence device.

The receiving lens aperture subtends a semi-cone angle of 8° at the inspection point and thus can only accommodate a finite range of slopes presented by the fluid surface - Figure 2.35. This clearly places an upper limit on detectable wave amplitude for a given wavelength. The equipment is nevertheless suitable for the requirements of this work.

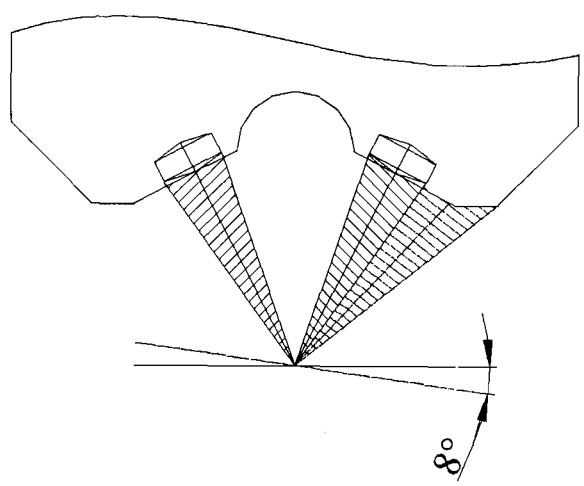

Anritsu displacement meter using KL132 sensor head

Showing how the maximum tilt angle when measurung displacement of a mirror-like surface is ±8°

Figure 2.35: Showing cone angle subtended at Anritsu receiver lens

Special attention was given to ensure safe working while operating the three lasers. Safety goggles were superfluous owing to there being at least two wavelengths emitted. The problem was resolved by mounting a safety guard pivoted about an axis near the cascade back-block. The guard was arranged to engage a safety interlock - wired in such a way that the lasers could only be energised with the safety guard lowered. The guard was so designed that under no circumstance could hazardous laser radiation enter the eyes of the operator or any other person in the vicinity – while allowing good access to the slot exits and slide when in the raised position – Figure 2.36.

The analog signals derived from the two triangulation devices were monitored and stored using a two channel Thurlby DSA524 digital storage adaptor coupled to an oscilloscope for display purposes.

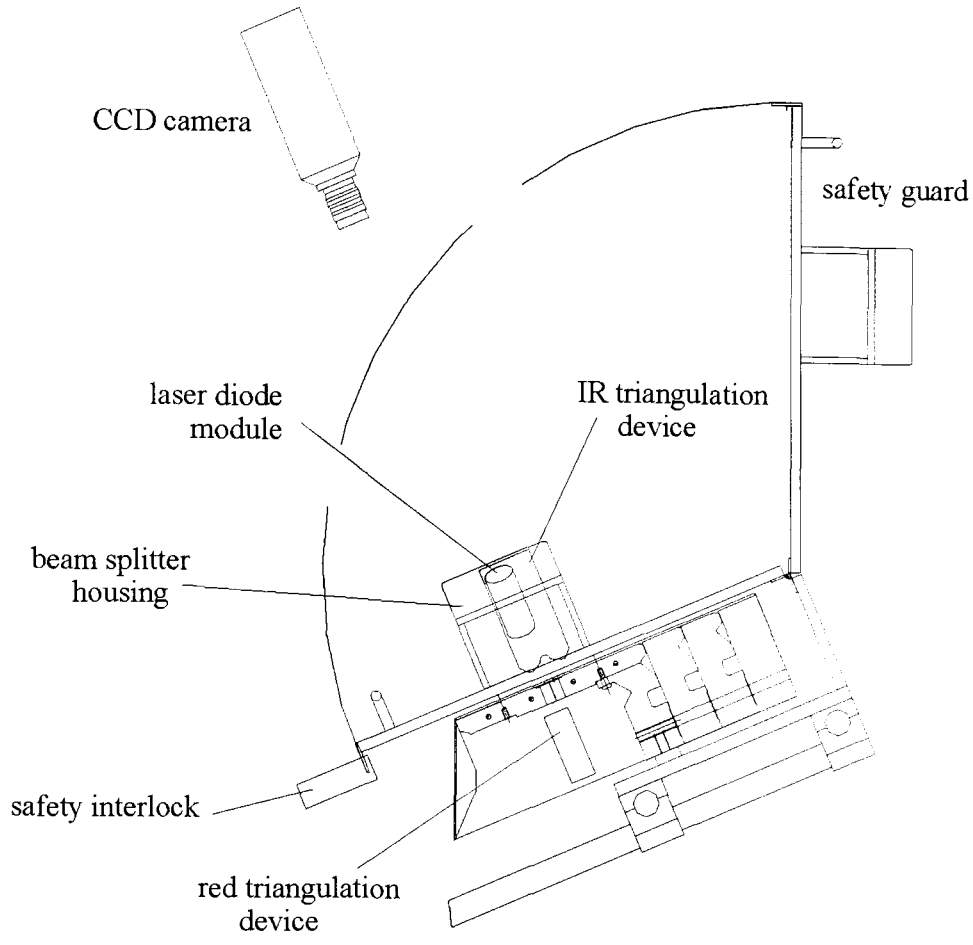

Figure 2.36: Assembly of optics for studying slide-waves

Each channel is capable of storing 4096 8-bit words per channel at sampling rates that can be varied as required. On triggering the device, data were saved to memory and analysed using Mathcad to present waveforms corresponding to the surface and interface. Due allowance was made for correcting phase-shift by calculating the time δt taken for point A_i to arrive at sensor S_2 at distance x from sensor S_1 – δt being given by:

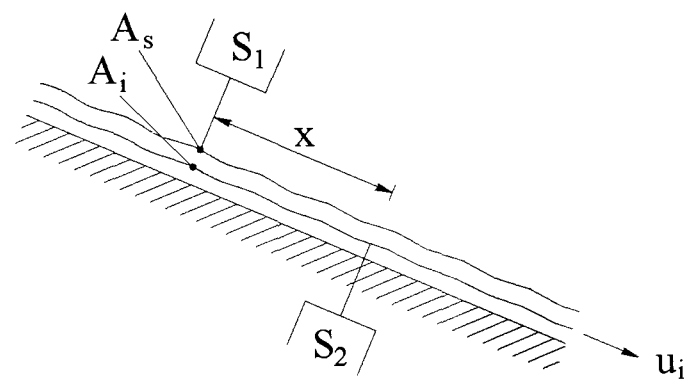

Figure 2.37: Allowance for phase shift due to displacement of two sensors

$$\delta t = \frac{x}{u_i} \tag{2.48}$$

where u_i is the velocity of the interface – Figure 2.37.

Here u_i is calculated by solving the equations for the fully established two layer flow for the given set of conditions studied – see Appendix I.

2.9 On-Line Measurement of Surface Charge Distribution

Electrostatic charge on the surface of a web is conventionally measured using a non-contacting electrostatic voltmeter – for example Hartman [1989]. A high speed Trek model 366 system was specially set up for carrying out experiments for studying the dynamic response of the coating bead to varying charge. The probe incorporates two vibrating reeds energised by an electro-mechanical modulator supplied by an oscillator – Figure 2.38.

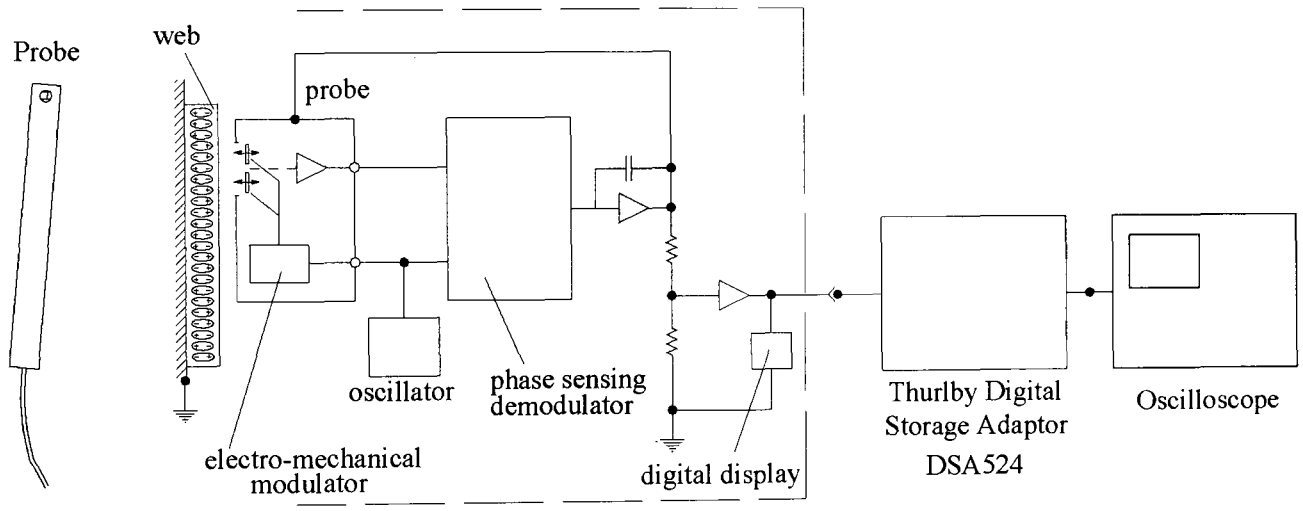

Figure 2.38: TREK Model 366 non-contacting Electrostatic Voltmeter

The reeds generate a signal that is responsive to the electrostatic field between the measured surface and the probe. Feedback is used to drive the electrostatic field to zero by changing the potential of the probe body to match the level on the part of the web surface in the vicinity of the sensor window. The system is capable of responding to potentials over the range ± 2kV with an accuracy of ± 0.05% full scale over a bandwidth of 15 kHz at the –3dB level. The output is an analog signal controlled to

1% of the web potential. A Thurlby DSA524 digital storage adaptor and accompanying oscilloscope as described in Section 2.8.2 were set up for the purpose of the work for displaying and recording charge waveforms.

In order to accurately determine the charge at the coating bead itself, it was deemed important to site the sensor as close to the coating head as possible by mounting the probe immediately underneath the coating roller as shown in Figure 2.39. Although the unit is designed to cope with humid conditions, special care was taken throughout the experiments to avoid undue splashing of the sensor to reduce risk of failure.

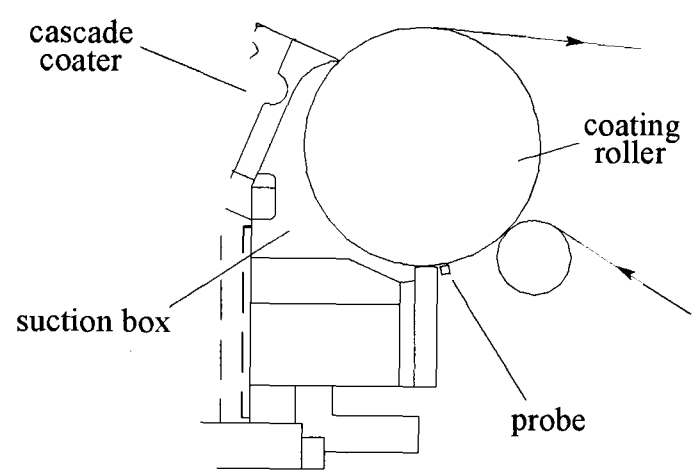

Figure 2.39: Mounting of the TREK probe at the coating head

2.10 On-Line Measurement of Dynamic Contact Angle

A needle coater developed by the author prior to the commencement of this project has been found useful for determining dynamic contact angle for key solutions when studying differences in a variety of web surfaces. The method is based on that of Zvan et al. [1992] and has been recently exploited by Bower et al. [2001] who found that with low polarity liquids, the DCA (dynamic contact angle) was a weak function of the substrate speed whereas for high polarity liquids, it was a strong function of substrate speed. The technique involves coating the substrate of interest with a micro-bead supplied via a syringe needle. Figure 2.40 shows the construction of a needle-coater originally built for mounting on the M22 ILFORD pilot coating machine described in Section 2.5.1 and shown in Figure 2.9.

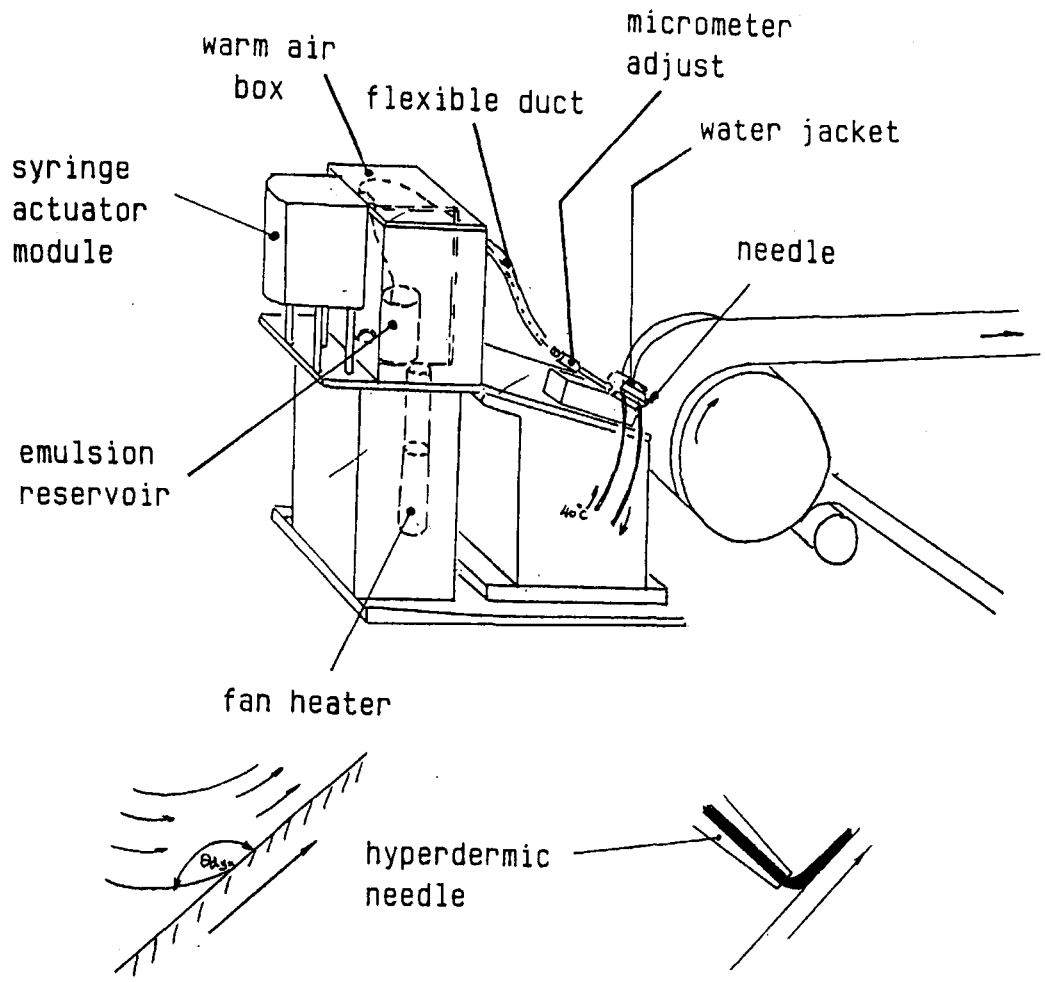

Figure 2.40: Needle coater used for measuring dynamic contact angle

Here the cascade has been replaced with an assembly comprising a needle mounted within a water jacket operating at 40°C. The jacket was affixed to a translation table to enable adjustment of coating gap. The solution supply system comprised a syringe actuator module housed within an enclosure supplied with air controlled at typically 40°C. The feed consisted of flexible PVC micro-tubing surrounded by a second water jacket again controlled at typically 40°C.

The needle tip was illuminated with light from either of two miniature tungsten filament lamps as shown in Figure 2.41. Lamp A was used for visual inspection while aligning the needle and establishing the coating bead during the forward stroke of the syringe pump. Lamp B was used for generating a sharp black silhouette image of the micro-bead. The Bausch and Lomb Monozoom optics coupled to a Cohu model 6712 CCD camera as described in Section 2.7.2 was used for recording the image - the line of view being arranged to receive specular reflections by mounting a small folding mirror as shown.

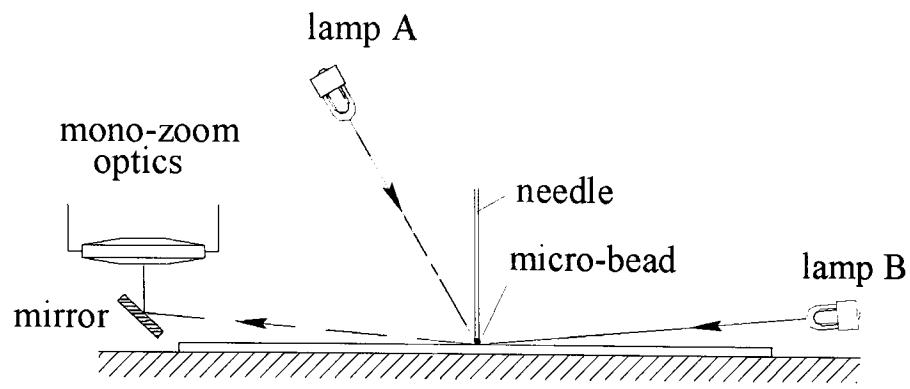

Figure 2.41: Method of illuminating the microbead

The silhouette image includes the reflection of the micro-bead in the surface of the web due to the extreme angle of grazing incidence – irrespective of surface roughness. The dynamic contact angle is determined to a precision of ± 3° by taking the coordinates of one set of three closely spaced points near to the dynamic wetting line and lying on the curve corresponding to the lower meniscus and a second set on its reflection in the web surface – see Figure 2.42.

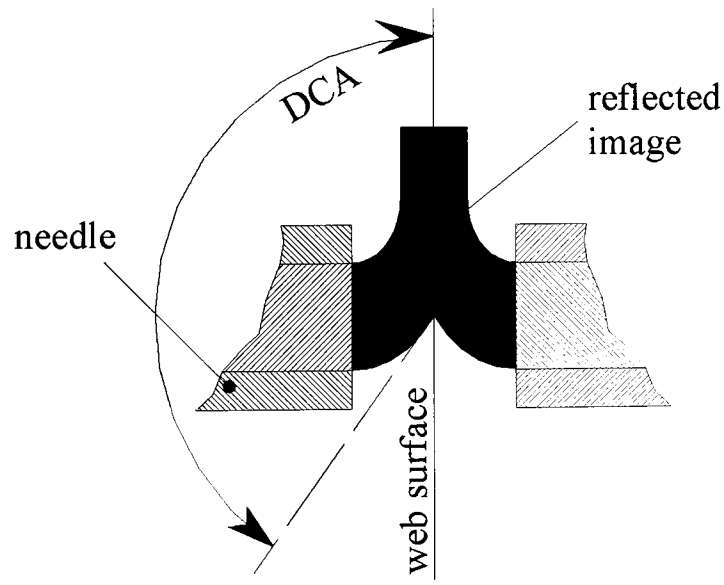

Figure 2.42: Method for extracting the dynamic contact angle from the image

Some care is needed when citing results due to the errors associated with the cylindrical geometry of the liquid emerging from the needle. The method also suffers from vulnerability to the presence of static, especially when studying the wetting properties of plastic triacetate webs used for the manufacture of photographic film.

The technique is nevertheless useful when making comparison between the surfaces of various pre-coated paper webs.

2.11 Determining the Coating Window

The concept of a coating window is well established as a means of defining limits, within which it would be expected to achieve a coating governed by a given set of criteria. Chen and Scriven [1992] defined three nested coating windows, the inner one being a 'quality window' describing limits, within which the uniformity of the coating is considered adequate for end-use of a given industrial product. This quality window lies within a 'stability window' or 'operability window', which in turn lies within a 'feasibility window'. These subtle differences in definition are unfortunately often ignored in the literature.

This study was run in collaboration with coating technologists specialising in optimising the quality of photographic and ink-jet media. It therefore made sense to take the quality window as being most relevant in this case. Various methods of depicting coating windows for the slide bead process have been proposed – including generalisations in terms of dimensionless numbers – Schweizer [1988]. This approach, however, presents difficulties to industrialists unfamiliar with fluid dynamics. As pointed out by Hens and Van Abbenyen [1997], a more popular and practical method is to plot the window in space defined by pressure difference across the bead as ordinate and web speed as absissca. Limits of maximum and minimum allowable suction pressure indicate the onset of undesirable departures from uniform coating due to various causes - typically but not exclusively air-entrainment, ribbing, rivulets and edge break - Hens and Van Abbenyen [1997].

This latter method was selected for this work but extended to cover two distinct modes of operating the coating process. In the first, the more general case of defining the coating gap for optimum coating quality was taken. In the second, the effect of opening the gap to a value sufficient to allow through an inter-roll splice was studied. Combining the two 'windows' yields a 'process operability window' applicable to the continuous coating of several rolls without incurring the risk of bead-break at a splice

and consequential fouling of face-on rollers located after the dryer (Katagiri et al. [2003] - see also Section 3.2.1).

Three methods were available to define suction pressure at the onset of unwanted effects – a) visual inspection of the coating as it left the coating head b) inspection using a laser scanner and c) sampling. These techniques will now be described in more detail.

2.11.1 Visual Inspection of the Moving Coating

It was found possible to assess the onset of air entrainment or ribbing by observing the near grazing reflection of a white light filament lamp in the wet surface – Figure 2.43. Ribbing can be readily seen by distortions in the image of the lamp. Air entrainment can be discerned from small flecks of light apparently sourced near the surface indicative of the presence of minute air bubbles in the coating. The determination of suction thresholds to an adequate degree of precision required practice and frequent cross-checking against observations from sampling. Once confidence was gained, however, it was then possible to generate sufficient coating window data while continually pumping solution over the head for a run lasting only a few minutes – an important consideration in terms of reducing costs to a reasonable level.

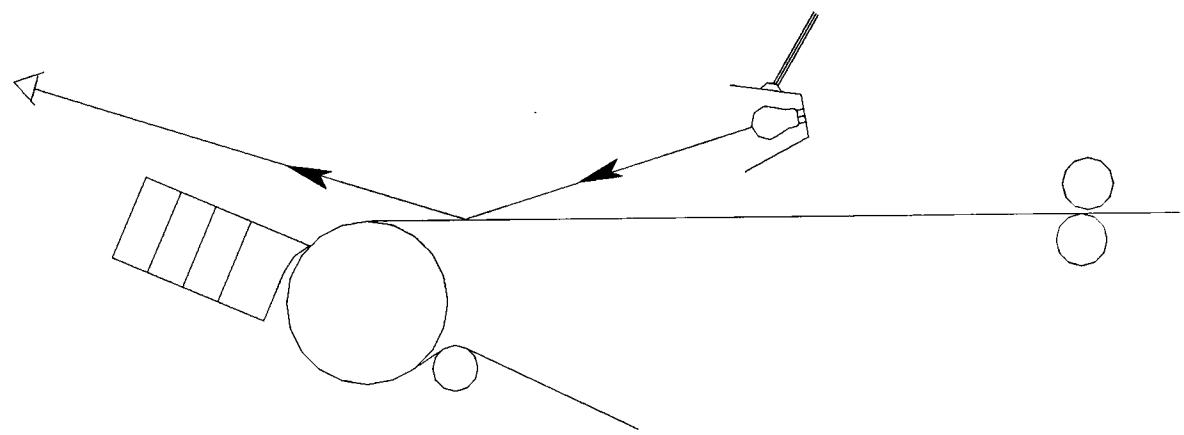

Figure 2.43: Illumination for visual inspection of a moving coating

2.11.2 On-Line Inspection using a Laser Scanner

A laser scanner originally developed by the author prior to the commencement of this work has been found useful as a means of displaying the onset of ribbing and air entrainment. The layout of the scanner and receiving optics is shown in Figure 2.44. A beam of light of wavelength 633nm emitted by a 2 mW helium neon laser is

directed by plane mirrors and expanded and refocused by a series of precision lenses to form a light spot at the surface of the wet coating. The spot is scanned across the wet coating at the top dead centre of the coating roller by means of an aluminised polygonal spinner – with instantaneous fly-back. In the absence of any disturbance to the coating, the light is reflected by two plane mirrors and directed through a cylindrical lens to be reflected by a curved mirror formed by bending a sheet of aluminised pre-stressed glass. The cylindrical lens and curved mirror are so arranged that the undisturbed reflected scan reconverges to a point at the centre of the photocathode of a photomultiplier tube. The diameter of the photocathode is 100 mm and therefore capable of receiving light either side of the central point. As a disturbance in the wet coating arrives at the inspection point, the laser beam becomes deflected or scattered away from its normal path as it is scanned over the defect.

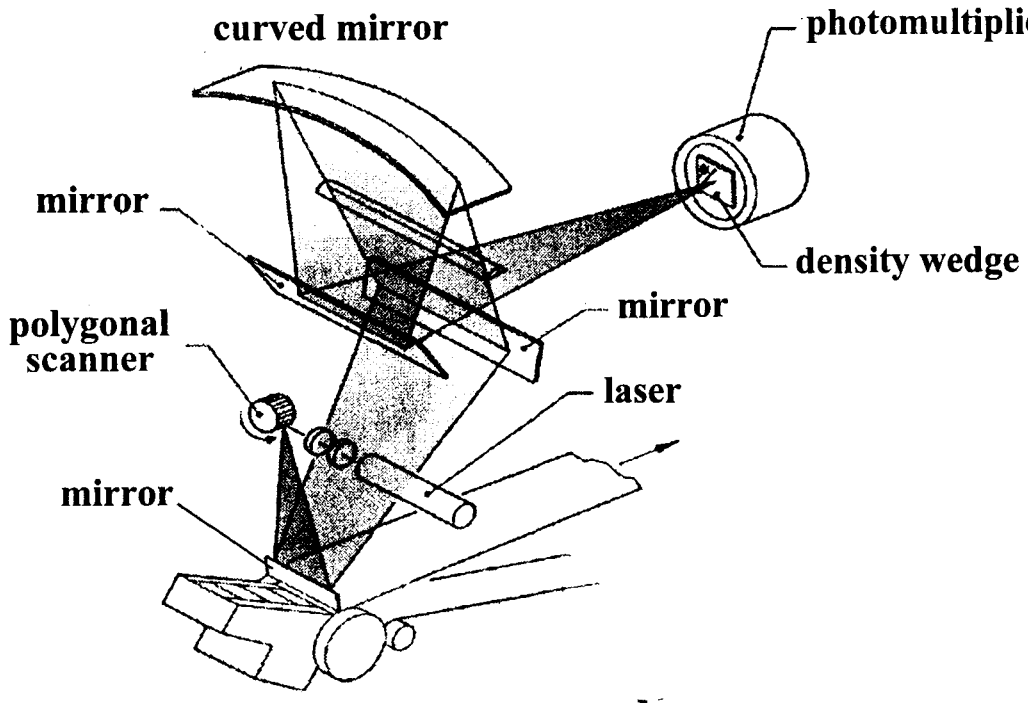

Figure 2.44: Laser scanner used for displaying ribbing and air entrainment

Subtle streaks and ribbing result in local changes to the gradient of the surface measured in the cross-width direction. Taking the case of ribbing in a single layer coating as represented by a sinusoidal change in wet thickness h(x) in the cross-width direction represented by:

$$h(x) = h_0 + \delta h.\sin\left[\frac{2\pi x}{\lambda}\right] \qquad (2.49)$$

where h_0 is the mean wet thickness, x is the distance cross-width from the datum edge and λ is the wavelength, it can be seen – Figure 2.45 – that the beam is deflected away from its normal path through an angle $2\alpha(x)$, where $\alpha(x)$ is given to the first order of approximation by $\tan\alpha(x)$ in the expression:

$$\tan\alpha(x) = \frac{dh}{dx} = \left[\frac{2\pi\delta h}{\lambda}\right].\cos\left[\frac{2\pi x}{\lambda}\right] \qquad (2.50)$$

The optics is such that the laser beam at this instant impinges on the photocathode at a point displaced by distance s(x) given to the first order of approximation by:

$$s(x) = - C.\tan\alpha(x) \qquad (2.51)$$

where C is a constant. Sensitivity to displacement away from the central point is effected by mounting a linear density wedge in front of and close to the photocathode – Figures 2.44 and 2.45.

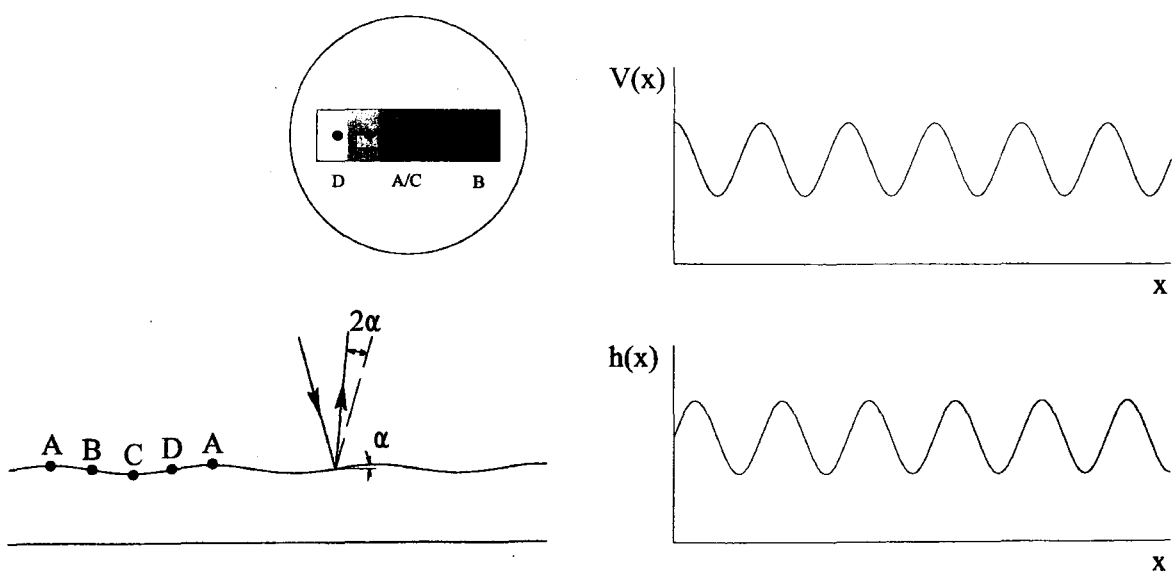

Figure 2.45: Showing how ribbing is displayed by the laser scanner

The optical density D(s) is thus given by:

$$D(s) = D_0 + B.s \qquad (2.52)$$

where D_0 and B are constants. The intensity I(x) of the beam finally incident on the photo-cathode is thus given by:

$$\log\left[\frac{I(x)}{I_0}\right] = D(s) \qquad (2.53)$$

and from (2.50),(2.51) and (2.52):

$$\log[I(x)] = \log(I_0) + D0 - \left[\frac{2\pi BC\delta h}{\lambda}\right].\cos\left[\frac{2\pi x}{\lambda}\right] \qquad (2.54)$$

By feeding the photomultiplier output signal to an inverting logarithmic amplifier circuit, the final output V(x) is then proportional to -log[I(x)] - and from (2.54), therefore replicates the ribbing waveform at the inspection plane after allowing for a 90° phase shift as shown in Figure 2.45. The Thurlby DSA524 digital storage adaptor and accompanying oscilloscope as described in Section 2.8.2 were used for displaying and recording the final waveform V(x).

The scanner based inspection system is also highly sensitive to sporadic outbreaks of air entrainment. An entrained air bubble scatters the laser beam as it scans across the defect resulting in loss of light finally reaching the photocathode. Figure 2.46 shows two waveforms corresponding to defect free coating and to the onset of air entrainment.

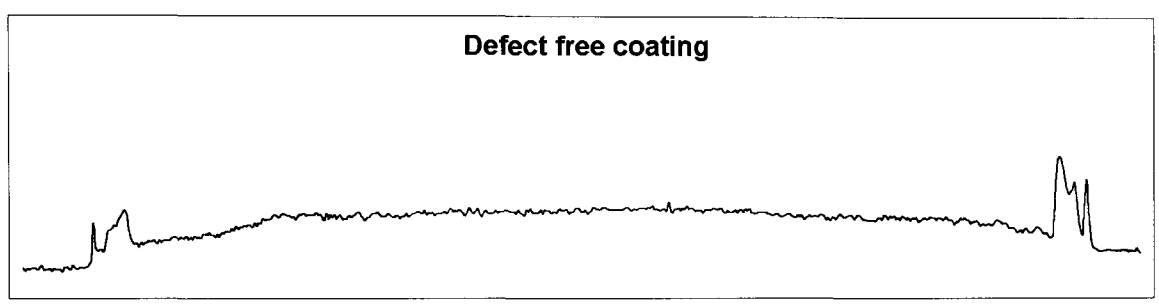

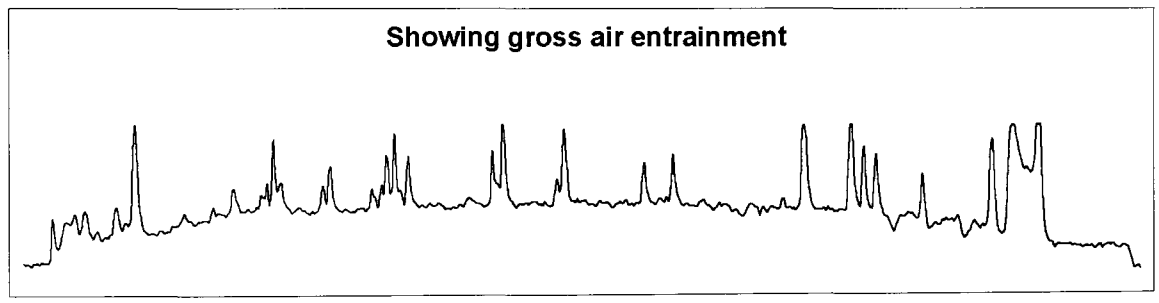

Figure 2.46: Typical laser scanner waveforms

2.11.3 Sampling

The methods described in 2.11.1 and 2.11.2 were satisfactory once air entrainment or ribbing had become fairly well established. Once having approximately determined a suction limit by these two methods, it was often proved necessary to check the actual onset of either air entrainment or ribbing by taking samples. It is only by close inspection that it can be confidently stated that the coating quality is generally adequate and free of subtle ribbing lines or sporadic outbreaks of very small bubbles

sometimes associated with the onset of air entrainment – as discussed in Section 1.3. The method was simple, although time consuming, and consisted of initiating a computer controlled sequence by which the first scrape-off roller was lifted to allow through a 1 metre length of coating without disturbance. The sample was firstly brought to rest over the chill bed and chilled by raising the bed to make contact with the back of the web. The sample was then transported to the air impingement dryer and dried using a profile simulating that considered optimum for the product or case study and as described in Section 2.5.1.7. The material was finally removed for inspection after transporting the sample to a point near the end of the machine. Inspection was best afforded by viewing under a 60 W bulb using both diffuse illumination and glancing reflection angles – using a magnifying lens if necessary. Further testing was required where surface quality was highly critical. Mottle on photo-paper coatings, for example, was assessed by carrying out the coating in 'safe-light' conditions to avoid pre-exposure by actinic light and exposing and processing the samples using standard procedures laid down by the company. Minute blow-holes or other defects on the surface of inkjet media attributable to excess drying were best revealed by subjecting the samples to a variety of printing tests considered optimum for the particular defect.

2.12 Method for Profiling the Lower Free Surface at the Bead Forming Zone

The development of a method to address a vitally important need to profile the lower meniscus when coating an opaque web as typically used in the photographic and paper coating industries formed a key part of this project. Techniques for visualising coating flows using transparent fluids such as glycerine or gelatin are well established where confined to the use of a scraped coating roller – Schweizer [1988] and Chen [1992]. These techniques, however, are not applicable to the opaque fluids often found within coating industry. Methods have accordingly been developed to study the performance of the bead when attempting to explain the cause of poor coating quality when manufacturing specific products. Ikin [1997(1)] set up a method for profiling the lower meniscus when coating a transparent web with such fluids by installing a hollow Perspex coating roller and viewing and recording backscatter from a laser light knife

through the roller wall (see Section 3.2.2 and Figure 3.8). Valentini et al. [1991] used a stationary glass skid to stabilise the web at the coating point and viewed and recorded the bead profile in a similar way. These methods fail to replicate what happens when attempting to coat a rough or textured paper substrate near to the limit of air entrainment. The techniques are moreover unsuitable for studying the effects of polar charge on a substrate that has been precoated with an opaque resin as the web must then be supported by an earthed metal roller at the coating point in order to ensure the dipoles are correctly orientated in the vicinity of the bead – Kisler et al. [1984].

2.12.1 Principles of the Visualisation Method

The method used is to illuminate the meniscus with a sharply focused light knife. This time, the beam is aimed through the gap between the cascade lip and web in a direction within the plane of the lip face. The beam axis is inclined at an angle of 45° as shown in Figure 2.47.

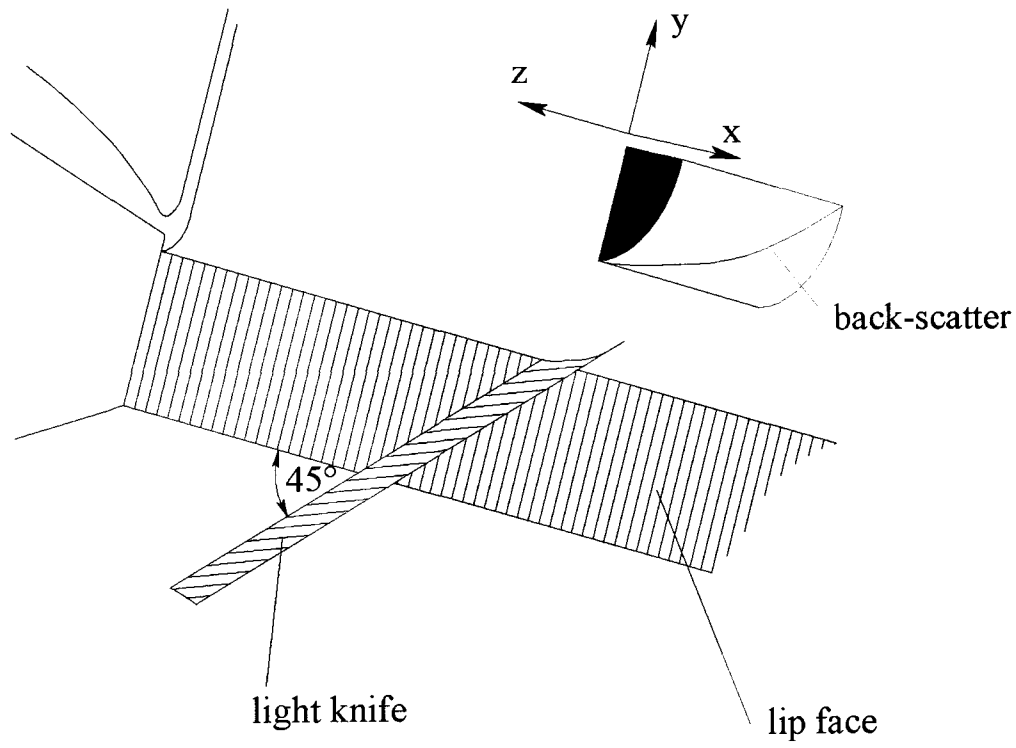

Figure 2.47: Principle of Visualisation Method used for the Lower Meniscus Monitor

A bead can be considered such that its profile measured in the xy plane as defined in Figure 2.47 is given by:

$$y = f(x) \qquad \text{– for all values of } z \tag{2.55}$$

The direction of the laser beam and hence the cross-section illuminated by the beam is given by:

$$y = -z \qquad \text{– for all values of } x \tag{2.56}$$

and substituting for y from (2.56) in (2.55):

$$z = -f(x) \qquad \text{– for all values of } x \tag{2.57}$$

Hence, the view of the back-scatter from the opaque fluid illuminated by the light knife as seen in the y direction is a replica of the profile if it were possible to view it along the z direction.

There is therefore scope for introducing the illumination from the side of the suction box and through the gap well away from the edge of the bead itself. This is important owing to the tendency for the bead to be ill defined at the extreme edges resulting in the suction plate becoming opaque with liquid residue in this region.

Developing a method for viewing along direction y presented two major challenges. Firstly, some way had to be found to mount suitable beam diverting optics within the very confined space between the moving web and the front face of the cascade. Secondly, the housing and method of use needed to be such as to minimise the risk of the optics becoming fouled – especially when starting up the coating process and also when finally washing up the coating head.

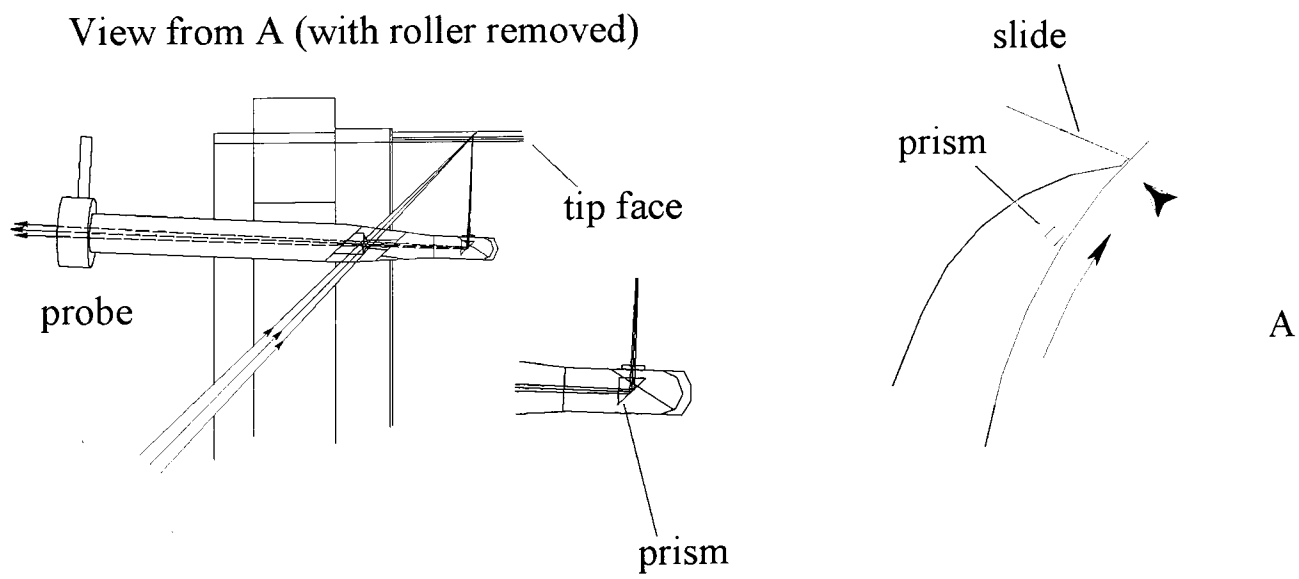

Figure 2.48: Method of mounting viewing prism beneath coater lip

The solution eventually adopted was to mount a right-angle prism (Melles Griot Product Number 01 PRS 407) of dimensions 2mm x 2mm at the receiving and transmitting faces within a specially designed miniature probe – Figure 2.48.

The manufacture as well as the design of the prism housing and associated probe posed yet a further challenge. Design work was undertaken using AutoCAD LT. A search was made for suitable resource to make the probe after making initial enquiries at Leeds University and within the Engineering Department at ILFORD Imaging UK Limited. The problem was eventually resolved by resorting to the specialist machining skills of Rayner [2001] - a model maker, who used high quality turning and milling equipment available within the Finishing Department within ILFORD Imaging UK Limited with the company's permission.

The development of a method for fixing the probe accurately in position after having established coating - and removing it before withdrawing the coating head - was also an important issue. The problem was resolved by designing a brass block incorporating a precision machined sleeve, enabling the probe to be rapidly inserted into the void within the suction box – Figure 2.49.

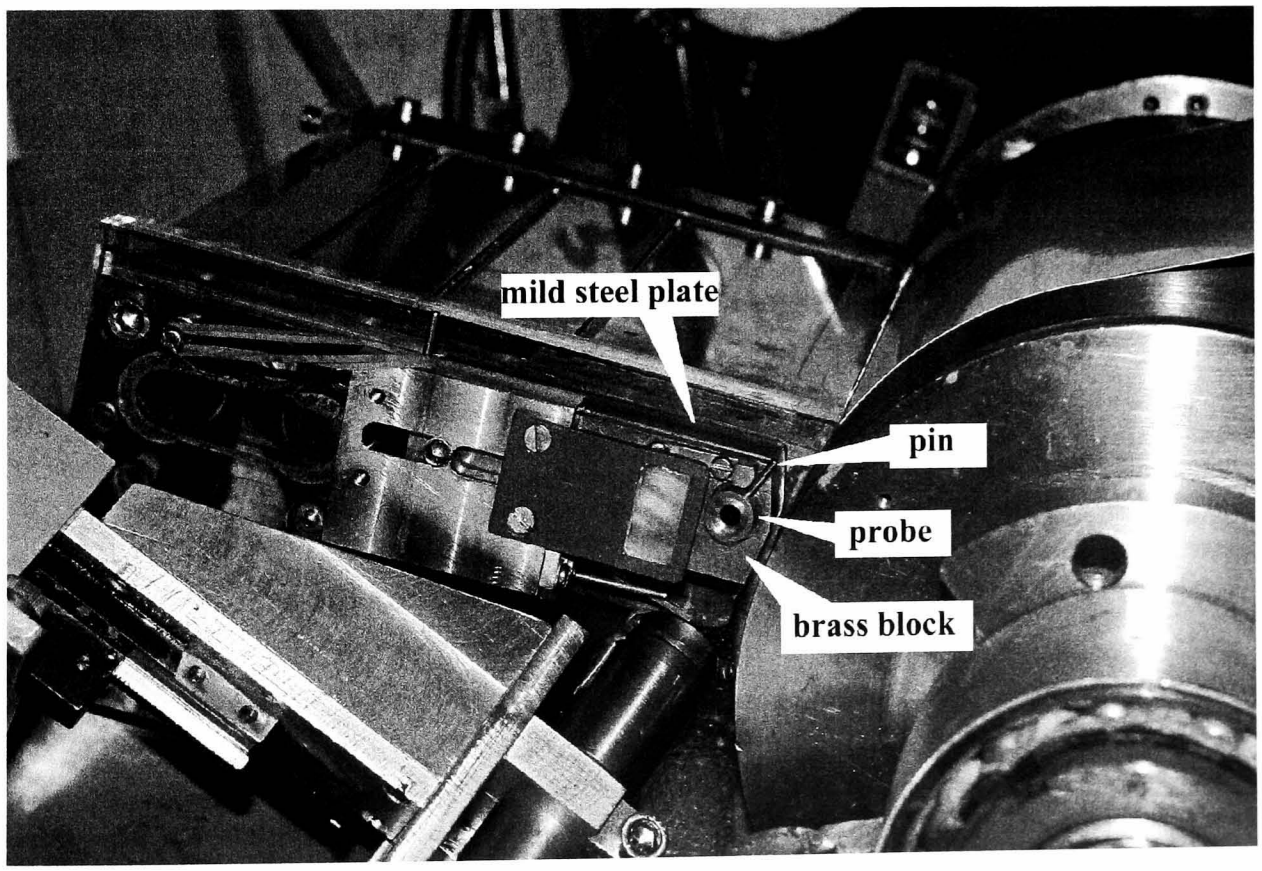

Figure 2.49: Method of mounting probe in cascade suction box

The brass block incorporated two pot magnets and three rounded location pins and was designed to interface magnetically with a nickel plated steel guide-plate fixed to the side of the cascade. The probe carried a pin enabling the prism to be correctly orientated for viewing the meniscus by locating against an adjustable stop mounted on the brass block.

2.12.2 The Initial Validation of the Method

Having established the feasibility of viewing the meniscus from beneath, the next step was to validate the basic method before embarking on the design of the mechanics for mounting the illumination source and receiving optics. This was carried out off-line using a specially designed jig - Figure 2.50 - in order to save costly abortive trials on the pilot coating machine.

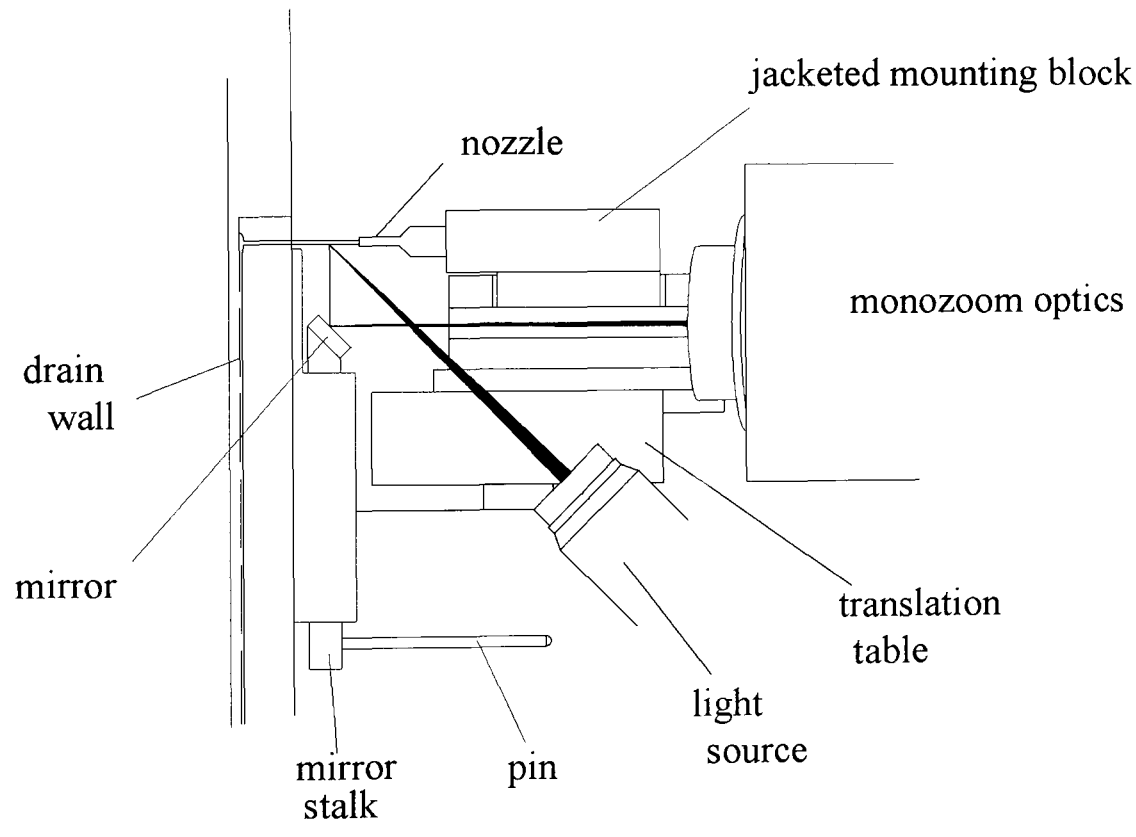

Figure 2.50: Jet apparatus for validating method for profiling the lower meniscus

The apparatus incorporated a nozzle supplied from a pressurised paint spray can pre-loaded with gelatin and photographic emulsion acting as a scattering agent. The nozzle was mounted within a block fitted with a water jacket maintained at 40°C and fixed to the moving surface of a translation table. The table was arranged to enable the jet orifice to be inserted into a hole in a vertical drainage channel prior to applying

pressure to the fluid and withdrawn once the jet was established. The diameter of the fluid jet was such as to mimic the lower meniscus within the bead forming zone at the cascade as viewed through the gap – Figure 2.51. Two adjustable blades were set beneath the trajectory of the liquid jet and served to represent the optical boundaries presented by the tip face and moving web – Figure 2.52.

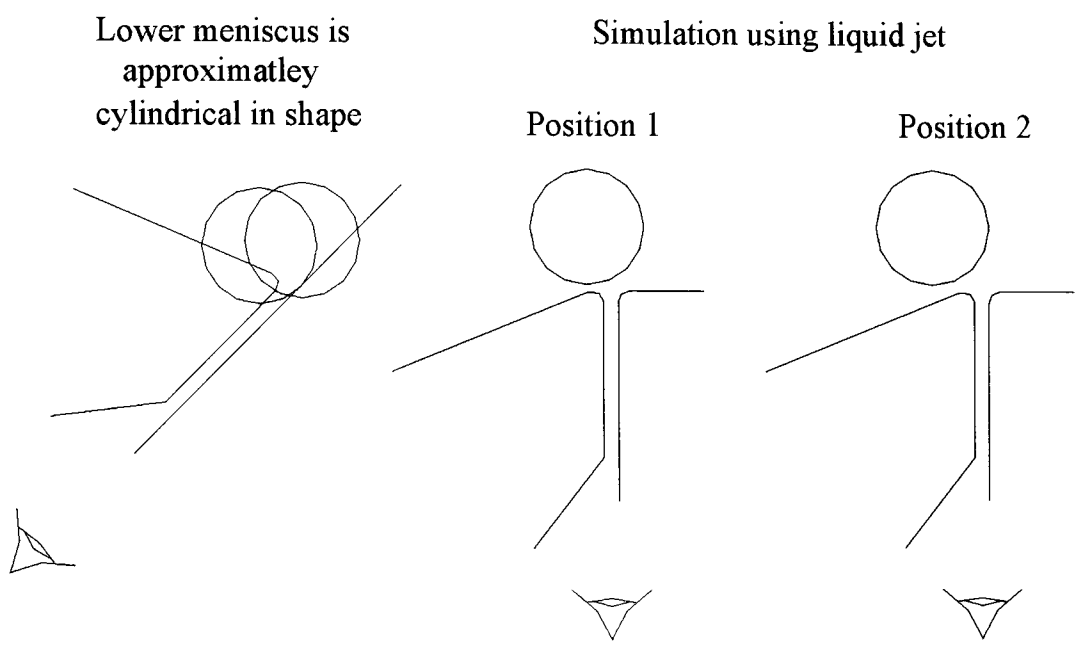

Figure 2.51: Showing how a fluid jet can mimic the lower meniscus in the bead forming zone

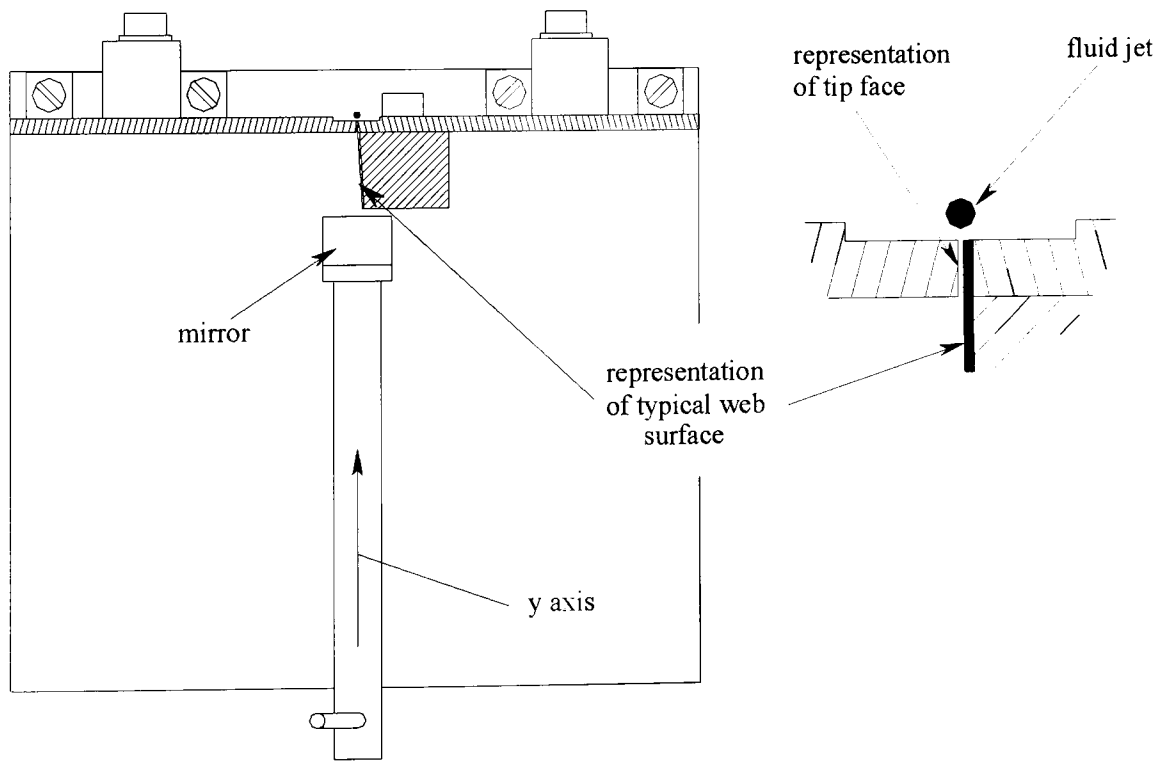

Figure 2.52: Layout of blades for representing the coating gap

Initial experiments were carried out using a white light source comprising a 25μm air slit imaged onto the liquid jet using a microscope objective of focal length 44 mm. The slit was illuminated by a 160W Truflector tungsten filament lamp with integral ellipsoidal back-reflecting mirror via a fibre-optic bundle of diameter 4.5 mm – as shown in Figure 2.53. The Bausch and Lomb Mono-zoom-7E optics and associated Cohu model 6712 CCD camera – as described in Section 2.7.2 – were set up for viewing and recording the image of the back-scatter from the liquid jet – as shown in Figure 2.50.

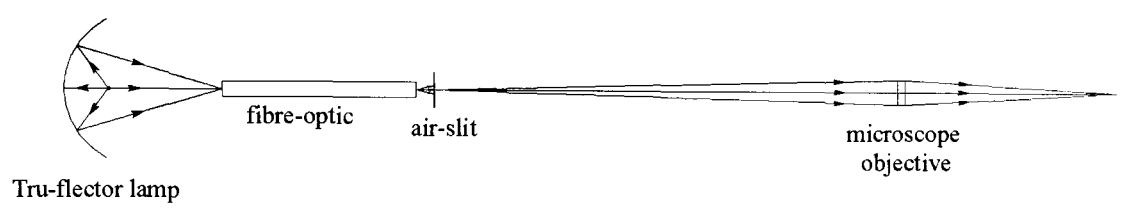

Figure 2.53: White light source initially used for lower meniscus monitor

It quickly became obvious that ensuring accurate alignment with the gap walls is highly critical – as can be readily appreciated from Figure 2.54. A check was made to ensure there was no detrimental consequences of rotating the mirror - representing the prism - about the y axis in order to increase clearance between the probe and coating roller. The image at the camera plane was seen to be free of any distortion other than undergoing a tolerable identical rotation about the camera axis.

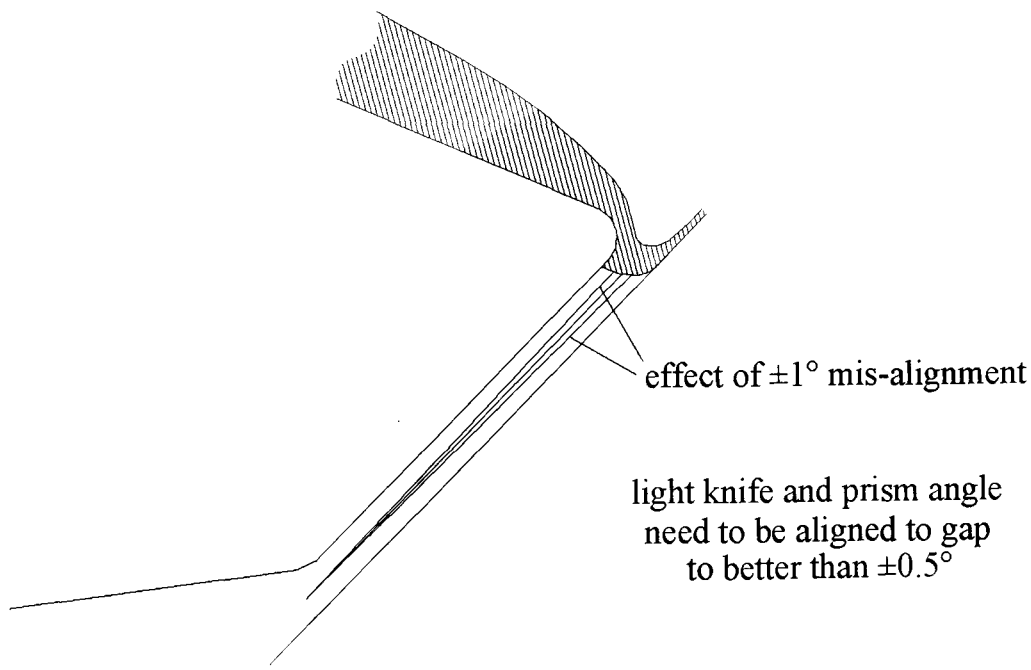

Figure 2.54: Effect of misalignment with respect to the gap

The initial images obtained with the system were inadequate in both sharpness and contrast for accurately profiling the lower meniscus. A criterion was arbitrarily set in which it was specified that the width of the image of the back-scatter should not exceed 10% of the gap width in order to resolve the shape of the meniscus, measure the dynamic contact angle and determine the position of the static wetting line. The minimum practically achievable coating gap is typically 125μm - when taking into consideration machining errors and thermal effects for a coating head designed to coat widths of the order of 1.5 metres or more. The aim was therefore to achieve back-scatter of width of no more then 13μm.

This limit placed constraints on both the illumination system and the scattering properties of the working fluid. The image of the 25μm air slit was examined by setting up an EGG radiometer owned by ILFORD Imaging UK Limited just beyond the image plane. Spot readings of intensity were taken as a sharp blade was moved across the focal point. The differences between consecutive readings for equal displacements of the blade were taken to reveal the profile and a fit made to a gaussian distribution given by:

$$I(x) = I_0.\exp\left[\frac{2x^2}{a^2}\right] \tag{2.58}$$

where 2a is the beam width at the e^{-2} points and here determined as about 180 μm – far in excess of the target of 13μm. Replacing the air slit with another one of width 10μm reduced the width of the image to 56μm at the e^{-2} points – a significant improvement but still well in excess of aim. The irradiance at the image plane for these two sources was determined as peaking at 0.09 $mW.m^{-2}$ and 0.11 $mW.m^{-2}$ respectively.

The problem was resolved by locating a suitable laser based source. The range of Lasiris MFL Micro-Focus lasers offered by StockerYale proved to be ideal for the purpose. These are arranged to focus a fine line using patented factory-set line generating optics. The company claims that line widths down to 12μm are possible for a working distance of 30 mm when operating at a wavelength of 670 nm. A variety of laser powers ranging from 1 to 100 mW are available for the standard operational wavelength of 635nm within the visible red region. Lasers fitted with similar optics

and operating in the blue region at 440 nm, the extreme violet at 404 nm and in the near infra-red at 1150 nm are also available but are more costly and can suffer from shorter life. The choice of wavelength is dependent on the absorption charcteristics of the scattering agent used for the bottom layer. The density for a given path length should be as high as possible. A sample of photographic emulsion of type considered optimum for the purpose and readily available from ILFORD Imaging UK Limited was taken and the spectral density for a 20μm path length measured for the visible region using a Perkin Elmer Lamda 5 UV/VIS Spectro-Photometer. The results – Figure 2.55 – show that the density is fairly uniform throughout the visible spectrum and close to maximum when working in the red. The added expense of using a wavelength other than 635nm was thus clearly not justified.

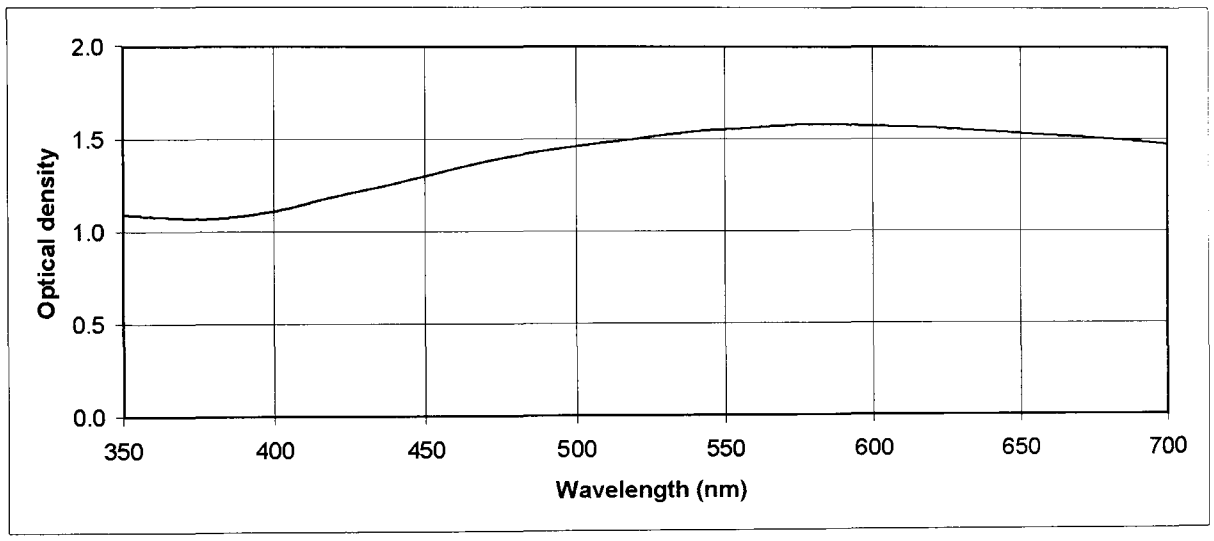

Figure 2.55: Spectral density of photo-emulsion for 20μm path length

A laser generating 5mW at the standard wavelength of 635 nm and set for focusing at a working distance of 65 mm was accordingly ordered on a sale-or-return basis and is depicted in Figure 2.56. The profile at the image plane was measured as being of width 13μm at the e^{-2} points - Figure 2.57.

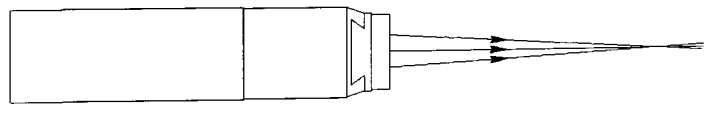

Figure 2.56: Micro-Focus Laser used for lower meniscus monitor

The irradiance was determined as being 569 $mW.m^{-2}$ and thus 5000 times brighter than when using the air slits. Various tests using the fluid jet apparatus showed the

device to be well suited for the task. Laser speckle – a problem when viewing stationary surfaces under laser light due to interference of coherent light scattered by individual particles - became negligible in the presence of the fast moving fluid.

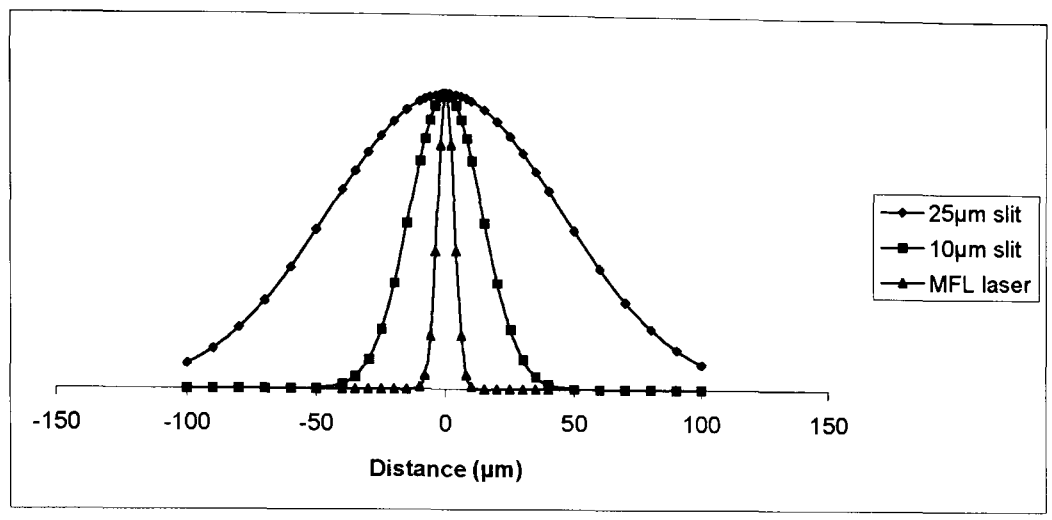

Figure 2.57: Intensity profiles for three alternative light sources

The final requirement was to establish a method for optimising the scattering agent concentration in the lower layer in order to achieve optimum image sharpness and contrast. Practical calculations on the transmission of radiation through turbid media such as photographic emulsion are very complicated. This is partly owing to the fact that the particle size – typically 350 nm - is of the same order of magnitude as the range of wavelengths, and also due to the need to take into account multiple scattering – Ditchburn [1976]. From a study of light scattering by a range of ILFORD products carried out by Ikin [1974], it would be reasonable to assume that the forward and backward scatter IF and IB from a typical liquid photo-emulsion illuminated by an infinitesimally narrow beam of light and incident normal to the surface would change with increasing concentration as illustrated in Figure 2.58.

It will be seen that as concentration C increases, the intensity of the light transmitted normal to the surface decreases while that scattered laterally and in the forward and backward directions increases. The lateral spread of back-scatter when viewed normal to the surface may be crudely represented by a gaussian function given by:

$$Ip(x) = I_0.\exp\left[\frac{-2x^2}{b^2}\right] \qquad (2.59)$$

where 2b is the width at the e^{-2} points. The normalised scatter distribution Iscat(s) is then given by:

$$Iscat(s) = \frac{\int_{-\infty}^{\infty} I(x).Ips(s-x).dx}{\int_{-\infty}^{\infty} I(x).Ips(x).dx} \qquad (2.60)$$

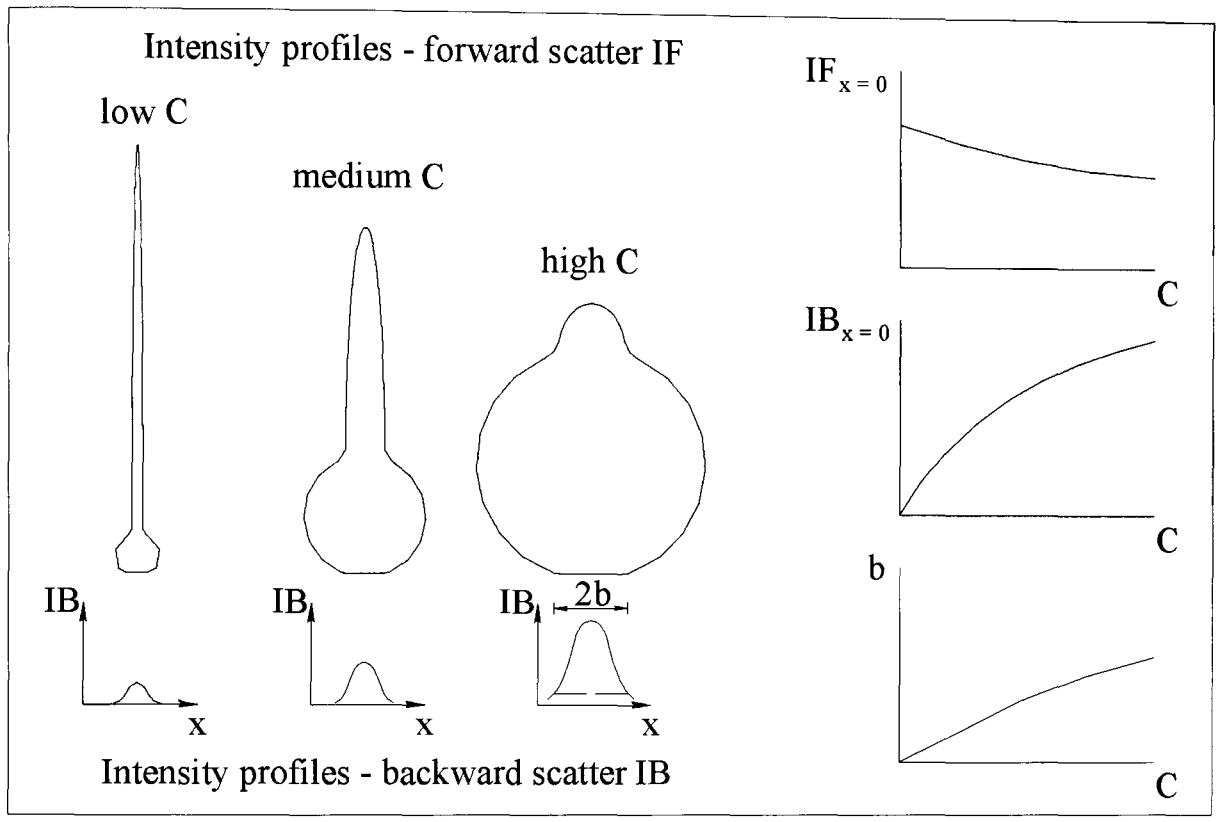

Figure 2.58: Illustration of forward and backward scatter from liquid emulsion

Figure 2.59 shows that b must be 9μm or less to achieve a half power width of the order of 13μm.

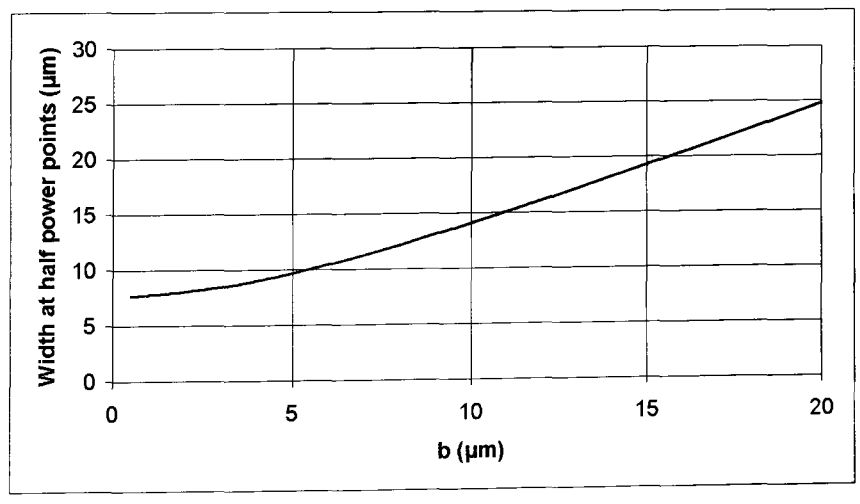

Figure 2.59: Back-scatter half power width as a function of b

Turbidity τ is a useful measure of the scattering properties of a fluid. This is defined by Kerker [1969] in terms of the measured values of the intensity of forward scatter $IF_{x=0}$ emerging at distance y for a given incident intensity I_0 by the expression:

$$IF_{x=0} = I_0.\exp(-\tau y) \qquad (2.61)$$

A densitometer was constructed for measuring values of scatter $IF_{x=0}$ and I_0 - Figure 2.60. A flow cell comprising two glass plates separated by 20μm was set up in front of the sensing unit of an EG&G model 450 radiometer/photometer system. The system was illuminated by collimated light from a tungsten filament lamp. Red light was used by transmitting the light through an interference filter passing wavelengths centred about 635 nm. Solution was circulated through the cell using a syringe pump via 1 mm bore micro-tubing.

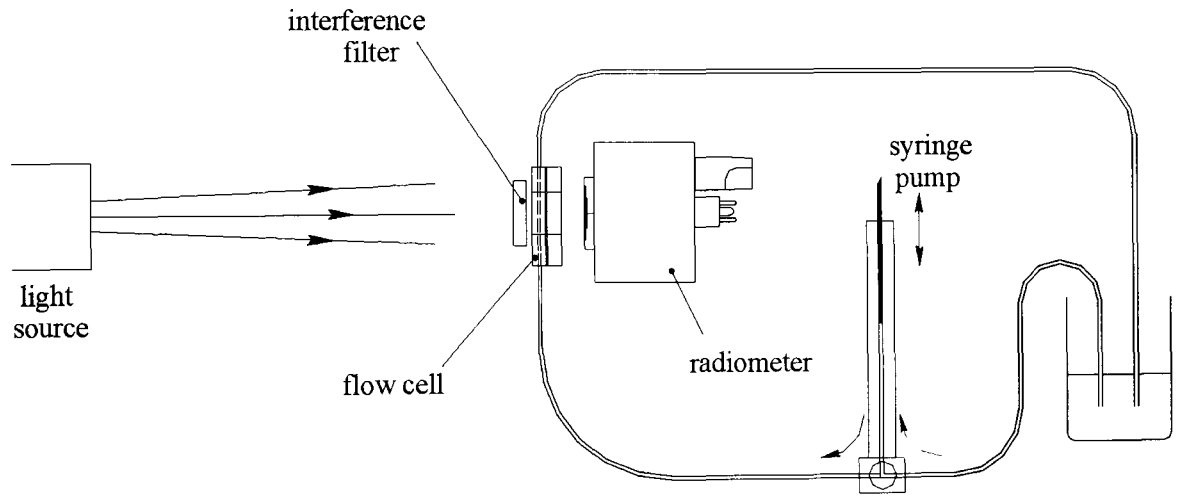

Figure 2.60: Densitometer for measuring turbidity of bottom layer

Figure 2.61 shows the relationship between log(τ) and solids concentration when sampling a typical ILFORD photo-emulsion as scattering agent. This is essentially linear and thus closely follows Beer's law when the concentration is low – Longhurst [1960]. Trials using the liquid jet apparatus showed the optimum turbidity to be of the order of 4×10^4 m^{-1} and the corresponding solids concentration 11%. Lower concentrations, however, are admissible, where necessitated by the lower viscosities characteristic of carrier layers – albeit the images suffer from poorer contrast.

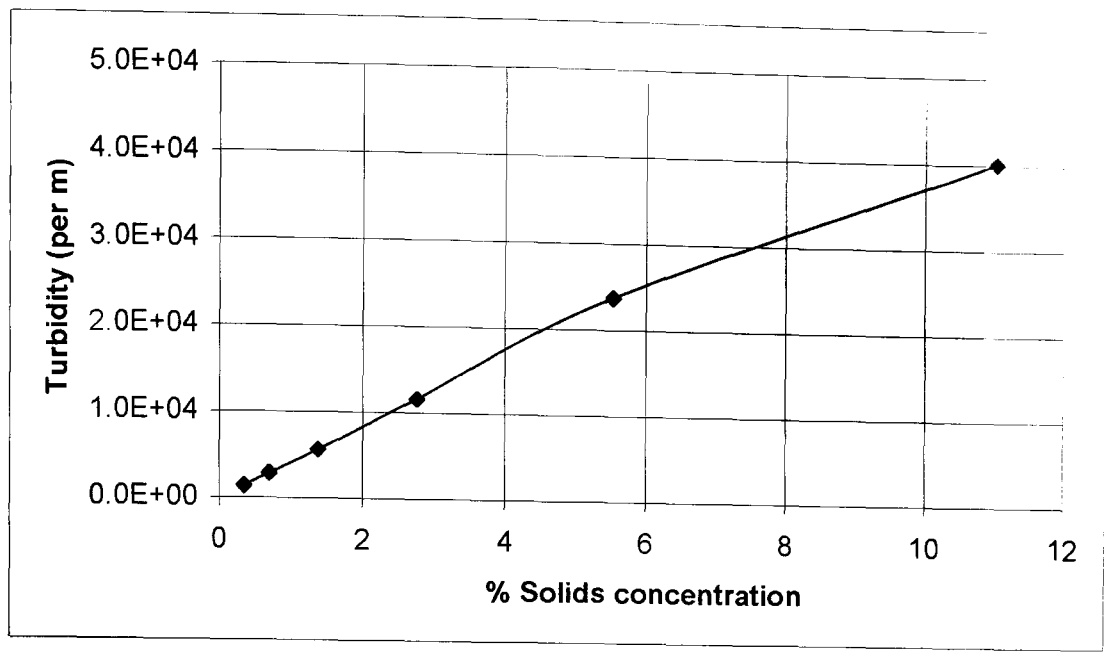

Figure 2.61: Turbidity as a function of solids concentration

2.12.3 The Final Experimental System

Figure 2.62 shows a view of the final installation on the pilot coating machine seen from the side. The main frame surfaces are parallel to the xz (y = 0) plane or to the yz (x = 0) plane to enable convenient mounting of the optical components and their associated adjustment mechanisms.

Figure 2.63 shows a view along the x axis and thus from behind the coater and in a direction inclined at 45° to the horizontal. Figures 2.62 and 2.63 serve to indicate how the frame is mounted on a pivot enabling the optics to be swung away from the side of the machine when not being used for recording the lower meniscus profile. This ensures minimum risk of fouling or splashing the optics while preparing the coating head or finally washing up. It also allows convenient access to the probe when the frame is withdrawn - thereby ensuring this can be rapidly inserted after making the bead and removed prior to opening up the gap at the end of recording.

Figure 2.64 shows the detail of the six translation mechanisms built into the system. Three orthogonally mounted modules control the position and focus of the laser and three the position and focus of the mono-zoom optics.

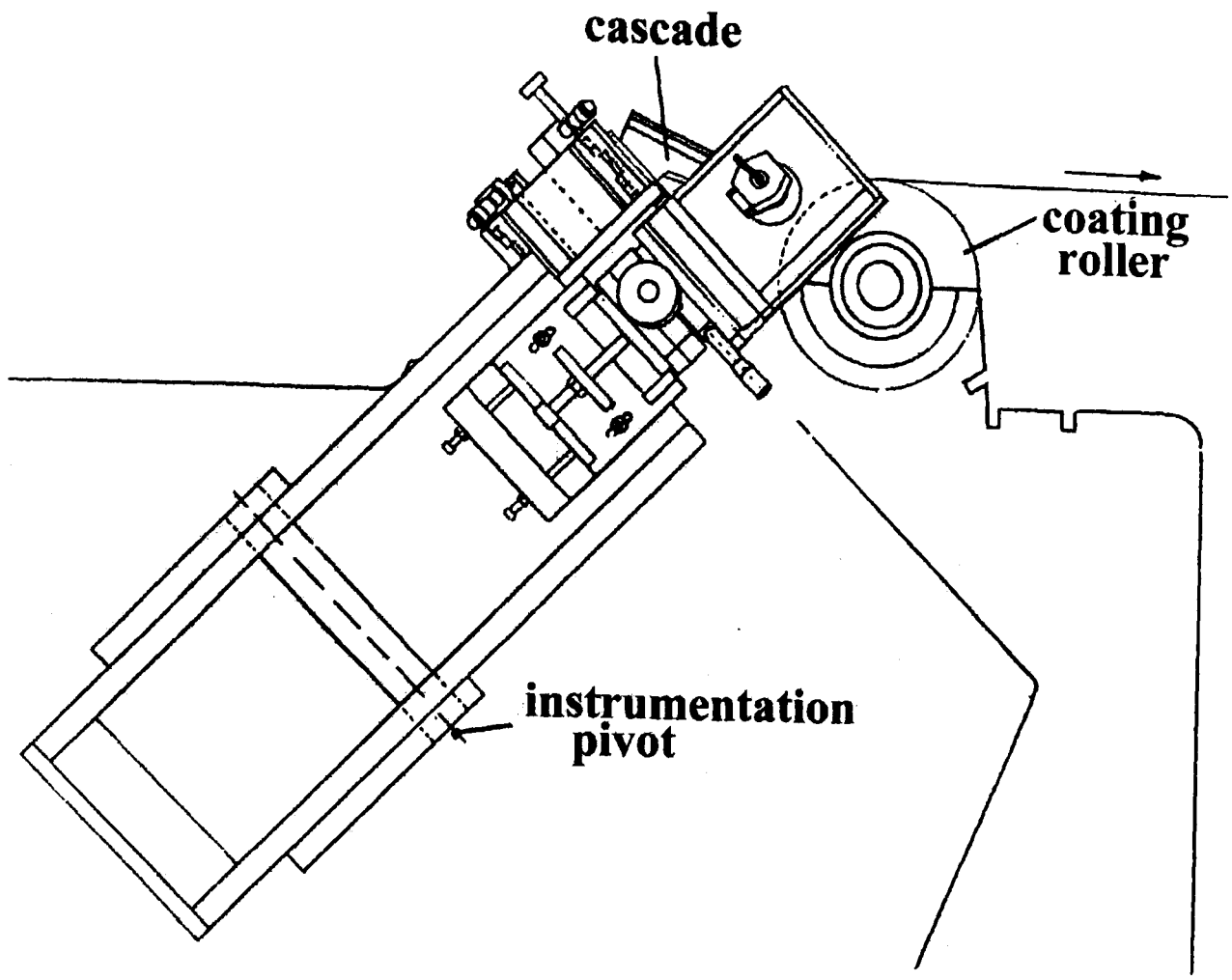

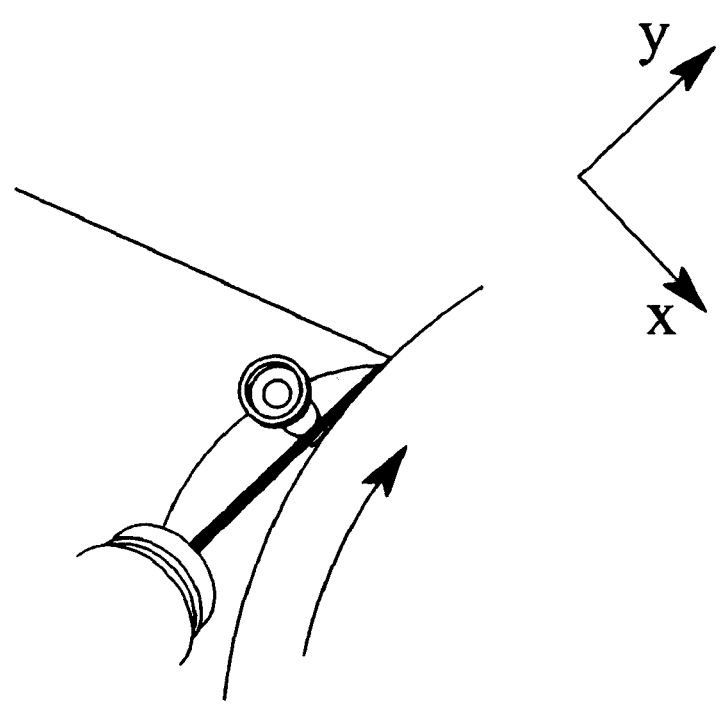

Figure 2.62: Lower Meniscus Monitor – side elevation

Figure 2.65 shows the view of the monitor seen along the y axis from above and demonstrates the advantage obtained in rotating the prism housing about the y axis

through an angle θ - set at 7.5° - in order to gain adequate clearance between the probe and the coating roller.

RECORD POSITION

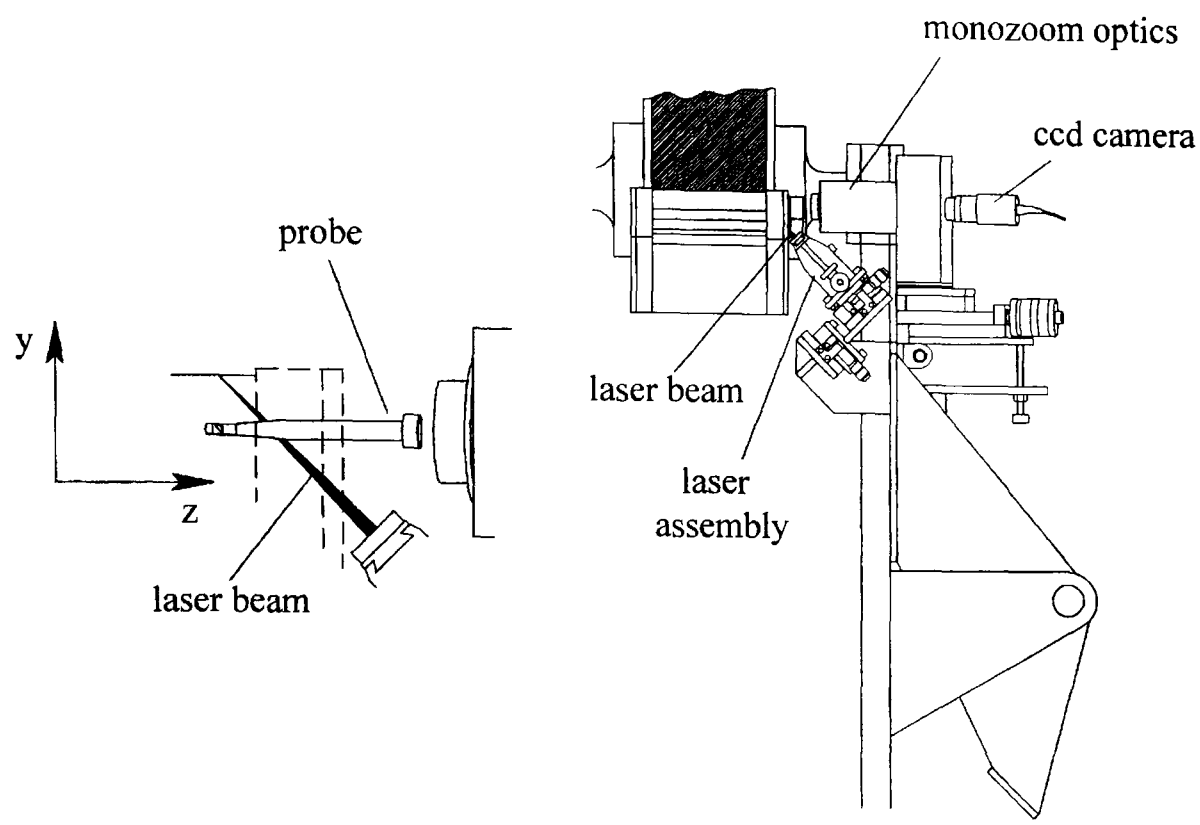

HOME POSITION

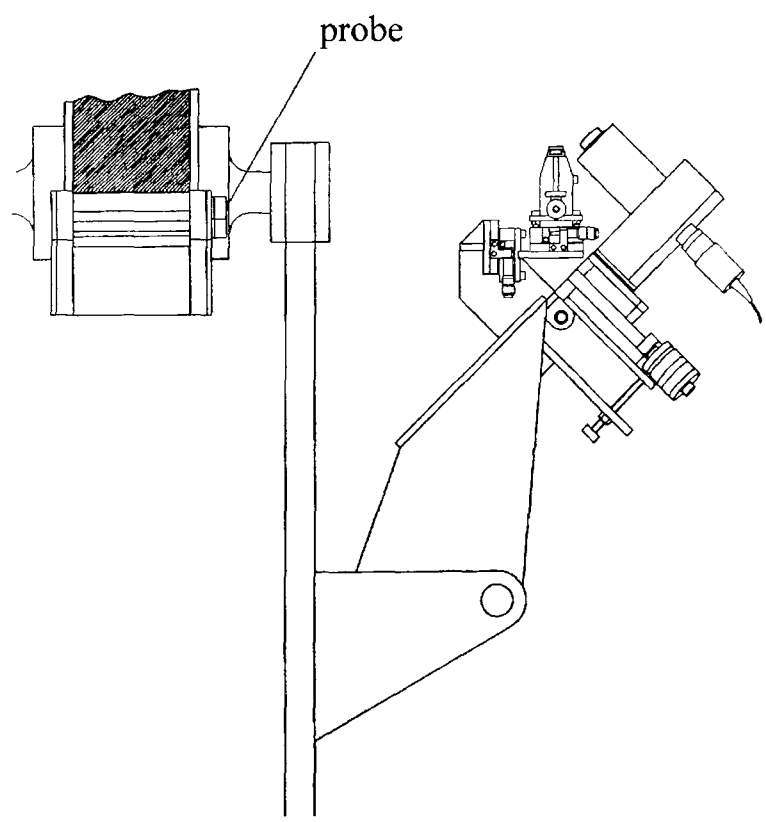

Figure 2.63: Lower Meniscus Monitor – view from behind the coater

Initial alignment was carried out using a metal block bridging the coating gap and acting as a scattering surface in the absence of coating. An engineer's slip gauge well suited the purpose after re-grinding one face to reduce the corner radius to a minimum – typically 50μm – and applying a thin coating of white matt paint to provide scatter – Figure 2.66.

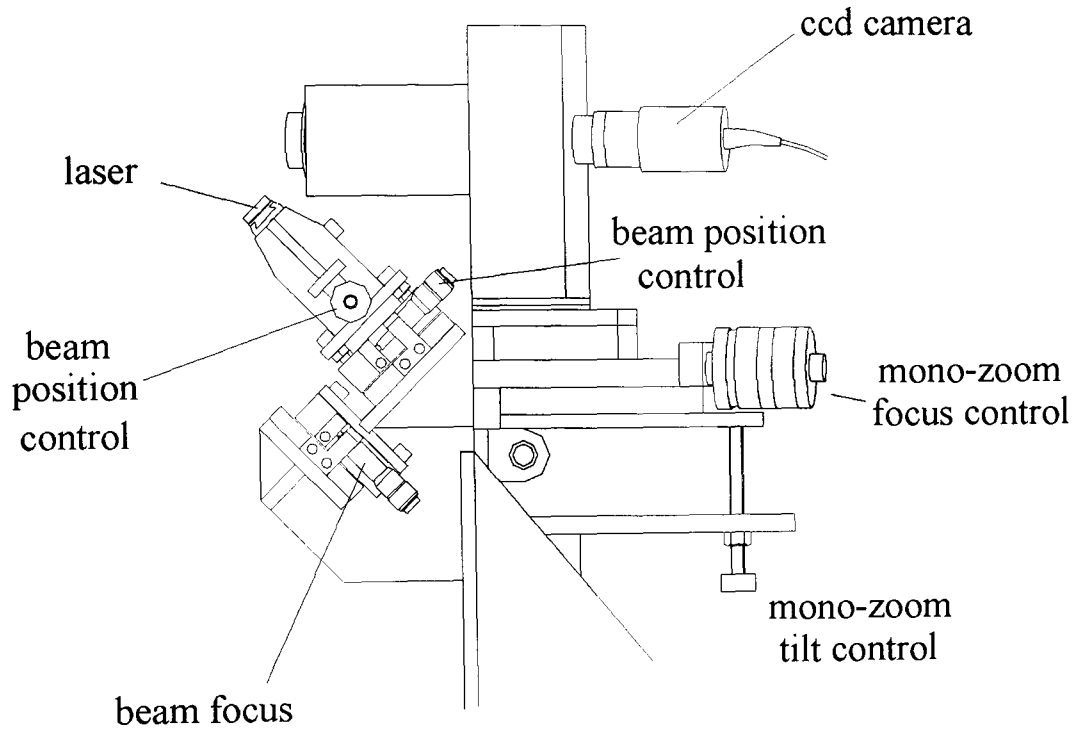

Figure 2.64: Translation mechanisms – Lower Meniscus Monitor

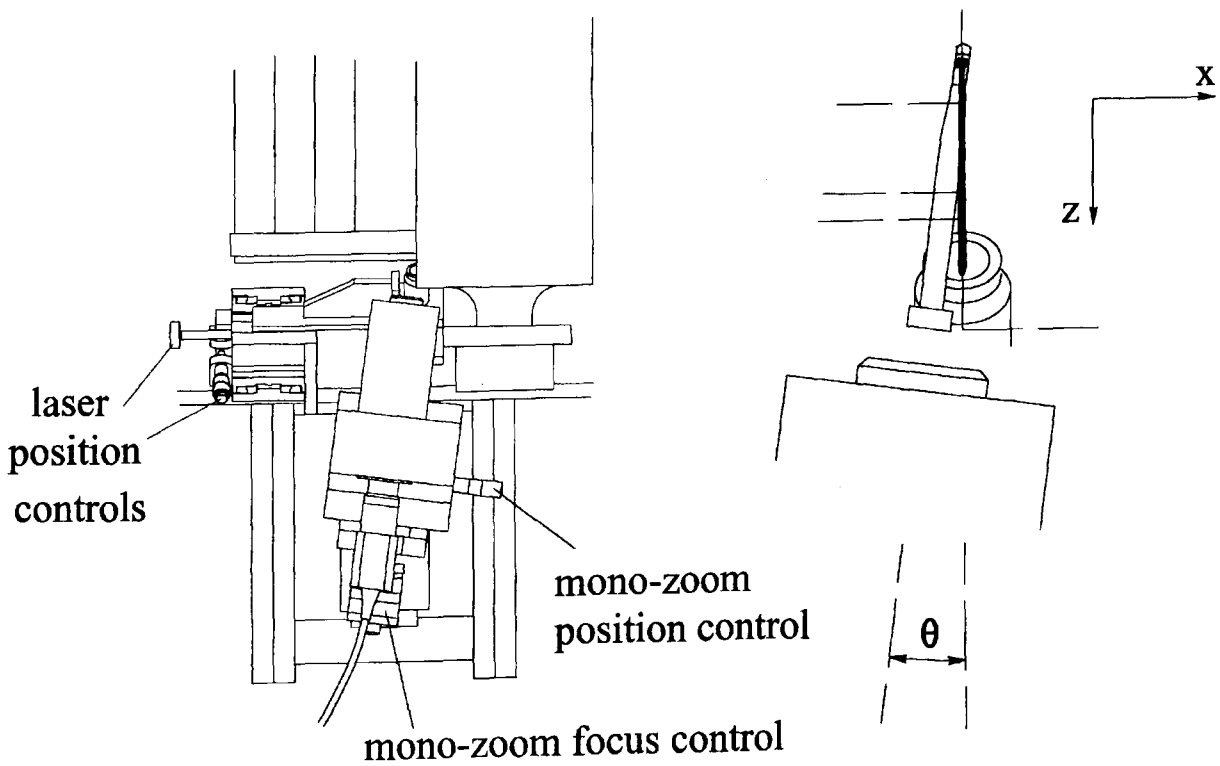

Figure 2.65: Lower Meniscus Monitor – view from above the coater

Initial coating trials confirmed that sharp high contrast images of the lower meniscus were obtainable by this method. Refinements focused on improving the mechanical robustness of the equipment and included fitting of a cross-brace linking the laser clamp and the monozoom optics housing – as shown in Figure 2.67. The torque on the fixings was increased in concert with final adjustments to the position and focus of both systems to secure reproducible alignment of the target block image with the camera image plane, as the instrument was moved to and fro between the home and recording positions.

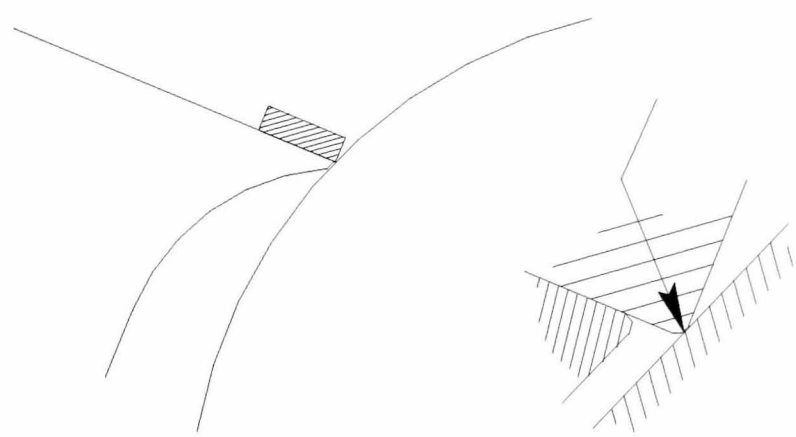

Figure 2.66: Use of a target block when setting up the Lower Meniscus Monitor

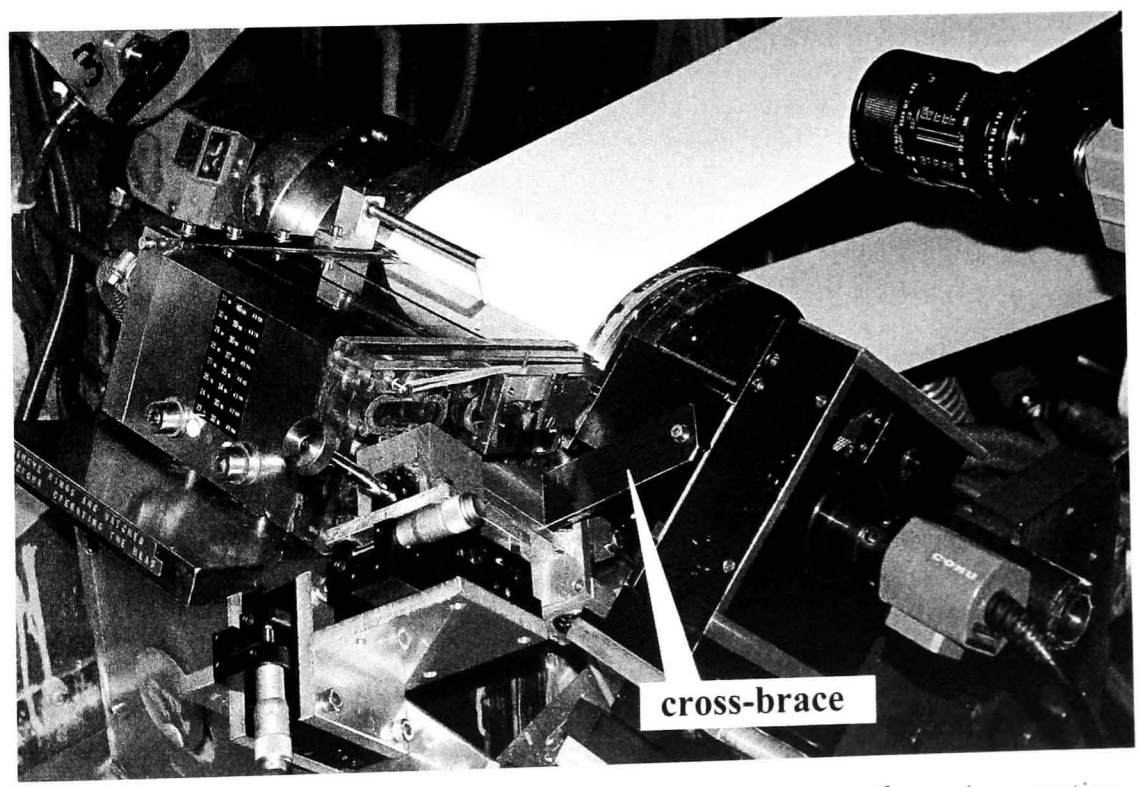

Figure 2.67: Cross-brace used for linking the laser and receiver optics

It is general practice to incorporate some form of optical reference when visualising coating flows to enable the precise location of key features relative to the solid surfaces – Schweizer [1988]. This presented a formidable challenge owing to the high magnification necessary for resolving the meniscus. Ikin [1992] made use of the shadow of an illuminated scratch on the substrate bearing surface of the hollow Perspex coating roller to identify the static and dynamic wetting lines. Valentini et al. [1996] report the same technique when drawing the web over a cylindrical glass skid. The method is not applicable here. The problem was resolved in two stages. The first involved machining a step in the face of the coater lip in an area considered by prior experience unlikely to affect the flow field for the range of suction pressures of industrial interest – Ikin [1992].

On running a coating trial with this step present, the corresponding image suffered from poor contrast. There was an additional problem in that the step encouraged the formation of droplets of variable shape as the solutions poured over the lip when priming the coating head – Figure 2.68. Stable reference images of adequate sharpness were eventually obtained by partly filling the cavity formed by the step with a wedge of epoxy resin pre-mixed with white oil based household paint to provide back-scatter as also shown in Figure 2.68.

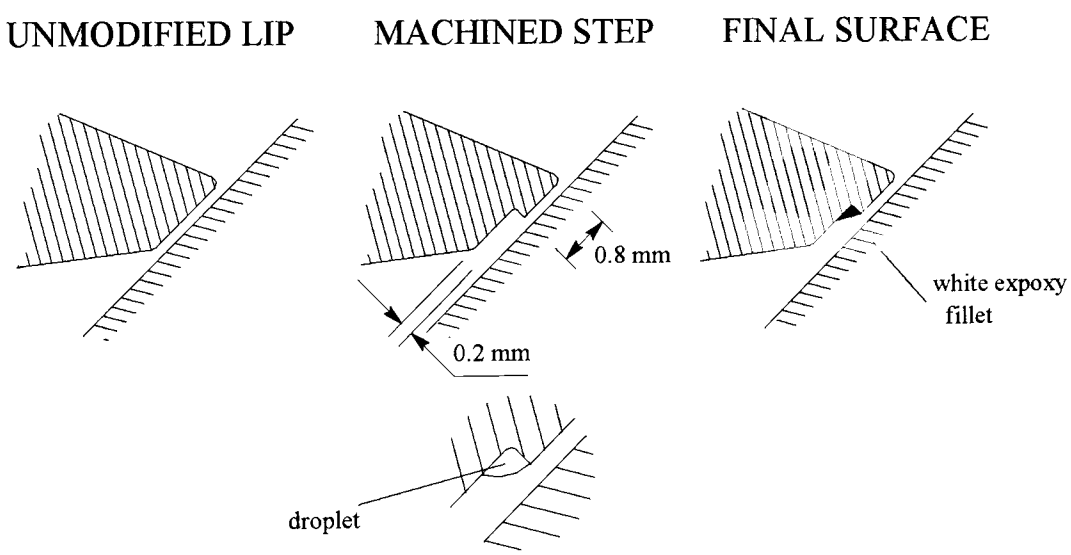

Figure 2.68: Method for generating a reference surface

The system was still deficient in that it was impossible to attain an adequately sharp focus on both the reference surface and the meniscus at the same time. The axial distance over which the laser remains in sharp focus is finite and is governed by the

laws of gaussian beam optics – Kogelnik [1965]. The semi-width of the beam measured at the e^{-2} points in the x direction as it emerges from the focusing lens varies with propagation distance ζ according to the expression:

$$w(\zeta) = w(0)\left\{1 + \left[\frac{\lambda\zeta}{\pi w(0)^2}\right]^2\right\}^{1/2} \qquad (2.62)$$

where w(0) is the semi-width at the beam waist measured at the e^{-2} points and λ the wavelength. It was found possible to increase the effective depth of focus without significantly compromising the beam waist by masking down the beam width from 8 mm to 4 mm at the laser aperture and thus reducing the convergence angle – as shown in Figure 2.69.

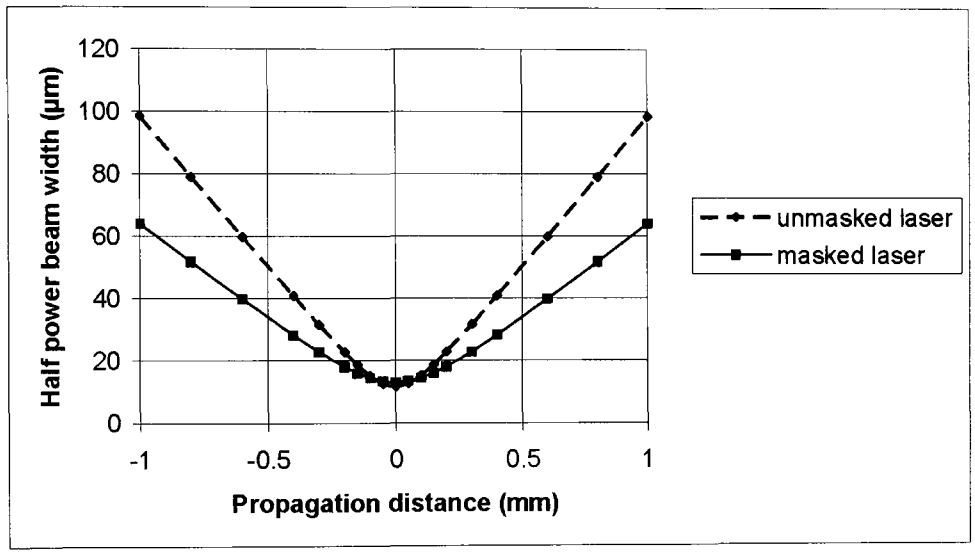

Figure 2.69: The effect of masking the laser beam

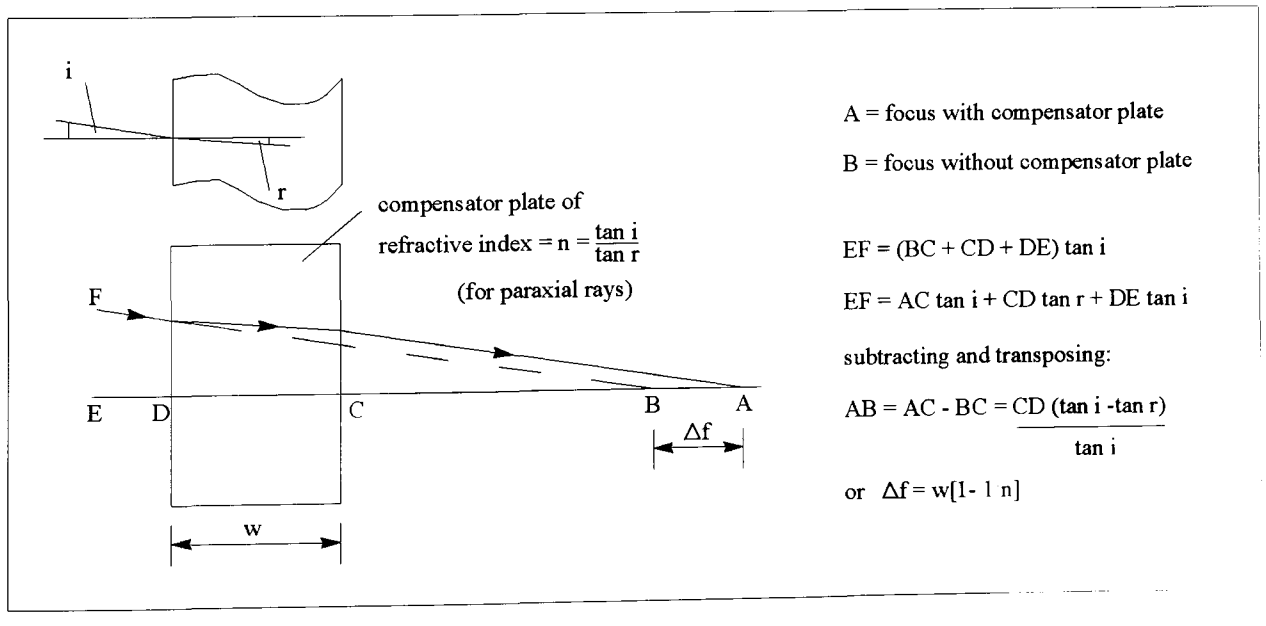

Figure 2.70: Principle of compensator plates

Adequate performance was finally achieved by setting up two thin optical compensator plates made of polycarbonate. These were mounted on a slider free to move in a set of grooves cut into the brass block shown in Figure 2.49. One plate of thickness 3 mm, on insertion into the laser beam, enabled the focal point to be transferred from the reference surface to the region generally occupied by the lower meniscus. The principle is well known and illustrated in Figure 2.70. The second plate, which was of thickness 1.5 mm, when inserted in front of the monozoom entrance aperture advanced the focal plane in a similar manner. Figure 2.71 shows how the plates were configured and mounted on the slider.

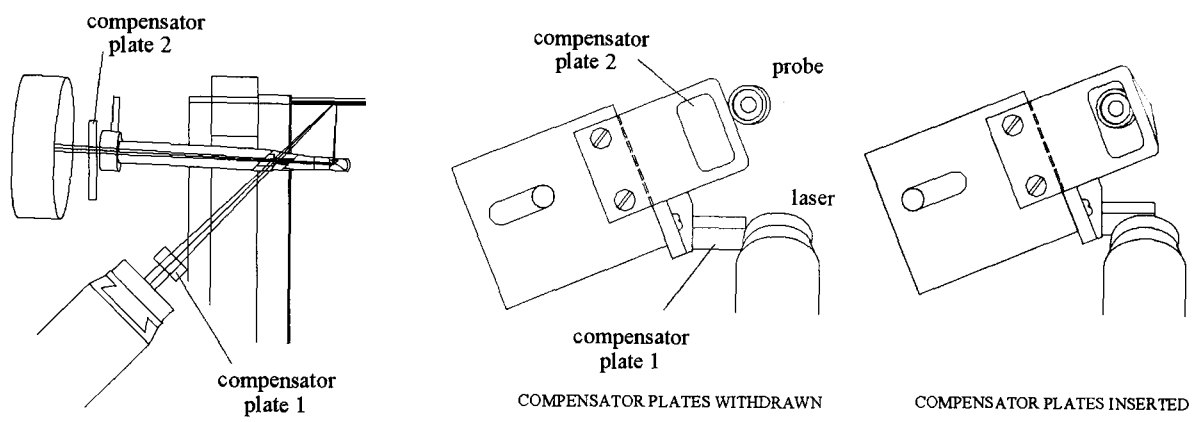

Figure 2.71: Compensator Assembly – Lower Meniscus Monitor

2.12.4 The Final Validation of the System

Figure 2.72 shows the images observed at the monitor displaying the camera output for a) when the target block is placed across the coating gap for aligning the optics and b) when coating. A reflection image is seen due the fact that inspection is at grazing incidence relative to the substrate. The reflection is strongest when coating glossy surfaces but still present even with matt ones. The reflection, although initially confusing, does serve a very useful purpose in that the dynamic wetting line and the dynamic contact angle can be determined with good precision – as already described earlier and illustrated in Figure 2.42.

The images of the meniscus were digitised using the OPTIMAS image analysis software and individual points superimposed onto a drawing in AutoCAD LT after

suitable scaling in a way similar to that described for studying slot exit flows – Section 2.7.2.

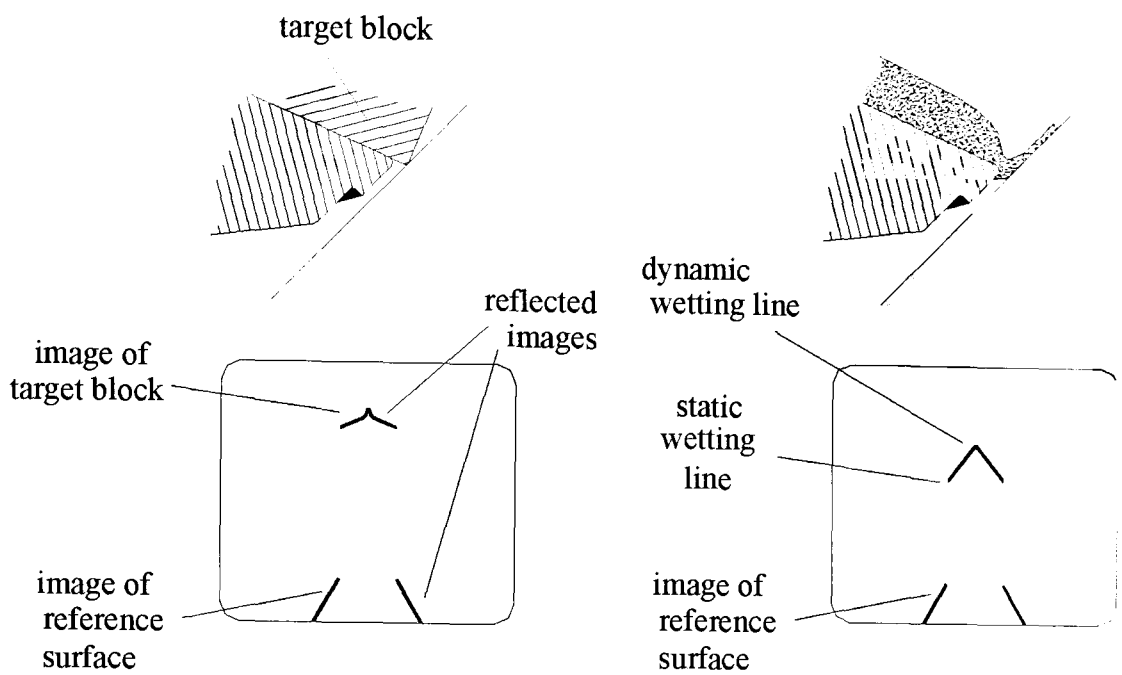

Figure 2.72: Typical images seen on monitor screen – Lower Meniscus Monitor

2.13 Method for Profiling the Upper Free Surface at the Bead Forming Zone

2.13.1 The Principles of the Method

The method used follows on from that employed by Valentini et al. [1991] in which they illuminated the free surface with a light sheet and viewed the scatter from the fluid from the side and slightly above the slide plane. It is also essentially as used for visualising the upper free surface at the exit of the carrier layer slot and described in Section 2.7. Scattering agent was added at approximately the same concentration as for the profiling the lower meniscus.

2.13.2 The Experimental System

The camera used for imaging the upper meniscus was a Cohu High performance B/W CCD unit – model 4912 – fitted with a 62 mm diameter TAMRON SP zoom lens. The laser used for generating the light knife was identical to that reported in Section 2.7.

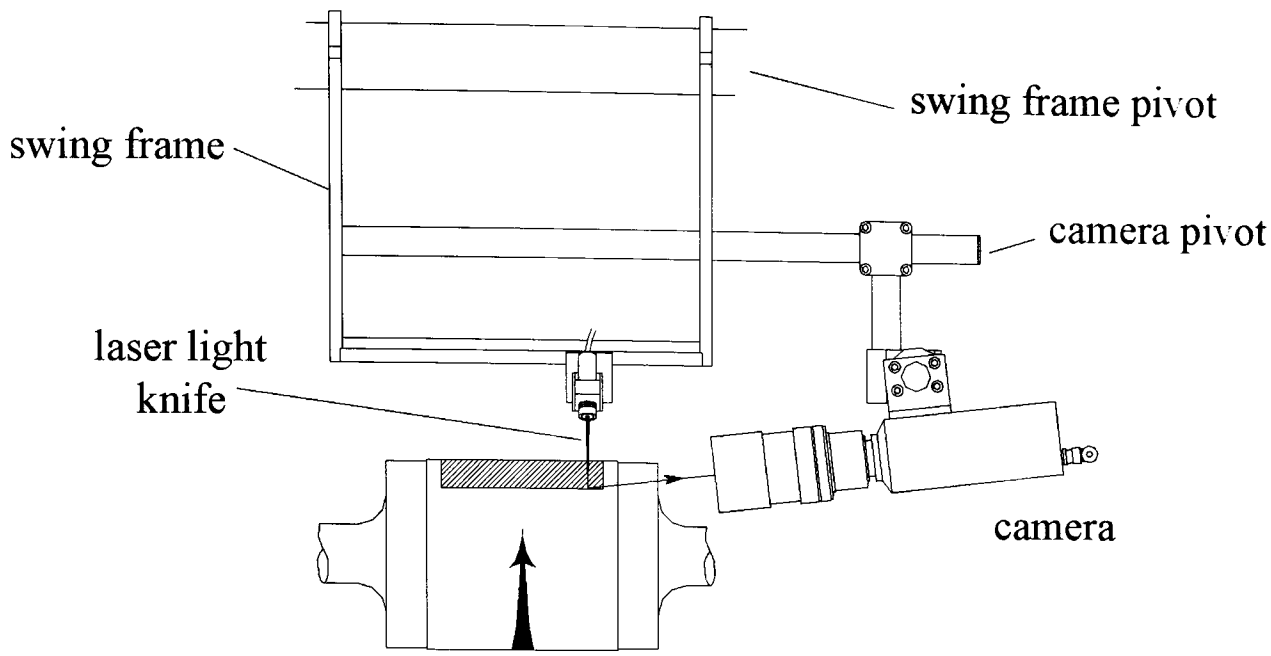

Figure 2.73: Upper Meniscus Monitor – front elevation

The swing frame spanning the web and designed for mounting the first folding mirror reflecting light from the laser scanner described in Section 2.11.2 provided a convenient means for mounting the laser light knife. The camera was initially mounted on a subframe designed for fixing onto the lower meniscus monitor swing frame after first removing the mono-zoom optics. As the development of the lower meniscus monitor advanced to incorporate cross-bracing and other refinements, it became increasingly time consuming to interchange the optics between recording trials. A decision was therefore taken to mount the camera for recording the upper meniscus from the same swing frame as used for supporting the laser light knife. The final installation is shown in Figures 2.73 to 2.75.

Figure 2.73 shows a view of the system from behind the coating head – with the cascade removed for clarity. The camera is inclined to the horizontal by a small angle sufficient to ensure the line of sight clears the top of the cascade edge guide.

Figure 2.74 shows the method for mounting the laser and the camera on the scanner swing frame. The system incorporates two pivots enabling the camera to be lifted up and over the coating roller and stowed well clear of the path of the lower meniscus monitor when moved from its home to recording position.

A pointer with a bull's eye target pattern was set up over the cascade in similar fashion to that used when recording the upper free surface at the slot exit as shown in Figure 2.75.

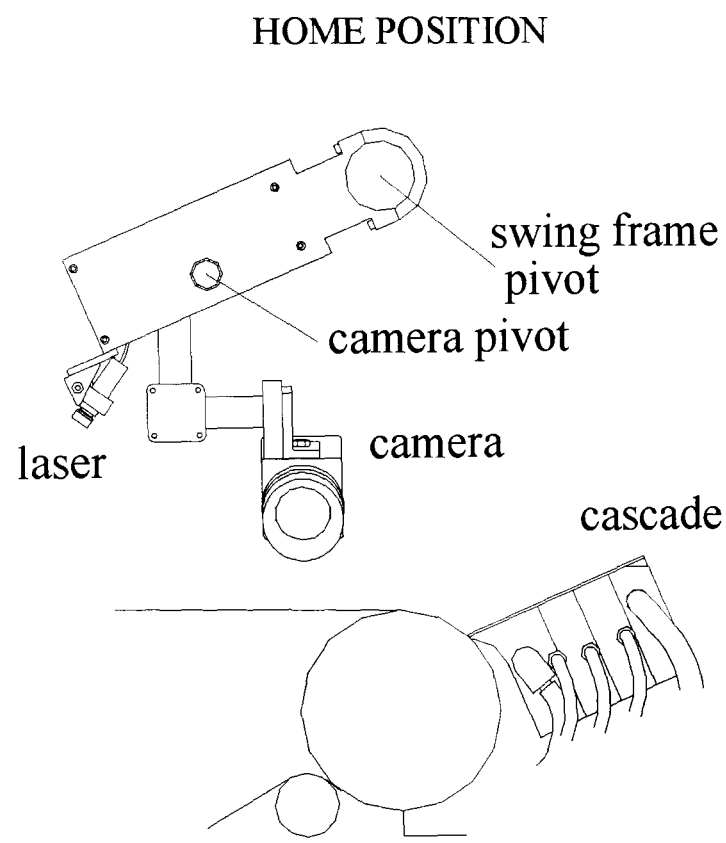

Figure 2.74: Upper Meniscus Monitor - side elevation

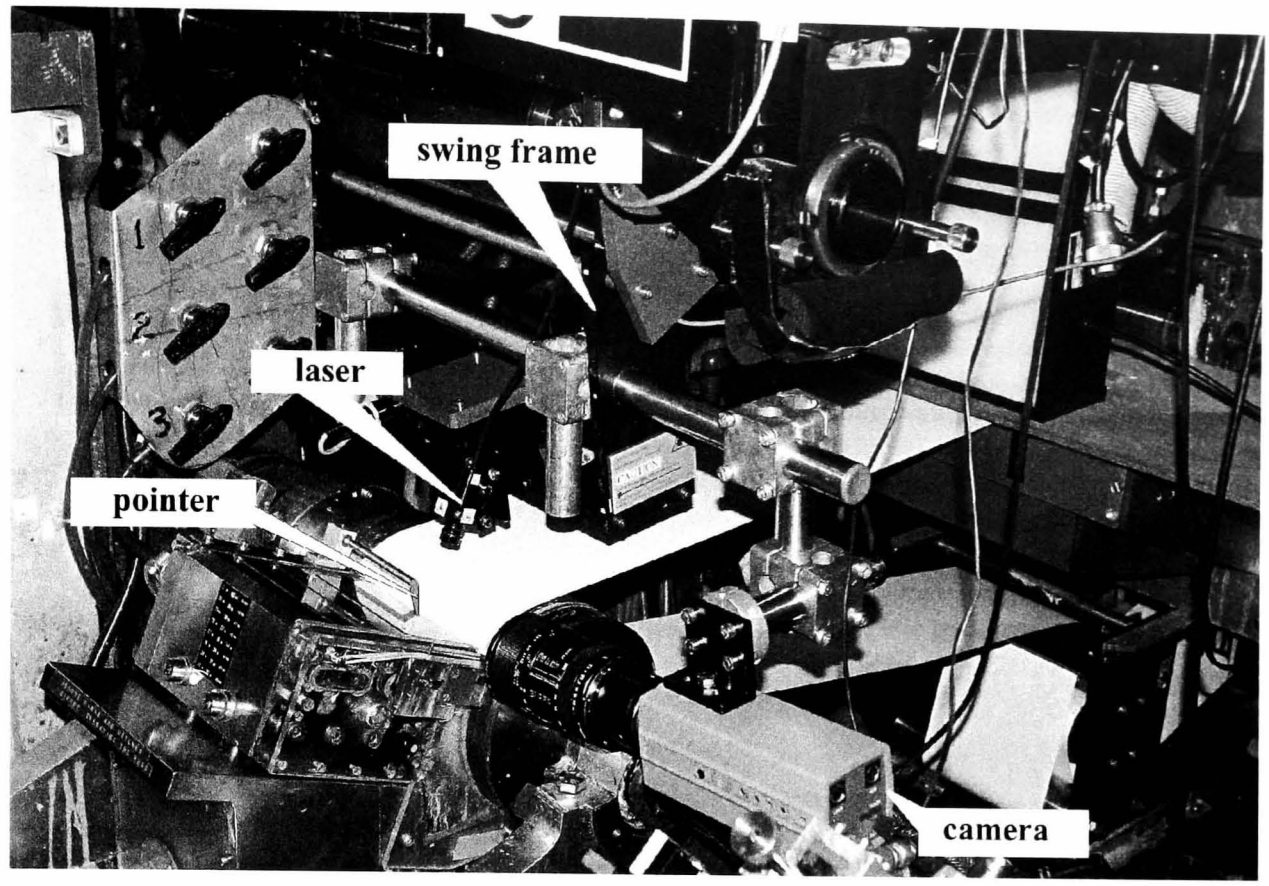

Figure 2.75: General view of Upper Meniscus Monitor and Reference Pointer

2.14 Methods for Studying Air Induced Disturbances in Wet Coatings

2.14.1 Justification

Problems arising from the drying of thick low viscosity coatings using an air impingement dryer are well known – Cohen and Gutoff [1992]. These authors designate the term mottle as descriptive of defects arising from air motion and show how the effect can be reduced or eliminated by decreasing the air speed or increasing the concentration of the coating solutions. This latter action results in the dual benefit of increasing viscosity and reducing wet thickness (Cohen and Gutoff [1995], Miller and Neogi [1995] and Bell et al. [2000]). The traditional approach used within the photographic industry has been to chill the wet coating to about 2°C to 4°C between coating and drying. This achieves either solidification or a very significant increase in viscosity before the surface becomes exposed to air from the dryer owing to the properties of the gelatin used as binder for photo-sensitive coatings.

Interest in optimising the drying of multilayer coatings containing polymers other than gelatin has increased over the past two decades owing to the advent of inkjet printing

technology and the need to coat compatible printing media. Bell et al. [2000] showed that mottle can be eliminated by directing the air parallel to the web surface with the air speed matching that of the web. Iwado [2003] proposed the use of two dryers, the first being where the air speed is limited to less than 30 m/s and of length such as to ensure achieving adequate robustness against disturbances. The second dryer is designed to yield high solvent evaporation rates.

The purpose of this study was to:

1. Establish the mechanism responsible for such defects
2. Quantify the disturbance as a function of solution properties, air speed and nozzle-to-web gap
3. Quantify the benefit of using a carrier layer
4. Quantify the benefit of optimising the gap and air pressure profile

The work is of prime interest to industry due to the fact that drying capacity is often perceived to be a key limit to the overall coating process - as described in Section 3.4.3.3 and Figure 3.26.

The experimental part of the study was accordingly split into three key areas of investigation. In the first, use was made of the rotary dryer briefly introduced in Section 2.5.1.7 and described in more detail in Section 2.14.2. The aim was to establish how the coating becomes unstable and disturbed by surface waves as the web continuously passes under a very long array of air impingement nozzles. The second and major part of the work made use of the stationary linear dryer as described in Section 2.5.1.7, once having established a range of web speeds compatible with reproducing the effects. The third involved the measurement of heat transfer coefficient to enable a realistic drying model to be established and hence an estimate to be made of the benefits to drying speed accruing from optimising the coating formulation and nozzle-to-web gap.

2.14.2 The Design of the Rotary Dryer and the Associated Methods for Studying Air Induced Defects

The rotary dryer was designed by Ikin [2000(2)] just prior to the commencement of this study to allow continuous relative motion between a wet coating and an array of air impingement nozzles. The system is shown in Figure 2.76 and comprises eighteen nozzles mounted on the periphery of a hollow cylindrical drum.

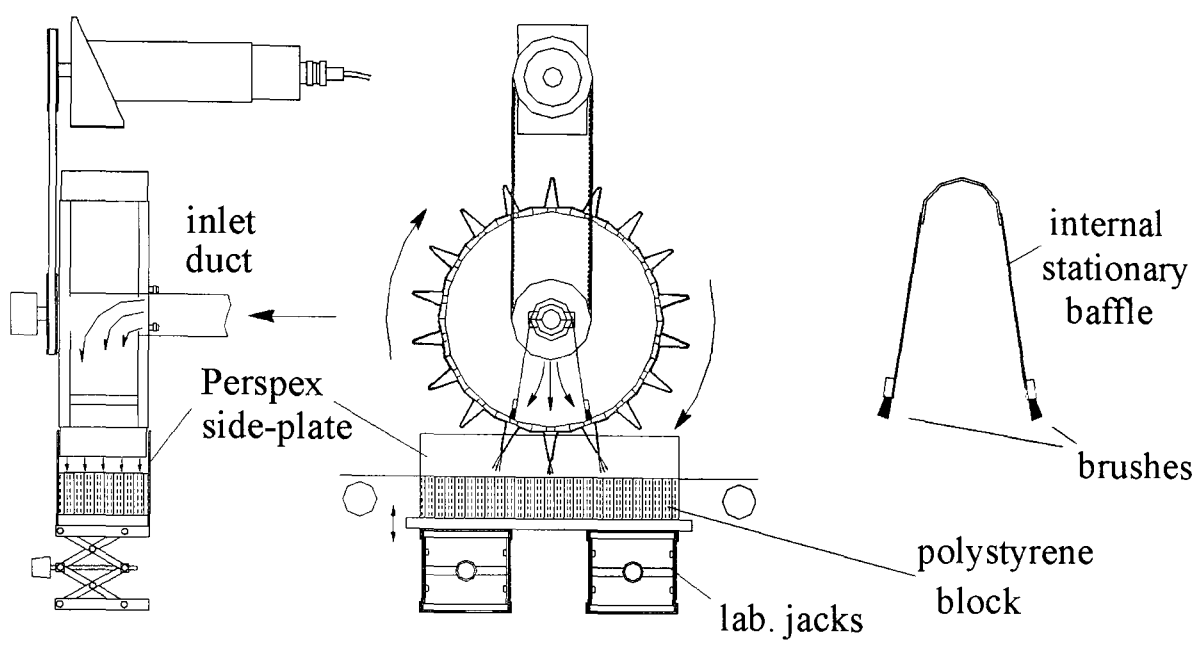

Figure 2.76: Design of the rotary dryer

The drum is free to rotate on bearings and powered by a variable speed DC motor using a toothed belt. The motor is typically run at 118 rpm in order to achieve a peripheral speed of 200 m/minute. Air is fed axially into the drum and constrained by a pair of internal stationary baffles to emerge though a maximum of three nozzles at any one instant to impinge on the web clamped horizontally beneath the drum. Brushes are mounted at the ends of the two baffles to minimise air leakage while allowing free movement of the rotor. When operating the dryer, the sample is supported on a polystyrene insulator block. The block is mounted on two laboratory jacks, which allow the web-to-nozzle gap to be varied as required.

A CCD camera was used for recording disturbances to the wet surface as a sample was brought to rest under the rotating dryer wheel. A light box housing four fluorescent tubes mounted behind a diffusing screen served to illuminate the sample near grazing incidence. The camera was mounted to receive specularly reflected light via a mirror – as shown in Figure 2.77.

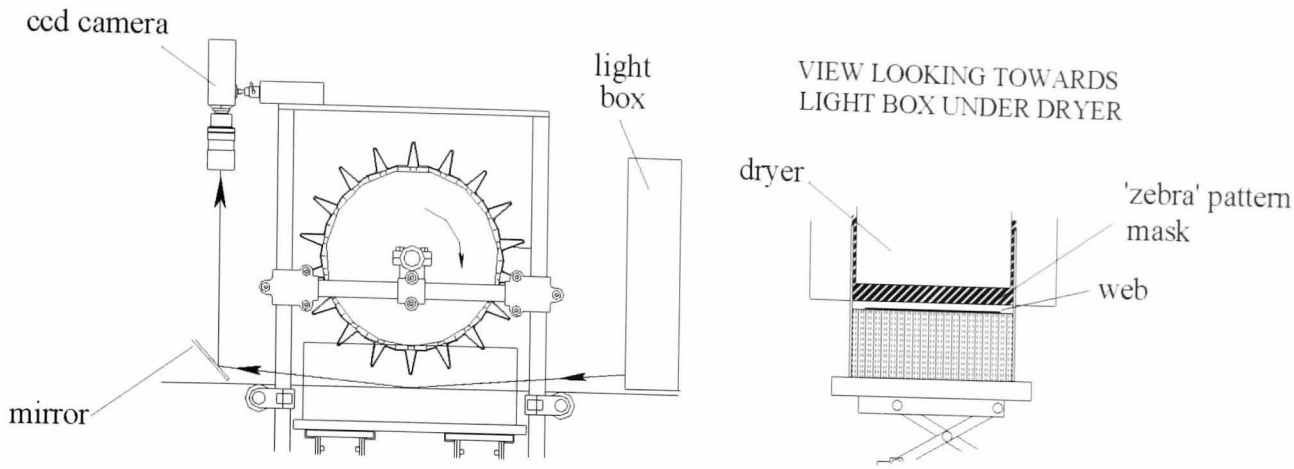

Figure 2.77: Method for visualising air induced disturbances under the rotary dryer

A mask comprising equi-spaced diagonally mounted opaque strips set up in a "zebra-stripe" pattern acted as visual aid for observing the break-up of the wet surface into waves – the camera being focused on the area immediately below the drum. A video clip showing a typical recording is appended with this thesis – see Appendix II – sequence # 6.

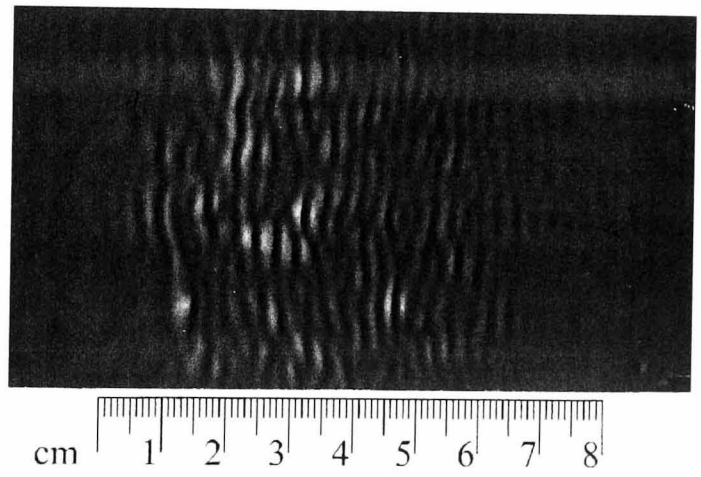

Figure 2.78: Appearance of disturbances due to air from the rotary dryer

Figure 2.78 depicts a photo-emulsion coating that had become severely disturbed by the air emerging from the rotating nozzles. The wet thicknesses and viscosities of the formulation were as shown in Table 2.5.

Layer	Wet thickness (μm)	Viscosity (mPa.s)
Top	40.3	22.8
Middle	63.9	46.0
Bottom	20.0	16.5

Table 2.5: Formulation used for rotary dryer test

The speed of the nozzles was effectively 200 m/min. relative to the web, the minimum nozzle-to-web gap10 mm and the air pressure controlled at 900 Pa.

Neglecting frictional losses, the speed of the air emerging out of a nozzle – Figure 2.79 – can be approximated by applying Bernoulli's equation (2.63) and the continuity equation (2.64) – as shown for example by Fox and McDonald [1973].

$$\frac{P_1}{\rho} + \frac{V_1^2}{2} = \frac{P_2}{\rho} + \frac{V_2^2}{2} \tag{2.63}$$

where P_1 and P_2 are the pressures and V_1 and V_2 the peak velocities on the upstream and down stream side of the nozzle respectively and ρ the density of the air.

$$\rho V_1 A_1 = \rho V_2 A_2 \tag{2.64}$$

where A_1 and A_2 are the respective areas of cross-section.

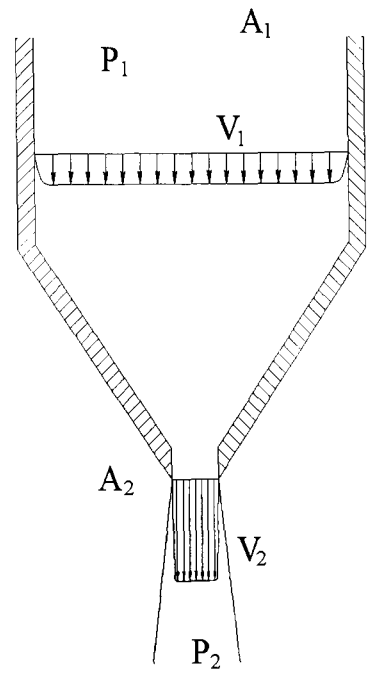

Figure 2.79: Flow field for air emerging from a dryer nozzle

(2.64) simplifies to:

$$V_2 = \frac{V_1}{\beta} \tag{2.65}$$

where β is A_2/A_1.

Substituting for V_1 in (2.63) yields:

$$P_1 - P_2 = \rho\left[\frac{1-\beta^2}{2}\right]V_2^2 \tag{2.66}$$

or:

$$V_2 = \left[\frac{1}{(1-\beta^2)^{1/2}}\right]\left[\frac{2(P_1-P_2)}{\rho}\right]^{1/2} \tag{2.67}$$

The density ρ of the air is dependent on air temperature T °C and is, to a first order of approximation, given in terms of ρ_{NTP}, the density measured at NTP, by the law for an ideal gas – Newman and Searl [1957]:

$$\rho = \rho_{NPT}\left[\frac{293}{(273+T)}\right] \tag{2.68}$$

and substituting for ρ in (2.67):

$$V_2 = \left[\frac{1}{(1-\beta^2)^{1/2}}\right]\left[\frac{2(P_1-P_2)(273+T)}{\rho_{NPT}(293)}\right]^{1/2} \tag{2.69}$$

In actuality, V_2 is less than as indicated by (2.69) owing to frictional losses. It is common practice – Fox and McDonald [1973] - to lump together the expression $\left[\frac{1}{(1-\beta^2)^{1/2}}\right]$ and the allowance for friction in a term C_d called the discharge coefficient to finally yield:

$$V_2 = C_d\left[\frac{2(P_1-P_2)(273+T)}{\rho_{NPT}(293)}\right]^{1/2} \tag{2.70}$$

C_d reaches typically 0.98 for a well designed nozzle - Fox and McDonald [1973]. On taking this value and assuming the density of air at NTP to be 1.29 $kg.m^{-3}$, the velocity of air impinging on the sample shown in Figure 2.78 would thus have been 36.3 m/s.

It is evident that the effect of excessive air motion tends to surface waves showing a pattern similar to that seen on a car windscreen after applying anti-freeze solution and driving at slow speed without operating the windscreen wipers. Similar patterns are seen on thin layers of fluid deposited on the lower wall of a wind-tunnel section when sheared by a turbulent air flow – Cunha and Carbonaro [1995], Özgen et al. [2002] - and when wiping a thin film coating on a rotating cylinder with an impinging slot jet – Gosset and Buchlin [2003].

2.14.3 Visualisation of Surface Waves using the Linear Array of Stationary Nozzles

The rotary dryer, although useful for simulating continuous high speed drying, has the disadvantage that it is difficult to obtain accurate qualitative data on the waves so generated. The length of the sample subjected to air motion is small and spans only a few tens of wavelengths – typically 25 - see Figure 2.78. More importantly, the gap between each nozzle and the web varies as it traverse the sample. This becomes more significant as the minimum gap is reduced. Light used to illuminate the sample necessarily becomes interrupted as each nozzle traverses the beam. Reverting back to using the linear dryer array was thus preferable if it could first be demonstrated that this dryer was capable of reproducing the defect in some way.

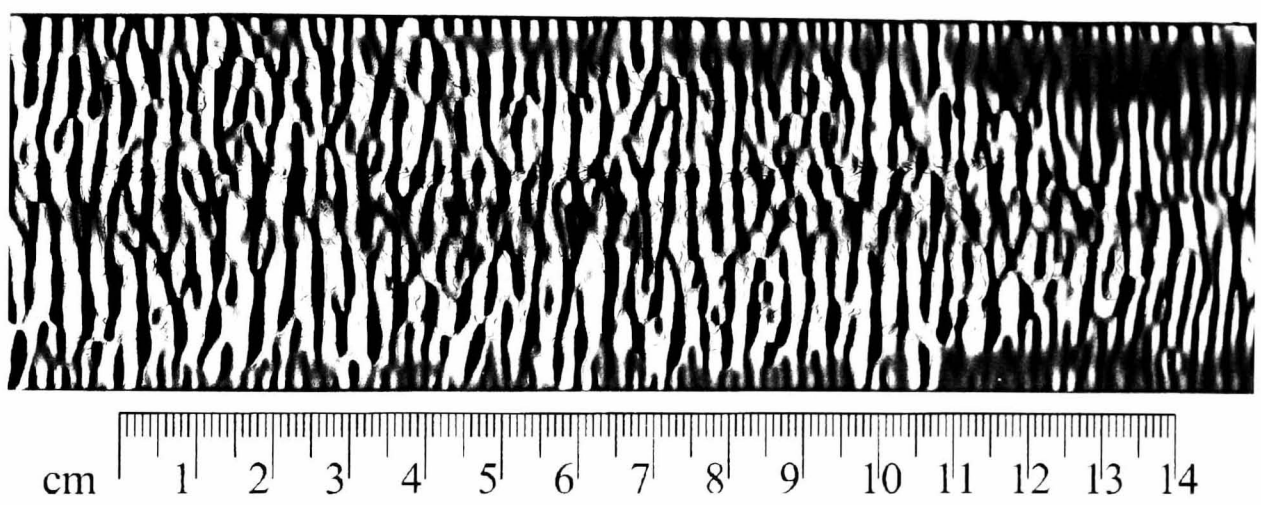

Figure 2.80: Disturbances from transporting a sample through a dryer at 6m/m

Subsequent trials using three different pilot air impingement dryers have indicated that the patterns generated on the surface of a coating when transported continuously but slowly beneath an array of air impingement nozzles are in fact very similar to those seen in Figure 2.78. The linear dryers were of different designs, one being that installed on ILFORD Imaging's pilot line, another being an experimental air flotation dryer and the third a pilot line in the workshops of Dec-E-Tech – MA - USA - incorporating the dryer nozzle type patented by Petros [1988]. This latter design introduces vortex generating slots in between adjacent air impingement nozzles. The aim is to dissipate the energy associated with the impinging air in such a way as to more effectively break up the moisture laden boundary layer carried by the moving web. Figure 2.80 depicts the resulting disturbances when subjecting a single layer

coating comprising PVOH and magenta dye to the Dec-E-Tech pilot dryer. The viscosity of the coating solution was 257 mPa.s when measured at the temperature corresponding to the point of entering the dryer and the wet thickness was 100μm. The air speed was ramped up from 22 m/s to 70 m/s over the 26 second exposure time resulting from the sample traversing the 2.6 metre length of dryer at 6 m/min.

The importance of ensuring that the web is continuously being transported through the dryer in the same direction is demonstrated in Figure 2.81. Here the sample was stopped under the dryer thereby allowing the fluid to gather into bands spaced at the nozzle pitch. Too high a web speed, on the other hand, gives insufficient time to achieve realistic exposure to the air owing to the finite length of the dryer. The optimum web speed is studied in Section 4.4.2 in detail on determining the time required for waves to become established and giving some consideration to the velocity profile beneath each nozzle.

Achieving steady web motion at these very low speeds presented a major challenge. The modified system incorporating the rubber tracking wheel described in 2.5.2.6 unfortunately became unstable at speeds less than 20 m/min resulting in variations of the order of ± 5%. This in turn led to variations in coating thickness of the same order of magnitude. Operating the machine totally manually was prohibited due to the need to accurately control the air pressure at the dryer. The problem was resolved by inhibiting feedback from the follower roller and operating the web control system in open loop mode using a variable DC power supply and correcting speed drift using a suitable shunting resistor. This enabled the speed to be reproducibly controlled to better than ± 1% after reoptimising web tensions before and after the coating roller and imposing a lower limit to the diameter of the stock roll.

Visualising the disturbances in the restricted space between the web and nozzles was also challenging. Work in this field has either focused on quantifying waves in the vicinity of a single jet or along the lower surface of a wind tunnel. In the former case, Gosset and Buchlin [2003] have investigated methods for imaging disturbances by both reflected and transmitted light. Imaging by reflection using a high speed camera capable of recording at 500 frames per second, although incapable of profiling the local film thickness, nevertheless enabled the predominant wavelength and wave

speed to be determined. They found the wave speed to equate to the web speed for the range 120 to 400 mm /second. They found the type of laser triangulation device reported by Ikin [2001(2)] to be also useful for profiling the surface waves and report the development of a technique based on the absorption of transmitted light by adding a purple dye to the coating solution and using a green filter at the camera to enhance contrast. Wind tunnel experiments have also used the light absorption technique – Özgen et al. [2002]. Craik [1966] imaged the shadows caused by surface waves cast on a white paper sheet placed beneath the plexiglass tunnel floor when illuminated at glancing incidence using a small spot light mounted at one end of the channel.

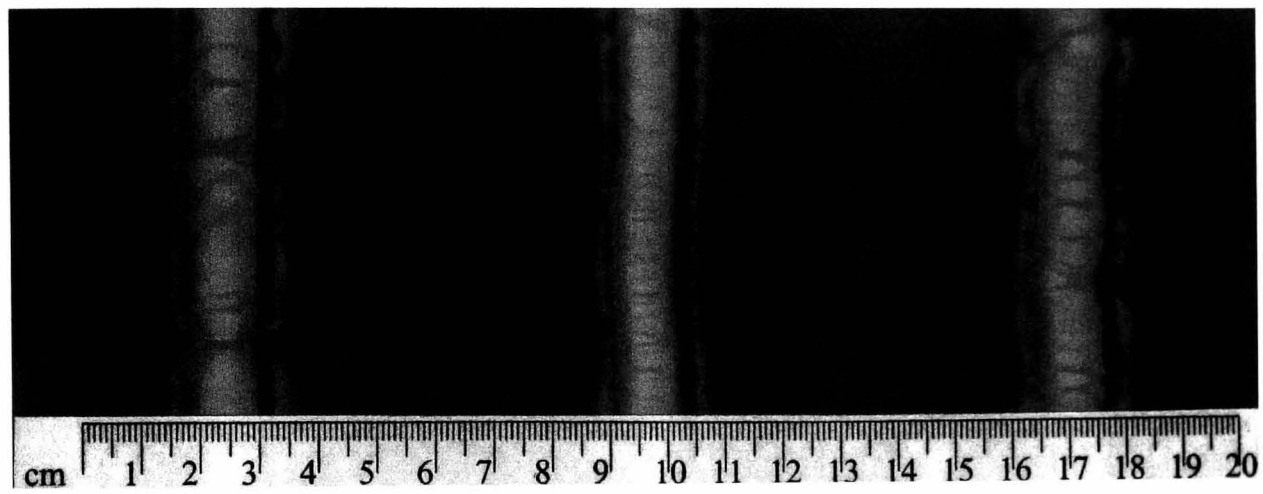

Figure 2.81: Dryer bands

The two methods developed for this work were essentially an extension of the light absorption technique reported by Gosset and Buchlin [2003]. The first technique enabled the disturbances to be imaged from the instant when the sample was initially subjected to the air flow to a point beneath the dryer where the surface waves had become well established. The second method was used for profiling the waveforms as the sample traversed a fixed point beneath the dryer.

2.14.3.1 Method for Recording the Build-up of the Waves

A Cohu model 4912 camera was mounted on a carriage free to move along rails pre-aligned with the machine direction – Figures 2.82 and 2.83.

The associated zoom lens was adjusted to achieve a field of view of 60 mm. The carriage was powered by a capstan driven by a DC motor using woven nylon cord –

pulling against an opposing force provided by a counter-weight – Figure 2.83. The carriage speed control was calibrated to enable the camera to move at the same speed as the web – namely 7 m/min. The first two nozzles in the linear array were blocked off to ensure the camera captured the true start of drying as it traversed the dryer. The web was of transparent film base and pre-marked with a line drawn cross-width to act as reference for checking phase shifts in the waveform as the sample progressed through the dryer. The lower outward surfaces of the jet box were rendered matt white to achieve adequate image brightness when reflecting light from a fluorescent tube back through the coated web – Figure 2.82.

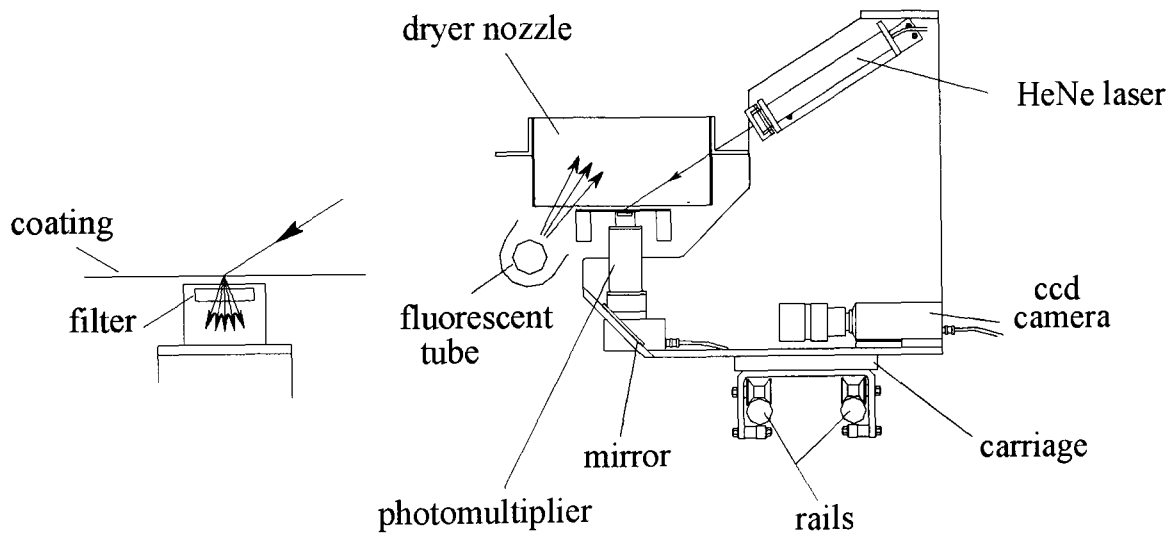

Figure 2.82: Installation for recording surface waves viewed in the machine direction

The web was supported at the edges on flat horizontal metal rails and by narrow cross-members placed at intervals of about 0.3 metres. The purpose of the latter was to prevent the web sagging downwards into the void between the rails under the action of the impinging air.

The coating solution used for the study contained a green dye. A magenta filter was installed at the camera aperture to enhance contrast. Lambert's law states that equal paths in the same absorbing medium absorb equal fractions of the light entering them – Longhurst [1960]. Hence, for an elementary path of length dx, the intensity is increased from I to I + dI where:

$$\frac{dI}{I} = -k.dx \qquad (2.71)$$

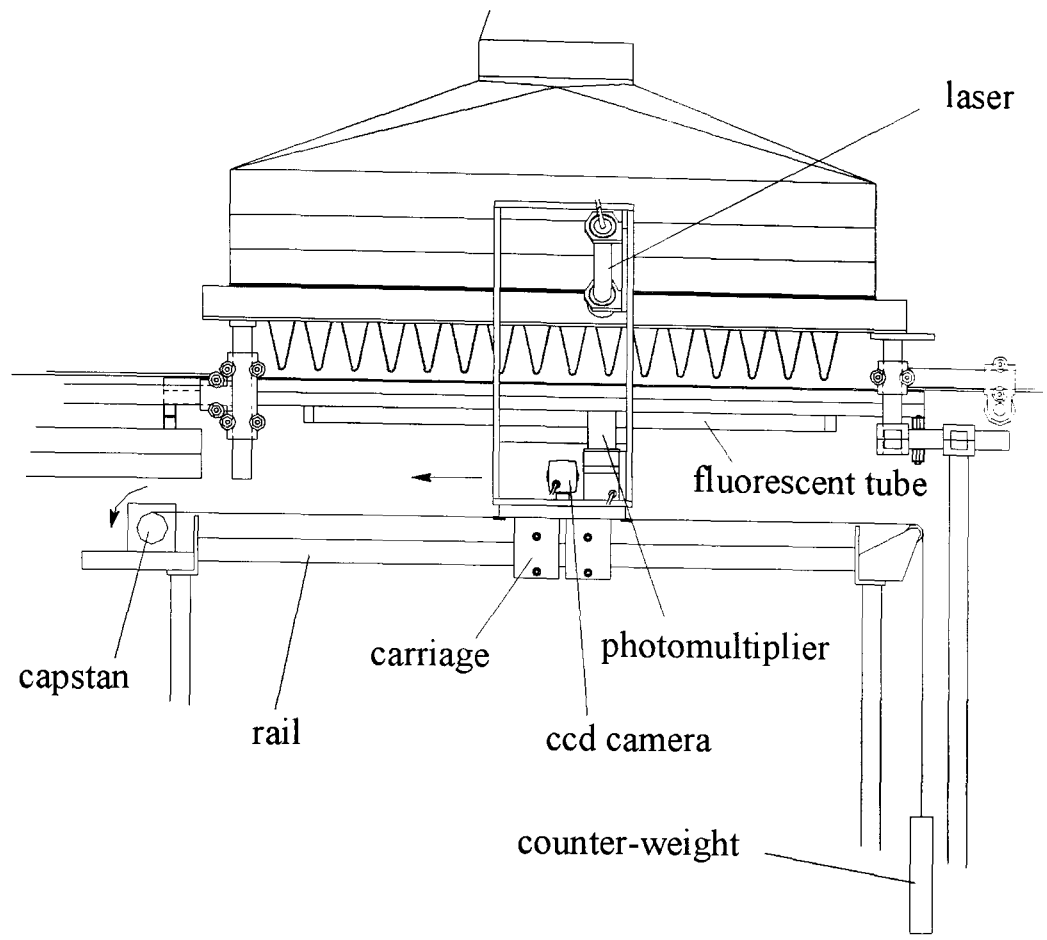

Figure 2.83: Side view of the installation for recording surface waves

where k is the absorption coefficient. Integrating:

$$\ln(I) = -k.x + C \qquad (2.72)$$

where C is a constant. The log intensity distribution across the recorded image in a direction parallel to the web motion thus yields the thickness profile. This was readily determined using the OPTIMAS software described in Section 2.7.2. Unwanted slowly varying density components were removed by computing the fast fourier transform using Mathcad, discarding all frequencies below a threshold frequency and transforming back to the space domain by determining the inverse fast fourier transform. The results of this analysis are given in Section 4.4.2.

2.14.3.2 Method for Profiling Film Thickness at a fixed point beneath the Dryer

Web flutter, although limited by the edge rails, was such as to preclude the use of the laser triangulation method – Ikin [2001(2)] and Gosset and Buchlin [2003]. The light absorption method was therefore selected as optimum for this work. A light source comprising a HeNe laser operating at 2mW and emitting a wavelength of 633 nm was mounted on the same carriage as used for recording wave build-up – Figures 2.82 and

2.83. The beam was directed at an inclined angle to enter midway between any pair of adjacent nozzles and well away from either support rail. The mechanics was arranged to allow the carriage to be clamped at ten fixed positions to enable further measurement of wave development as the sample moved down the dryer. Cost considerations dictated the use of paper web instead of the film base used in the previous study. The increased opacity of the web necessitated the development of a highly sensitive densitometer system. A green absorbing dye was again used to gain sensitivity to wet thickness variations. Light transmitted through the coating and paper web was collected over a semi-cone angle of about 45° by the photocathode of a sensitive photomultiplier also mounted on the carriage. An interference filter transmitting a narrow band centred about the HeNe emission wavelength was mounted over the receiver aperture to minimise effects due to ambient light.

A DC offset amplifier circuit was designed and constructed – Figure 2.84 – to gain sensitivity to subtle variations in transmitted light while ensuring that the output signal remained within the input range acceptable to the Thurlby Digital Storage Adaptor used for recording waveforms. (This latter system and associated oscilloscope was as described in Section 2.8.2.2.)

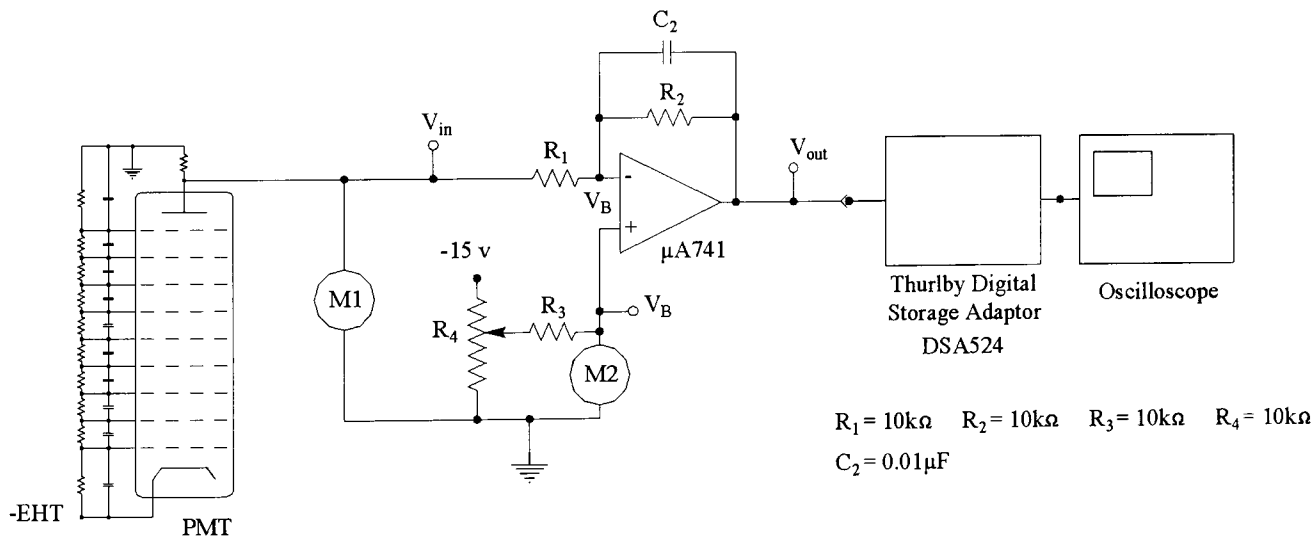

Figure 2.84: DC Offset Amplifier used in Densitometer

The EHT voltage was set to achieve a –5 volt signal at M1 with uncoated web present under the dryer. On establishing coating at a given wet thickness, the sample was stopped at the densitometer head and the DC offset control potentiometer R_4 adjusted to achieve a null to within 5 mV at the oscilloscope display and the bias voltage V_B at

meter M2 noted. The equilibrium (DC) voltage V_{out} at the output of the operational amplifier is given in terms of input voltage V_{in} and bias voltage V_B by the well known expression (de Waard and Lazarus [1966]):

$$V_{in} - V_B = V_B - V_{out} \tag{2.73}$$

giving:

$$V_{in} = 2V_B - V_{out} \tag{2.74}$$

The intensity I of light transmitted by the coating is given by:

$$I = AV_{in} \tag{2.75}$$

where A is a constant dependent on the gain of the PMT (photomultiplier tube). Hence, using (2.72), the thickness of the coating x is related to the PMT response V_{in} by:

$$-k.x + C = \ln(I) = \ln(A) + \ln(V_{in}) \tag{2.76}$$

and taking $V_{in} = V_{in}(0)$ for uncoated base,

$$C = \ln(A) + \ln(V_{in}(0)) \tag{2.77}$$

the final expression for x is obtained from:

$$-k.x = \ln(V_{in}/V_{in}(0)) \tag{2.78}$$

Hence, plotting x versus $\ln(V_{in})$ for a range of coating thicknesses enables the determination of k, from which it is readily possible to interpret the densitometer response to air induced disturbances directly in terms of percentage change in coating thickness. Signals were subjected to a form of digital filtering using Mathcad. A windowing function was first applied to 1024 consecutive coating thickness assessments in order to remove end effects. The fast fourier transform was then computed to determine the predominant spatial wavelengths. These were isolated by multiplying the spectral information with a suitable pass-band filter and the inverse transform taken to transfer the information back into the space domain to yield a final assessment of rms amplitude made for comparison purposes (Schweizer [1997(1)]). Results and consequent conclusions for a series of trials aimed at studying the influence of air speed, viscosity and wet thickness on the wavelength and amplitude of the surface waves are presented in Section 4.4.3.

2.14.4 The Measurement of the Heat Transfer Coefficient

This part of the work addressed three basic requirements:

1. To determine how the drying rate is related to the maximum air velocity for tolerable surface waves for a given nozzle-to-web gap and temperature of the impinging air
2. To profile the air flow beneath the array of impingement nozzles – measured at the web plane
3. To provide an apparatus that could be readily ported to a range of experimental and industrial dryers of interest to ILFORD Imaging UK Limited and the University of Leeds

The method essentially followed that reported by Bria and Quass [1997] and later adapted by Noakes et al. [2002(2)] when determining the heat transfer characteristics of an experimental air flotation dryer. Refinements included the use of a smaller heat flux sensor to enable improved resolution of the heat transfer profile in the web plane and a technique for measuring the thermal conductivity of the heat flux sensor.

The system developed for this study was as shown in Figure 2.85. The heat flux sensor was a solid state heat pump CP1.0-7-06L manufactured by MELCOR and supplied by Radio Spares as stock number R/S 229-9549. This is a semi-conductor thermoelectric device utilising the Peltier effect.

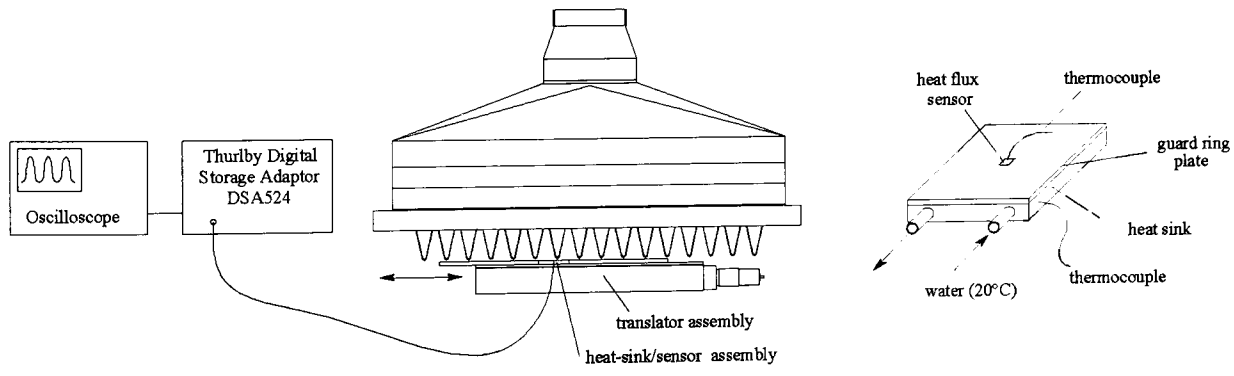

Figure 2.85: Heat transfer coefficient apparatus when mounted under a dryer

When subjected to a source of heat, the applied temperature gradient between the ceramic face plates of the sensor generates a small voltage. The dimensions of the face plates were 8mm x 8 mm and the thickness of the device 3.6 mm. The Thurlby Digital Storage Adaptor and associated oscilloscope described in Section 2.8.2.2 served to

display and store the output signals from the device. The sensor was bonded to a heat sink – Figures 2.85 and 2.86. The heat sink was cooled by water flowing at about 1 litre/min. and controlled to 20°C.

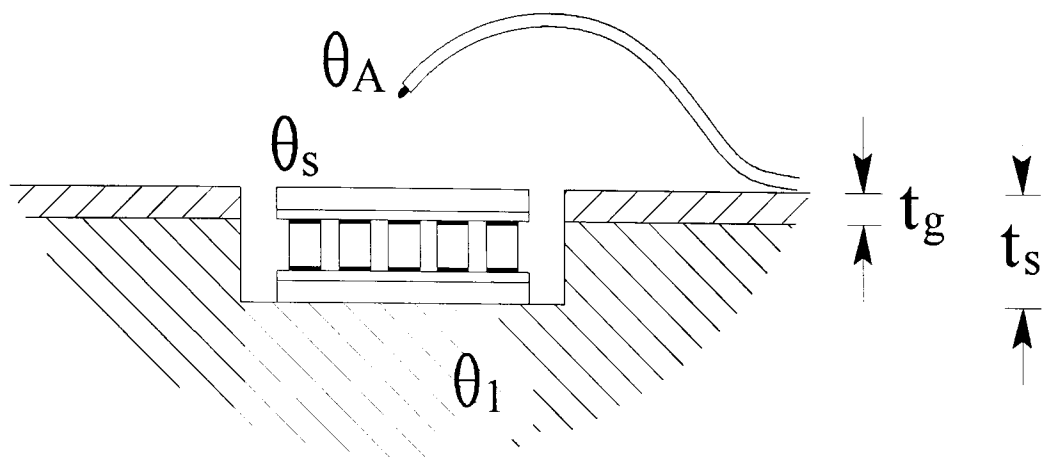

Figure 2.86: Heat flux sensor and guard ring

A translating table was designed and built to enable the sensor assembly to be transported at constant speed beneath the nozzles. The span was such as to cover typically three nozzle pitches. The traverse speed was reduced by trial and error until the ensuing response had achieved at least 95% of the estimated peak signal and finally set at 0.87 mm/s. A guard ring plate of external dimensions 100 mm x 100 mm was constructed to ensure the heat transfer per unit area through the plate matched that through the sensor as closely as possible to minimise edge effect errors – Noakes et al. [2002(2)]. This was accomplished by ensuring the thermal conductivity k_g of the guard ring and its thickness t_g were related to the thermal conductivity k_s of the sensor and the sensor thickness t_s by the relation:

$$\frac{k_g}{t_g} = \frac{k_s}{t_s} \tag{2.79}$$

Polycarbonate of thickness 1 mm well suited this requirement when taking into account the values of k_s and t_s cited by the manufacturers of the sensor. The depth of the well ($t_s - t_g$) was machined into the heat sink to ensure the upper surfaces of the sensor and guard ring were coplanar.

The sensor was calibrated using the method of Noakes et al. [2002(2)] in which an electrical heater matt also of dimensions 100 mm x 100 mm was suspended just above the heat sink. The complete assembly was thermally insulated from the environment using polystyrene foam blocks and the sensor voltage determined as a function of the product of heater current and applied voltage.

Having calibrated the sensor, it was then necessary to obtain an accurate value for k_s rather than rely on data supplied by the manufacturers. This was achieved by machining a conical cup having a base of cross-section exactly matching that of the sensor – Figure 2.87. Warm water of temperature θ_w acted as heat source and cold water of temperature θ_3 acted as heat sink. A value for k_s was determined from the expression:

$$k_s = \frac{Q_k t_s}{A_s(\theta_w - \theta_3)} \tag{2.80}$$

where Q_k was the heat transfer rate determined from the heat sensor calibration.

To determine the heat transfer coefficient of the dryer, the bulk temperature θ_A of the air impinging onto the sensor assembly when under the dryer was measured using a thermocouple mounted 3 mm above the sensor – Figure 2.86. The heat transfer coefficient h is defined (Cohen and Gutoff [1992]) by the expression:

$$Q_h = h.A_s(\theta_A - \theta_s) \tag{2.81}$$

where Q_h is the rate of heat transfer through a surface area A held at temperature θ_s. In practice, it was found difficult to measure θ_s with sufficient precision and the temperature θ_1 of the heat sink was determined instead using a thermocouple – Figure 2.85. In this case, the heat transferred through the sensor is given by:

$$Q_h = k_s.A_s\frac{(\theta_s - \theta_1)}{t_s} \tag{2.82}$$

and hence:

$$\theta_s = \frac{Q_h t_s}{k_s A_s} + \theta_1 \tag{2.83}$$

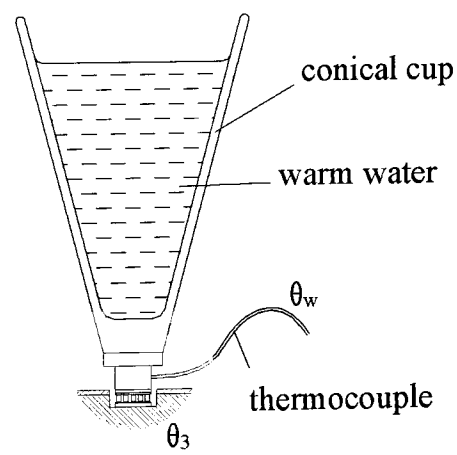

Figure 2.87: Method for determining the thermal conductivity of the sensor

and from (2.81):

$$h = \frac{Q_h}{A_s\left(\theta_A - \frac{Q_h t_s}{k_s A_s} - \theta_1\right)} \tag{2.84}$$

2.15 Summary

The work involved in setting up the experimental methods formed a substantial part of this thesis and may be summarised as falling into the following broad categories:

1. The exploitation of existing equipment and well established methods to full advantage
2. The development of existing equipment to enable the extension of studies to more demanding limits
3. The development of specialised equipment for studying basic mechanisms affecting the coating and drying of multilayer assemblies

1. <u>The exploitation of existing equipment</u>

- Rheometers owned by HARMAN technology Limited and the University of Leeds have been used for characterising the rheology of coating solutions. The choice of rheometer is dependent on an estimate of the maximum shear rate applicable to the flow region being studied. The choice of rheological model is also important. The Carreau model appears most suitable for characterising gelatin based solutions whereas the Sisko model is best suited to those of high solids content.

- Static surface tension, albeit of limited usefulness, is readily determined using existing equipment and well established methods.

- Dynamic surface tension is determined using a Wilhelmy plate on an inclined plane specially built by ILFORD Imaging UK Limited prior to the commencement of this project. A four parameter model suggested by Tricot [1997] is used to characterise DST for solutions of interest.

- The surface roughness of substrates is conveniently measured using a Wyko white light interferometer owned by the University of Leeds. Consideration is given to the choice of statistical parameter when correlating roughness with coating performance.

- The surface energy of the substrate is measured by determining the contact angle for one or more liquids. Consideration is given to the application of the method of Owens and Wendt [1969] as most appropriate when correlating surface energy with coating performance – as claimed by Blake and Morley [1997].

- A needle coater built for use on the pilot coating machine has been used for determining how dynamic contact angle may relate to the coatability of ultra-smooth substrates.

- The facilities originally available at HARMAN technology's site at Mobberley enabled some limited work on determining coating windows and provided a vital base for developing the specialised techniques necessary for visualising flows. A laser based inspection system has proved to be invaluable for identifying the onset of ribbing and air entrainment when running coating window trials. The in-built system mechanising the opening up of the coating gap during the passage of inter-roll joins has provided important insight into limitations affecting a typical production process. A rotary dryer has been exploited to establish the mechanism responsible for surface defects when a wet coating becomes exposed to excess air during the initial stages of drying.

2. The development of existing equipment

- Extensive work has been carried out as part of this study to further develop the pilot facilities within HARMAN technology Limited. Significant improvements have been made to the control of the temperature and hence the viscosity of the coating solutions. An additional scrape-off system has been installed to allow continuous coating at speeds up to 200 m/min. The systems for controlling and measuring surface charge have been modified to enable the study of the dynamic response of the coating bead to varying polar electrical charge carried by the substrate.

- Substantial assistance has been given over many months to a team of engineers responsible for improving the reliability of the pilot coating machine – especially when operating at speeds in excess of 100 m/min.

3. The development of specialist equipment

- A simple needle applicator has been constructed for recording the rate of transfer of an aqueous ink into the surfaces of small porous substrate samples when considering the effect of porosity on coating performance.

- An off-line cascade with extended slide has been designed and built using transparent Perspex to enable unobstructed visualisation of flows as layers merge at the exit slots and proceed to move down the inclined plane.

- A special solution supply system capable of delivering a highly uniform flow rate has been developed for use when quantifying slide waves.

- Novel methods have been developed for visualising and recording:

  i. The interface and free surface at the bottom slot exit used for delivering a carrier layer

  ii. Slide wave disturbances at both the interface and free surface for two layer flows

iii. The lower free surface within the bead forming zone by viewing through the gap thus enabling the study of the influence of surface charge and surface roughness when coating opaque paper substrates

iv. Air induced disturbances to the wet coating during the early stages of drying using both the rotary dryer and the linear array of air impingement nozzles

- A method has also been specially set up for monitoring the upper free surface within the bead forming zone without compromising the rapid deployment of the equipment designed to monitor the lower meniscus.
- Apparatus has been designed and built based on the method used by Noakes et al. [2002(2)] and exploited to enable the heat transfer coefficient of HARMAN technology's experimental linear air impingement dryer and other dryers to be determined as a function of air speed, air temperature and nozzle-to-web gap.

Chapter III

Substrate Effects in Slide Coating

3.1 Introduction

The role played by the substrate in determining the coating window has received only scant attention outside of industry. It is often tacitly assumed that the wetting performance is largely dictated by the properties of the fluid used for coating an industrial product – or in the case of a multilayer coating system, the properties of the solution forming the lowermost layer.

The effects of the surface properties of the substrate on yield and coating quality are also poorly understood within industry. Investigative work is largely pragmatic and undocumented – other than what can be gleaned through the patent literature – ref. – Section 1. Specifications agreed between coating industry and the base suppliers for controlling the surface topography, for example, are mainly dictated by marketing considerations concerning cosmetic issues and the end-user performance. The coating technologist generally has little choice other than resorting to expensive and time consuming coating trials to optimise the process to ensure that ever increasing demands for high quality as well as high yield can be met.

In this chapter, preliminary experiments are described which serve to highlight these issues by exploiting the experimental techniques described in Chapter 2. The benefits as well as the limitations of using a carrier layer are studied for examples outside of the conditions cited in the patent literature – for example, Dittman and Rozzi [1977], Choinski [1978], Ishizuka [1989(1)] and Ishizuka [1989(2)].

The surface properties considered are surface energy, roughness, surface electric charge and porosity. In Section 3.2, the coating window and bead profiles for typical smooth uncharged webs are presented as a base from which comparison can be made when considering these effects.

A review of what little is published on the effect of surface roughness is given in Section 2.3.1 – see for example Buonopane et al. [1986], Hartman et al. [1989], Suga et al. [1993] and Clarke [2002]. Consideration is given in Section 3.3 to the effect of surface energy as determined by the chemistry of the surface prior to proceeding to Section 3.4, which shows some experimental results depicting how increasing roughness can be detrimental to slide bead coating and how the use of a thin low viscosity carrier layer can be beneficial under certain conditions.

The traditionally accepted criteria for a carrier layer (Dittman and Rozzi [1977], Choinski [1978], Ishizuka [1989(1)] and Ishizuka [1989(2)]) are shown in Section 3.4 to fail when attempting to coat some of the commercially available precoated paper webs presenting a rough texture. The effects of increasing the slide inclination angle following the suggestions of Burket et al. [1984] are examined in detail. The concept of what can be truly defined as an optimum carrier layer is then reviewed as taking into account the coating of a rough substrate.

Results are shown in Sections 3.5 and 3.6 which demonstrate how the presence of free charge can be detrimental to slide bead coating whereas re-orientating bound polar charges present in the surface of the web can assist coating (Vandaele and Vancoppenolle [1999]). Bead profiles are shown which give hitherto unpublished evidence of how charge assisted coating can moreover be exploited to gain higher robustness against coating streaks (Ikin et al. [1997]).

The final section 3.7 presents case studies, which serve to illustrate the benefits and limitations of a carrier layer where the substrate is porous.

3.2 The Coating of Ultra-Smooth Substrates

3.2.1 The Coating Window for a Typical Smooth Photo-Paper Substrate

A formulation was selected for this first case study that was known to present difficulties when attempting to coat a substrate of rougher texture. Although generally

coated as three separate layers, the differences in composition of the layers were very small and can for the purposes of this study be neglected. The formulation – here designated G-C mix #1 – comprised a mixture of gelatin and cellulose of viscosity 44 mPa.s when measured at a shear rate of 100 s^{-1} using the Ferranti viscometer described in Section 2.2.1.5. Measurements with a Bohlin CVO rheometer as also described in Section 2.2.1.5 show the coating solution to be mildly shear thinning – see Figure 3.1.

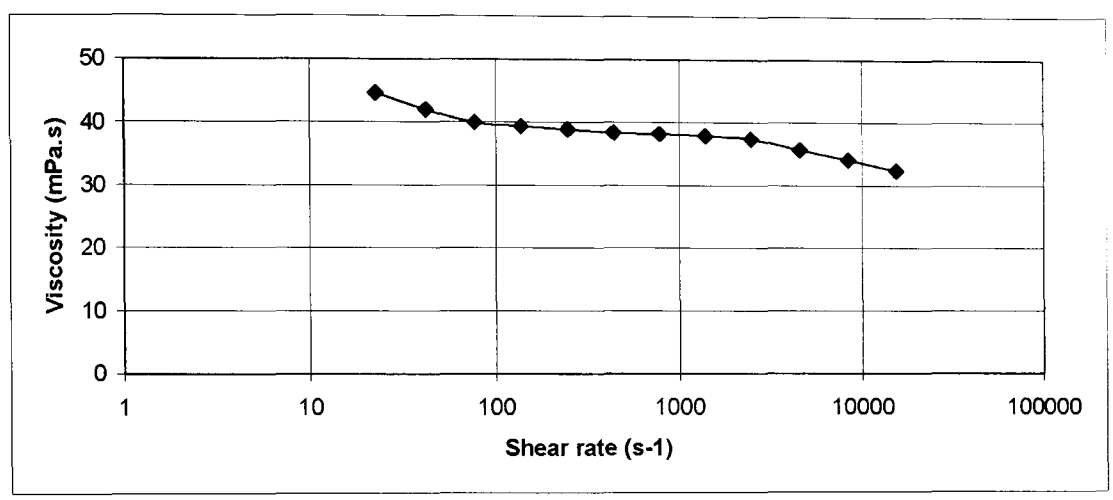

Figure 3.1: Rheology of G-C Mix #1 Coating Solution

For shear rates < 767 s^{-1}, the data best fit the Sisko model given by:

$$\mu = \mu_\infty + k(1/\dot{\gamma})^m \tag{3.1}$$

where μ is the viscosity in mPa.s, $\dot{\gamma}$ is the shear rate in s^{-1}, $\mu_\infty = 37.7$ mPa.s, $k = 80$ and $m = 0.80$. (See Section 2.2.1.6 for model)

For shear rates > 767 s^{-1}, the Carreau model with μ_∞ set to zero best applies. In this case, the viscosity μ is given from (2.13) by:

$$\mu = \frac{\mu_0}{[1 + (\lambda\dot{\gamma})^2]^{(1-n)/2}} \tag{3.2}$$

where $\mu_0 = 38.3$ mPa.s , $\lambda = 4.0 \times 10^{-4}$ s and $n = 0.905$.

The dynamic surface tension characteristics of the coating solution were determined using the inclined plane equipment and method described in section 2.2.3. The data are shown in Figure 3.2 and were hand fitted to a four parameter equation:

$$\sigma = \sigma_M + \frac{\sigma_0 - \sigma_M}{1 + (t/t^*)^n} \tag{3.3}$$

where σ is the surface tension in $mN.m^{-1}$, $\sigma_M = 38\ mNm^{-1}$, $\sigma_0 = 56\ mNm^{-1}$, $t^* = 1.125$ s and $n = 1.482$.

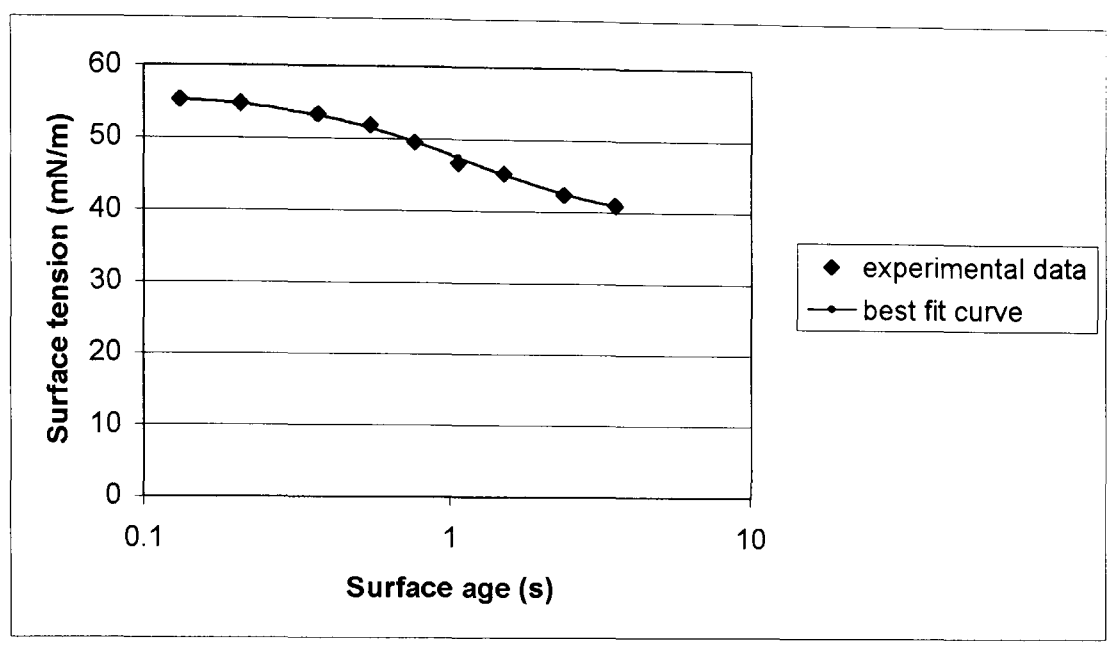

Figure 3.2: Dynamic Surface Tension Characteristics for G/C Mix #1 Coating Solution

These parameters can be used for assigning surface tension as a function of surface age when setting up a computational model designed for studying this flow in future work. Near the slot exit, the surface age will be of the order of 0.1 s. In this case study, the surface age on the free surface near the end of the slide but prior to acceleration due to viscous drag forces varies over the range 0.6 to 1.4 seconds for the coating speeds studied. Hence the surface tension on the free surface is of the order of 55 $mN.m^{-1}$ near the slot exit and falls to 48±3 $mN.m^{-1}$ towards the end of the slide – the value depending on flow rate and hence coating speed. Steep gradients in surface concentration and hence surface tension occur on the upper meniscus due to the acceleration in flow – Schunk [1989]. The acceleration along the lower meniscus is such that the age the freshly formed surface will reach is typically only a fraction of a millisecond – Tricot [1997]

Figure 3.3 shows the overall coating performance when attempting to lay down a wet thickness of 96.5 μm on ultra-smooth (glossy) polyethylene coated photo-paper base.

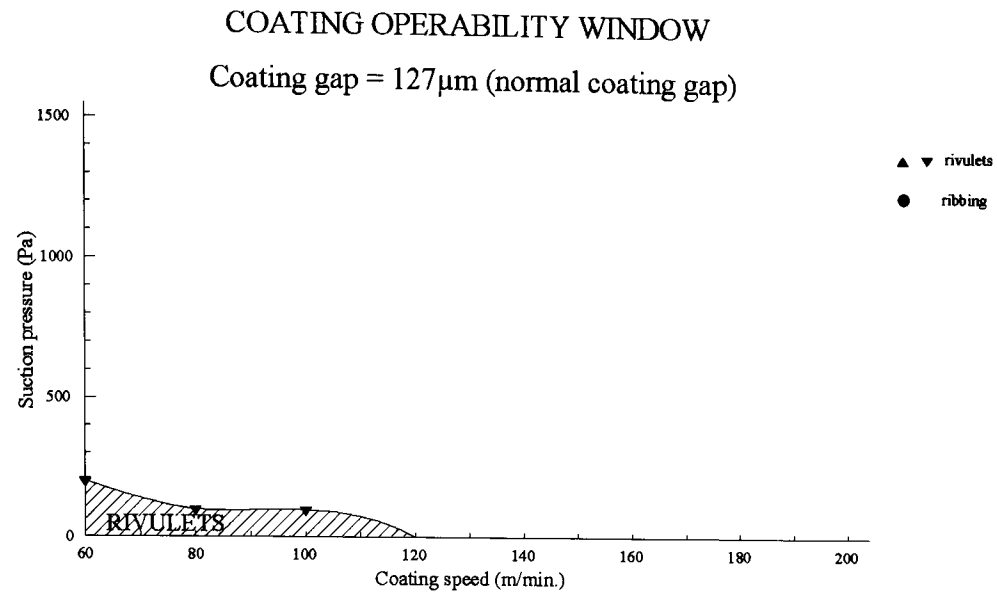

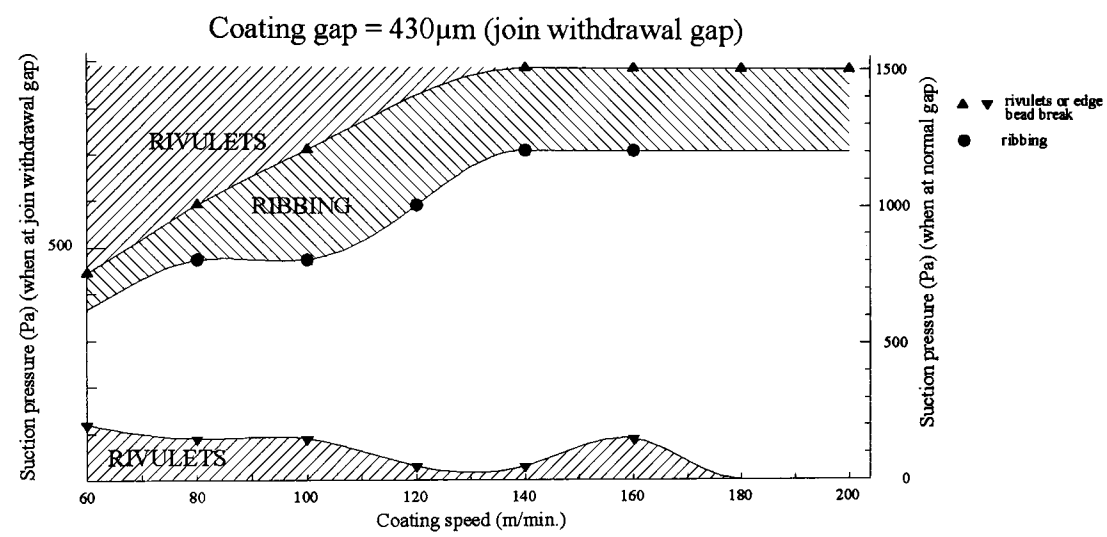

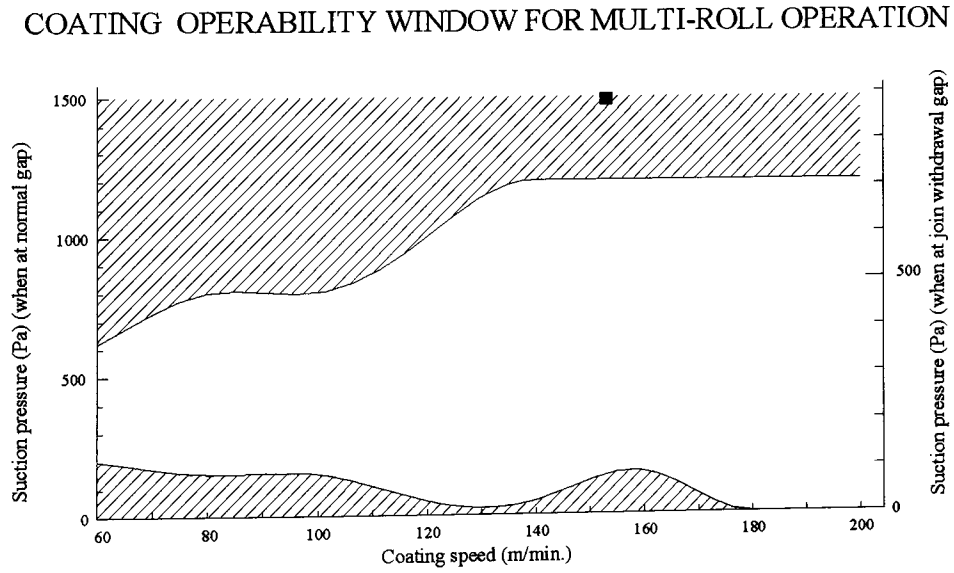

Figure 3.3: Coating Operability Windows for G-C Mix # 1 coated on RC Glossy Base

Here, the base was provided by the suppliers without a gelatin "subbing" pre-coated layer and was subjected to on-line corona treatment as described in Section 2.5.1.2. Two coating windows are presented, one corresponding to normal coating conditions where the gap between the cascade applicator and the web was pre-set to 127 μm and the other where the gap was temporarily opened up to 430 μm to allow an inter-roll splice to pass unimpeded. Each window is a plot showing the minimum and maximum bead pressure differential dictating acceptable coating performance. In general, the lower limit relates to the onset of either bead break at the edges (Valentini et al. [1991] and Hens and Abbenyen [1997]) or sporadic outbreaks of air entrainment.

The purpose of the second window is to depict reliable operating conditions when coating multiple rolls. It is important, in this case, that the bead should remain stable as the gap is opened up to accommodate inter-roll splices as they traverse the coating roller. Due to the fact that the dryer is usually driven to full solvent removal capacity, any failure inevitably leads to under-drying of regions where the fluid has gathered into rivulets on the web – these being necessarily of higher local thickness than the mean value normally laid down. This in turn results in fouling of face-on rollers at the end of the dryer – as pointed out by Katagiri et al. [2003]. The coating operability window shown in the lowest plot on Figure 3.3 results from taking the lowest maximum and the highest minimum pressure differentials shown by the two coating windows corresponding to the narrow and wide coating gaps.

In this example, it will be evident that coating speeds well in excess of 200 m/min are readily achievable without unacceptable defects.

3.2.2 The Coating of Single Layers on Ultra-Smooth Film Base

Short trials were also run using ultra-smooth film base as substrate – this being inherently flatter than glossy photo-paper due to the absence of fibres making up the bulk. The exercise, being carried out in an industrial environment, was aimed at establishing the optimum solids concentration required for coating a single layer of specified coating weight. This approach is generally of greater interest to the coating technologist rather than generating limits based on separately varying the viscosity and

the wet laydown. The formulation chosen was an aqueous mixture of gelatin, cellulose, a small quantity of photo-emulsion added as scattering agent and finally surfactant. In varying the concentration, care was taken to ensure the surfactant concentration was maintained constant in order to minimise variations in dynamic surface tension properties.

It is generally found (Schweizer [1992]) – that the viscosity μ varies with solids concentration according to the expression:

$$\mu = A\, e^{Bc} \tag{3.4}$$

where c is the solution concentration by volume and A and B are constants. This indeed was found to be the case for the formulation used in this case study - as shown in Figure 3.4.

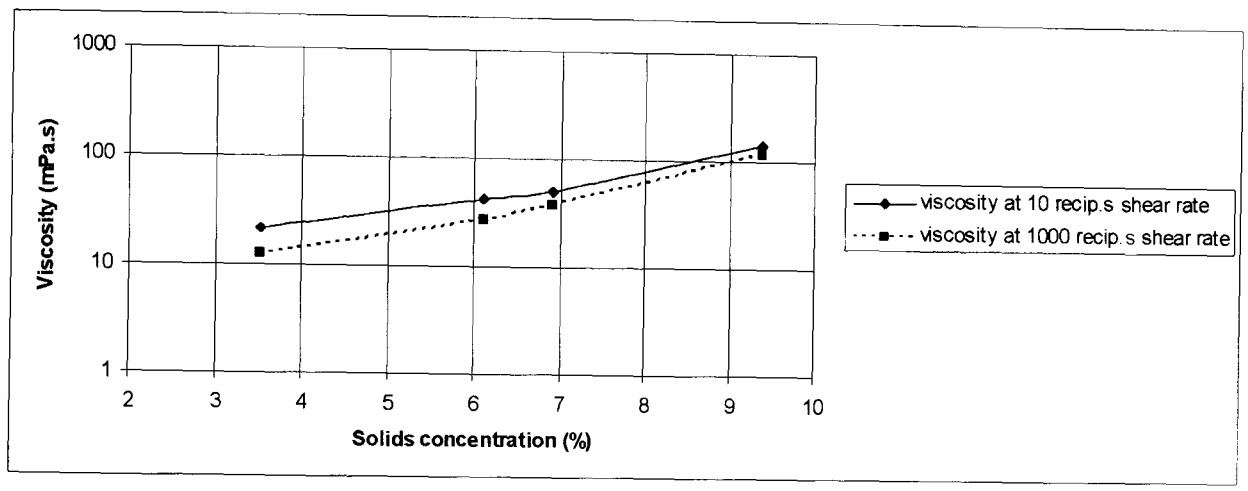

Figure 3.4: Relationship between Viscosity and Concentration

The viscosities at two shear rates and the densities of the four concentrations selected for this study are shown in Table 3.1. The dynamic surface tension characteristics shown in Figure 3.2 also apply to these solutions.

Solids Concentration (%)	Viscosity at 100 s^{-1} (mPa.s)	Viscosity at 10^4 s^{-1} (mPa.s)	Density ($kg.m^{-3}$)	Wet Laydown (μm)
3.53	12.3	11.8	1008.7	190
5.70	28.1	24.4	1013.8	117
8.15	71	55	1019.6	81.6
9.06	100	75	1021.7	73.2

Table 3.1: Properties of Four Fluids and Wet Laydowns

Figure 3.5 depicts the rheology of the four solutions from measurements using the Bohlin CVO rheometer. The data show fall-off with increasing shear rate similar to that seen with gelatin – see Section 2.2.1 and Figure 2.2 – but are also characterised by a rise in viscosity with falling shear rate at the lower end of the shear rate range. This is possibly attributable to the presence of the cellulose in the mixture.

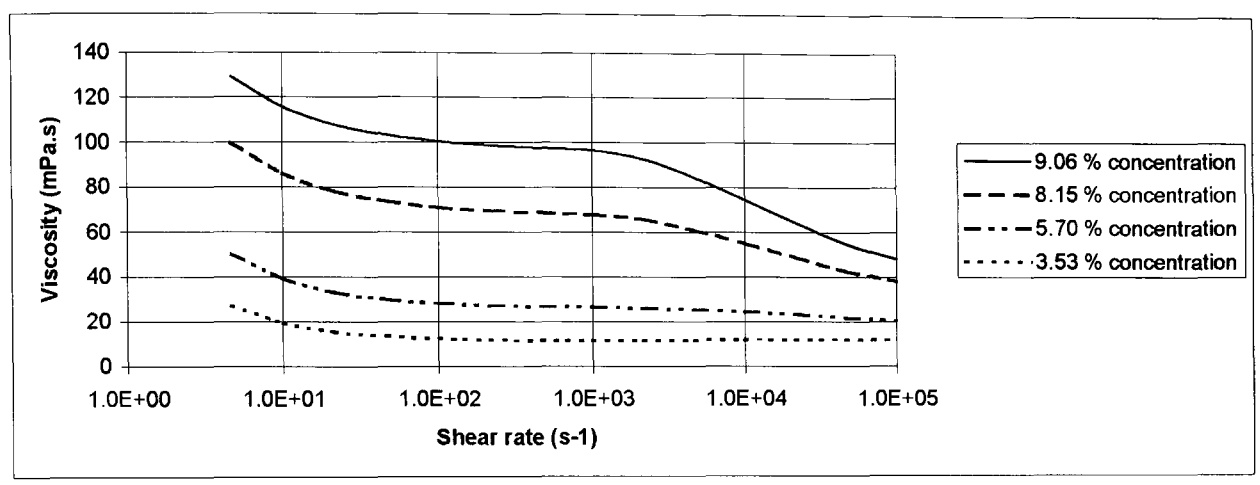

Figure 3.5: Rheology of the Four Solutions used in the Case Study

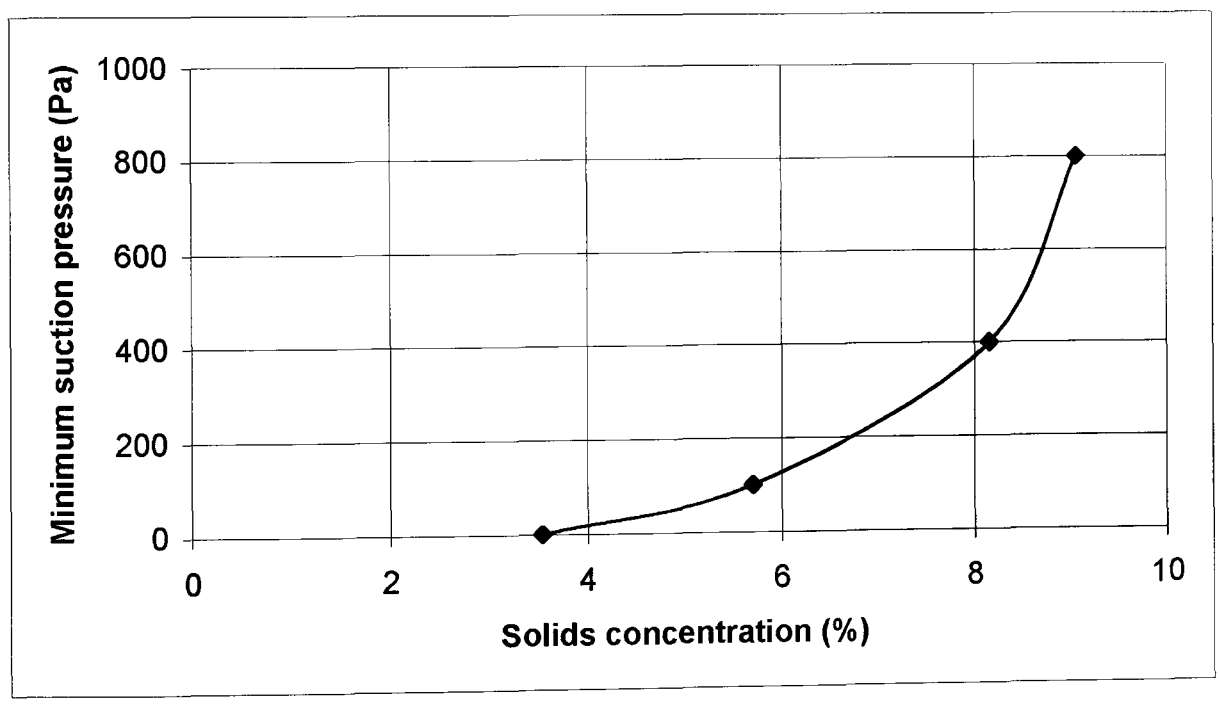

Figure 3.6: Minimum Stabilisation Suction Pressure required for Making the Bead

Figure 3.6 shows results on attempting to coat the four formulations at 100 m/minute using a coating gap of 125 μm. The suction pressure required to stabilise the bead against edge break or the formation of rivulets across the entire width of the web

increases rapidly on increasing the solids concentration, the upper limit being about 10 %.

It is of interest to compare the results of this study with those obtained by Garin and Vachagin [1972] (Cohen and Gutoff [1992]). They found, when studying the low flow limits of coatability for a slide coater used in an industrial process for manufacturing cine films, that the minimum wet laydown H_∞ for a web speed V, viscosity μ, surface tension σ, density ρ and coating gap H_G is given in terms of the suction pressure δP by the expression:

$$H_\infty > 2.19 \frac{\sigma^{0.25}}{\rho^{0.25} H_G{}^{0.25}} \frac{\mu V^{0.5}}{\delta P} \qquad \text{if} \frac{\delta P}{\rho V^2} < 3.32 \tag{3.5}$$

or

$$H_\infty > 2.00 \frac{\sigma^{0.1} \delta P^{0.3} \mu^{0.7}}{g^{1.25} \rho^{1.2} H_G{}^{1.05}} \qquad \text{if} \frac{\delta P}{\rho V^2} > 3.32 \tag{3.6}$$

When applying these criteria to this case study, the maximum value for $\frac{\delta P}{\rho V^2}$ is 0.341, so equation (3.5) applies.

Cohen and Gutoff [1992] point out that the limits dictating the maximum coating speed for a given coating thickness and those determining the lowest coating thickness at a given coating speed are in fact the same and known as the low flow limits of coatability. The mechanisms for these limits are recognised as being due to ribbing flows and edge bead failure (Tallmadge et al. [1979]) or air entrainment or breakdown of the coating to form dry patches interspersed with coated areas (Gutoff and Kendrick [1972]). It would seem plausible, by a similar argument, to suggest that the terms in equations (3.5) can be transferred to give expressions for minimum suction pressure:

$$\delta P > 2.19 \frac{\sigma^{0.25}}{\rho^{0.25} H_G{}^{0.25}} \frac{\mu V^{0.5}}{H_\infty} \tag{3.7}$$

On substituting the experimental values for μ, σ, V, H_G, ρ and H_∞ for the four concentrations used for the case study, the criteria of Garin and Vachagin would thus apparently predict a relationship between minimum suction pressure and concentration as shown in Figure 3.7. The shape of the curve is remarkably similar to that obtained in this study showing that it is indeed plausible to apply their criteria in this way. The

reason for the large differences in magnitude of the minimum suction pressure values obtained from the two sets of experiments is complex and affected by a number of possible factors. These include:

- Variations in the surface energy of the substrate – as highlighted in Section 3.3
- The effect of edge guide design on inhibiting edge bead break – see for example, Barstow [1966] and Ikin [2001(1)]
- The effect of the design of the suction box – see for example Yapel [1999]

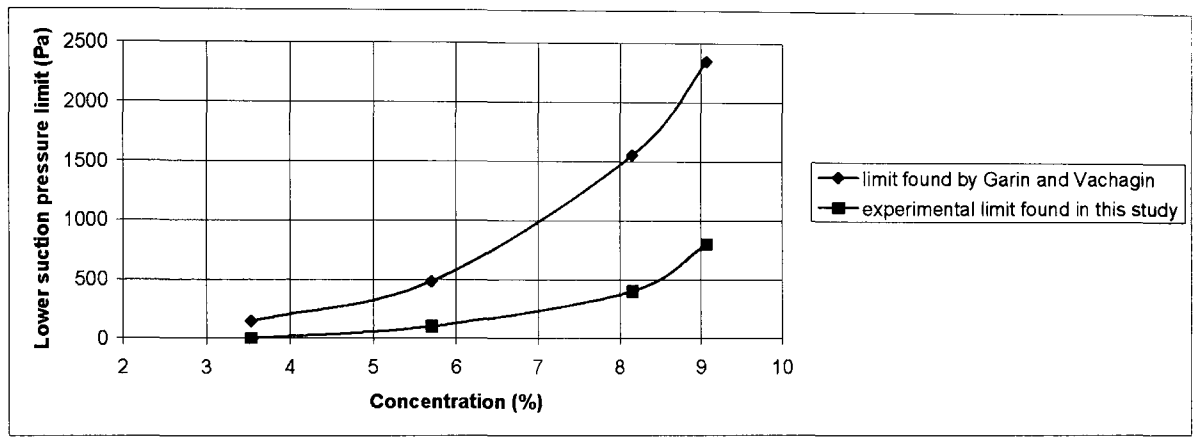

Figure 3.7: Comparison of Experimental Data with those of Garin and Vachagin

The bead was profiled for the four sets of conditions in order to gain further insight into the process for single layers. The upper free surface was determined in each case using the apparatus and method described in Section 2.13. The method for profiling the lower meniscus used an endoscope mounted within the confines of a hollow Perspex coating roller as shown in Figure 3.8. (This well-established technique (Ikin [1997]) was used rather than that described in Section 2.12 for two reasons. The first was to take advantage of the fact that the web was transparent and the second was to reduce unnecessary waste and cost incurred by the long run times associated with the use of the lower meniscus monitor.)

It will be seen from the bead profiles shown in Figure 3.9 that the swl (static wetting line) ascends to become locked to the upper corner of the cascade lip face as solids concentration is increased while operating the system near the lower limit for stabilisation suction.

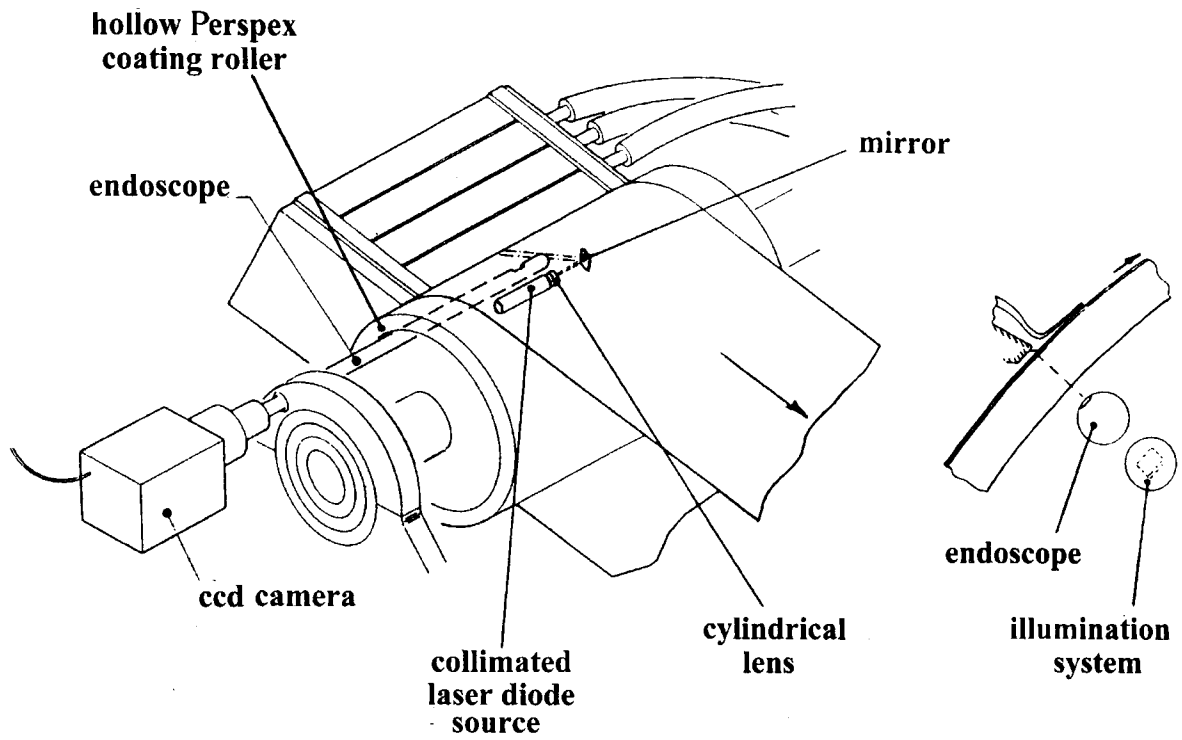

Figure 3.8: Apparatus used for Profiling the Lower Meniscus

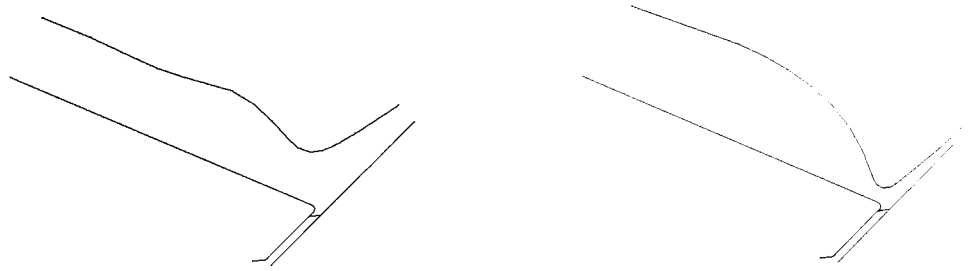

3.53 % solids content
189.6 µm wet laydown

5.70 % solids content
117.0 µm wet laydown

8.15 % solids content
81.6 µm wet laydown

9.06 % solids content
73.2 µm wet laydown

Figure 3.9: Bead Profiles for the Four Case Studies coated at 1.67 m/s

This is advantageous as then recirculations near the swl shrink to insignificance with a consequent lower risk of generating streaks (Noakes et al. [2002(1)].) It is also evident that the radius of curvature of the upper free surface near the bead forming zone decreases sharply as concentration is increased. The values are shown in Table 3.2.

Solids Concentration (%)	Radius of Curvature at Upper Free Surface (μm)
3.53	520
5.70	310
8.15	180
9.06	145

Table 3.2: Radius of Curvature of the Upper Free Surface for the Four Case Studies

Following Cohen and Gutoff [1992], the radius of curvature r is given in terms of the pressure drop ($P_0 - P_2$) shown in Figure 3.10 by the expression:

$$P_0 - P_2 = \frac{\sigma}{r} \tag{3.8}$$

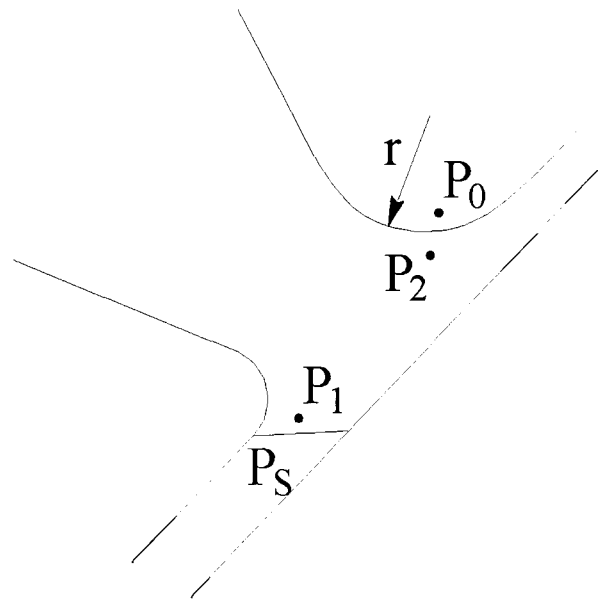

Figure 3.10: Pressure either side of the Upper and Lower Free Surfaces

In most practical situations applicable to industrial practice, the lower meniscus shows very little curvature (Cohen and Gutoff [1992] and Faust [1975]). The pressure P_1 just

within the fluid at the lower free surface is therefore close to that within the suction box. Hence, for a given momentum flux down the slide, increasing the stabilisation suction will increase the pressure drop (P_0-P_2) resulting in a decrease in the value of r. As pointed out by Cohen and Gutoff [1992], the pressure within the slide flow well upstream of the bead is close to ambient by reason of the low curvature of the upper free surface in this region. There is consequently a negative pressure gradient at the terminus of the slide which must be accompanied by an increase in resistance to flow in the form of a necking in of the liquid to form a bead waist H_W as shown in Figure 3.11.

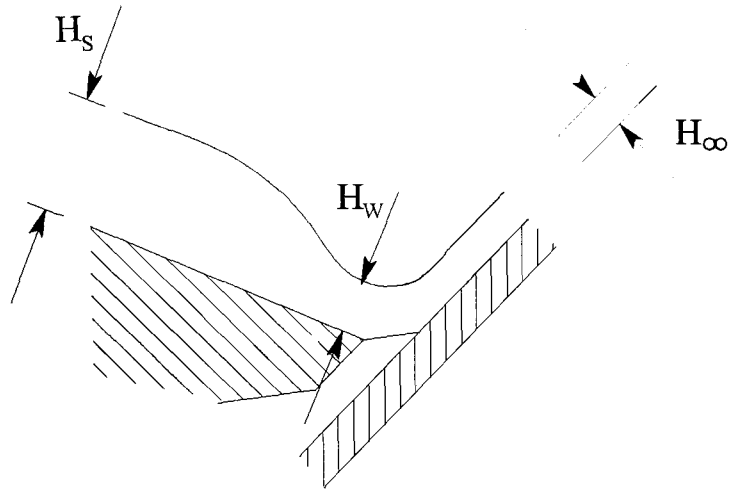

Figure 3.11: The formation of a Bead Waist H_W

Schweizer et al. [2003] showed that the propensity for ribbing flow increases as the ratio H_w/H_s decreases and that the data corresponding to the onset of ribbing conveniently falls on the master curve shown in Figure 3.12 relating the Weber number We to H_w/H_s – where We is defined by:

$$We = \frac{\rho H_\infty U^2}{\sigma} \tag{3.9}$$

H_∞ being the wet thickness and U the coating speed.

Also shown in Figure 3.12 are the points $C_1 - C_4$ - corresponding to the data applying to the four case studies run here. Whereas ribbing was not clearly identified in these experiments, the results of Schweizer et al. show the conditions investigated to be close to the critical threshold for stability. Increasing solids concentration results in a

decrease in H_w/H_s as can be seen in Figure 3.9 and Table 3.3 and will inevitably lead to narrowing of the suction coating window formed by the lower suction limit due to edge bead break and the upper limit due to the onset of ribbing. A point is reached beyond which coating is no longer possible.

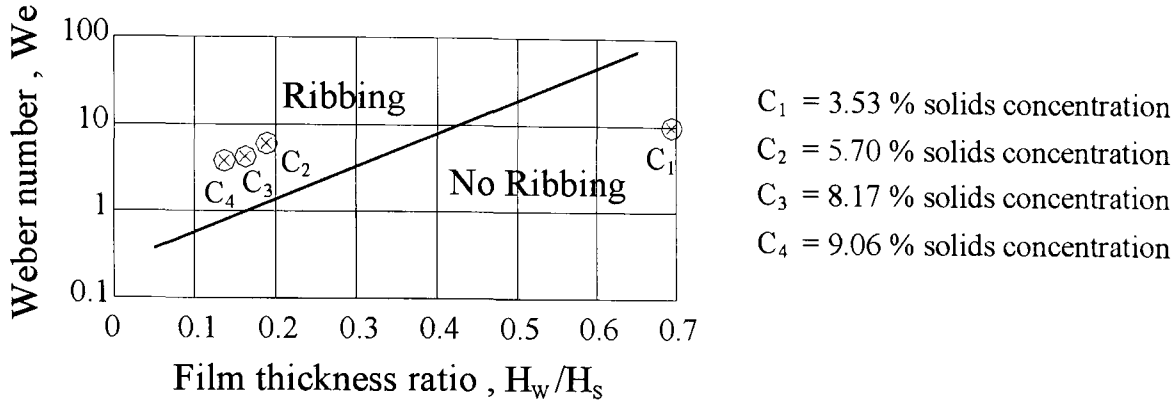

Figure 3.12: Master Curve for the Onset of Ribbing, after Schweizer et al. [2003]

Solids Concentration (%)	H_s (mm)	H_w (mm)	H_w/H_s (-)
3.53	1.383	0.96	0.694
5.70	1.617	0.305	0.189
8.15	2.055	0.334	0.163
9.06	2.264	0.311	0.137

Table 3.3: Ratio of H_w/H_s for the Four Case Studies

The conclusion from this work is that there is a finite range of concentrations for laying down a given coating weight as a single layer dictated by the tendency for static wetting line migration and streaky coating when too low and the onset of ribbing and ultimately break-up into rivulets when too high.

Moreover, consideration of equation (3.5) shows that for a given required single layer wet thickness, there will be a maximum viscosity above which it becomes impossible to achieve coating and that this critical viscosity decreases with increasing coating speed.

3.3 The Effect of Surface Energy

A screening exercise was initiated and analysed by the author in order to segregate various types of substrate made available for experimental coating trials by comparing established coating performance criteria with measurements of advancing contact angle and surface energy.

Data were first collated on coatability and adhesion from general routine observations within the ILFORD Imaging organisation and summarised by Wraith et al. [2003]). Adhesion was assessed taking a fully dried sample and subjecting it to scoring to quantify how well the coating resisted delamination. The criteria for coatability were broadly the maximum achievable coating speed, the band of suction pressures enabling bead make, whether manual assistance was required when making the bead and whether or not the bead remained stable during join withdrawal. The formulations tested cannot be divulged for commercial reasons but the properties and overall wet laydown were similar to those described in Section 3.2.1. The exercise covered four distinct substrate types, all being paper based and precoated with polyethylene to render them impervious to moisture. Further variations included:

- The presence or absence of a gelatin "subbing" layer precoated onto the polyethylene surface
- Whether or not the substrate was subjected to on-line corona treatment prior to being transported to the coating head

The pre-treatment status and conclusions on adhesion and bead-make performance are summarised in Table 3.4.

The second part of the exercise to measure the advancing contact angle for distilled water and surface energy was also initiated by the author, the actual measurements being carried out by Gillian Fossdyke of Harman technology Limited – to whom thanks is due. The results are summarised in Table 3.5. The precision of the surface energy measurement is calculated on the basis that the most significant error corresponds to the determination of contact angle. This involved taking three repeat measurements and ensuring the sample was free from contamination and maintained flat. Individual contact angle readings were seen to vary within ± 1°.

Base type	Subbing Layer	On-line corona treatment	Bead make	Adhesion
"glossy" #1U	No	No	5	1
"glossy" #1C	No	Yes	5	2
"pearl" #2U	No	No	4	1
"pearl" #2C	No	Yes	4	2
#3S	Yes	No	1	3
#3U	No	No	3	1
#3C	No	Yes	3	2
#4S	Yes	No	1	3

Bead make ratings: 5 = easy; 4 = fairly easy; 3 = fairly difficult; 2 = difficult; 1 = very difficult

Adhesion ratings: 3 = good; 2 = fair; 1 = poor

Table 3.4: General Coatability and Adhesion Survey for a Range of Substrates

Base type	Advancing Contact Angle (deg)	Dispersive Surface Energy (mN/m)	Polar Surface Energy (mN/m)
"glossy" #1U	88 ± 1	37.0 ± 0.7	0.4 ± 0.2
"glossy" #1C	72 ± 1	41.7 ± 0.7	1.2 ± 0.4
"pearl" #2U	97 ± 1	37.1 ± 0.8	1.5 ± 0.5
"pearl" #2C	84 ± 1	40.1 ± 0.7	0.5 ± 0.2
#3S	69 ± 1	35.4 ± 0.6	4.8 ± 0.6
#3U	92 ± 1	36.4 ± 0.8	0.3 ± 0.2
#3C	81 ± 1	38.0 ± 0.7	0.3 ± 0.2
#4S	69 ± 1	35.8 ± 0.5	7.5 ± 0.7

Table 3.5: Advancing Contact Angles and Surface Energy Components

The results using the method of Good [1964] for the measurement of advancing contact angles for drops of pure water deposited on the surfaces of the samples, see Figure 3.13, correlate well with adhesion as expected (Gutoff and Cohen [1995]) but are contradictory when applied to predicting coating performance. Blake [2005] has found that the receding contact angle for water in fact gives a more reliable measure of the adhesion benefit of corona treatment.

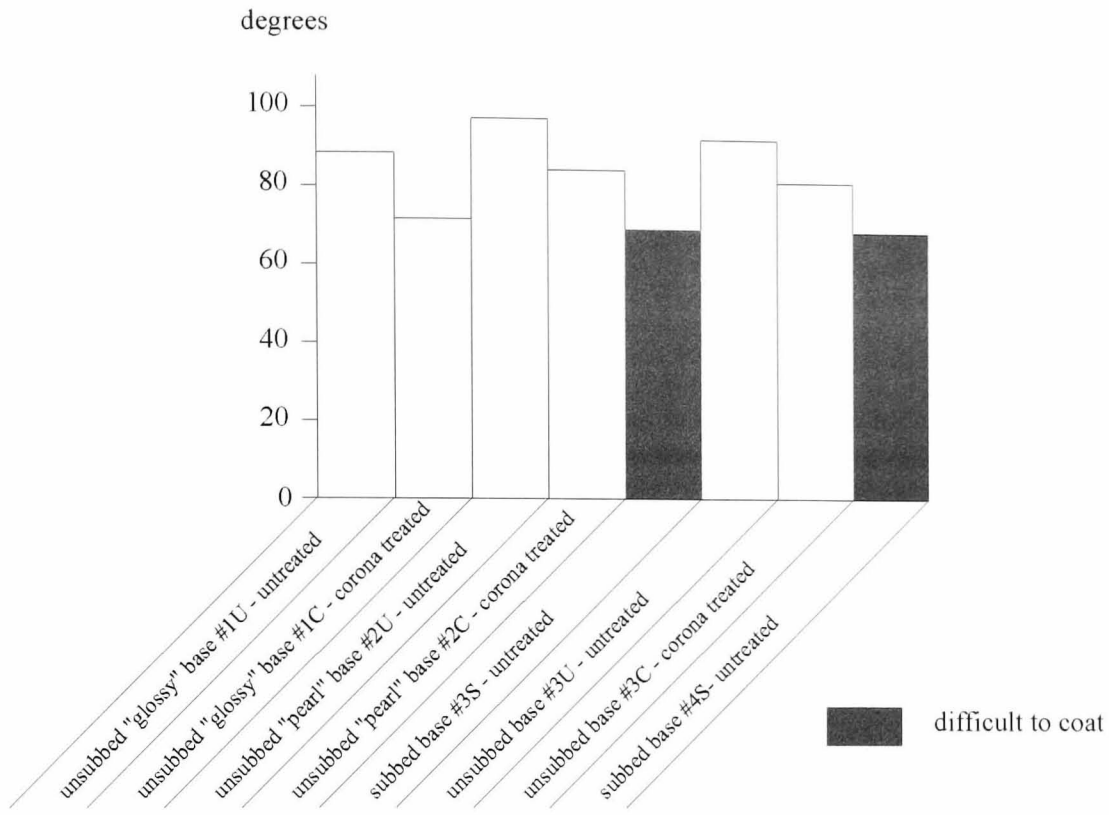

Figure 3.13: Advancing Contact Angle for Pure Water for Range of Substrates

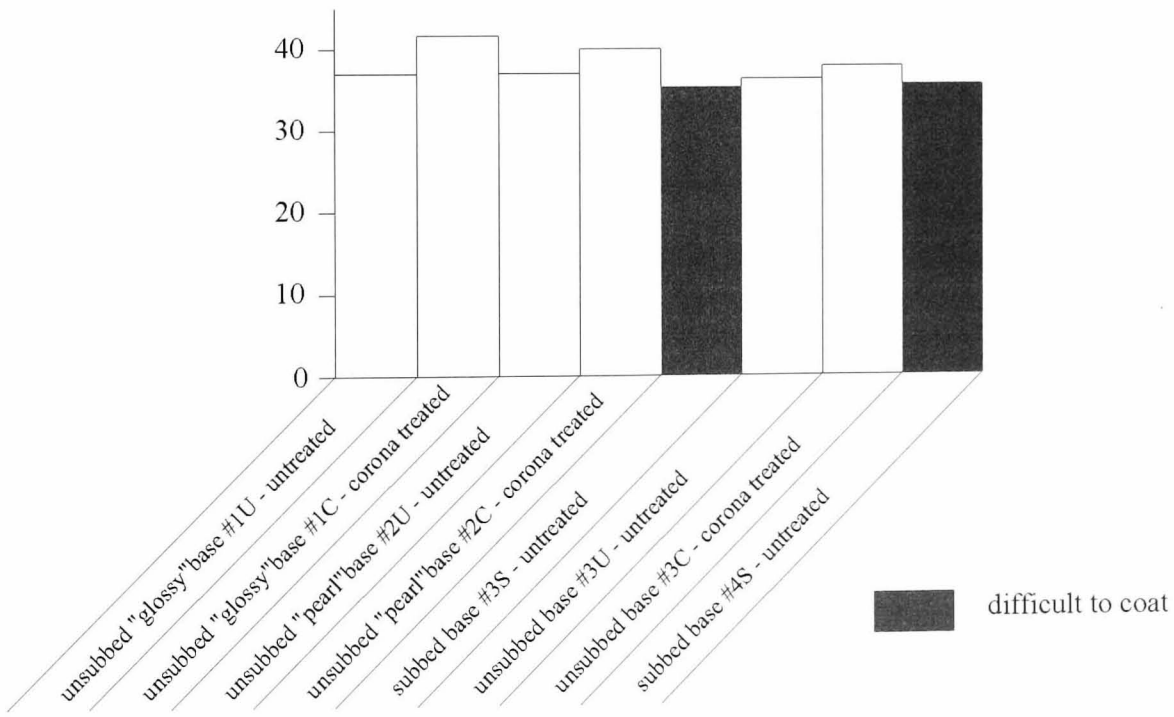

Figure 3.14: Dispersive Energy Component for Range of Substrates

Figures 3.14 and 3.15, on the other hand, show how decomposing the surface energy using the method of Owens and Wendt [1969] into the dispersive and polar energy components more successfully relates to coating behaviour. The test liquids used were

1-bromonaphthalene and 2,2'-thiodiethanol as having essentially non-polar and polar properties respectively and employed by Blake and Morley [1997].

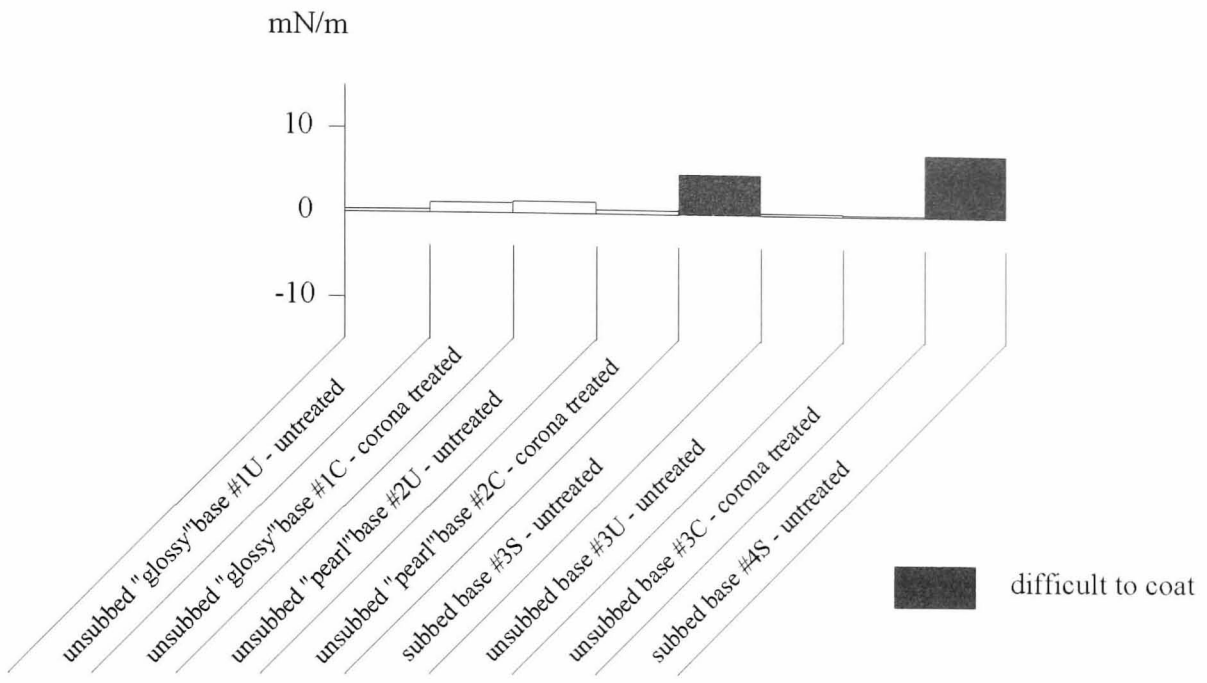

Figure 3.15: Polar Energy Component for Range of Substrates

The results show that an increase in surface energy associated with van der Waals' dispersive forces encourages dynamic wetting. The presence of gelatin, however, significantly increases the polar component. This is explained by the presence of OH, NH and SH groups within the molecular structure of gelatin, whereas polyetheylene contains CH groups and is essentially non-polar (Fossdyke 2004]). Bonding to form well adhered coatings post-drying is encouraged by the presence of the gelatin, but the polar groups evidently resist dynamic wetting at the bead forming zone.

Care must be taken in assessing the significance of the data for these materials as they include those showing appreciable roughness. As pointed out by Zisman [1964], errors in assessing surface energy due to contact angle hysterisis increase with roughness – as more fully discussed in Section 3.4 – see Johnson & Dettre [1964] and Dettre & Johnson [1964]. There is thus the possibility that the wetting liquid may not penetrate the troughs between the asperities in the roughened surface, in which case the apparent contact angle no longer represents the local value as determined by the surface energy. It is evident from an inspection of Table 3.5, however, that any differences in the polar surface energies of the unsubbed, corona treated base types #1C,#2C and #3C due to

variations in surface roughness are small compared with the distinct change when comparing the polar energies of subbed base type #3S and unsubbed untreated base type #3U.

This finding supports the ideas proposed by Blake and Morley [1997] albeit that they examined the maximum speed of coating by curtain in contrast to this work, which looks at the ease of bead-make at a fixed speed using slide bead coating. They showed that the coating speed for curtain coating for a fall height of 3 cm, application angle 0°, viscosity 65 to 75 mPa.s and flow rate of 3 to 3.5 cm^2s^{-1} increases as the polar component falls below 10 mN/m, where the dispersive component exceeds 30 mN/m and where the calculated static advancing contact angle for pure water lies between 65° and 100°. The importance of the role of the polar component as distinct from the dispersive component has also been established by von Bahr et al. [2004] when studying the wettability and contact angle hysterisis characteristics of AKD-sized papers.

An important conclusion from this study is that surface energy measurements from observing the advancing contact angle for pure water, albeit useful as a predictor of the strength of adhesion of the fully dried coating, are highly misleading as an indicator of coatability. Resort must be made to the more complex method of Owens and Wendt. It is also seen from these results, that whereas corona treatment is highly beneficial to the ultimate strength of adhesion after drying (Gutoff and Cohen [1992]), it does not significantly affect coatability.

Having established that the presence of the gelatin subbing layer is distinctly detrimental to dynamic wetting, importance was placed in the ensuing work to ensure that substrates were suitably segregated to take this into account when assessing the effects of surface roughness on coatability.

3.4 The Effect of Surface Roughness

3.4.1 Introduction

One of the key constraints when considering the effect of roughness on the maximum achievable coating speed using slide bead coating is air-entrainment (Clarke et al. [2003]). This is also true of curtain coating as shown for example by Blake et al. [1995] and Cohu [1999]. In this latter process, there are two distinct limits on the maximum speed for defect free coating speed for a given flow rate – dependent on whether the web speed is increasing or decreasing (Blake et al. [1995] and Cohu [1999]). This hysterisis effect is explained by Blake et al. [1995] in the following way. The optimum position for the dynamic wetting line for inhibiting air entrainment as the speed is increased is found to be close to the point where the projection of the line of free fall of the curtain meets the web surface. At the onset of air entrainment, however, the dynamic wetting line is swept downstream thereby causing a reduction in the maximum shear rate seen at the dynamic wetting line and a consequent increase in local viscosity due to the shear thinning properties of a typical coating solution. This in turn results in a greater propensity for air entrainment, whereby the limit for recovery of defect-free coating can only be achieved at a significantly lower speed. The region between the two limits is metastable, in that air entrainment can prematurely occur through disturbances incurred by irregularities in the web surfaces or transient effects seen at start-up.

In this work, a similar apparently unreported effect has been observed in that minute air bubbles are sometimes seen to be initially entrained at start-up but can then frequently be eliminated by temporarily opening up the gap as typically undertaken for allowing through passing inter-roll joins. This is illustrated in the experimental coating window shown in Figure 3.16. This particular result was obtained when coating a substrate of roughness given by a value of 13.3μm for Rz with three layers having properties and wet laydown thicknesses as shown in Table 3.6. The dynamic surface tension characteristics for each layer were essentially as shown in Figure 3.2. Sporadic air entrainment evident at speeds in excess of 170 m/minute using a gap of 127 μm could be dispelled by temporarily opening up the gap to 430 μm and subsequently restoring the gap back to 127 μm using the mechanism described in Section 2.5.1.4.

	Lower layer	Middle layer	Upper layer
Viscosity at 100 s^{-1} (mPa.s)	40	132	138
Density (kg/m^3)	1015	1024	1022
Wet laydown (μm)	36.3	23.5	23.5

Table 3.6: Properties for Experiment demonstrating Coating Gap Hysteresis

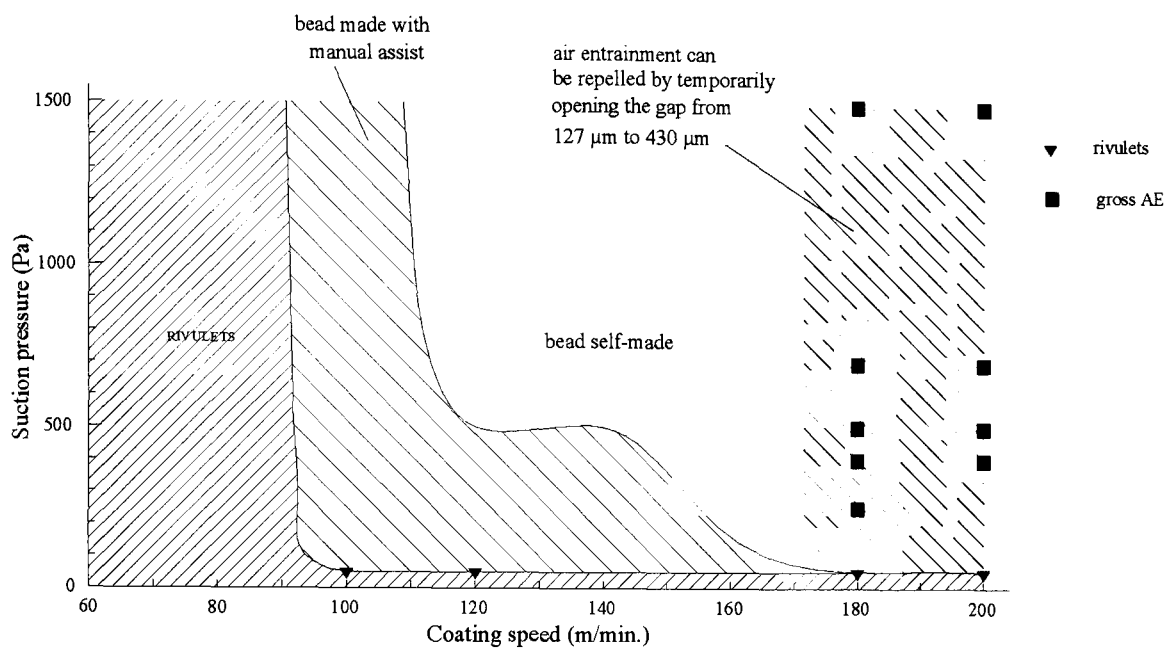

Figure 3.16: Coating Window demonstrating Coating Gap Hysteresis

It is well established for curtain coating that air entrainment can be postponed by taking advantage of the momentum carried by the falling curtain. This is realised in practice when the dynamic wetting line is directly at or slightly downstream of the projection of the back curtain surface onto the web – Blake et al. [1994] – see also Section 3.4.4.6 and Figure 3.34.

The onset of air entrainment is often seen at the trailing edge of an inter-roll splice – see for example Yapel [1999]. In this case, the gap is momentarily reduced by the presence of the splice and then increased back to its original value at the trailing edge. There is often insufficient momentum associated with flow down the slide to force the fluid further across the wider gap caused by the trailing edge and air becomes entrained over a finite length of the coating. It is suggested that a possible mechanism for the hysteresis effect depicted in Figure 3.16 is the above effect in reverse. Here, local air entrainment is initially triggered at start-up by random perturbations in the surface of the web, bubbles in the solution or splashes incurred during the "dipping-

in" process. The dynamic contact angle in this case is likely to be high and approaching 180° and the dynamic wetting line misaligned relative to the key forces associated with the momentum of the fluid on the slide - Figure 3.17(a). On opening up the gap – Figure 3.17(b) – the static wetting line migrates down the lip face and the dynamic wetting line accordingly pulled back upstream to a more favourable position. On restoring the gap back to its original setting – Figure 3.17(c) – the pressure within the fluid in the bead forming zone is temporally boosted to enhance the effect of the momentum of the slide flow to resist the dynamic wetting line being pulled once more downstream. It is plausible that the dynamic wetting line then remains in this more favourable positon unless once again disturbed by random perturbations.

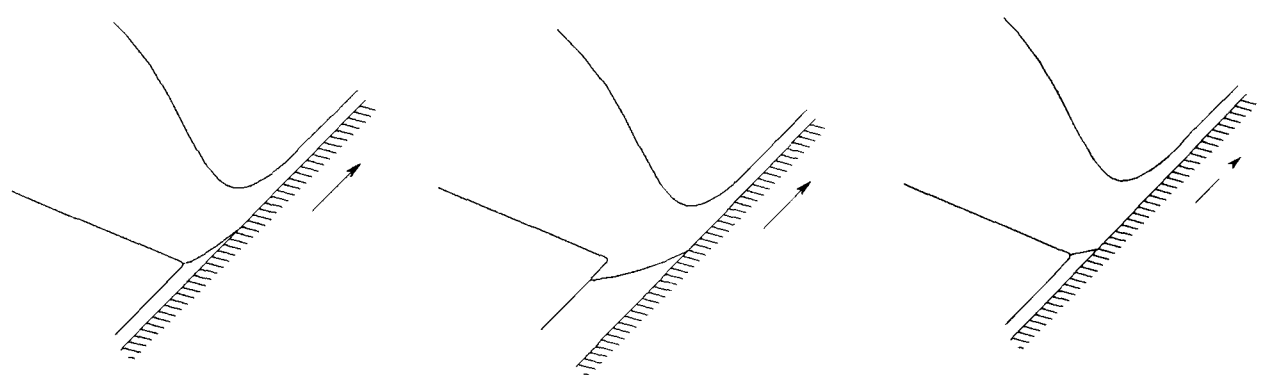

Figure 3.17: Possible Mechanism for Gap Hysteresis Effect

The effect calls for further study, for which the lower meniscus monitor described in Section 2.12 is well suited. Unfortunately, the difficulties in reproducing the perturbations triggering sporadic air entrainment combined with the lack of materials and resource prevented further study using this device in this work

An important outcome of this finding was that in all ensuing work in determining coating windows, care was taken to check the effect of cycling through gap changes in order to finally assess the limits due to air entrainment.

3.4.2 Preliminary Observations on Two Types of Rough Substrate Surface

In pursuing the study of the effect of roughness, work was limited to four web materials generally available for use on the pilot coating machine. All of the substrates were basically of paper overcoated both sides with polyethylene and either supplied "unsubbed" or "subbed" with a further thin overcoat of gelatin. One of these materials was as described in the study of the coating of a smooth photo-paper web in Section 3.2.1 and also designated as unsubbed "glossy" type #1C in Table 3.4. The second type was designated unsubbed type #2C – having a slight pearl-like sheen by nature of the depth of embossing carried out during the chilling of the upper polyethylene overcoat during base manufacture. The third and fourth types comprised the same basic polyethylene overcoated paper substrate, type #3C being unsubbed and type #3S being subbed.

It was deemed useful to initially compare the coating windows obtained with the three unsubbed corona treated surfaces as having nominally the same chemical composition and thus similar surface energies - see Table 3.7. It will also be seen from the table that the values for Rz as obtained from the topographical data using the Wyco white light interferometer described in Section 2.3.1 are very similar for the base types #2C and #3C while both significantly higher than for the glossy base type #1C. R_z is a 10 point average peak-to-peak height as defined by equation (2.22) in Section 2.3.1.

Base type	Rz (μm)	Dispersive surface energy (mN/m)	Polar surface energy (mN/m)
"Glossy" #1C	2.02	41.7 ± 0.7	1.2 ± 0.4
"Pearl" #2C	15.67	40.1 ± 0.7	0.5 ± 0.2
#3C	13.33	38.0 ± 0.7	0.3 ± 0.2

Table 3.7: Surface Properties of Three Unsubbed Corona Treated Substrates

A coating trial was run using the same single layer formulation G-C Mix#1 as described in Section 3.2.1 and Figures 3.1 and 3.2 – the viscosity measured at 10^3 s^{-1} being 38 mPa.s and the laydown 96.5 μm as previously. The resultant coating windows using a coating gap of 127 μm are shown in Figure 3.18.

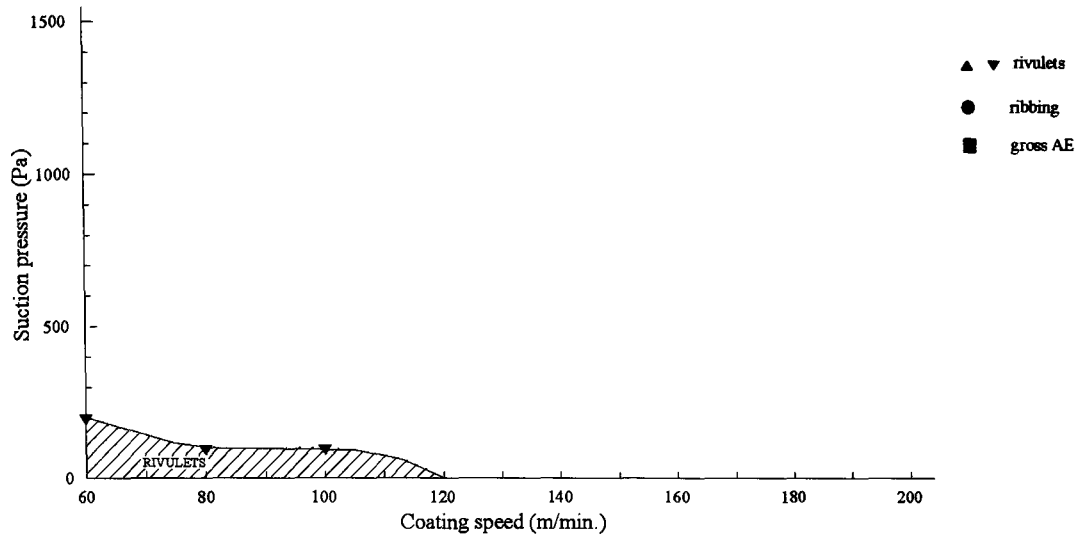

Unsubbed corona treated "Glossy" Polyethylene Coated Base #1C

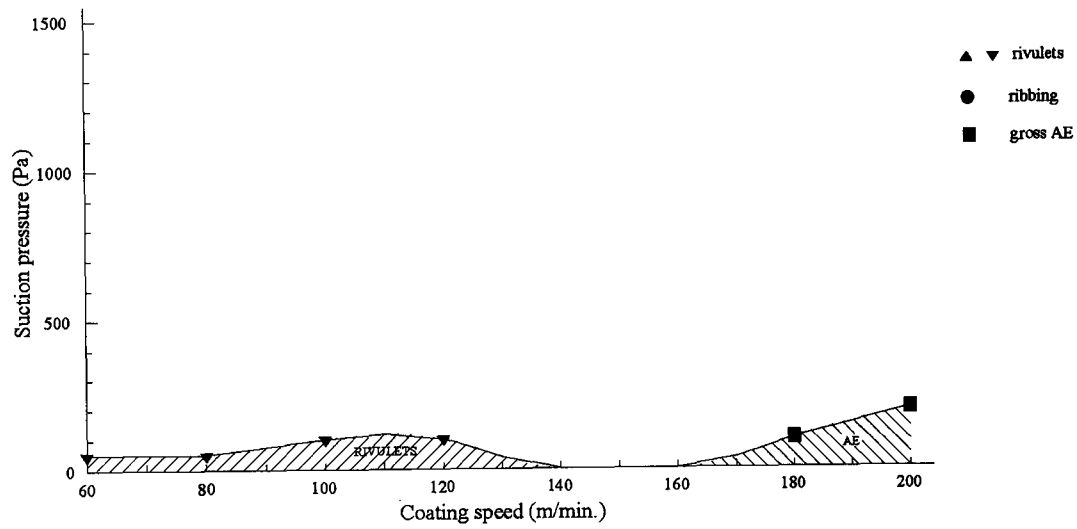

Unsubbed Corona Treated "Pearl" Polyethylene Coated Base #2C

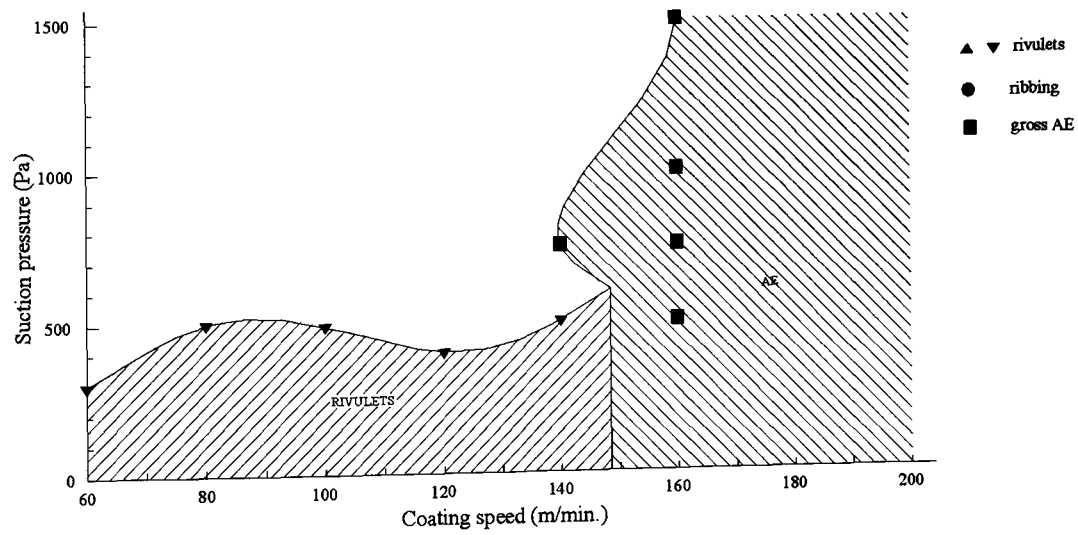

Unsubbed Corona Treated Polyethylene Coated Base #3C

Figure 3.18: Coating Windows for G-C Mix # 1 coated on Three Different Substrates

There is some indication of gross air entrainment at low suction pressure when coating "pearl" base type #2C as the coating speed increases above 160 m/minute but otherwise the window shows the formulation to be readily coatable. The result for the base type #3C is, however, entirely different. Coating is only possible up to a speed of the order of 150 m/minute, beyond which air entrainment occurs for all values of suction pressure. At speeds lower than 150 m/minute, the bead breaks into rivulets for suction pressures less than 500 Pa. Any reduction in air entrainment speed due to increased roughness is not unexpected – Hartman [1989]. Clarke [2001] showed that the air entrainment speed for a curtain coater fell from typically 5.5 m/s to 4.3 m/s as R_z was increased from 0.6 μm to 4.4 μm.

The fact that the coating performances are so very different for the base types #2C and #3C while the Rz parameters characterising the surface roughness and the surface energies are apparently similar calls for further investigation. Careful delamination of 50 mm x 50 mm square samples taken from the two base types and weighing the components revealed the grammage values shown in Table 3.8.

Base type	#2C	#3C
Weight of upper polyethylene layer (gsm)	39.7	31.8
Weight of paper (gsm)	176.7	88.7
Weight of lower polyethylene layer (gsm)	38.0	28.0
Total weight (gsm)	254.4	148.5

Table 3.8: Weights of Components making up Base Types #2C and #3C

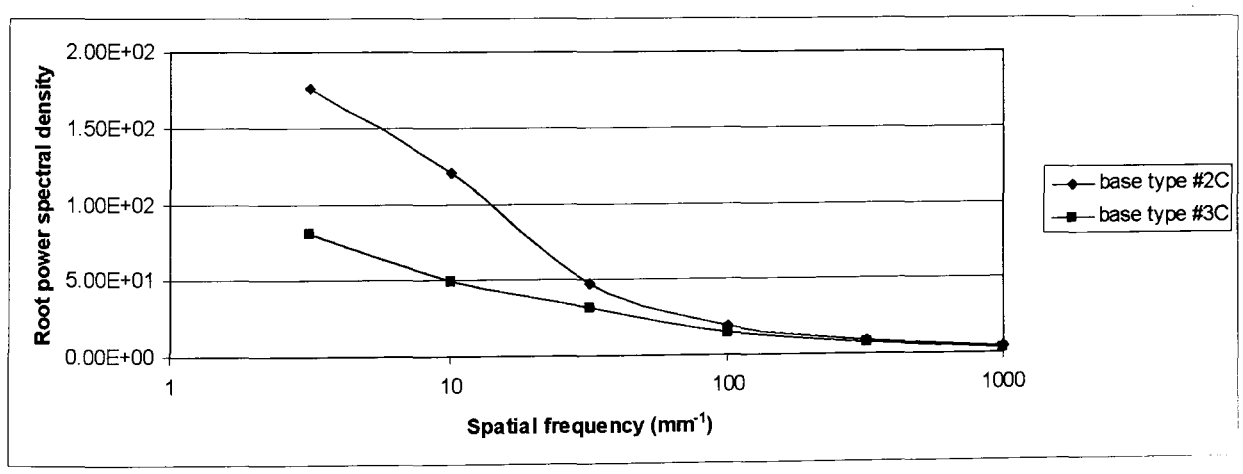

Figure 3.19: Spectral Density Plot for Base Types #2C and #3C

It is clear that Rz alone as initially suggested by Clarke [2002] is not sufficient for characterising the topography of the surface. Figure 3.19 shows a spectral density plot

for the two base types. There are thus structural differences that are not revealed by Rz alone. The respective Ra values for type #2C and #3C surfaces are 0.97 and 0.52.

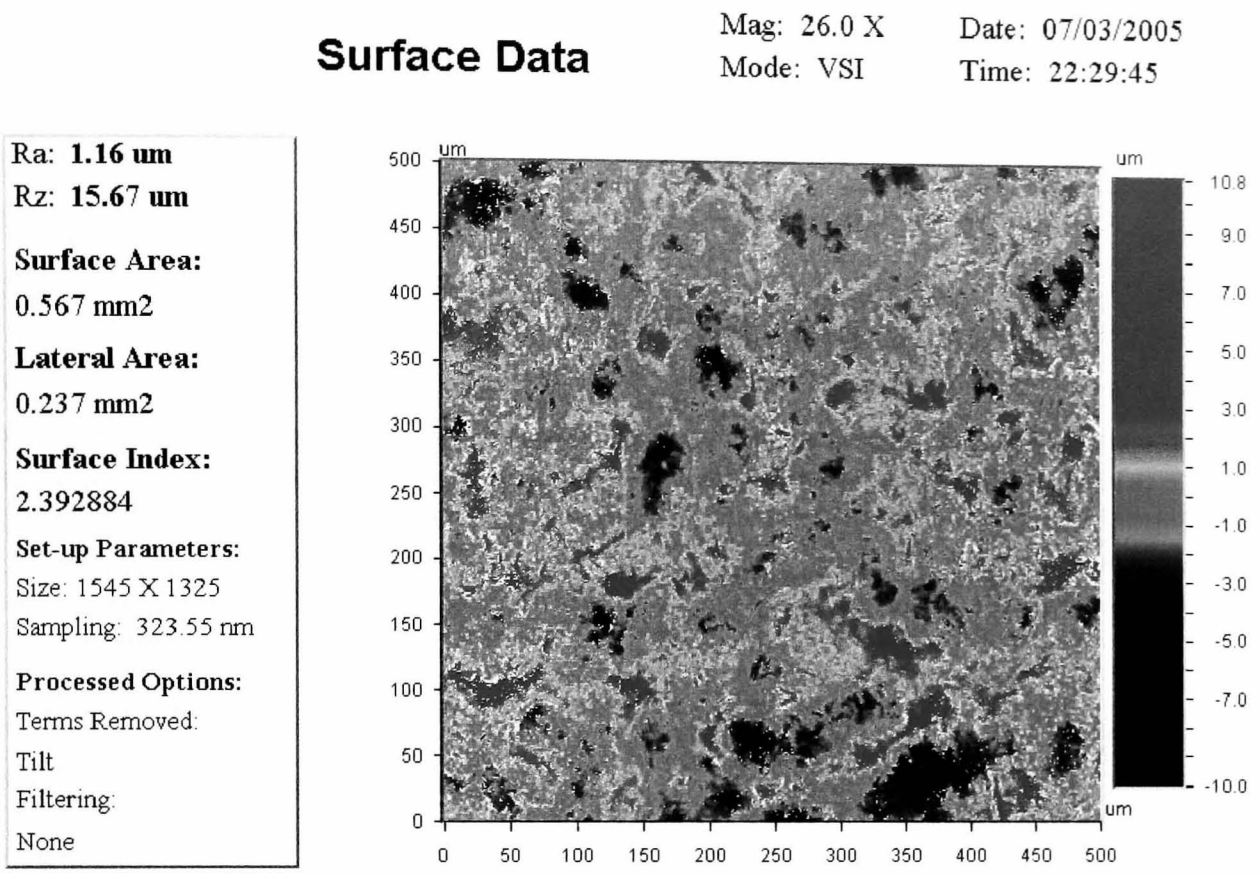

Figure 3.20: Unfiltered Topography of Base Type #2C

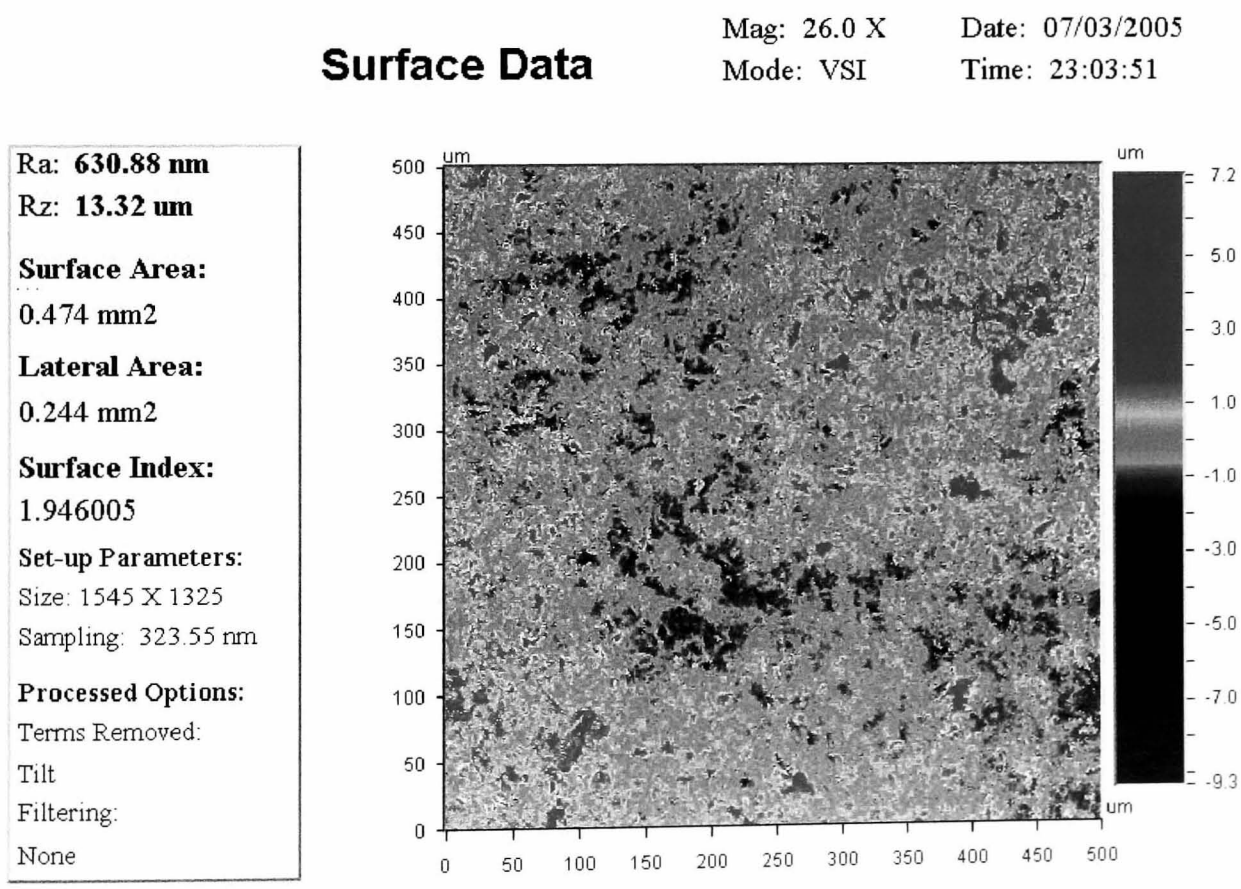

Figure 3.21: Unfiltered Topography of Base Type #3C

These structural differences are further highlighted in Figures 3.20 and 3.21, which show the topography of the two surfaces without applying any filtration. It is clear from these images that the base type #2C contains significantly more peak-to-trough excursions per unit area than #3C, while the peak-to-trough depths are similar.

Further insight is obtained by taking cross-sections in the machine direction. Figure 3.22 depicts equal scales for the distance along the surface and the heights of the asperities. Both surfaces show occasional needle-like asperities.

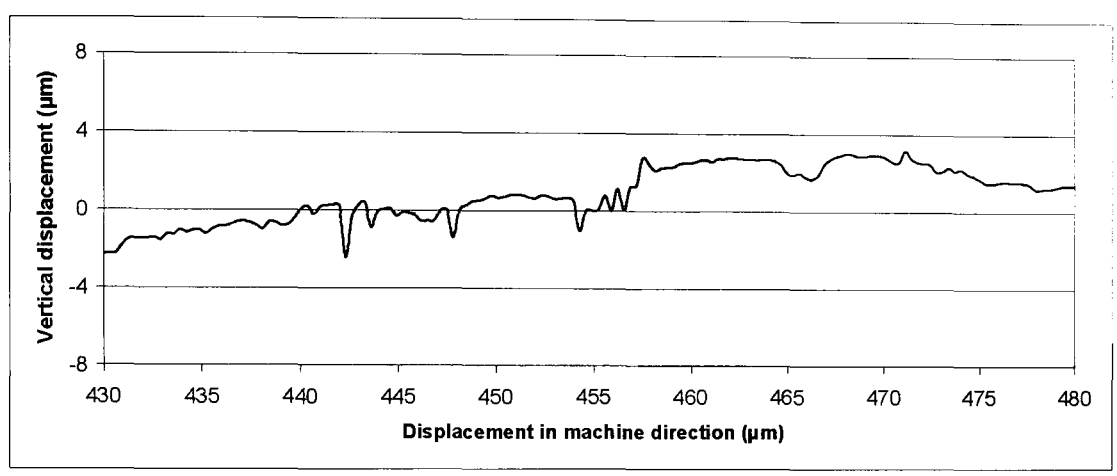

Unsubbed "Pearl" Polyethylene Coated Paper Base #2

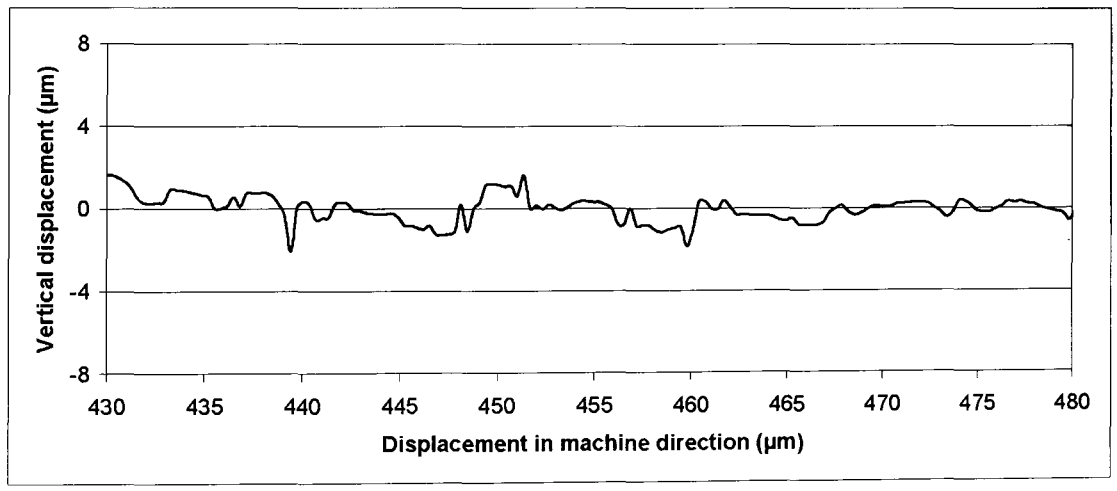

Unsubbed Polyethylene Coated Paper Base #3

Figure 3.22: Typical Cross-Sections for the Base Types #2C and #3C using Equal Scales

The studies of the wetting mechanisms of leaves (Bico et al. [1999]) suggests that a surface showing a structure in the form of closely packed needles like a 'fakir carpet' is highly hydrophobic by reason of air becoming trapped in the troughs when attempting to wet the surface. The early ground breaking work of Johnson and Dettre

[1964] and Dettre and Johnson [1964] showed surfaces displaying significantly deep troughs and high peaks induce a composite wetting surface – where the name "composite" refers to the fact that the interfaces between the wetting liquid are both liquid-air and liquid-solid. They quantified contact angle hysterisis in terms of differences in $\cos(\theta_a)$ and $\cos(\theta_r)$, where θ_a and θ_r are the advancing and receding contact angles respectively. They showed both theoretically and experimentally that a composite wetting interface causes this hysterisis to dramatically decrease as roughness increases above a critical value. Wolfram and Faust [1978] showed that when placing drops of water on a flat supported surface and carefully tilting the support there is a critical tilt angle at which the drop begins to slide or roll. They found that the contact angles for chemically equivalent surfaces of varying roughness converge to a point as the critical tilt angle reduces to zero, the single value being the Young contact angle for that surface.

Miwa et al. [2000] extended the work of Wolfram and Faust [1978] and found they could create a superhydrophobic surface comprising boehmite particles overcoated with a hydrophobic silane based material. They varied the packing density of the particles by varying the solvent concentration used during sublimation and in so doing obtained a range of roughnesses revealed by SEM images and quantified by scanning with an AFM (atomic force microscope). They found a packing density that gave a very low critical tilt angle – of the order of 1° - at which the drops became extremely mobile. The acceleration was then very close to g.sin1°- thus displaying practically no resistance to motion. A useful criterion for defining the steepness of the asperities forming a surface is the surface area ratio defined by the true surface area per unit projected area. Miwa et al. [2000] calculated this from the topographical data derived from the AFM derived data to be 1.82 for the most hydrophobic surface film studied. The values for other boehmite-ethanol ratios, which provide a measure of particle packing, were not stated in their paper but have been forwarded by Nakajima [2005], to whom thanks is expressed. Figure 3.23 shows the dependence of the sliding angle on boehmite-ethanol ratio and the strong correlation with surface area ratio.

The data analysis provided within the Wyko software also provides for the calculation of surface area ratio – designated surface index in Figures 3.20 and 3.21. The results

for the three base surfaces are given in Table 3.9. It is interesting to note that the surface area ratio for the type #2C base is significantly higher than for type #3C.

Conditions favouring composite wetting have been studied extensively for curtain coating by Clarke et al. [2000(1)] and Clarke [2002] and also for slide bead coating - Clarke et al. [2003]. They showed for curtain coating that for a range of roughness given by $2\mu m < Rz < 20\mu m$, the limit on the maximum air entrainment speed could be significantly increased under certain conditions.

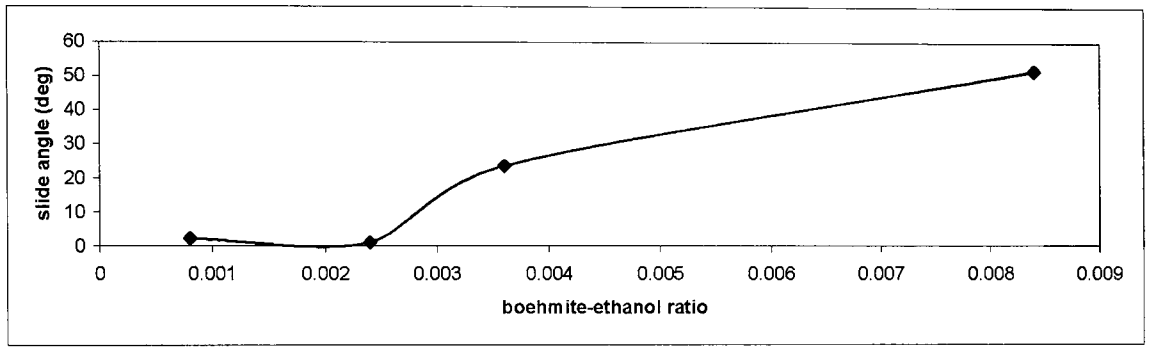

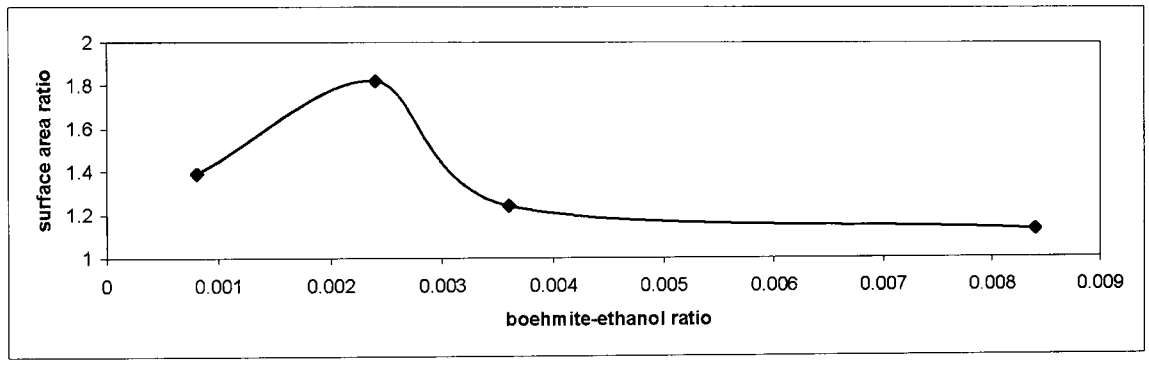

Figure 3.23: Relationship between Boehmite-Ethanol Ratio, Critical Sliding Angle and Surface Area Ratio (courtesy Miwa et al. [2000] and Nakajima [2005])

Base type	#1C	#2C	#3C
Surface area ratio	1.003	2.393	1.946

Table 3.9: Surface Area Ratios for Base Types #1C ,#2C and #3C

This could only be explained by the existence of composite wetting. For this to occur, they found that the viscosity μ_1 of the bottom layer was required to exceed limits dependent on Rz, the curtain impingement velocity U, the application angle θ, the total

volumetric flow rate Q per unit width, the surface tension σ_1 of the bottom layer and the minimum density ρ of the coating solutions according to the expression:

$$1818\sigma_1^{1/3}\,Rz\left\{\frac{1}{0.0002}\,\mu_1 U\cos(\theta)\left[1+\Omega\frac{\rho Q}{20\mu_1}\right]\right\}>1 \qquad (3.10)$$

where

$$\Omega=\frac{25}{25+\left\{\frac{\rho Q}{\mu_1}-8\right\}^2} \qquad (3.11)$$

and is a Lorentzian factor relating to the influence of momentum (Clarke et al. [2004].) As recognising that the steepness of the local asperities should also be taken into consideration as well as defining Rz, Clarke et al. [2004] added the condition that the curtain height H should be limited by the expression:

$$\frac{\rho g H}{4\sigma_1}<\frac{Rz}{\lambda^2} \qquad (3.12)$$

where λ is the average periodicity of the roughness measured by counting the number of zero-crossings per unit length.

Clarke et al. [2003] extended the consideration of roughness assisted as well as charge assisted wetting to the slide bead coating process. They found that the combination of increasing the viscosity of the bottom layer to between 35 mPa.s and 200 mPa.s and the application of charge assist at voltages in excess of 600 v allows coating speeds to substantially increase for rough substrates. Moreover, the air entrainment speed was then found to increase with roughness. They show an example where it is found possible to coat a substrate having an Rz value of 9.7 μm at a speed of 270 m/min using the combination of only 250 v charge assist and a bottom layer viscosity of 62 mPa.s, the viscosities of the middle and upper layers being 100 mPa.s and 40 mPa.s respectively and the total laydown 75μm. They point out that the shear rate applied when measuring the viscosity of the bottom layer needs to be 10^4 s^{-1} to reflect the shearing action at the dynamic wetting line.

In considering the comparison in coating performance of types #2C and #3C bases, there is a similarity with Clarke's results (Clarke et al. [2003]) in that the roughness values Rz are of the same order of magnitude and the polar charge induced surface voltage about + 200 volts as measured using the method described in Section 2.9. It is

suggested that the reason for type #2C base being more readily coatable than type #3C points to the composite wetting mechanism playing a role in determining the wetting kinetics.

Having established that the two base types #2C and #3C showed very different coating performances for a given formulation and set of coating parameters, a decision was taken to optimise coatability for each substrate in turn – as will be seen from the following sections.

3.4.3 A Case Study to Optimise the Coating of Unsubbed Base Type #2C

The aim of this case study was to optimise the rheology of a formulation originally designed as comprising two layers in order to secure the highest possible line speed.

3.4.3.1 First Set of Coating Trials

A preliminary set of coating trials was run to quantify the potential benefit of reducing the viscosity of the lower layer for three alternative two layer photo-paper formulations P#1, P#2 and P#3 when coated on this base. The wet thicknesses were maintained constant. Table 3.10 shows the values along with the three viscosities selected for the lower and upper layers.

	Bottom layer	Top layer
Wet thickness (μm)	65.0	16.3
Viscosity at 100 s^{-1} – formulation P#1 (mPa.s)	19.0	18.0
Viscosity at 100 s^{-1} – formulation P#2 (mPa.s)	23.0	18.0
Viscosity at 100 s^{-1} – formulation P#3 (mPa.s)	32.2	18.0

Table 3.10: Viscosities and Wet Laydown Thicknesses of Three Paper Formulations

The resulting minimum stabilisation suction for withstanding sporadic air-entrainment as a function of coating speed was as shown in Figure 3.24.

The onset of air-entrainment was determined by observing the output waveforms derived from the laser scanner described in Section 2.11.2. The results clearly confirm that the viscosity of the lower layer has a major influence on the air-entrainment speed

for this type of web surface. The fact that coatability improves with decreasing bottom layer viscosity suggests that the troughs as well as the peaks are being wholly wetted in this case. Attaining adequate coating stability with the smallest possible suction pressure is generally regarded by coating practitioners as an overall aim. Koepke et al. [1986], for example, points out that achieving a stable coating using suction pressures ranging from zero to 300 Pa is preferable to a range up to 800 Pa in order to attain optimum quality. Other considerations relate to the tendency for foam generated from the inrush of air into the suction box to become increasingly drawn into the suction fan and associated ductwork as suction pressure is increased.

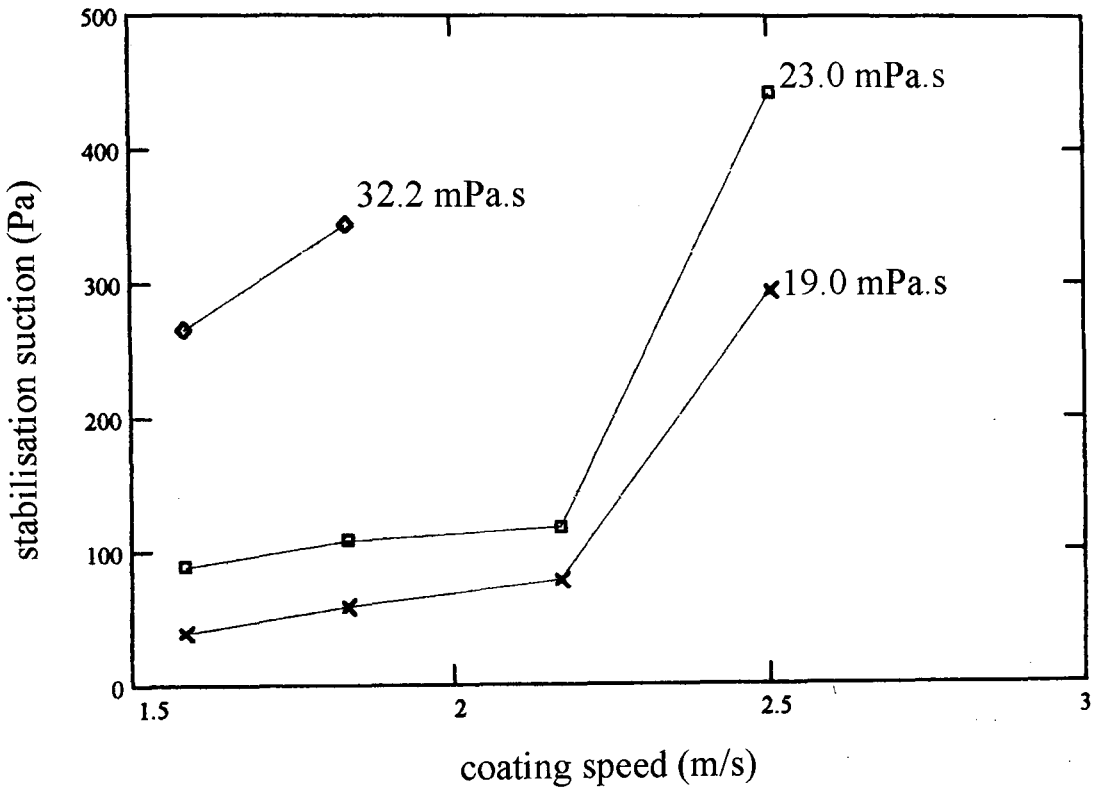

Figure 3.24: Effect of Lower Layer Viscosity Limits due to Air Entrainment

3.4.3.2 Second Set of Coating Trials

A second set of coating trials was run on the pilot coating machine to quantify the benefit of incorporating a thin low viscosity "carrier" layer when coating a typical photo-paper formulation on this base. Table 3.11 compares the key properties of the original two layer system with the new three layer system including the carrier layer.

Here, the solids content in the original main emulsion layer has been redistributed between the two new lower layers. The viscosity of the main layer has been increased

from 25.8 mPa.s to 59 mPa.s by removing water while that of the lower carrier layer has been set at 10 mPa.s by adding water. The net effect is an overall reduction in water load from 75.5 gsm to 65.6 gsm..

	Lower emulsion layer	Main emulsion layer	Upper layer	Total
Formulation P#4a				
Solids content (gsm)		8.5	1.4	9.9
Water content (gsm)		60.4	15.1	75.5
Viscosity (mPa.s)		25.8	10.0	
Coating weight (gsm)		68.9	16.5	85.4
Wet laydown (μm)		65.0	16.3	81.3
Density (kg/m^3)		1060	1010	
Formulation P#4b				
Solids content (gsm)	0.6	7.9	1.4	9.9
Water content (gsm)	9.5	41.0	15.1	65.6
Viscosity (mPa.s)	10.0	59	10.0	
Coating weight (gsm)	10.1	48.9	16.5	75.5
Wet laydown (μm)	10.0	45.1	16.3	71.4
Density (kg/m^3)	1010	1084	1010	

Table 3.11: Key Properties of the Layers used when determining the Benefit of a Carrier Layer when coating onto "Pearl" Base Type #2C

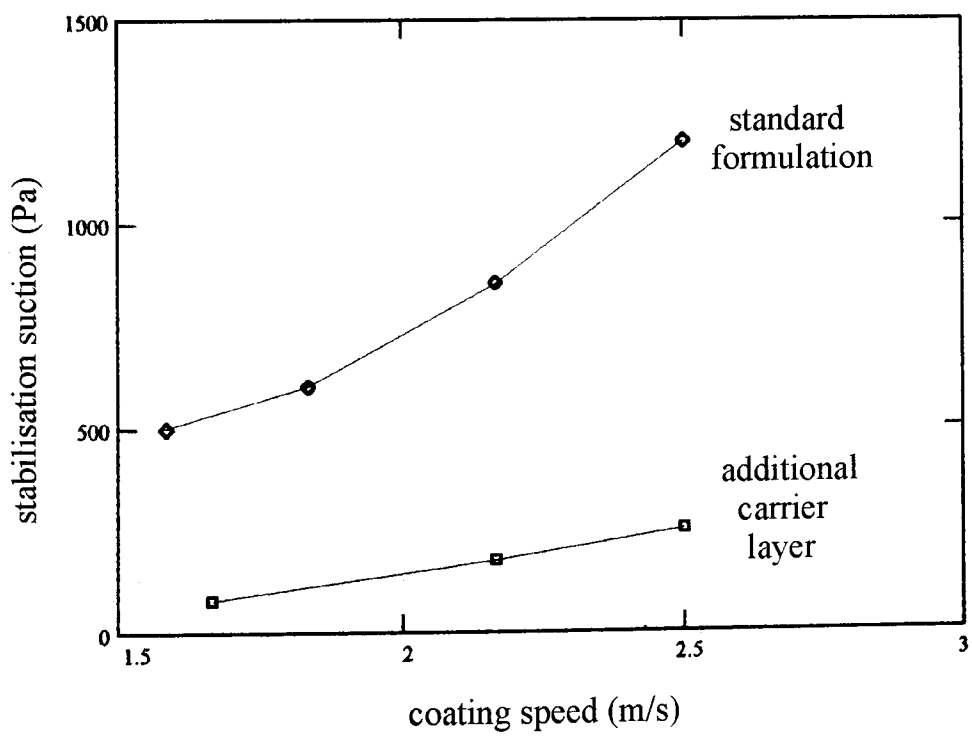

Figure 3.25: Effect of using a Carrier Layer on Suction Limit for Air Entrainment

The trials showed, Figure 3.25, that the additional carrier layer enables defect free coating at much lower levels of stabilisation suction. The maximum achievable coating speed for good end quality is thus increased from typically 90 m/min to well over 150 m/min by adding the thin lower "carrier" layer.

3.4.3.3 Concept of a Coating Process Operability Diagram

As pointed out by Endoh et al. [1997], optimising the viscosity of the coating solution impacts on the whole coating process from solution supply to drying. The results presented here suggest that an operability diagram similar to Figure 3.26 can be drawn for the entire coating process – including solution supply and drying. Possible variations are, for example, the concentration of a main layer solution plotted against process line speed. The diagram serves to illustrate how the maximum concentration for such a layer is typically limited by the ability to supply bubble-free solution at a required flow rate, the ability to coat and by drying. A key benefit arising from the use of a thin low viscosity carrier layer is that this allows the concentration of the other layers to be increased to an optimum value. The raising of this constraint then allows the maximum achievable process speed to increase from S_1 to S_2 as shown.

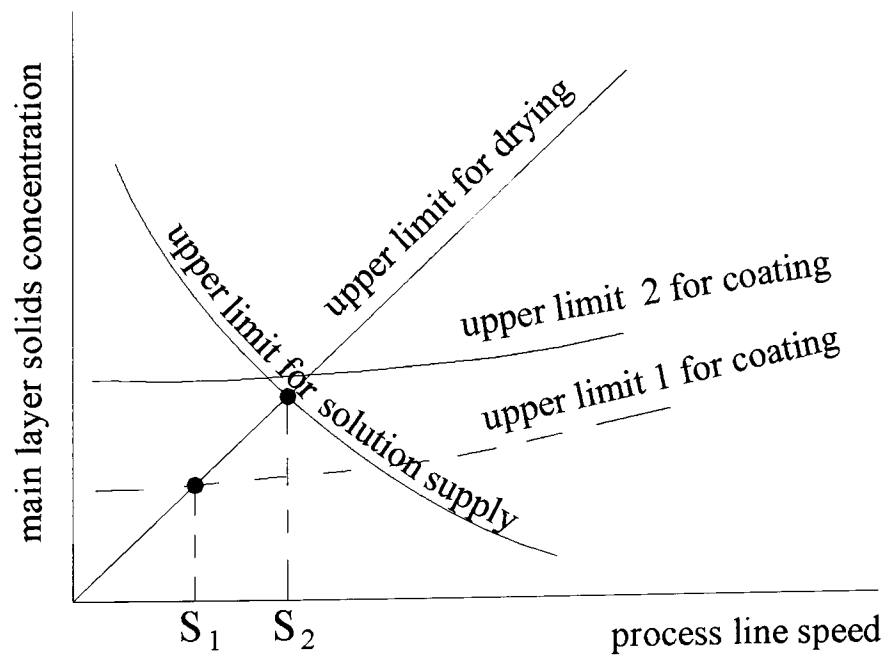

Figure 3.26: The Benefit of a Carrier Layer to Ultimate Process Line Speed

A second important benefit arises from the fact that increasing the average viscosity causes the static wetting line to more readily lock to the corner of the lip face and

hence results in the elimination of vortices forming in a stagnant zone trapped just above the static wetting line – as highlighted in the work of Noakes et al. [2002(1)]. They were able to demonstrate that it is then possible to reduce the outbreak of fine streaks by typically 50% with a consequential savings in waste.

3.4.4 A Case Study to Optimise the Coating of Subbed Base Type #3S

As discussed in Section 3.3, the gelatin subbed rough base type #3S presented the greatest difficulty for the range of substrates studied – see Figures 3.13 – 3.15. Attention was therefore focused in this study on optimising the coating of this material. The work followed on from some preliminary coating trials carried out by Brace [2002], to whom thanks is expressed for permission to publish his results.

3.4.4.1 Preliminary Coating Trials

The formulations comprised the same mixture of gelatin and cellulose designated G-C Mix #1 except for varying water content. The solutions were applied as three layers with freedom to vary the concentration of each individual solution while ensuring the total solids laydown remained constant. The dynamic surface tension characteristics were essentially as shown in Figure 3.2.

It will be seen from Table 3.12 trial #1, that removing water to yield a viscosity of 165 mPa.s for all three layers results in the assembly being uncoatable at a coating speed of 60 m/minute. Trial #20 shows that diluting the lower layer to attain a viscosity of 6 mPa.s and attempting to apply this at a wet thickness of 6.7 μm is no longer effective in restoring coatability. Figure 3.27 shows this is not altogether unexpected. Here, an arbitrary assumption is made that the interface between the lower layer and the adjacent layer initially mimics the topography of the substrate – in order to highlight the fact that the thickness of the "carrier" layer and the roughness are of similar orders of magnititude. Further inspection of Table 3.12 shows that it is only as the thickness of the lower layer approaches or exceeds the value of R_z – in this case 13.3 μm – can stable coating be achieved. Brace showed from his data that it was only possible to achieve stable bead-make without manual assistance by increasing both the coating speed and the total wet thickness of the coated assembly as shown in Figure 3.28.

Trial.	μ_1 (mPa.s)	μ_2 (mPa.s)	μ_3 (mPa.s)	WL_1 (µm)	WL_2 (µm)	WL_3 (µm)	WL_{total} (µm)	S (m/min)	δP (Pa)	Bead make	Quality
#1	165	165	165	23.0	23.0	23.0	69.0	60	NA	Rv	
#2	120	120	120	26.5	26.5	26.5	79.5	60	461	Rv	
#3	50	50	50	32.2	32.2	32.2	96.6	60	461	MA	Good
#4	50	50	50	32.2	32.2	32.2	96.6	80	531	SM	AE
#5	50	50	50	32.2	32.2	32.2	96.6	100	495	SM	Poor
#6	50	50	50	32.2	32.2	32.2	96.6	120	490	SM	Good
#7	50	50	50	32.2	32.2	32.2	96.6	120	278	SM	Good
#8	50	50	165	32.2	32.2	23.0	87.4	120	288	SM	Poor
#9	50	50	165	32.2	32.2	11.5	75.9	120	295	SM	Poor
#10	70	70	70	28.8	28.8	28.8	86.4	100	475	SM	Good
#11	50	50	50	32.3	32.3	32.3	96.9	80	NA	SM	AE
#12	50	50	50	32.3	32.3	32.3	96.9	60	315	Rv	
#13	50	50	50	32.3	32.3	32.3	96.9	70	325	MA	AE
#14	70	70	165	28.8	28.8	23.0	80.6	70	518	Rv	
#15	70	70	165	28.8	28.8	23.0	80.6	90	513	Rv	
#16	70	70	165	28.8	28.8	23.0	80.6	90	557	MA	
#17	50	50	165	32.3	32.3	23.0	87.6	90	561	Rv	
#18	20	165	165	41.4	23.0	23.0	87.4	90	565	MA	EB
#19	20	165	165	41.4	23.0	23.0	87.4	90	571	MA	EB
#20	6	165	165	6.7	33.5	33.5	73.7	60	492	Rv	
#21	6	165	165	29.9	29.9	29.9	89.7	60	492	Rv	
#22	6	165	165	29.9	29.9	29.9	89.7	80	502	MA	Good
#23	6	165	165	40.0	28.0	28.0	96.0	80	497	MA	Fair
#24	6	165	165	29.9	29.9	29.9	89.7	90	497	Rv	
#25	6	165	165	16.1	32.2	32.2	80.5	80	328	MA	Fair
#26	6	165	165	14.9	29.9	29.9	74.7	80	492	Rv	
#27	6	165	165	6.7	33.5	23.0	63.2	90	492	AE	
#28	6	165	165	23.0	30.0	30.0	83.0	80	492	Rv	
#29	30	100	100	28.0	28.0	28.0	84.0	60	490	MA	Good
#30	30	100	100	28.0	28.0	28.0	84.0	80	502	MA	Good
#31	30	100	100	28.0	28.0	28.0	84.0	70	497	MA	Good
#32	30	100	100	16.1	32.1	32.1	80.3	80	492	MA	Good
#33	30	100	100	16.1	32.1	32.1	80.3	60	497	MA	Good
#34	30	100	120	15.5	31.0	31.0	77.5	85	495	MA	Good
#35	30	100	120	15.5	31.0	31.0	77.5	70	560	Rv	
#36	30	100	120	15.5	31.0	31.0	77.5	85	560	MA	Good
#37	41	41	41	28.8	28.8	28.8	86.4	60	560	MA	Good
#38	41	41	41	28.8	28.8	28.8	86.4	80	569	MA	Good

Viscosities measured at 100 s^{-1}. WL = wet laydown. Subscripts 1,2& 3 = layers 1,2 &3. S = web speed. dP = suction pressure.

Rv = rivulets. MA = manually assisted. SM = self making bead. AE = air entrainment. EB = edge break.

Table 3.12: Summary of Brace's Trials to Optimise a Three Layer Formulation for Subbed Base Type #3S

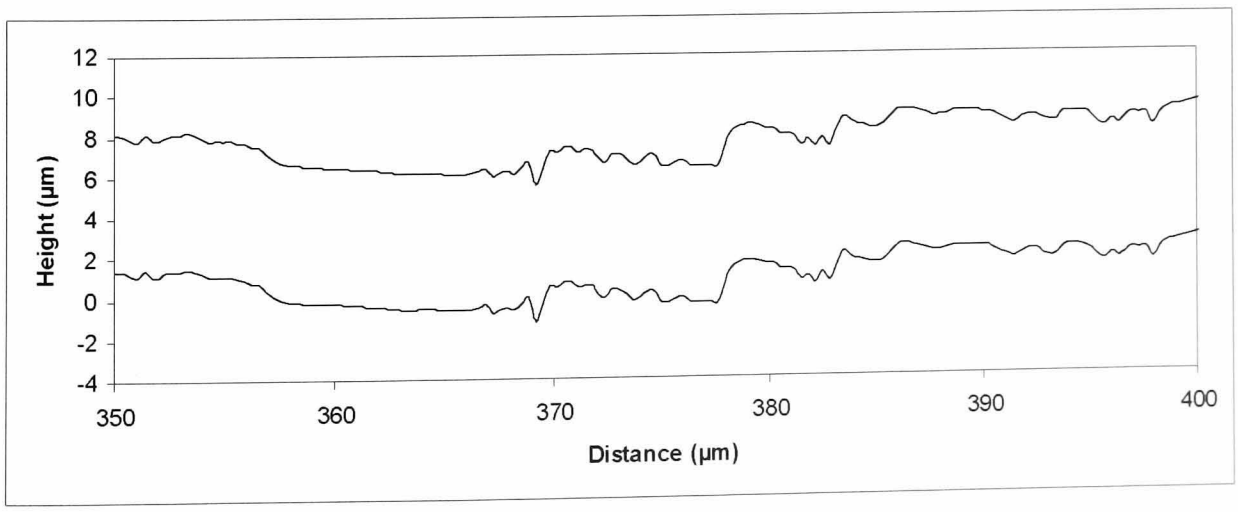

Figure 3.27: The Surface Topography Displaced by the Thickness of the Carrier Layer

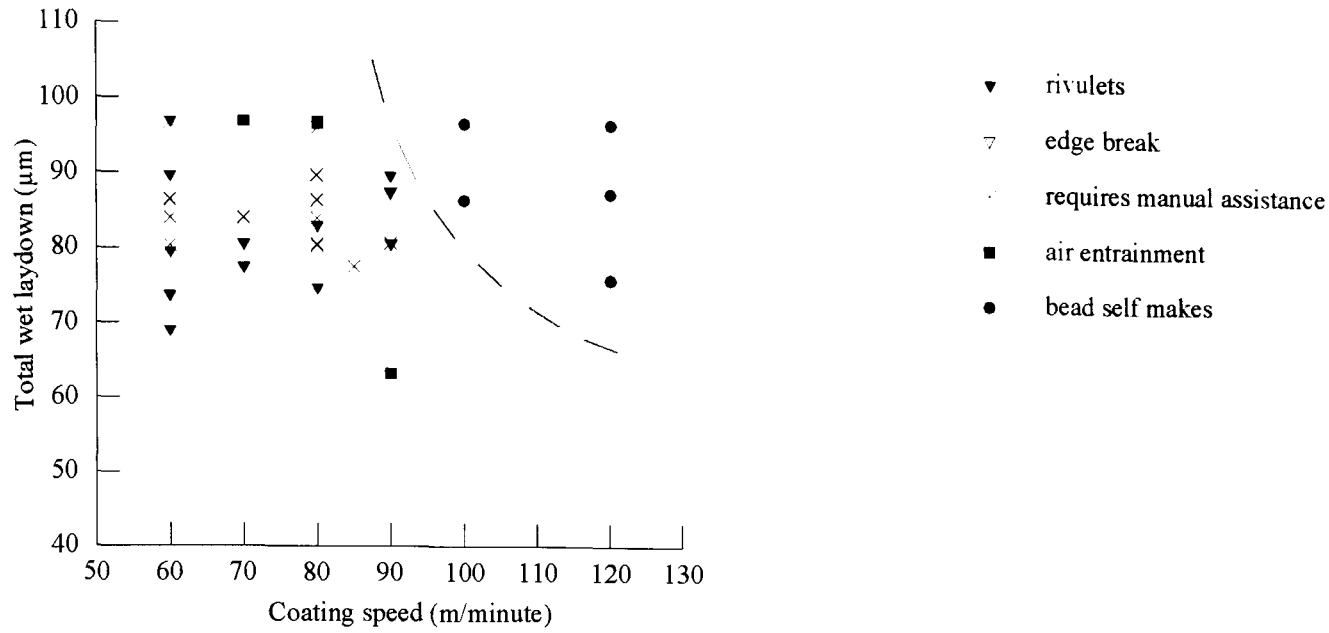

Figure 3.28: Brace's Trials to Optimise a Three Layer Formulation for Subbed Base Type #3S

3.4.4.2 The Effect of Join Withdrawal

A coating window experiment was run for a single layer of viscosity about 50 mPa.s comprising G/C Mix #1 – this being close to optimum for all the formulations of equivalent total solids content tested by Brace – see highlighted section of Table 3.12. The coating window covered the use of two coating gaps, one being 127 µm as studied by Brace and the other being 430 µm for ensuring safe provision for a passing inter-roll join. It will be seen from Figure 3.29 that the trial confirmed Brace's findings for the 127 µm gap that the bead only self-made at speeds exceeding a threshold of the order of 90 m/minute and that the coatability improved as the speed was increased to 120 m/minute. On opening up the gap to 430 µm, however, the bead generally fails by breaking up into rivulets or entraining air. The performance is such as to run the risk of very significant waste when attempting to coat the formulation onto consecutive rolls. The results gave impetus to reviewing the process to see if the coating equipment and method of use could be optimised in order to increase yield when coating this and similar formulations onto this type of base.

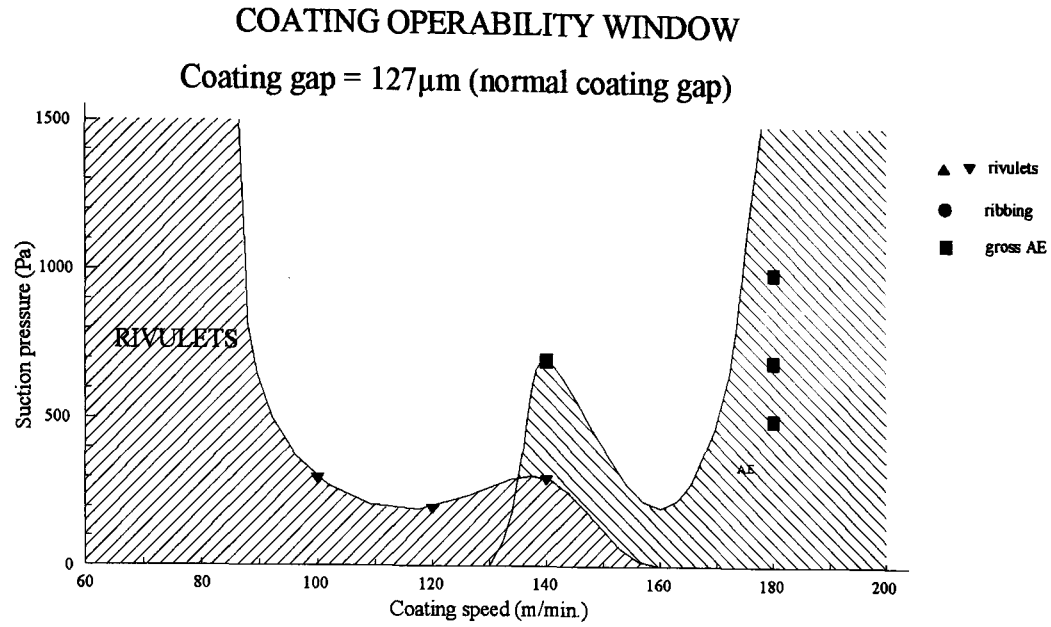

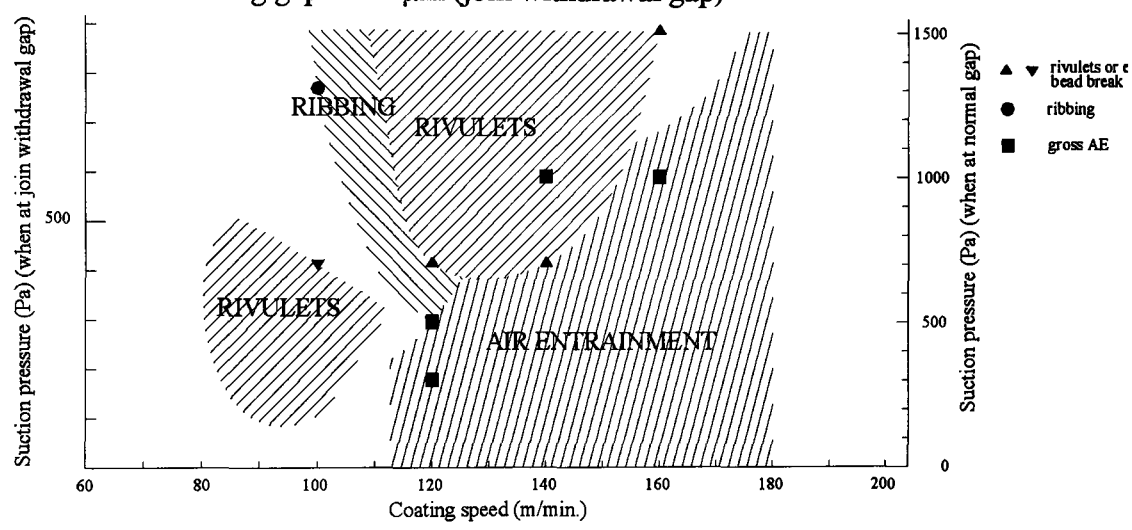

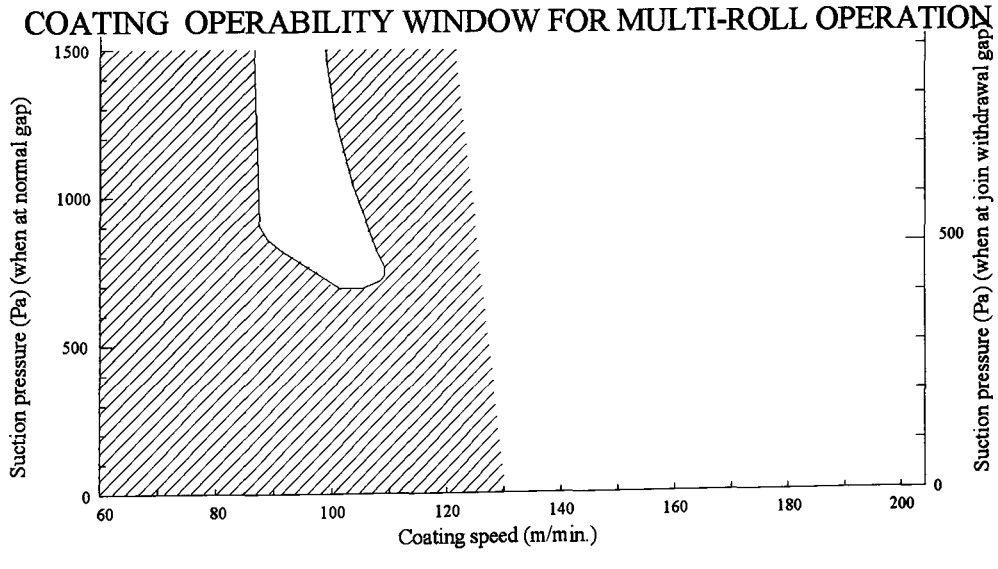

Figure 3.29: Coating Operability Windows for G-C Mix # 1 coated on Subbed Base Type #3S

3.4.4.3 The Justification for Increasing the Slide Inclination Angle

The curtain coating process is known to better cope with rougher substrates than the slide bead process – presumably for the more typical conditions where roughness assisted wetting does not apply (Hartman [1989]). The curtain process has the advantage of providing increased momentum normal to the web in the vicinity of the dynamic wetting line. For the slide bead process, a modest increase in momentum can be achieved by increasing the slide angle, the limit being dictated by the onset of slide waves (Burket et al. [1984]).

Blake & Ruschak [1997] and Schweizer [1997(2)] suggest that the maximum advantage obtained from a falling curtain for holding back air entrainment is obtained when the dynamic wetting line is located at the point of maximum pressure generated by the momentum of the falling curtain. Schweizer et al. [2001], in applying this concept to slide bead coating, show that the benefit from the slide flow momentum is maximum where the slide is inclined normally to the web at the dynamic wetting line – see Figure 3.30.

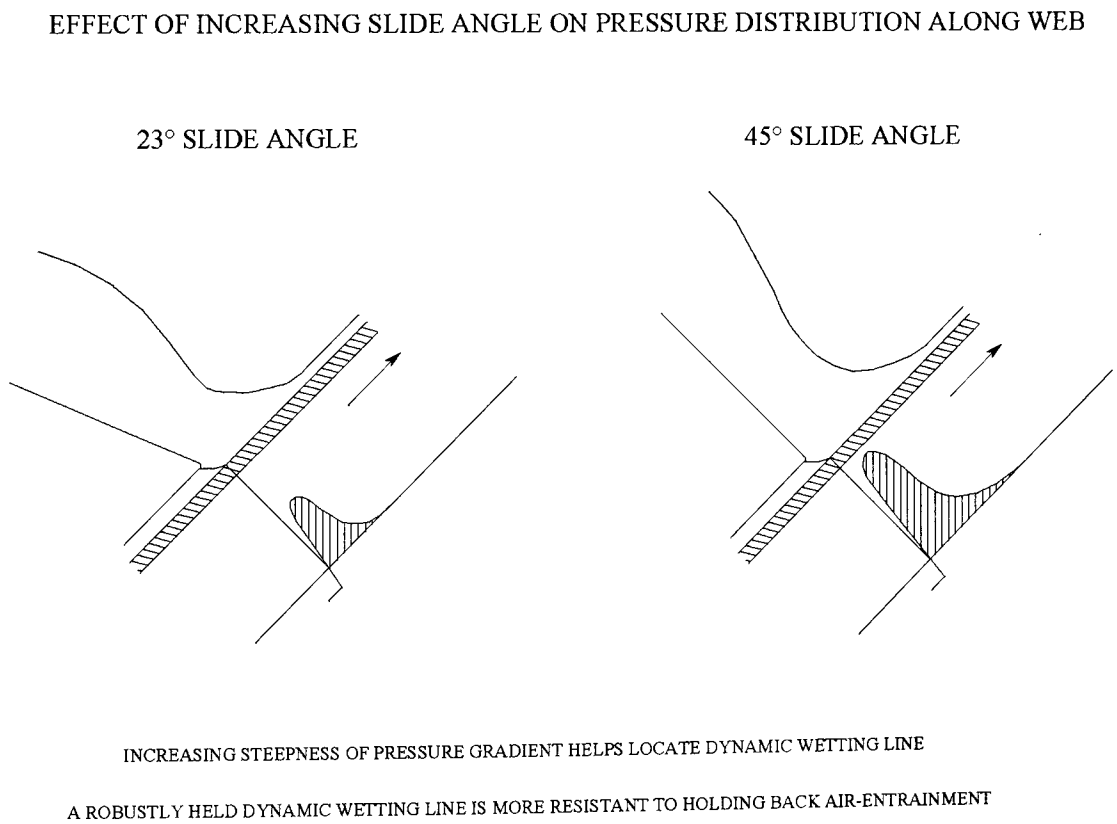

Figure 3.30: Concept for Ideal Slide Coater Geometry, after Schweizer [2001]

This concept is confirmed by Burket et al. [1989], who found that the coating window may be widened by increasing the slide angle to about 45° and setting the application point on the coating roller at 45° above the horizontal. Brace's results moreover strengthen this arguement as showing that coatability is improved by increasing flow rate through diluting the layers and increasing the coating speed.

3.4.4.4 Project to Increase the Slide Inclination Angle to 45°

A project was undertaken to enable the cascade to be reconfigured to present a slide inclination angle of 45° to the horizontal. The specification of requirements, design, installation and commissioning was carried out in direct support of this work – with no support from ILFORD Imaging UK Limited other than resourcing the manufacture of parts and assisting with the final assembly, see Figure 3.31.

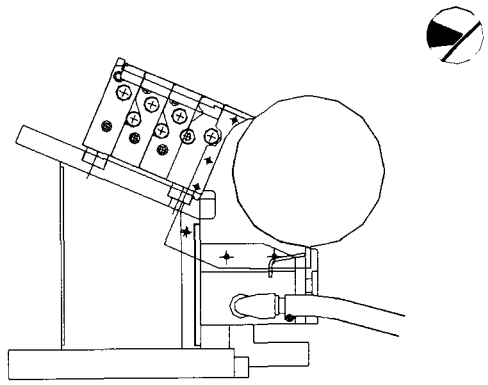

a) Geometry for 23° slide inclination angle

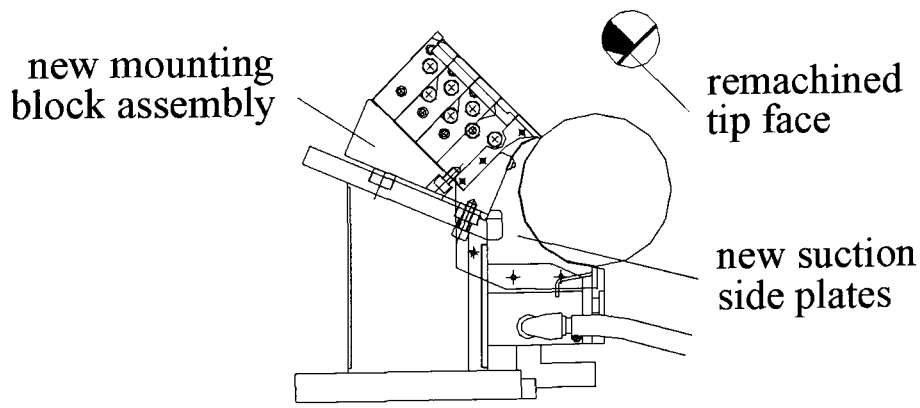

a) Geometry for 45° slide inclination angle

3.31: Modifications to Coater to achieve a 45° Slide Inclination Angle

The work involved designing a new mounting block, new suction side plates and ancillary parts. The tip face was re-machined as shown in order to ensure that it

remained essentially parallel with the web at the point of application, which was set at 45° above the horizontal.

3.4.4.5 The Benefit from the Increase in Slide Inclination Angle

Comparison of Figures 3.29 and 3.32 shows how increasing the slide inclination angle to 45° while retaining the application angle at +45° very significantly enhances the coating window for the single layer G/C Mix #1 of viscosity 44 mPa.s laid down at 96.5 μm wet thickness. The limits imposed by air entrainment at speeds in excess of 170 m/minute are removed when coating with a gap of 127 μm due to the effect of the increased momentum.

It is also of interest that the bead remains more stable against break-up into rivulets as the gap is opened up to 430 μm. The tendency for rivulets is understood to be a severe form of ribbing flow, which is apparently triggered by an increased curvature at the upper free surface (Schweizer et al. [2003]). Further work is clearly needed to fully establish the mechanism explaining the differences in performance, for which both the upper and lower meniscus monitors are ideally suited.

3.4.4.6 The Optimum Rheology when taking advantage of the Increased Slide Angle

The water load carried by the test solution G/C Mix #1 was 89.7 gsm. The motivation for optimising rheology was to reduce the water load as much as possible while maintaining adequate coatability. The first obvious choice was to remove water in the upper layers and to use a thin carrier layer as shown in Table 3.13, for which the water load was reduced to 69.7 gsm.

	Lower layer	Middle layer	Upper layer
Viscosity at $100s^{-1}$ (mPa.s)	8.1	113	132
Density (kg/m^3)	1008	1022	1022
Wet laydown (μm)	6.7	35.6	34.2

Table 3.13: Properties for Carrier Layer Trial using 45° Slide Angle and Type #3S Base

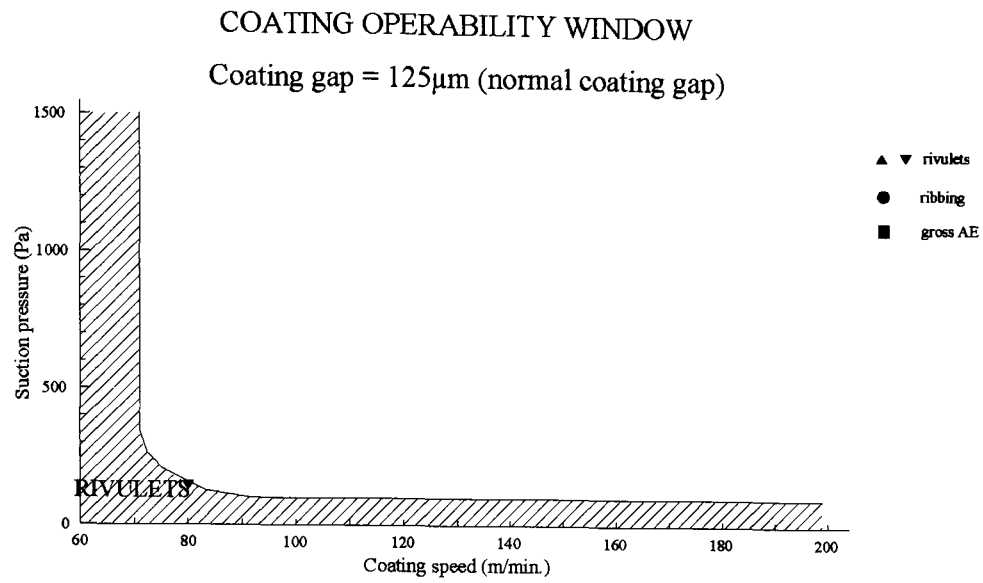

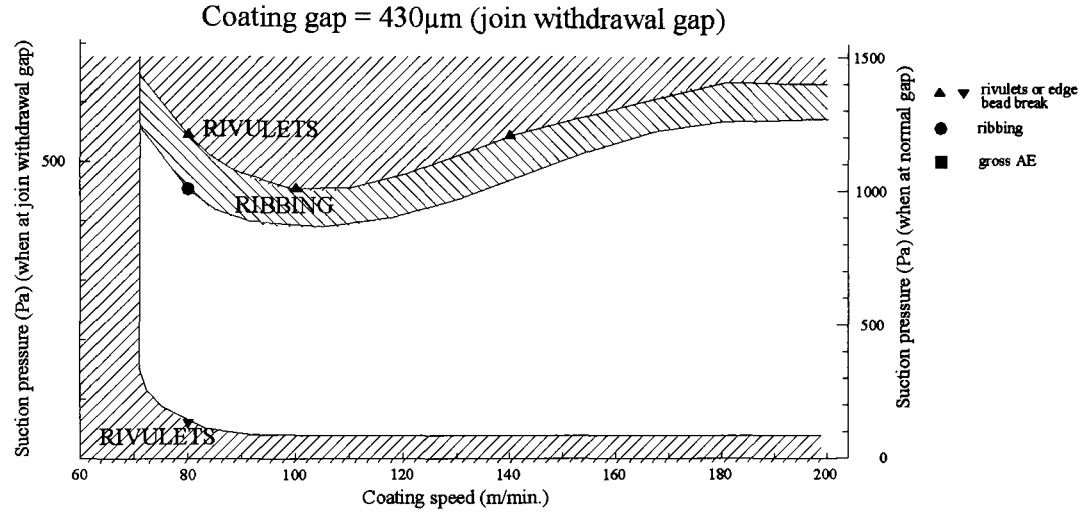

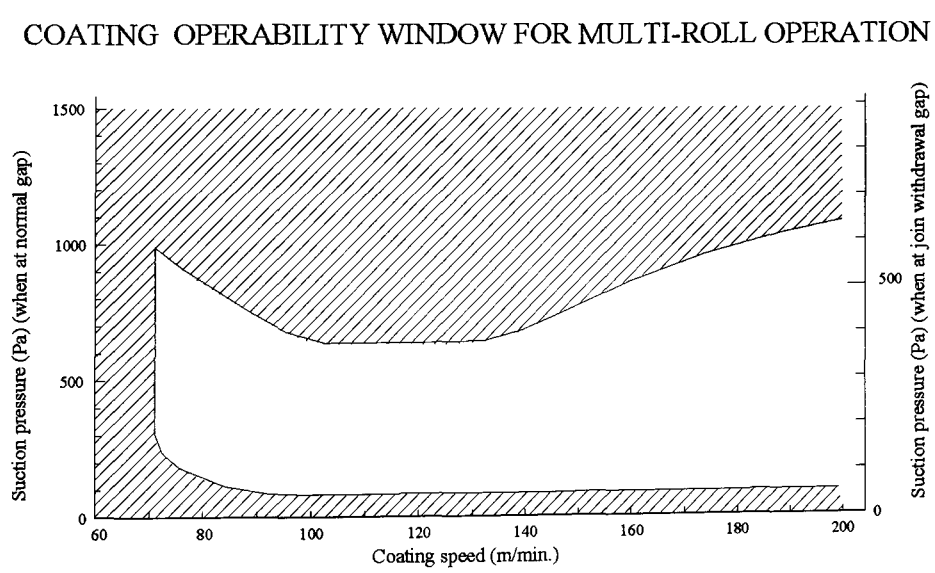

Figure 3.32: Coating Operability Windows for G-C Mix # 1 coated on Subbed Base Type #3S using a Slide Angle of 45°

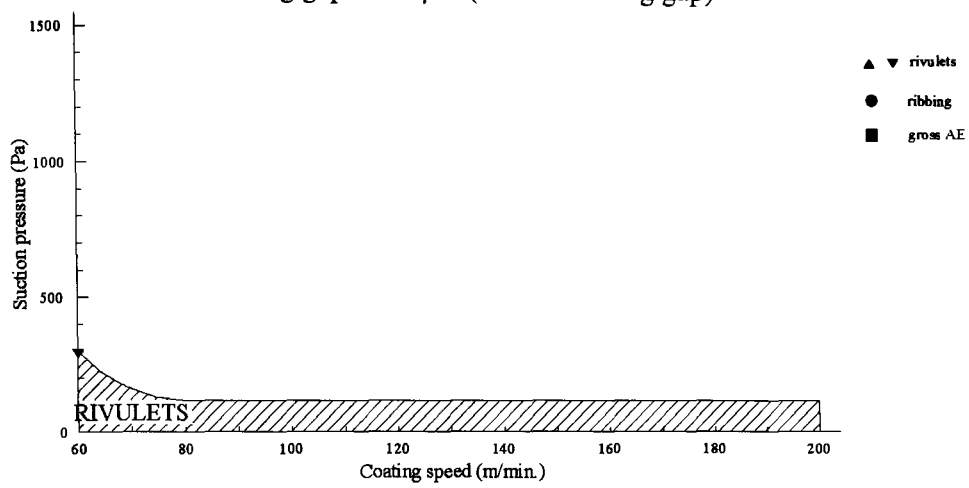

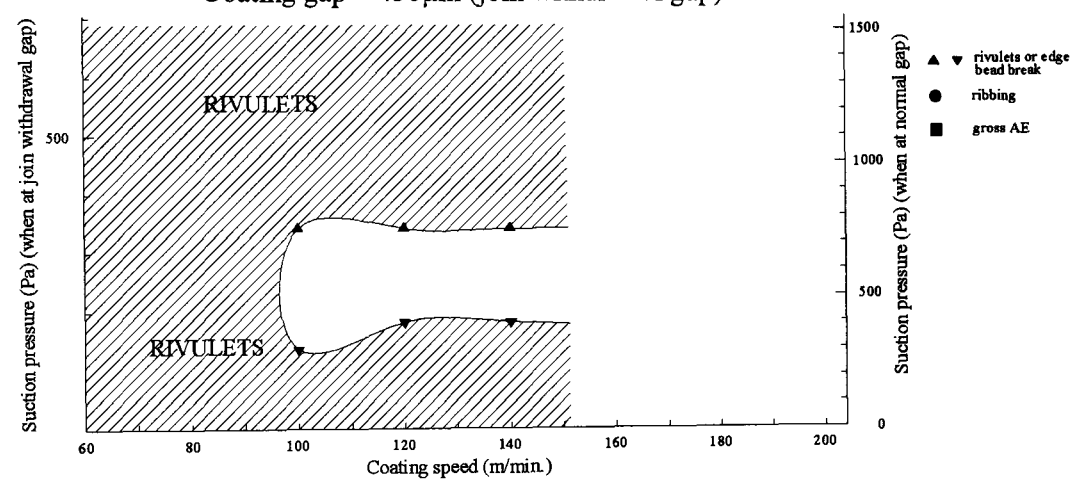

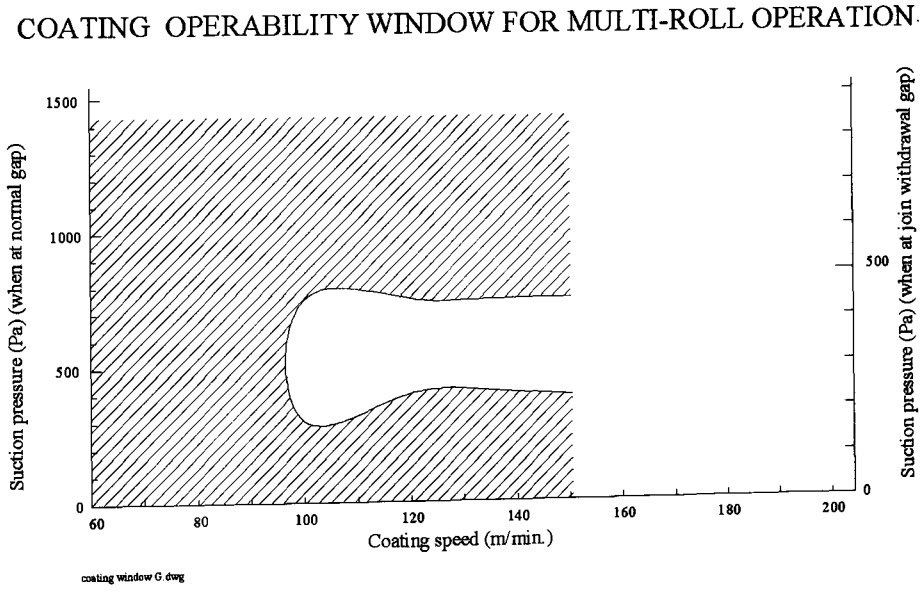

Figure 3.33: Coating Operability Windows using a Thin Carrier Layer coated on Subbed Base Type #3S using a Slide Angle of 45°

As indicated by Figure 3.33, this carrier layer based assembly stills fails to achieve coatability using the rough substrate at the wider gap of 430 μm despite having the advantage of increased slide flow momentum - see Section 3.4.4.5. At coating speeds below 100 m/min, the bead breaks up for all practical levels of applied suction. As pointed out by Blake [2005], this is similar to what is seen with curtain coating where, at low coating speeds and high flow rates, a "heel" is formed at the upstream side of the curtain in the region of the dynamic wetting line – see Schweizer [1997(2)]. Recirculations within the heel result in break-up of the coating into rivulets – a phenomenon often described as "puddling". The ability of the falling curtain to wet the web surface is dictated by the position of the wetting line relative to the bounds of the fully established falling curtain well upstream of the dynamic wetting line.

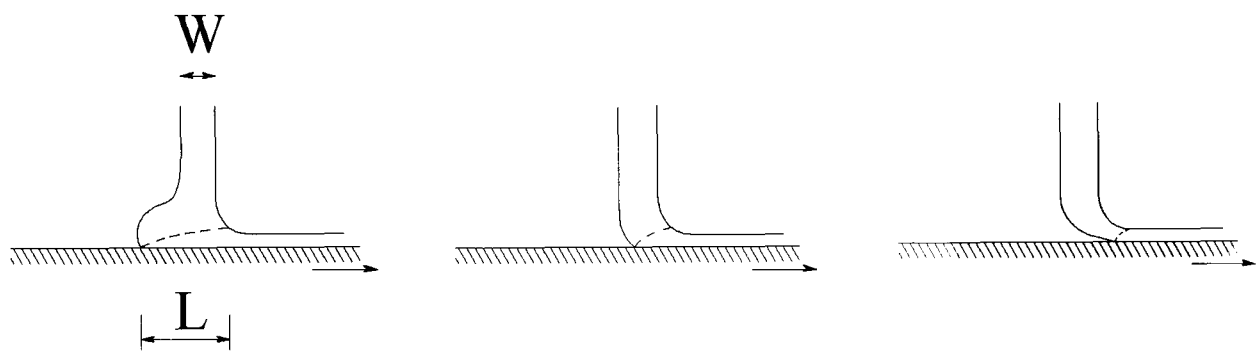

Figure 3.34: The Influence of Wetting Line Position - Curtain Coating

Blake et al. [1994] defined the position of the dynamic wetting line relative to the projection of the falling curtain by a dimensionless relative wetting line position given by:

$$l = \frac{L}{W / \cos(\alpha)} \tag{3.13}$$

where L is length of the boundary layer, W is the thickness of the curtain well upstream of the dynamic wetting line and α is the inclination of the web relative to horizontal. Here, the figure is drawn for where α is zero to draw an analogy with the bead coating study where the slide is inclined normal to the web. Blake et al. [1994] showed that when $l > 1$, this tends to the formation of a heel and hence the tendency for puddling – Figure 3.34(a) – and when l is much less than unity the dynamic contact

angle starts approaching 180° resulting in air-entrainment – Figure 3.34(c). Optimum conditions are attained for where *l* is typically between 1 and 2 – Figure 3.34(b).

Figure 3.35 shows results from profiling the bead using the methods described in Sections 2.12 and 2.13 in order to gain further insight into the reason for why the thin carrier layer failed. It will be seen that the dynamic contact angles are very similar, being 150° ± 3° and 148° ± 3° respectively. These were determined by taking the coordinates of one set of three closely spaced points near to the dynamic wetting line and lying on the curve corresponding to the lower meniscus and a second set on its reflection in the web surface.

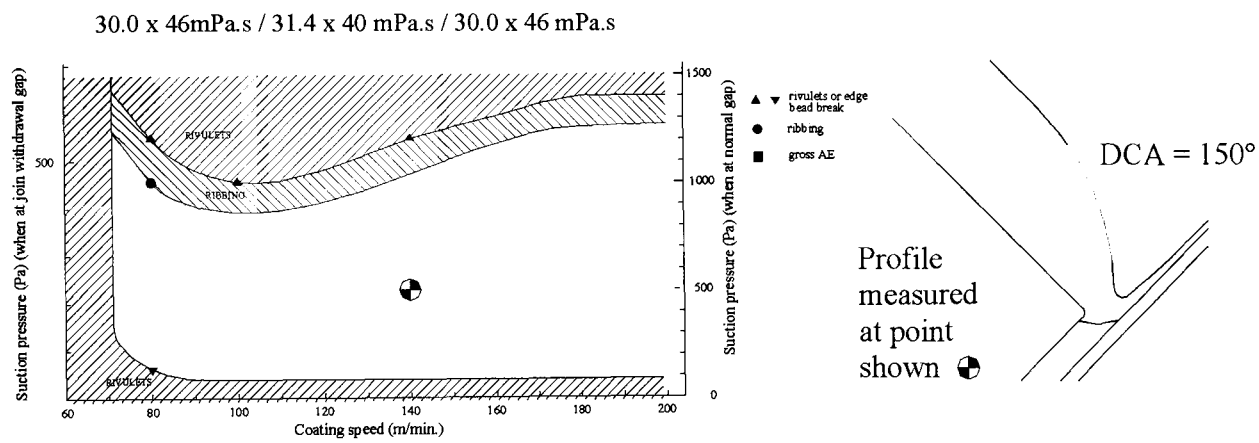

Figure 3.35: Bead Profiles for Conditions shown in Figures 3.32 and 3.33

It will be seen that, whereas the dynamic contact angles are remarkably similar, the position of the dynamic wetting line for the formulation shown in the upper diagram is further down-stream than for the more vulnerable carrier layer based formulation shown in the lower diagram. This compares well with what is observed for curtain coating. It would thus appear from these limited findings that it is the relative position of the dynamic wetting line rather than dynamic contact angle that dictates coating stability under these conditions.

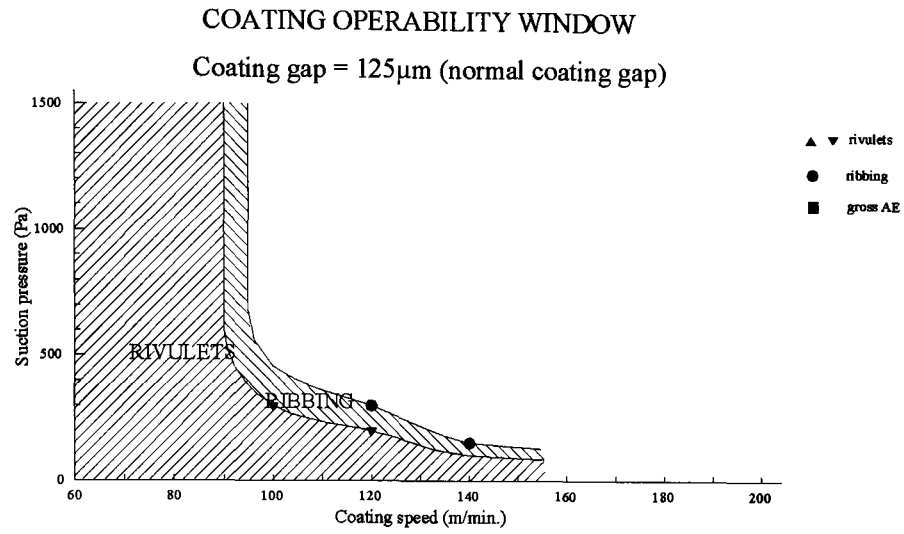

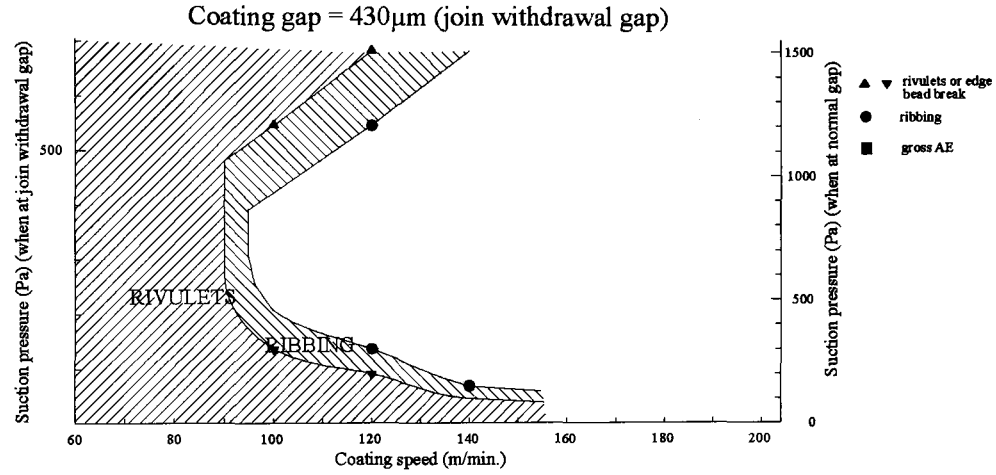

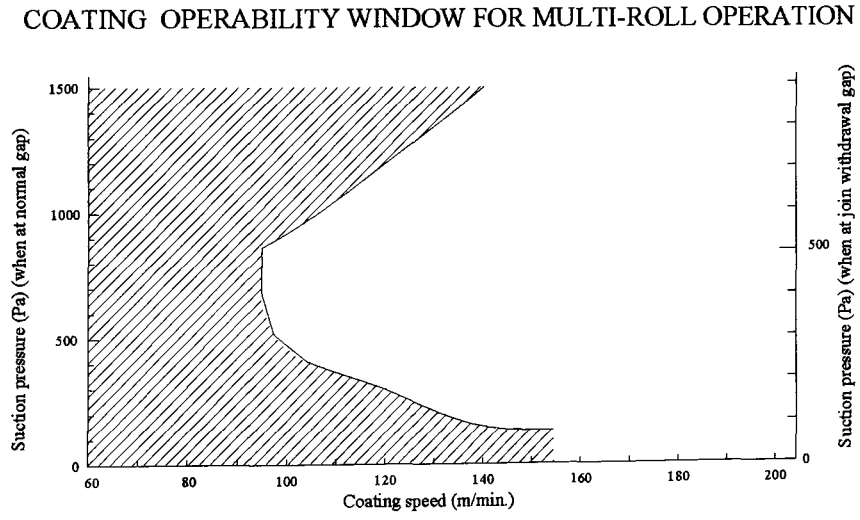

Figure 3.36: Coating Operability Windows using Optimised Formulation coated on Subbed Base Type #3S using a Slide Angle of 45°

The optimum assembly was found to be as shown in Table 3.14 for which the water load was 77.9 gsm and resulted in the coating window shown in Figure 3.36.

	Lower layer	Middle layer	Upper layer
Viscosity at $100s^{-1}$ (mPa.s)	31.0	105	132
Density (kg/m^3)	1008	1022	1022
Wet laydown (μm)	36.3	24.9	23.5

Table 3.14: Properties of Optimised Formulation using 45° Slide Angle and Type #3S Base

These results would again appear to suggest that the wet thickness of the bottom carrier layer should exceed the roughness parameter Rz and the viscosity a few tens of mPa.s in order to secure an adequately wide coating window.

3.4.5 The Effect of Surface Property on the Performance of a Thin Low Viscosity Carrier Layer

A further experiment was run to compare the coating behaviour throughout join-withdrawal of the subbed surface #3S with that of the unsubbed corona treated polyethylene surface #2C when coated with a formulation conventionally considered for a carrier layer (Dittman and Rozzi [1977]) and shown in Table 3.12. The laydown was 76.5 μm thick overall and included two upper layers of viscosity exceeding 100 mPa.s and a 6.7 μm thick carrier layer of viscosity 8.1 mPa.s – see Figure 3.37.

The differences in wetting kinetics are once again more clearly revealed by the position of the dynamic wetting line rather than dynamic contact angle, the values being 150° for the subbed 3#S surface and 148° for the unsubbed #2C surface. The roughness assist mechanism described by Clarke et al. [2003] is unlikely to be functioning under these conditions owing to the very low viscosity of the bottom layer.

3.4.6 Conclusions and Discussion

The causes of variations in the coating window seen when coating rough substrates are highly complex – involving the onset of both air entrainment and ribbing and ultimately rivulets.

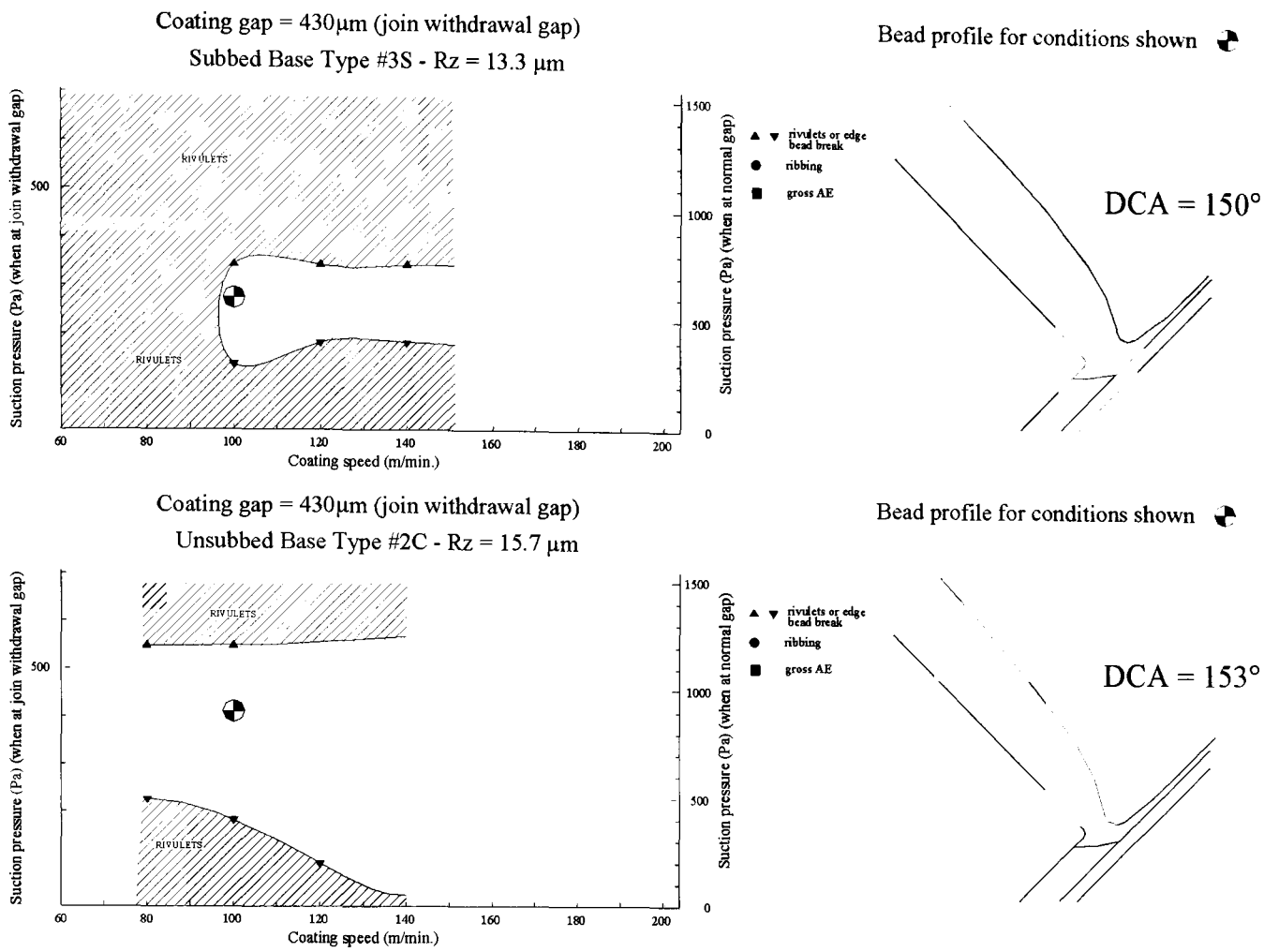

Figure 3.37: Use of a Thin Low Viscosity Carrier Layer for Base Types #2C and #3S

This study suggests metastable conditions can exist for the slide bead process where air entrainment is either present or absent, depending on starting conditions. A similar effect is well known for the curtain process but apparently not hitherto reported for the slide bead process. It has been frequently shown that under such conditions, defect-free coating can be achieved by temporarily opening up the gap and then restoring back to a value for ensuring a wide coating window. It is suggested that the position of the dynamic wetting line and hence stability against air entrainment can be moved from an unfavourable position to a favourable one through the action of the excess pressure exerted as the gap is restored after join-withdrawal. There is scope for investigating this effect further using the specially developed lower meniscus monitor.

Coating windows have been investigated for surfaces provided by three industrial paper webs precoated with polyethylene and characterised by a roughness Rz in the range 14.5 ± 1.2 μm.

Initial experiments were confined to investigating the performance of the two unsubbed web surfaces to avoid complications due to the effect of surface energy. The robustness against rivulets at low speed and air entrainment at higher speeds for a 96.5 μm thick 38 mPa.s single layer is significantly increased for the embossed "pearl" web of surface index 2.39 as compared with the unembossed web of surface index 1.95. It is suggested, following the work of Clarke et al. [2000(1)], Clarke [2002] and Clarke et al. [2004] for curtain coating and of Clarke et al. [2003] for slide bead coating that the pearl surface may be encouraging composite wetting at these slightly higher bottom layer viscosities to a greater degree than for the surface with lower surface index and hence smaller number of sharply spiked asperities per unit area. This view is supported by the fact that Clarke et al. [2003] found it was possible to coat a 75 μm three layer assembly onto unsubbed polyethylene coated base of roughness given by an Rz value of 9.7 μm at 270 m/min. using 400 volts charge assist where the bottom layer viscosity was 40 mPa.s. On increasing the lower layer viscosity to 70 mPa.s, the required surface voltage was found to be only 250 volts – a value approaching that measured in the experiments reported in this work.

It would thus appear that the surface area ratio is as important as the value of Rz and Ra when seeking to correlate roughness with the ease of coating. It is suggested that the measurement of critical tilt angle (Wolfram and Faust [1978] and Miwa et al. [2000]) for a pure water drop of controlled size could provide a possible indicator for the ease of coating. Alternatively the method of Menchaca-Rocha [1992] for determining the stopping distance for fast moving mercury drops could be developed for water drops to advantage. Such tests, once applied, may well show trends leading to further understanding on why coatability can vary over time when coating nominally consistent substrates.

The mechanism for roughness assisted wetting is believed unlikely for lower bottom layer viscosities as the viscous bending forces responsible for pinning the interface to the peaks of sharp asperities in the surface are much lower - Clarke et al. [2000(1)], Clarke [2002], Clarke et al.[2003] and Clarke et al. [2004]. In an experiment to investigate the coatability of an 81.3 μm thick two layer assembly on unsubbed web of surface index 2.39, the robustness against air entrainment at high speeds improved as

the viscosity of the 65 μm thick bottom layer was reduced from 32 to 19 mPa.s. A thin low viscosity carrier layer thus proves advantageous when coating this material.

Pre-coating the polyethylene surface with a gelatine subbing layer to improve adhesion induces further problems for coating owing to the adverse change in surface energy. The robustness against rivulets and air entrainment is severely reduced as the gap is increased to allow through passing joins. Stable conditions can be restored in this case by taking advantage of the increased momentum of flow down the slide by increasing the slide inclination angle from typically 23° to 45°.

A thin low viscosity carrier layer is no longer effective when coating this gelatine subbed material. The experiments suggest that only as the bottom layer thickness exceeds the roughness value Rz can the bottom layer viscosity be reduced with advantage. It is then possible to optimise the formulation for faster drying by increasing the solid content of the other layers.

Bead profiling studies appear to indicate that the robustness against rivulets at low coating speed is associated with the position of the dynamic wetting line relative to the projection of the slide surface onto the web – rather than on dynamic contact angle alone. This view is supported by experimentally proven evidence for curtain coating from which it is concluded that the maximum speed dictated by the onset of air-entrainment is where the dynamic wetting line lies immediately below the back surface of the falling curtain.

3.5 The Effect of Free Electric Surface Charge

The following case study involved attempting to coat a simple 10% gelatin solution of viscosity 19mPa.s at a wet thickness of 85 μm. The solution contained a small amount of surfactant and the aim was to coat at a speed of 45 m/min onto three different types of triacetete film base – supplied and manufactured by separate supply companies.

Two of the bases - A and B - presented no difficulty when making the bead, whereas base C completely failed to coat.

3.5.1 Dynamic Contact Angle Measurements

The dynamic contact angle for each film base surface was measured over a range of coating speeds varying from 10 m/min to 90 m/min – using the needle coating technique described in Section 2.10. The same gelatin solution was used for the tests as for the pilot coating trials and the results are shown in Figure 3.38.

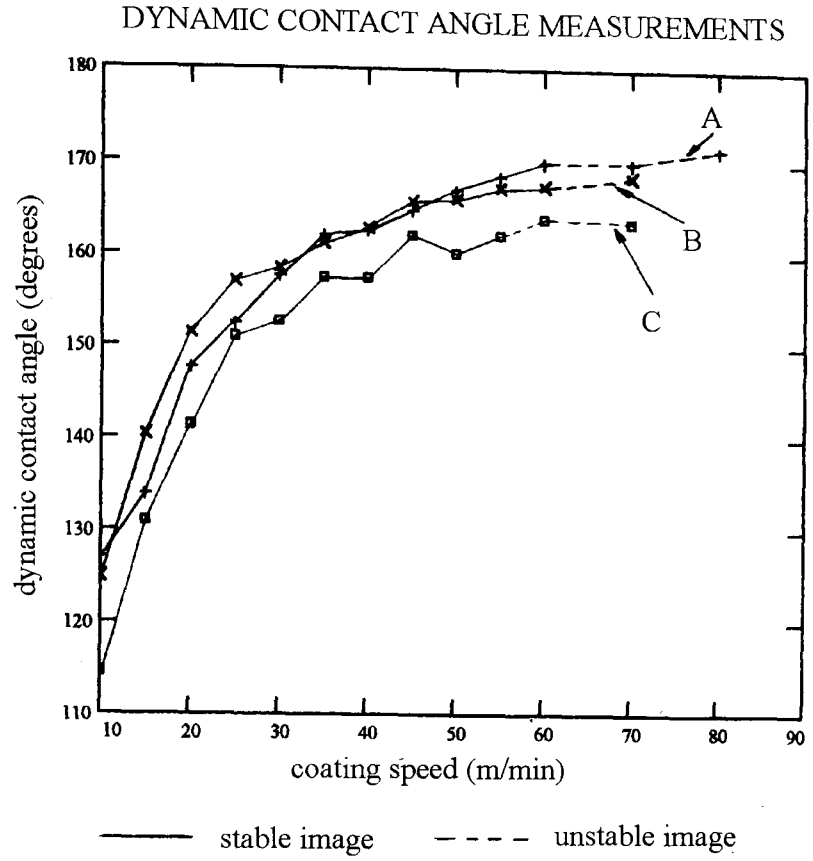

Figure 3.38: Dynamic Contact Angle Measurements on Three Film Base Surfaces

The dynamic contact angle measurements would apparently show that surface C was in fact more wettable than A and B. However, close observation of the image of the microbead showed this to be significantly less stable at higher coating speeds when coated on sample C as compared with sample A and B – as depicted by the dotted lines in Figure 3.3. Moreover, the microbead when applied on base C entrained air at significantly lower speeds than when applied to bases A and B.

From observations of the tendency for adjacent web surfaces to stick together at the unwind point, it became clear that base C was generating excessive free surface electric charge or "static". This was due to the fact that the material carried no antistatic coating – unlike base sample A and B. The effect of a varying electric charge is known to yield non-uniform coating thickness, Gibbons (1972). One possible

explanation is that the instability seen in the needle coating was associated with large variations in surface charge. This could explain the problems found when attempting to coat base C using the slide bead process.

3.5.2 Effect of Coating Gap and Stabilisation Suction

Pilot slide bead coating experiments showed that increasing the coating gap and increasing the stabilisation suction helped to restore the ability to make the bead for the defective base C. The reason for this interesting result has yet to be understood.

3.5.3 Effect of Diluting the Coating Solution

Diluting the gelatin formulation from 10% to 8% while maintaining the required dry coating weight also increased the robustness of the process against air entrainment. It is likely that this can be explained by two factors:

1. A decrease in dynamic contact angle caused by the corresponding reduction in viscosity from 19mPa.s to 11mPa.s viscosity
2. An increase in wet laydown by reason of the added water

Further dilution to 6.9% with a corresponding lowering of the viscosity to 8mPa.s resulted in yet further increase in robustness against air entrainment.

3.5.4 The Effect of using a Thin Low Viscosity Carrier Layer

The ultimate limit to reducing concentration is often dictated by the drying capacity of a given plant due to the corresponding increase in water load. Consideration was therefore given to two different assemblies each incorporating an additional carrier layer as shown in Table 3.15 - as a means of resisting entraining air while maintaining high solids content in the main layer required for the end use. Contrary to expectation, however, neither of these assemblies restored the ability to make the bead on base C – for reasons that are unclear.

	Carrier layer laydown	Carrier layer viscosity	Main layer concentration	Main layer viscosity
Assembly 1	10 μm	10 mPa.s	10.02 %	19 mPa.s
Assembly 2	10 μm	7 mPa.s	10.02 %	19 mPa.s

Table 3.15: Assemblies incorporating a Thin Low Viscosity Carrier Layer

3.6 The Effect of Polar Electric Surface Charge

3.6.1 Introduction

Consideration is given in this section to the effect of redistributing the orientation of bound polar charges residing within the web or its component layers. This is particularly applicable to paper webs that have been pre-coated on both sides with resin (typically polyethylene) in order to render the substrates impervious to water. The application of electrostatic assist to coating is well established within the coating industry in general – Kisler et al. [1984]. As discussed in more detail in Section 1.5.3, many techniques are available for enabling charge assisted coating as revealed in the abundant patent literature – see for example, Gibbons et al. [1972], Kisler et al. [1984], Hartman [1989] and Quiel et al. [2002]. The work of Clarke et al. [2000(2)] and Clarke et al. [2003] shows how charge assist can be used advantageously for rough as well as smooth substrates for both curtain and slide bead coating processes. A model proposed by Blake et al. [2000] shows how charge assist generates a force, which acts normally on the lower free surface in such a way as to reduce the dynamic contact angle and hence increases the speed of coating by postponing air entrainment. This model has been well validated for curtain coating but not for the slide bead process. Zaretsky et al. [2001] point out the necessity of ensuring the resistivity of the substrate exceeds well defined limits expressed by the "characteristic electrical length" and state this should ideally not exceed 100 μm – see Section 1.5.3.

It is now well established that charge assist, while advantageous to resisting air entrainment, results in increased susceptibility to ribbing - Vandaela and Vancoppenolle [1999] and Quiel et al. [2002]. Vandaela and Vancoppenolle [1999]

suggest this is caused by increased curvature in the downstream free surface but do not show concrete experimental evidence for this.

The lower meniscus monitor and the upper meniscus monitor described in Sections 2.12 and 2.13 provide a powerful means for furthering the understanding of what is happening at the free surfaces when investigating these effects. Two sets of trials were run using the charge control equipment installed on the pilot coating machine and described in Section 2.5.1.3 and modified as described in Section 2.5.2.4 and will now be described in detail.

3.6.2 First Set of Coating Trials

A case study was set up in which a single layer was coated at a wet laydown of 65 μm onto unsubbed on-line corona treated "glossy" paper base type #1C at 50 m/min. and subjected to a cyclically varying surface charge as described in Section 2.5.2.4. The coating gap was set at 165 μm and the suction pressure at 275 Pa. Provision was made for the coating gap to be subsequently opened to 508 μm by triggering the join-withdrawal activation mechanism described in Section 2.5.1.4. The stabilisation suction fell to 165 Pa under these conditions due to increased air leakage into the suction box. The solution comprised photo-paper emulsion and thus was ideal for enabling the bead to be profiled using the lower meniscus monitor described in Section 2.12 and the upper meniscus monitor detailed in Section 2.13. The viscosity of the coating solution was 24.2 mPa.s when measured at 100 s^{-1}. The dynamic surface tension characteristics were as shown in Figure 3.39. The four parameters defined in equation (3.3) in Section 3.2.1 were $\sigma_M = 19$ mNm^{-1}, $\sigma_0 = 46.5$ mNm^{-1}, $t^* = 0.3$ s and $n = 0.6$.

The voltage waveform measured using a TREK model 366 surface charge probe mounted beneath the coating roller was as shown in Figure 3.40. The lowest and highest voltages were +5v and +507v respectively and the period 4.2 seconds. The lower meniscus monitor was used to record the dynamic response of the lower free surface to this varying polar charge for both gaps. The video output was mixed with

that from a camera aimed at the oscilloscope screen displaying the charge waveform using the multiplexer described in Section 2.7.2 for ultimately showing both images in quadrature – as shown for example for the larger gap in Figure 3.41. The image on the left indicates the charge waveform and that on the right the lower meniscus seen at the camera focal plane. The vee-shaped profile is due to glancing reflection from the surface of the uncoated web (see Section 2.12.4 and Figure 2.72.) A video clip showing the response of the lower free surface for both gaps is appended with the thesis – see Appendix II – video sequences #5a and #5b.

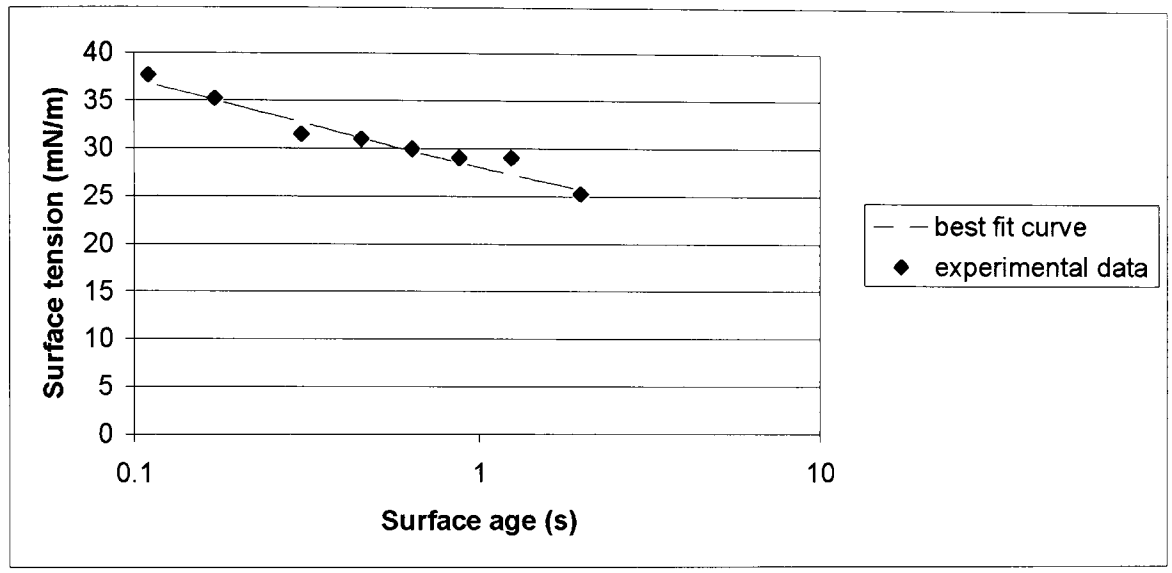

Figure 3.39: Dynamic Surface Tension Characteristics for Coating Solution

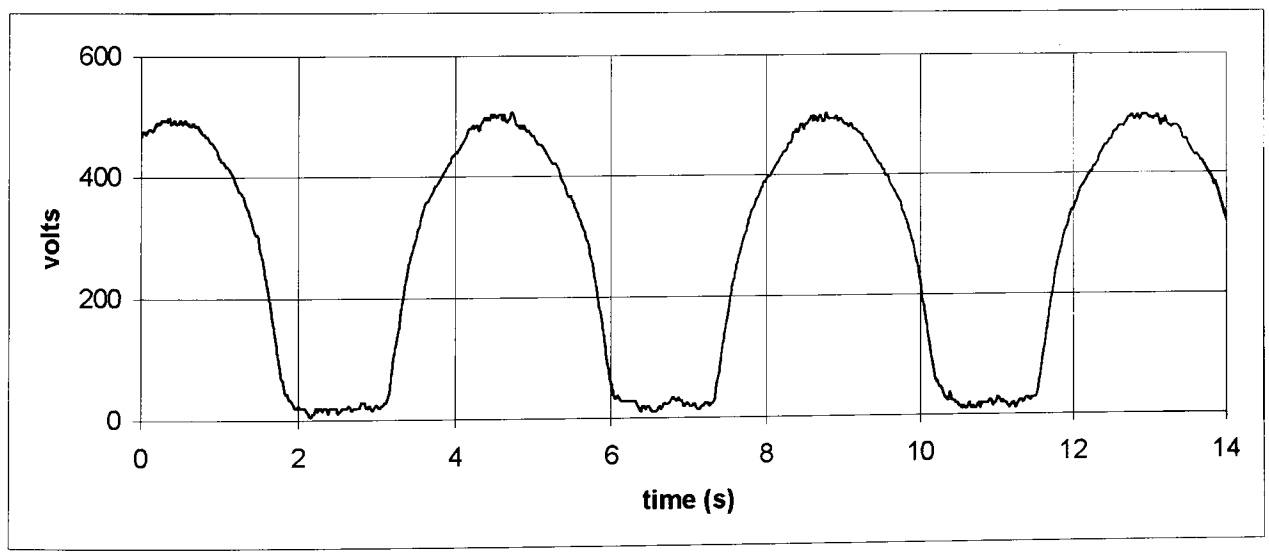

Figure 3.40: Charge Waveform used for the First Set of Charge Assist Trials

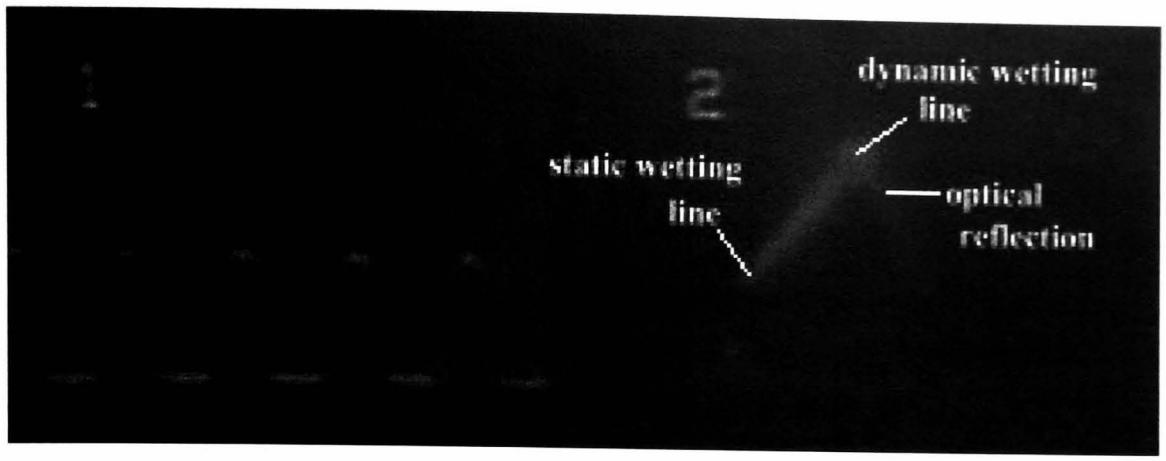

Figure 3.41: Typical Images comparing Charge with Response of the Lower Meniscus

Figures 3.42 and 3.43 show the position and shape of the lower free surface for both gaps when the charge is at the minimum and maximum values.

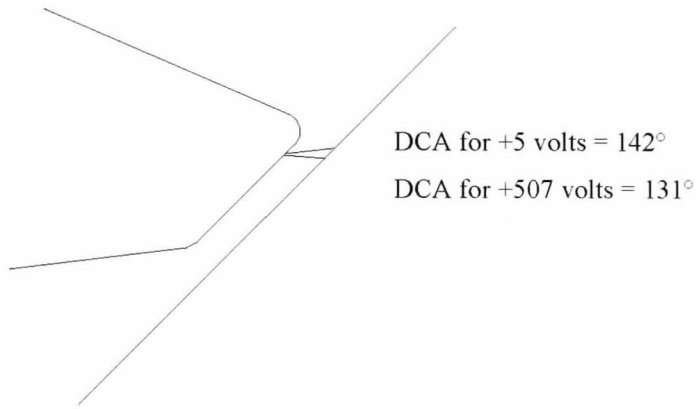

Figure 3.42: Response of the Lower Meniscus to Varying Charge for 165 μm Gap

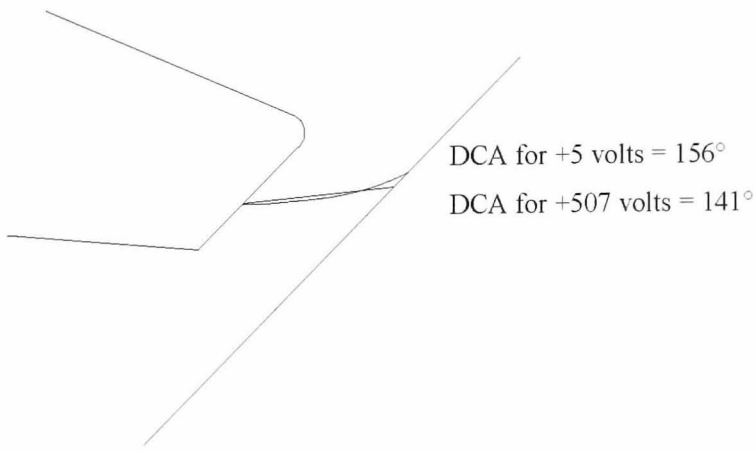

Figure 3.43: Response of the Lower Meniscus to Varying Charge for 508 μm Gap

Figures 3.44 and 3.45 show corresponding results for the response of the upper meniscus to varying polar charge with the gap set at 508 μm – see also Appendix II – video sequences #5c and #5d.

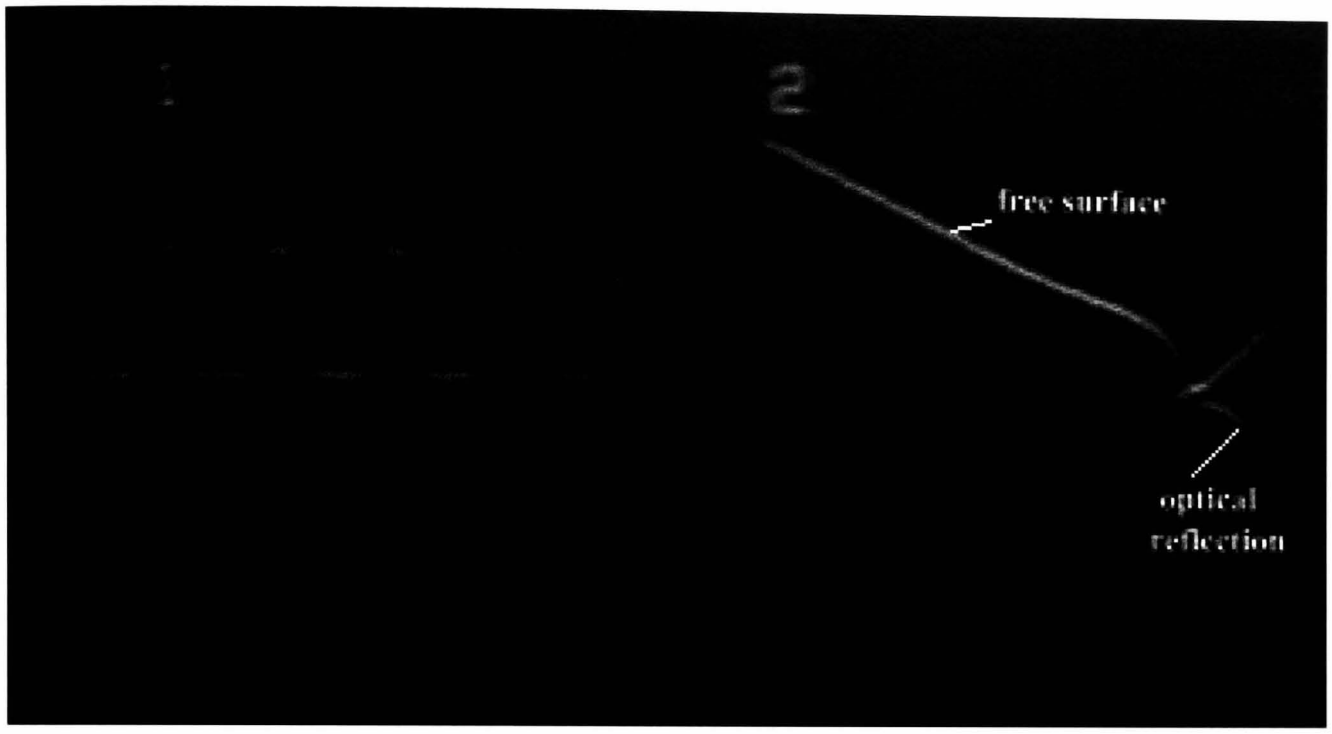

Figure 3.44: Typical Images comparing Charge with Response of the Upper Meniscus

3.6.3 Second Set of Coating Trials

The method for cycling the charge while continuously monitoring the free surfaces was especially useful for eliminating any errors in defining the response of the static wetting line to changes in charge level. This was due to the fact that the monitoring apparatus was maintained in one position throughout and thus mechanically stable. The method was, however, limited in that the maximum achievable web potential was constrained to about +500 volts and thus at the lower end of the range generally considered useful for charge assist – Quiel et al. [2002].

A second set of trials was therefore run in which the charge control system was optimally configured and adjusted over two separate runs to achieve firstly 0 volts and secondly +700 volts - as monitored by the Trek model 366 probe. A solution of viscosity 24.2 mPa.s was coated as a single layer onto unsubbed "pearl" base type #2C. The laydown was set at 70.6 μm and the coating speed at 80 m/min. The gaps were adjusted to 165 μm for normal coating and 495 μm for join-withdrawal, the

suction pressures being 492 Pa and 292 Pa respectively. Figure 3.46 shows the resultant change in bead profile as surface voltage increased from 0 volts to +700 volts.

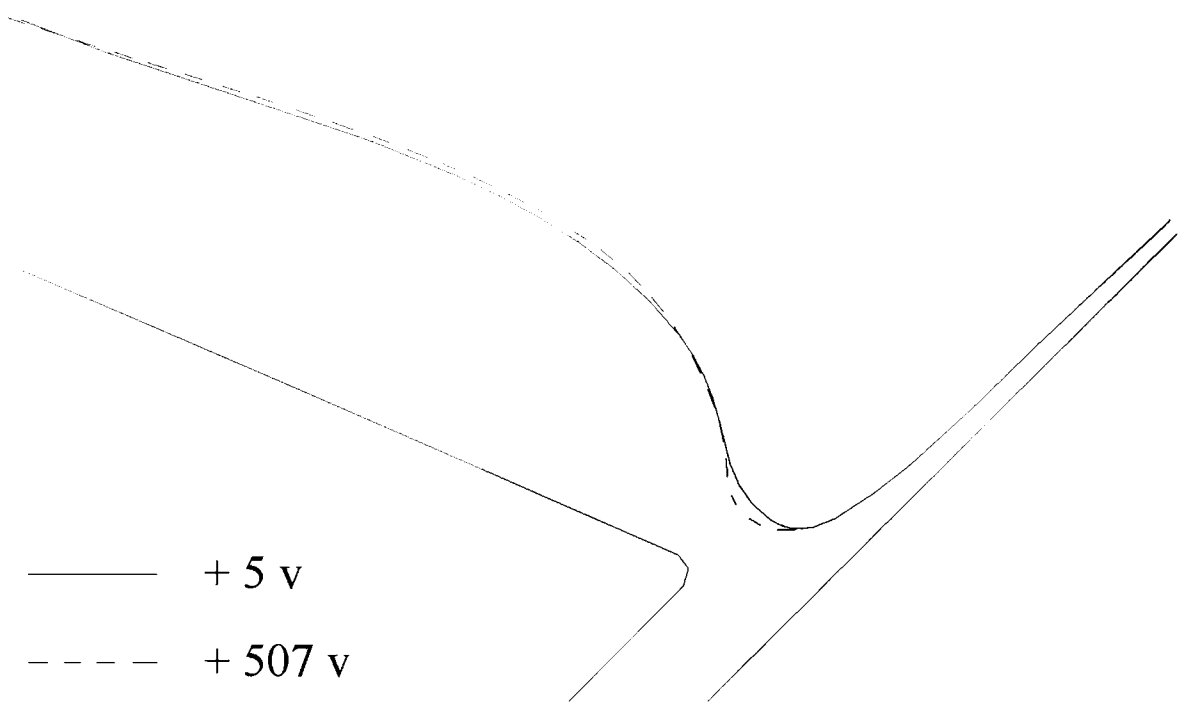

Figure 3.45: Response of the Upper Meniscus to Varying Charge for 508 μm Gap

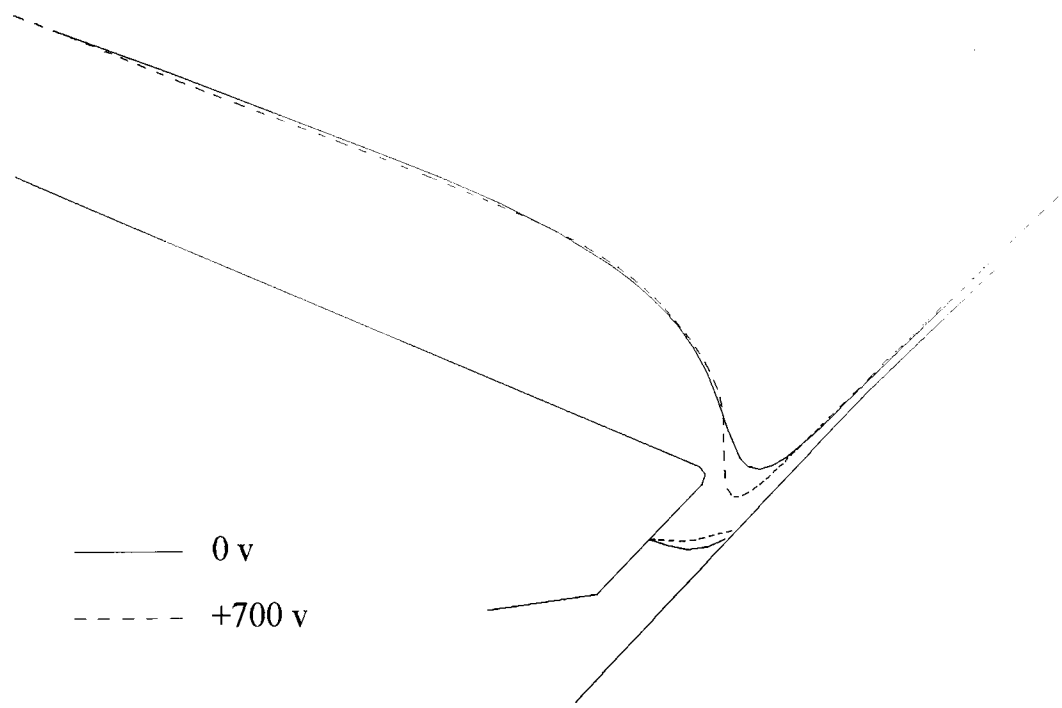

Figure 3.46: Response of the Free Surfaces to Varying Charge for 495 μm Gap

3.6.4 Conclusions and Discussion

Figures 3.42, 3.43 and 3.46 show that the dynamic contact angle decreases dramatically with increase in surface charge – see Tables 3.16 and 3.17.

Base voltage	+5 v	+507 v
Normal gap (165 μm)	142°	131°
Join withdrawal gap (508 μm)	156°	141°

Table 3.16: Dynamic Contact Angles for First Set of Charge Assist Trials

Base voltage	0 v	+700 v
Join withdrawal gap (495 μm)	164°	142°

Table 3.17: Dynamic Contact Angles for Second Set of Charge Assist Trials

The results thus qualitatively confirm the predictions from Blake's dynamic wetting model (Blake et al. [2000]). They additionally demonstrate that charge assist serves to pull back the dynamic wetting line by reason of the electrostatic force but that the static wetting line remains fixed. The electrostatic forces acting on the free surface thus predominate near the dynamic wetting line, whereas forces due to the suction pressure applied to the lower meniscus act equally over its entire length.

This result is especially interesting in that whereas charge assist serves to increase robustness against air entrainment, it also does so with less risk of downward migration of the static wetting line than when suction pressure is used alone. Downward migration of the static wetting line tends to larger recirculations in the stagnant region trapped between the tip face and the separation line – see Figure 1.12. Such recirculations are known to be associated with the formation of unwanted streak defects – Schweizer [1988], Ikin et al. [1997], Hens and Van Abbenyen [1997], Apps, Ikin and Thompson [1999], Gaskell et al. [1999] and Noakes et al. [2002(1)]. It is suggested that charge assist not only tends to increased air entrainment speeds but can also result in a significant improvement in the quality of the final coating.

The results shown in Figure 3.45 and especially Figure 3.46 depicting the upper free surface clearly demonstrate a deepening of the bead "waist" with increased surface charge. One possible explanation is that increased charge tends to decrease interfacial tension - Kisler et al. [1984] – and consequently reduces the radius of curvature of the meniscus for a given pressure within the fluid – as shown by equation (3.8) - Section 3.2.2. The effect of a deeper bead waist is known to be associated with an increased tendency for ribbing – Schweizer et al. [2003]. Unfortunately lack of materials prevented investigations into the tendency for ribbing instability in these experiments but the results nevertheless give some credence to the claim by Vandaele and Vancoppenole [1999] that the instability seen with charge assist is associated with increased curvature of the downstream free surface.

3.7 The Effect of Porosity and the Benefit of using a Carrier Layer

The coating of porous media adds yet further complexity to the mechanisms responsible for acceptable coating performance. The dynamic wetting of the pore structure is such that air can become trapped within the cavities to be released later as the pressure is restored to ambient – see Section 1.5.4. The motivation for studying these effects comes from the wide use of these materials within industry. A substrate can be porous by the nature of its manufacture. An impervious substrate can subsequently become porous when pre-coated with a layer of loosely bound particles.

Water will tend to diffuse out of the bottom layer to become imbibed into each pore. It may be assumed, for the sake of simplicity, that the depth $x(t)$ penetrated as a function of time t into a capillary of radius R for a liquid of viscosity μ is given by the Lucas-Washburn equation (Blake & De Coninck [2004]):

$$x(t) = \sqrt{\frac{\gamma_{LG} R \cos\theta}{2\mu}}\ \sqrt{t} \tag{3.14}$$

where γ_{LG} is the surface tension of the liquid and θ the effective contact angle between the liquid and the capillary wall. Taking t as being typically the transit time across the mouth of a single pore and given by:

$$t = 2R/U \tag{3.15}$$

and R as 2.5 μm for a typical porous surface, μ as 1mPa.s, γ_{LG} as 20 $mN.^{-1}$ and θ as 60°, then *x(t)* is given from (3.14) and (3.15) as 11.2 μm. The depth of penetration during this very short transit time is thus of the same order of magnitude as the wet thickness of a typical bottom layer. The rate of water imbibition is thus sufficient to cause the solids concentration and hence the viscosity to spontaneously increase at the dynamic wetting line to adversely affect coatability.

This section summarises some experimental results when attempting to coat substrates with varying amounts of surface porosity.

3.7.1 First Case Study

Practical experience in attempting to coat the three layer formulation shown in Table 3.18 onto paper webs pre-coated with a porous barrier layer have met with varying degrees of success. Some surfaces could be readily coated at 100 m/min whereas severe difficulties were found in making the bead on others.

	Bottom layer	Middle layer	Top layer
Wet thickness (μm)	26.25	28.37	27.84
Viscosity (mPa.s)	28.7	112.5	119.1

Table 3.18: Properties of Three Layers used to coat a Porous Surface

Dynamic contact angle measurements revealed no obvious reason why some surfaces were more difficult to coat than others whereas a clear correlation has been found between maximum coating speed and surface porosity.

3.7.1.1 Dynamic Base Wetting Test

A novel test was devised for enabling a quantitative measure of base wetting – under the conditions applicable to the problem being investigated. This makes use of the join-withdrawal mechanism on the pilot coater. The sample of web to be evaluated for wettability was spliced to a "leader" comprising material known to coat well. The machine was then run up to speed and the head dipped in on the leader. By activating the scrape-off lifting mechanism just as the splice arrived at an appropriate point, it was possible to arrange the 1 metre long sample to include the splice and thus reveal the coating behaviour either side of the join. Figure 3.47 shows a typical result.

The degree of incompatibility of dynamic wetting of the trailing base surface relative to that of the reference surface can be assessed by measuring the rate of edge retraction. A convenient method is based on measuring the characteristic angle subtended between the retracting edges.

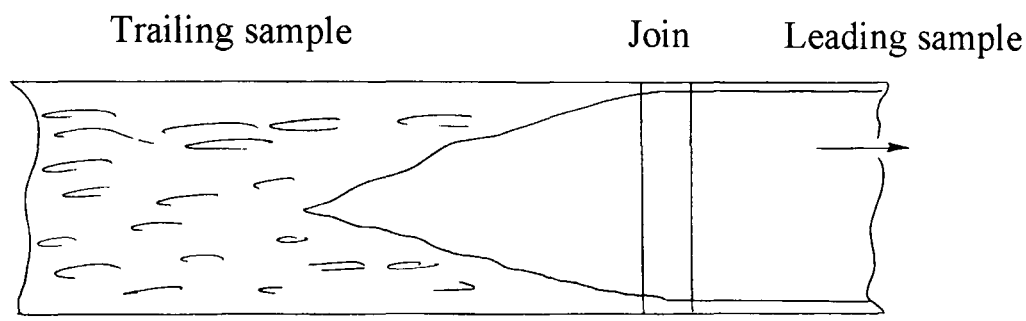

Figure 3.47: Edge Retraction over a Trailing Sample of Base of Poor Wettability

The test can be further applied to determine the web speed for which the edges no longer retract at the join. This showed that for a sample of more highly porous web, the maximum achievable coating speed was only 80 m/min as compared with 100 m/min using a less porous web.

3.7.1.2 The Effect of using a Thin Carrier Layer

Trials run on the pilot coater demonstrated that using an additional carrier layer of viscosity 20 mPa.s laid down at a wet thickness of 10 $ml.m^{-2}$ enabled the coating speed to be restored back to at least 100m/min for the more highly porous base.

3.7.2 Second Case Study

3.7.2.1 Defects due to Outgassing

Additional problems can occur when attempting to overcoat a porous surface – including, for example, a paper web pre-coated with a layer that is not completely impervious to water. The freshly applied coating only partially penetrates into the pores and traps minute pockets of air. These can then be released as pressure relaxes back to ambient leaving blowholes – typically as shown in the scanning electron micrograph image – Figure 3.48. This effect was obtained in one case study where a porous surface was overcoated at a speed of 30 m/min with a layer of wet thickness

145 µm - comprising solution containing 15.5% solids and of viscosity 12.8 mPa.s measured at a shear rate of 100 s^{-1}.

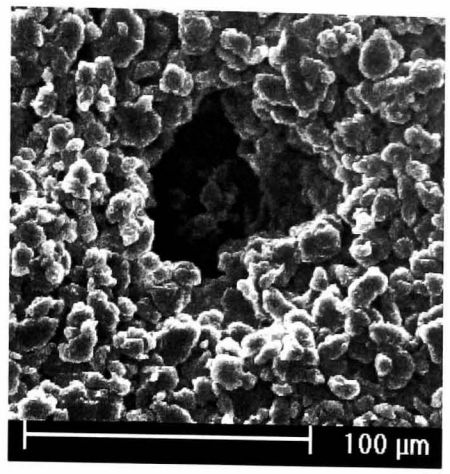

Figure 3.48: Typical Blow Hole due to Outgassing

3.7.2.2 The Effect of using a Thin Low Viscosity Carrier Layer

The above case study was extended to investigate if the outgassing resulting in the blowhole defects could be eliminated by concentrating up the solution to present a much higher viscosity while enabling coating using an additional thin low viscosity carrier layer.

After some initial experimentation, the two layer assembly shown in Table 3.19 resulted in defect-free coating quality.

	Solids content (%)	Viscosity at $100s^{-1}$ (mPa.s)	Wet thickness (µm)
Main layer	32.0	639	96.4
Carrier layer	10.0	15.2	10.0

Table 3.19: Two Layer Formulation used to successfully coat a Porous Web

The optimum bottom layer viscosity was found once again to be significantly higher than the 3 to 5 mPa.s range advocated by Dittman and Rozzi [1977], who presumably based their considerations on the coating of smooth non-porous substrates.

3.8 Summary

This chapter has addressed the effect of the properties of the substrate - an area that has been generally overlooked outside of industry – yet of vital importance to the coating technologist seeking to attain the highest possible yield while meeting the demand for ever higher process line speeds. In pursuing this study, emphasis was placed in extending the scope of coating window experiments to cover observations on what happens as the gap is temporarily increased to accommodate a passing inter-roll join – a second area of investigation largely ignored in published work.

In considering the importance of the role played by viscosity, recognition is given to the fact that this cannot be generally changed as an independent parameter within the coating industry. The formulation designer is typically constrained to limits dictated by maintaining a prescribed solids content while free to change the amount of solvent within limits determined by solution supply, stability during and after coating and drying load. This again is an approach that is often neglected in coating studies.

The work addressed the effects of surface properties generally considered to be of prime importance for multilayer slide bead coating – namely surface energy, roughness, electric charge and porosity. Use was made of the novel monitoring equipment developed for investigating the response of the coating bead to these properties where deemed important for further understanding. The work extended to a special project to design new coater mountings, side plates and ancillary parts enabling the effect of changing the inclination angle of the slide to be studied.

Key findings were as follows:

- There is an optimum solids concentration for coating a given solids content onto smooth substrates constrained by the tendency for static wetting line migration and hence the tendency for streaks when too low and the onset of ribbing when too high
- The criterion often adopted within industry for quantifying surface energy through the measurement of the contact angle for pure water drops is a useful

indicator for predicting the strength of adhesion of the finally dried coating but totally misleading for assessing coatability

- The work to determine surface energy using the method of Owens and Wendt [1969] confirms the claim made by Blake and Morley [1997] that good coatability is achieved as the polar component is kept as low as possible, the dispersive component kept above 30 mN/m and the calculated static advancing contact angle maintained between 65° and 100°
- The findings consequently suggest that gelatin subbed substrates are generally expected to be harder to coat than unsubbed substrates – care is therefore needed to screen substrates according to whether subbed or unsubbed before assessing the role played by surface roughness
- Whereas corona treatment is highly beneficial to maintaining adhesion for the final dried coating, it's role in determining coatability appears to be insignificant
- Metastable conditions can exist when coating rough substrates where the onset of air entrainment is either present or absent, depending on starting conditions – an effect hitherto unreported for the slide bead process. Under such conditions, it is possible to avoid air entrainment by temporally increasing the coating gap
- The results apparently confirm the findings of Clarke et al. [2003] who showed that two mechanisms for wetting can exist when bead coating rough industrial resin coated paper webs commonly used for the coating of photographic and inkjet products
- Topographical measurements show such webs display a proportion of needle-like asperities associated with composite wetting and identified by taking into account surface area ratio as well as the values of Rz and Ra generally cited for roughness control
- A highly stippled web surface showing a high surface area ratio has been found to coat more easily than one having similar surface energy components and a similar Rz value but of lower surface area ratio. It is suggested that the composite wetting mechanism is responsible for this improvement where the bottom layer viscosity is at least of the order of 40 mPa.s

- It is suggested that the measurement of critical tilt angle for sliding water drops (Wolfram and Faust [1978] and Miwa et al. [2000]) or possibly an adaptation of the method of Menchaca-Rocha [1992] could be useful for correlation with coatability
- A thin low viscosity carrier layer does not consistently broaden the coating window for rough substrates – a more generally successful approach is to ensure the wet thickness of the bottom layer equals or exceeds the value of Rz – a fact hitherto ignored in published work
- It would appear from limited measurements on bead profile when coating a rough substrate that the stability of the bead is enhanced as the dynamic wetting line is moved slightly downstream of the projection of the slide surface onto the web. Dynamic contact angle alone does not appear to correlate with robustness against rivulets and air entrainment.
- The coating window for roughened non wetting substrates can be significantly improved by increasing the inclination of the slide, the limit being dictated by slide waves
- Unbound electric charge (commonly termed static) can adversely affect coatability and the effect can be revealed by perturbations in the lower free surface when using a needle coater
- The results for polar charge assisted coating confirm the predictions from Blake's dynamic wetting model (Blake et al. [1999]) that the electrostatic forces reduce the dynamic contact angle
- The results additionally show that the forces predominate at the dynamic wetting line and thus enable stabilisation against air entrainment with less risk of static wetting line migration and hence a lower tendency for generating streak defects
- The results confirm that the tendency observed by Vandaele and Vancoppenole [1999] and Quiel et al. [2002] for the increased susceptibilty to ribbing when applying charge assist is likely to be associated with increased curvature of the downstream free surface

- The results, while limited, show porous substrates to present additional resistance to coating that can be revealed by a novel technique involving the determination of the edge retraction rate
- A porous substrate presents a further difficulty in that air can become trapped in the pores under the effect of the pressure exerted by the momentum of the fluid flowing down the slide to be later released to generate blow holes in the wet coating
- The susceptibility to blow holes can be significantly reduced by increasing the solids concentration of the main layer while enabling adequate wetting by incorporating a carrier layer of wet thickness typically10 μm – the optimum viscosity being of the order of 15 mPa.s rather than 3 to 5 mPa.s as advocated by Dittman and Rozzi [1997]

Chapter IV

Instabilities in Carrier Layer Flows

4.1 Introduction

Wherever fluid is caused to move under the influence of forces set up in a coating process, there will inevitably be limits beyond which the flow becomes unstable. One such instability mechanism considered in Chapter 3 is that leading to ribbing flow and ultimately to the break-up of the coating bead into rivulets. This limits the upper value of suction pressure that can be applied to stabilise the bead under a variety of conditions. In this chapter, three other areas of a typical industrial multilayer slide bead coating process are reviewed in which carrier layer flows play important roles in determining the onset of instabilities that can inhibit coating or adversely influence the quality of the final coated product. This is clearly of prime interest to the coating technologist endeavouring to attain adequately high quality at the highest possible line speed and yet remains largely unreported in the literature. The three areas considered are:

- The merging of the flows at the lower slot exit on the slide
- The flow on the slide downstream of the carrier layer slot exit
- The action of air impinging on a freshly coated web during initial drying

Results of two layer experimental case studies are presented in Section 4.2 using the specially developed methods described in Section 2.7. Here the flow rate of the carrier layer is reduced until a threshold is reached where the fluid no longer uniformly merges with the upper layer. This ultimately results in the wide diffuse bands of variable coating weight seen on full scale industrial coatings as described in Section 1.6.1.1. The influence of the design of the slot on the threshold flow rate is examined. The findings are compared with those of Leonard [1996], who studied the behaviour of fluids being pumped through slots in a cascade coater, where the slot walls and slide are of low surface energy. The mechanism responsible for triggering

the instability is reviewed in the light of evidence from numerical studies made by Apps [2000].

In carrying out these experiments, it was observed that the flow on the slide was adversely affected by waves, especially as the minimum sustainable carrier layer flow rate was approached. This led to some preliminary studies, which are presented in Section 4.3. Here the aim was to a) determine the mechanism responsible for these forced perturbations and b) distinguish them from inherent instabilities associated with the flow of two or more layers on the slide and extensively studied by a number of workers – notably Kao [1968], Wang, Seaborg and Lin [1978], Weinstein [1990], Smith [1990], Weinstein and Kurz [1991] and Kobayashi [1992]. Results, although limited, usefully highlight an important prediction made by Kobayashi [1992]. The novel and highly sensitive methods described in Section 2.8 were exploited to allow the amplitude of the waves to be quantified for a two layer flow at both the interface and the free surface - thus overcoming the limitations experienced by Kobayashi, who had to resort to the examination of the final coated layers.

Extensive work has been carried out by a number of workers to establish how the heat transfer characteristics of air impingement dryers are influenced by increasing the turbulence beneath the nozzles – for example Martin [1977], Petros [1988], Polat [1993] and Noakes et al. [2002(2)]. Surprisingly, only little study has been made of the limitations due to perturbations caused by the interaction with the wet coating itself – Bell et al. [2000], Bauer et al. [2001], Aydore [2003] and Iwado [2003] – as discussed in Section 1.6.2. Studies relating to air jet wiping and the rippling seen on thin films of de-icing and anti-icing fluids on aircraft wings nevertheless usefully relate to this field of investigation – Craik [1966], Buchlin et al. [1997], Özgen et al. [1999], Özgen et al. [2002] and Gosset and Buchlin [2003]. In Section 4.4, results are presented, in which wavelike disturbances are quantified as the coating traverses down a dryer comprising an array of equispaced slot nozzles – using the methods described in Section 2.14. The results show how the amplitude of the perturbations relates to the nozzle-to-web gap, the air speed and the viscosity and wet thickness of single layer coatings. The work extends to demonstrate how the use of a carrier layer additionally benefits the resistance to perturbations as well as reducing overall drying load.

4.2 Instabilities at the Carrier Layer Slot Exit

4.2.1 Predictions from a Computational Model

The motivation for this experimental study was to gain further understanding of the mechanism responsible for carrier layer starvation lines – see Section 1.6.1.1 and Figures 1.20 to 1.22 - while also following up work carried out by Apps [2000] on the numerical modeling of merging flows with further experiments.

Figure 4.1 shows a generalised view of a typical flow and indicates the parameters used for defining the exit geometry.

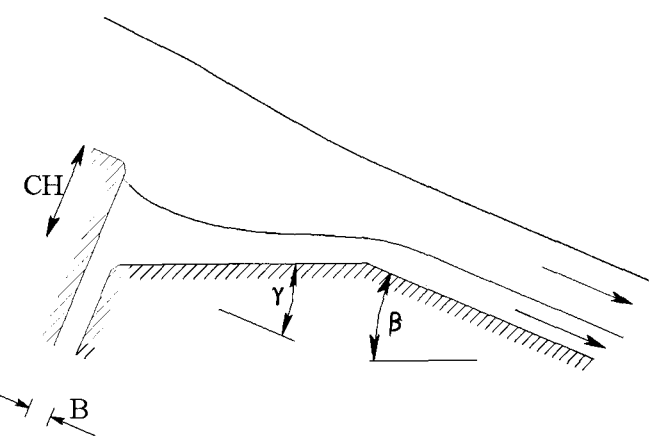

Figure 4.1: A typical merging of two layers at the slot exit

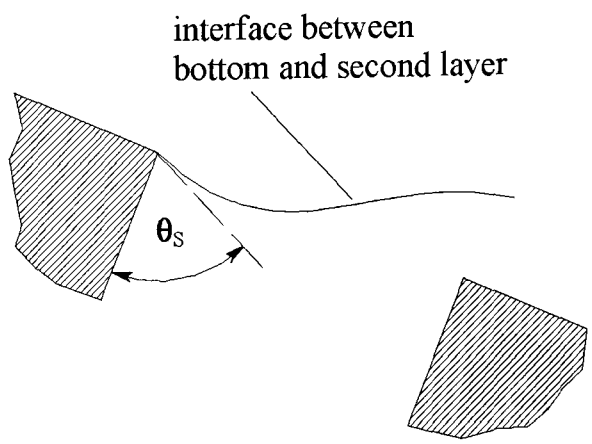

Figure 4.2: Static contact angle – slot exit flow – Apps [2000]

Apps assumed that the internal interface exhibited zero interfacial tension and was pinned to the upstream corner and that the radius of this corner was zero. It was also assumed from earlier experimental work by Ikin that solutions should be discarded as

being unstable for which the calculated contact angle θ_S shown in Figure 4.2 was less than 65°. The model was applied by Apps to investigate what happens as the flux through a parallel slot is reduced to a very low value typical of that commonly used for supplying a thin carrier layer – using the parameters in Table 4.1. The results shown in Figure 4.3 indicate that reducing the flux causes a vortex to be developed near the downstream corner and a decrease in the contact angle at the upstream wall.

	Carrier layer	Upper layer
Density (kg/m^3)	1020	1020
Viscosity (Pa.s)	0.5×10^{-2}	3.0×10^{-2}
Surface Tension (N/m)	5.0×10^{-2}	5.0×10^{-2}
Flux (m^2/s)	Variable	6.0×10^{-5}

Table 4.1: Flow parameters for the computational solutions in Figure 4.3

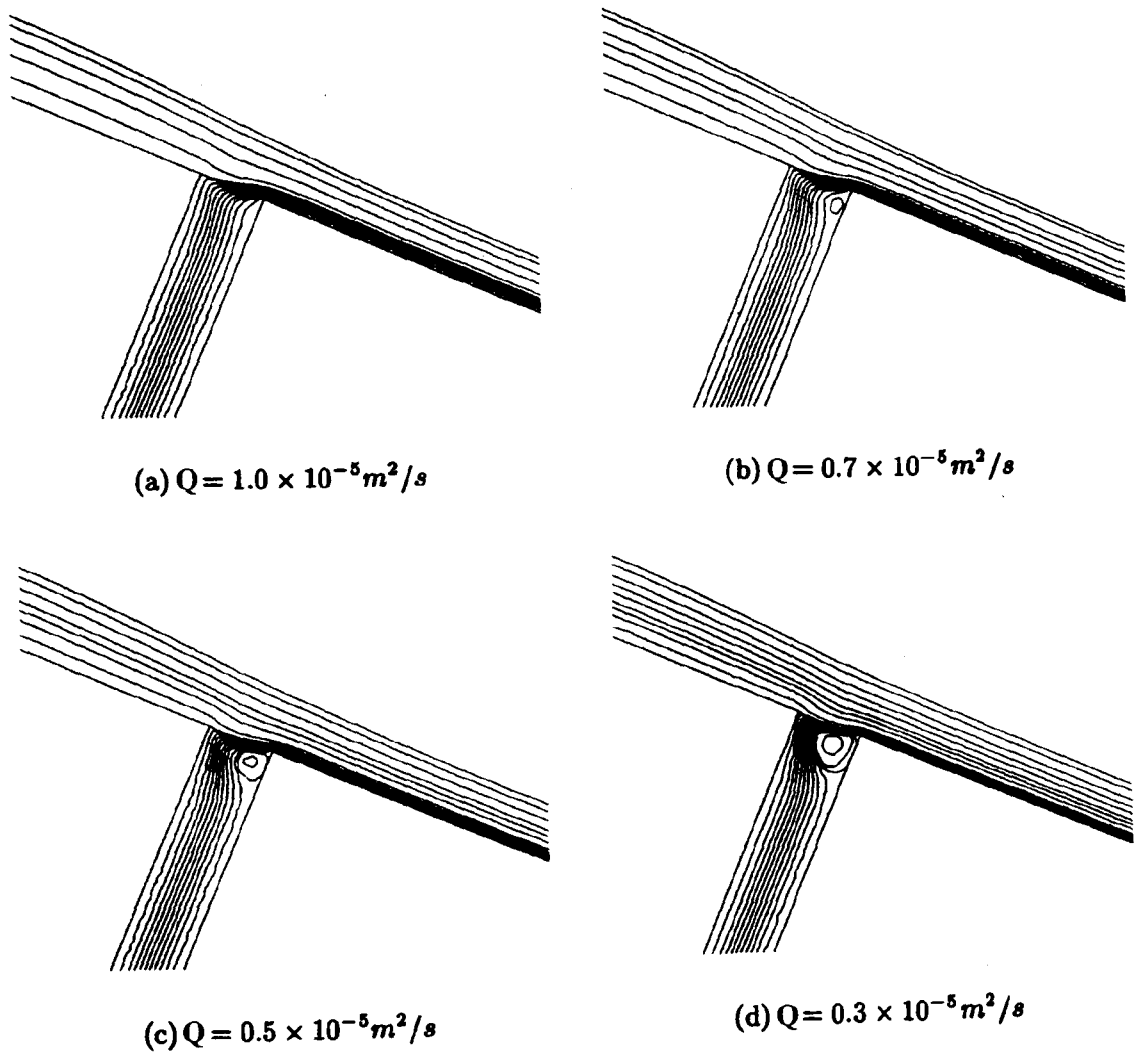

Figure 4.3: Flow structure of two layer carrier layer flows at very low flux – Apps [2000]

Apps postulated that the vortex, being close to the interface, could cause the layers to mix and hence act as a trigger for any instability resulting in irregular merging of the two layers.

4.2.2 Comparison with the Computational Model – Case Study #1

A clear PVOH solution of viscosity 15 mPa.s was used to form the carrier layer employed in this case study. The solution forming the main layer consisted of PVOH polymer containing 36% solids and was shear thinning of viscosity 400 m.Pa.s at a shear rate of 100 s^{-1} when measured at 40°C. The best fit to the data is shown in Figure 4.4. The rheology of the upper layer is given by an alternative form of the Sisko model expressed as:

$$\mu = \mu_{low} + [1 + (\lambda\dot{\gamma})^2]^{(n-1)/2} \qquad (4.1)$$

where $\dot{\gamma}$ is the shear rate in s^{-1}, $\mu_{low} = 6.5 \times 10^3$ mPa.s, $\lambda = 5.0$ sec. and $n = 0.5$.

Flow rates and surface tensions were as in Table 4.2.

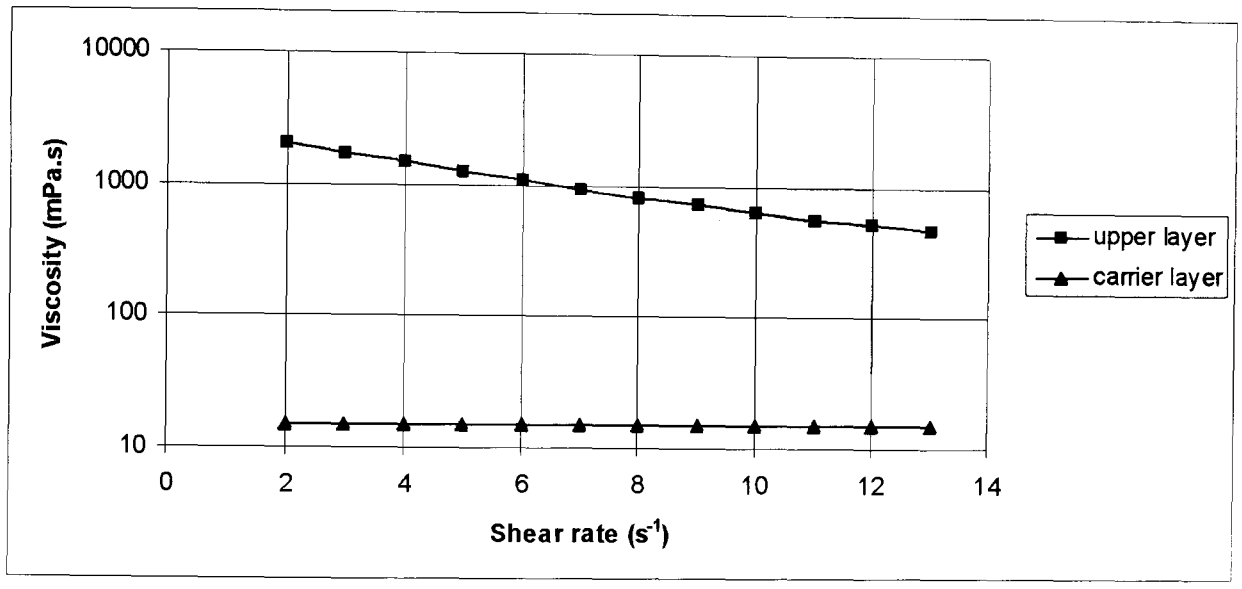

Figure 4.4: Rheology of the two layers used in case study #1

	Flow rate (m^2/s)	Surface Tension (N/m)
Upper layer	4.0×10^{-5}	2.8×10^{-2}
Carrier layer	0.5×10^{-5}	3.0×10^{-2}

Table 4.2: Parameters used in case study #1

A chamfered lower slot exit was selected for the study where CH = 1.167 mm, and $\gamma = 23°$ and the slot width B adjusted to 0.8 mm – see Figure 4.1. The slide angle β was set at 23°. The solutions were supplied from the pressure vessels described in Section 2.8.2 – see Figure 2.30. The temperatures of the water bath and water jacket were controlled to achieve 40°C ± 0.5°C at the entry points to the Perspex cascade as

monitored by thermocouples inserted into the pipes. The scattering properties were such as to enable the method described in Section 2.7 to be used for determining the profiles of the free surface and the interface. The static contact angle was found to be 84°.

The Leeds computational model for slot flow was again run by Noakes (née Apps) in an initial attempt to match the experimentally determined interfacial profile obtained in this case study. In attempting to model the flow at the liquid-liquid interface, a problem exists in that as there is no interfacial tension at this interface, defining a contact angle over-specifies the number of boundary conditions. Various authors have encountered this difficulty and have proposed a number of methods for locating the interface with varying amounts of success – Apps [2000]. Figure 4.5 shows the results obtained on prescribing that the interface terminates at the corner, which was assumed sharp (zero radius) while the contact angle was allowed to run free in the numerical model. Two sets of solutions were obtained based on the following assumptions:

a) The upper layer was Newtonian
b) The upper layer was shear thinning as governed by (4.1)

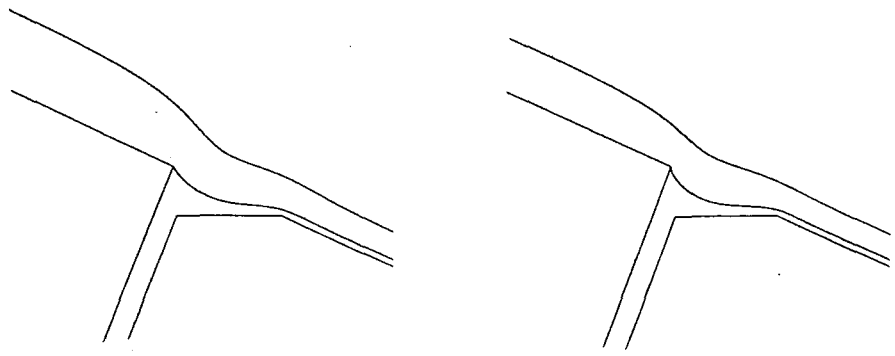

a) Upper layer Newtonian *b) Upper layer shear thinning*

Figure 4.5: Initial predictions from the computational slot flow model – case study #1

It will be seen that the model correctly predicts a thinner flow upstream of the slot exit on substituting for the shear thinning behaviour of the upper layer. Neither solution, however, gave a good match with the experimentally determined profile of the interface. Noakes then proceeded to adopt a different approach by allowing the numerical simulation of the interfacial contact line to run free while imposing the experimentally determined 84° static contact angle. This yielded an excellent match between experiment and the numerical solution - Ikin et al. [2001(2)] – see Figure 4.6.

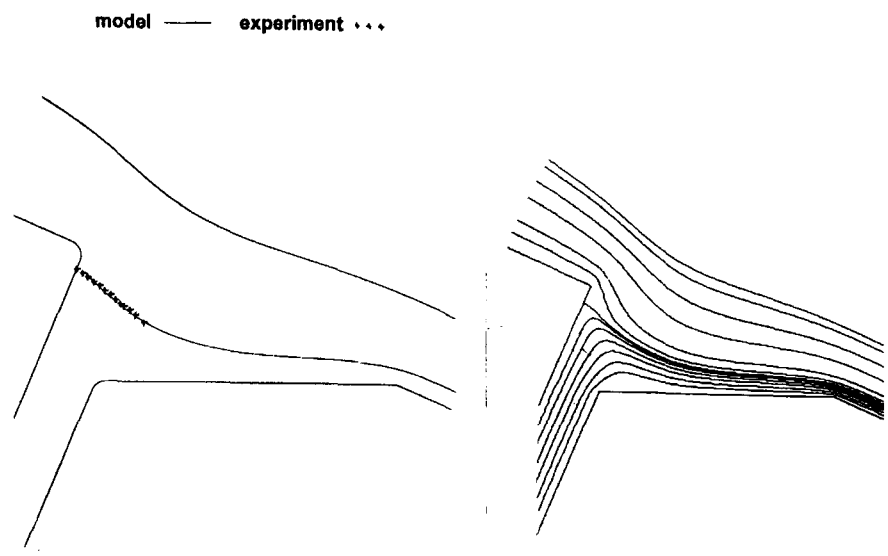

a)Profiles of free surface and interface *b) Streamlines*

Figure 4.6: Predictions from modified model compared with experiment – case study #1

This result, while helping resolve the dilemma concerning selecting an appropriate method for defining the location of the contact line, also gave credence to the general aspects of the model and hence to the predictions made by Apps concerning the presence of the vortex near the downstream slot corner.

4.2.3 Critical Carrier Layer Flow Rate – Case Study # 2

The model, while useful for predicting the detailed flow for any stable steady state flow field, is limited on account of not being readily extendible to time dependent instabilities. This second two layer case study was accordingly set up with the aim of determining the minimum flow rate at which the bottom layer continues to merge with the upper layer and to profile the free surface and interface as this limit is approached. A clear PVOH solution was again used to form the carrier layer. The fluid forming the upper layer comprised a more highly concentrated PVOH solution and the addition of silver chloro-bromide emulsion as scattering agent - prepared by a controlled crystal growth technique, the particle size being typically 350 nm. The solutions were this time supplied at room temperature using the conventional pumping system described in Section 2.7.2 and illustrated in Figure 2.23 – in order to ensure accurate flow control and minimise costly waste. The solution properties and flow rate set for the upper layer were as in Table 4.3. The effect of slot geometry was studied by

running three sets of trials, in which the Perspex cascade was configured to form three different exit geometries at the lower slot:

a) Chamfered where CH = 1.167 mm, and B = 0.80 mm – see Figure 4.1

b) Parallel with B = 0.80 mm

c) Parallel with B = 0.52 mm

	Carrier layer	Upper layer
Density (kg/m^3)	1005	1014
Viscosity (mPa.s)	5.4	75
Surface Tension (mN/m)	34.3	34.3
Flow rate (m^2/s)	Variable	6.15×10^{-5}

Table 4.3: Solution properties and upper layer flow rate for case study #2

4.2.3.1 Trials using the Chamfered Slot Exit

The apparatus and method described in Section 2.7 were used to record images of the free surface, the interface in the vicinity of the slot exit and the cross-width uniformity of the flow on the slide downstream of the bottom slot. Figures 4.7a and 4.7b show typical images of the free surface and interface under stable conditions and then at the point where the interface is seen to recede half way down the slot at a critical threshold of 0.82×10^{-5} m^2/s. (Note that the outlines superimposed on these figures correspond to the view of the interface as seen via reflection at the beam splitter and are displaced relative to the view of the upper free surface seen by direct transmission – ref. Figure 2.25.) Figure 4.8 shows how the cross-width profile on the slide downstream of the bottom slot remains fairly uniform for where the carrier layer flow rate is maintained near or above 0.96×10^{-5} m^2/s but becomes highly irregular at the critical threshold rate of 0.82×10^{-5} m^2/s.

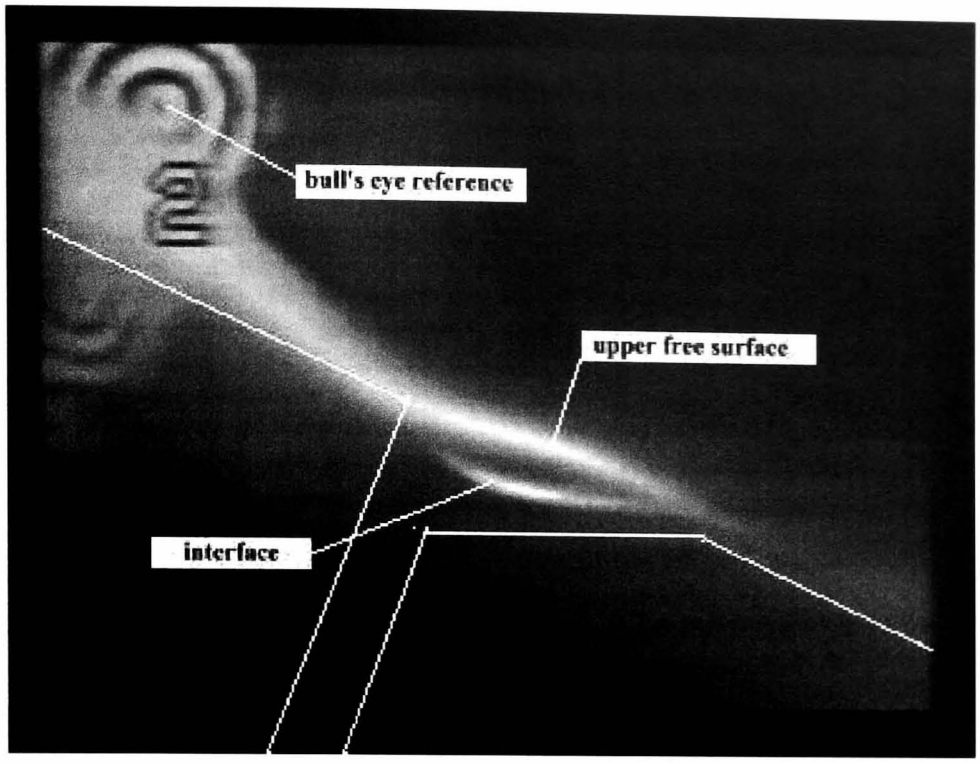

a) $Q_1 = 2.05 \times 10^{-5}\ m^2/s$

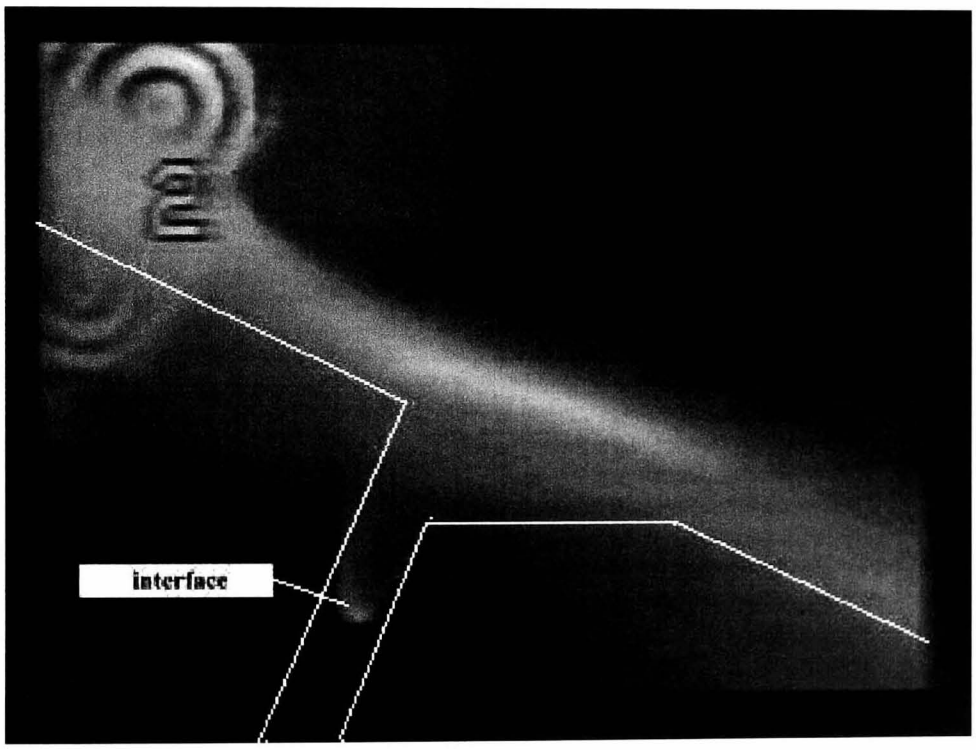

b) $Q_1 = 0.82 \times 10^{-5}\ m^2/s$

Figure 4.7: Images of the free surface and interface using a chamfered slot exit

Figure 4.9 shows the corresponding profiles of the free surface and interface. These are drawn to scale using AutoCAD after transferring data points in the key parts of the image obtained from the video recordings. A video clip showing the sequence is appended with the thesis – see Appendix II – video sequence #1.

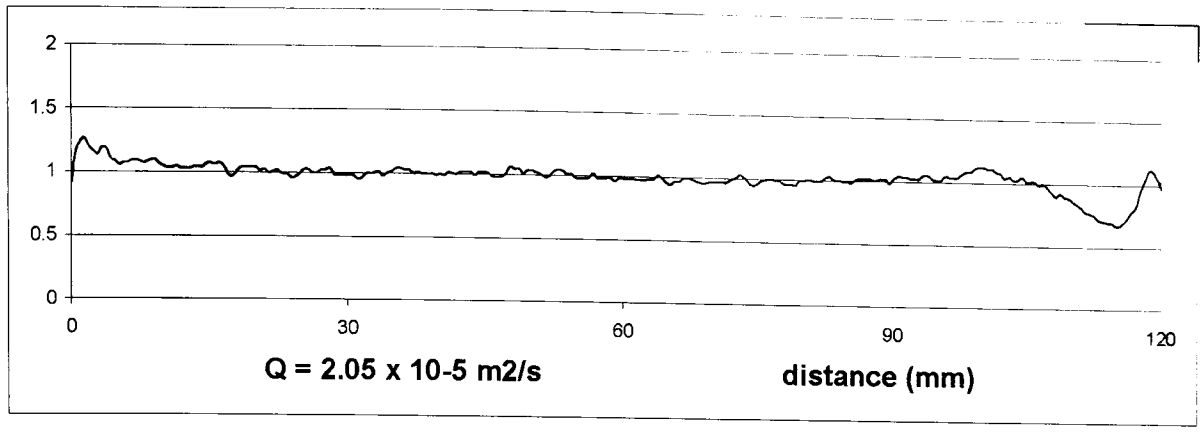

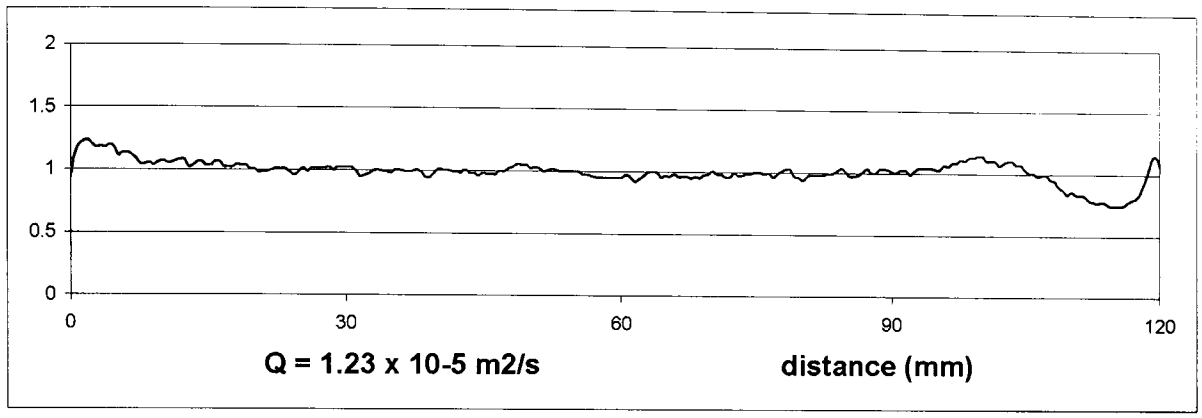

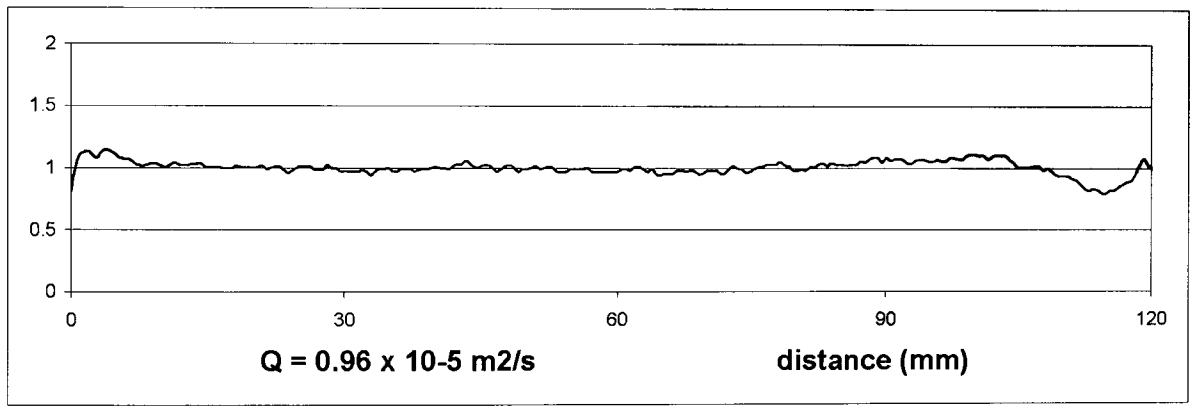

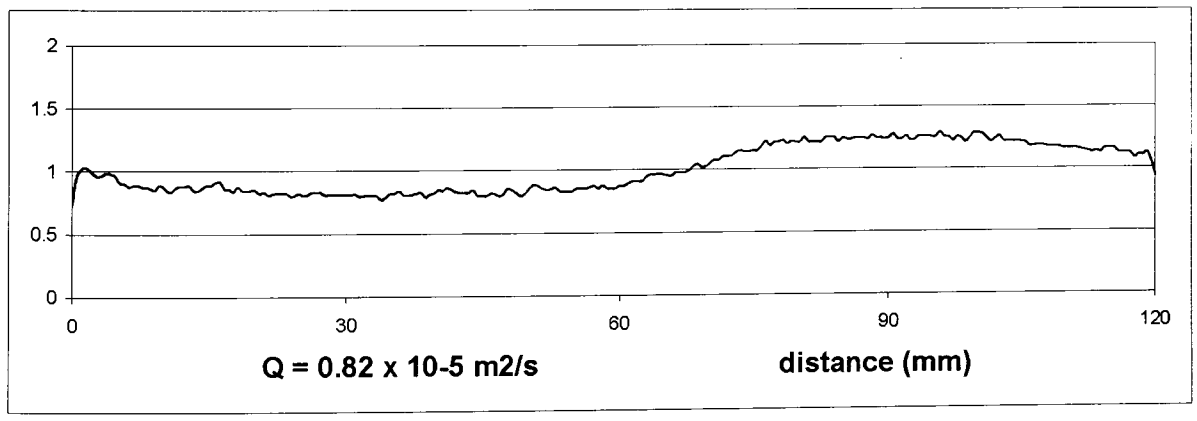

Figure 4.8: Cross-width film thickness uniformity as the carrier layer flow rate is reduced for a chamfered slot exit

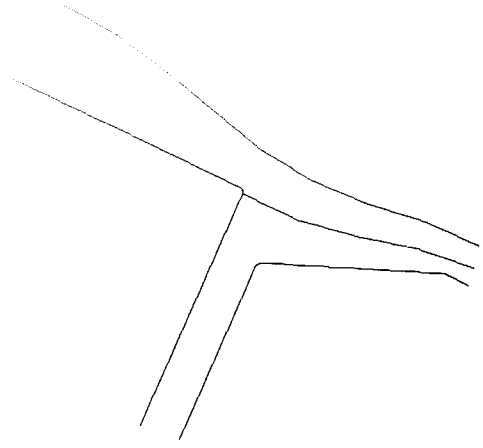

$\theta_s = 85°$

a) $Q_1 = 2.05 \times 10^{-5}$ m^2/s

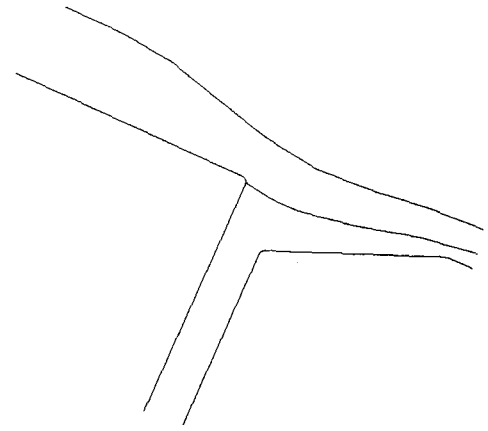

$\theta_s = 80°$

b) $Q_1 = 1.64 \times 10^{-5}$ m^2/s

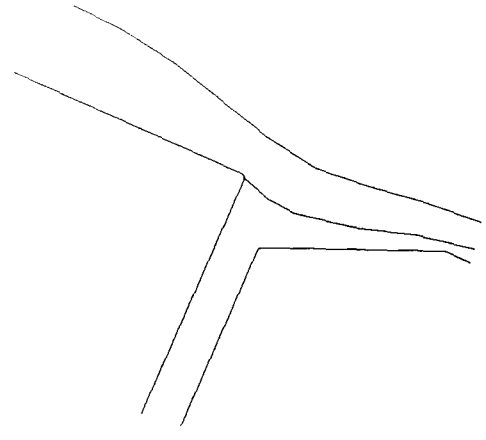

$\theta_s = 69°$

c) $Q_1 = 1.23 \times 10^{-5}$ m^2/s

Figure 4.9 a) –c): Experimental free surface and interface profiles for a chamfered slot exit

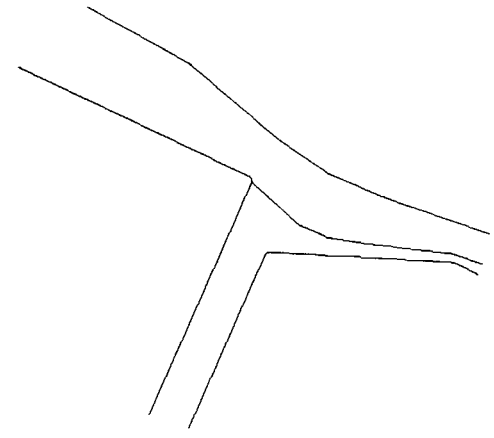

$\theta_s = 71°$

d) $Q_1 = 0.96 \times 10^{-5}$ m^2/s

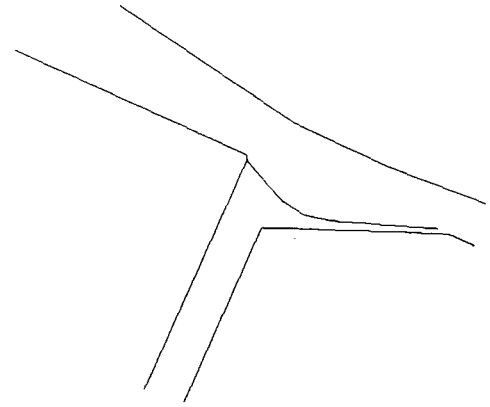

$\theta_s = 60°$

e) $Q_1 = 0.82 \times 10^{-5}$ m^2/s $T = 0$ s

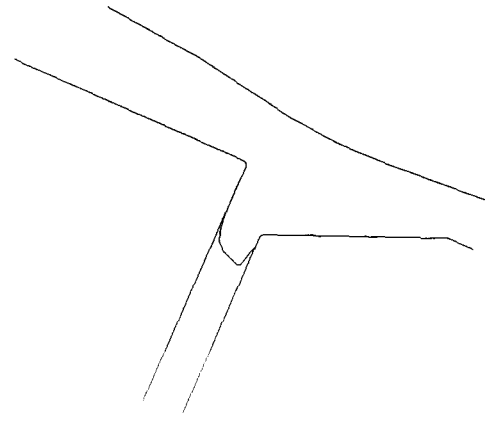

$\theta_s = 8°$

f) $Q_1 = 0.82 \times 10^{-5}$ m^2/s $T = 2$ s

Figure 4.9 d) –f): Experimental free surface and interface profiles for a chamfered slot exit

It will be observed from Figures 4.9 and 4.10 that the static contact angle decreases from a maximum of about 85° as the flow rate is reduced from 2.05 x 10^{-5} m^2/s, the lowest sustainable angle being between 60° and 70°, below which the contact line breaks away from the upstream corner. This confirms that the approach taken by Apps [2000] in which all solutions for $\theta_S < 65°$ were discarded was indeed correct.

It was also evident that reducing the carrier layer flow rate also causes the overall equilibrium thickness of the two layers on the slide to increase. This can be readily confirmed by solving the equations governing the fully established flow of two immiscible layers down an inclined plane. This is achieved by firstly assuming the heights of the interface and the free surface above the slide, calculating the corresponding flow rates, correcting the heights to a better estimate and repeating the steps iteratively until a converged solution is obtained – see Appendix I and Figure A.2. Results from applying the equations to this case study are shown in Figure 4.11.

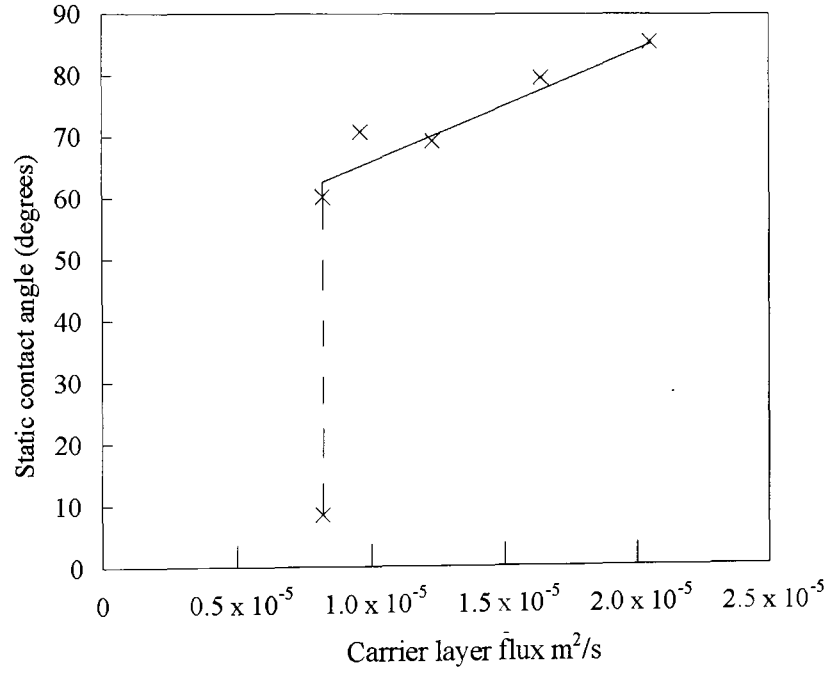

Figure 4.10: Effect of carrier layer flow rate on static contact angle – chamfered slot exit

Classical analysis of low Reynolds number flows constrained by two stationary walls inclined to one another by an angle 2α shows the existence of pairs of counter-rotating vortices mirrored about the axis of symmetry, provided that α exceeds 78° - Moffatt [1964]. The axis is characterised by zero shear. This has been applied to explaining

how vortices are generated in the stagnant wedge of fluid trapped near a static contact line where the boundary is a free surface and the shear accordingly also zero – see for example Schweizer [1997(1)]. Noakes et al. [2002(1)] showed that this was indeed the case when studying the flow at the upper slot exit of a cascade coater. A static contact angle of about 23° was found to result in excessive deposit growth at the upstream corner when continuously pumping gelatin containing a rapid hardening agent due to the recirculations trapped within the wedge of fluid. Such growths are very vulnerable to becoming dislodged and can result in coating streaks – Noakes et al. [2002(1)]. The latter found that on increasing the static contact angle to 90°, the deposit growth formed after a period of 4.5 hours reduced from a cross-section of 0.029 mm^2 to 0.002 mm^2 – see Figure 4.12. The viscosity ratio across the free surface was of the order of 0.002. In the case of two fluids merging at the lower slot exit, however, the viscosity is no longer close to zero but of the order of 0.072. To presume that an interfacial contact angle of less than 78° similarly poses a risk of deposit growth is no longer valid as no known work has been carried out for finite viscosity ratios. There is therefore a clear a case for extending Moffatt's work in order to draw firm conclusions on the generation of eddies and consequential deposit growth at the interfacial contact line.

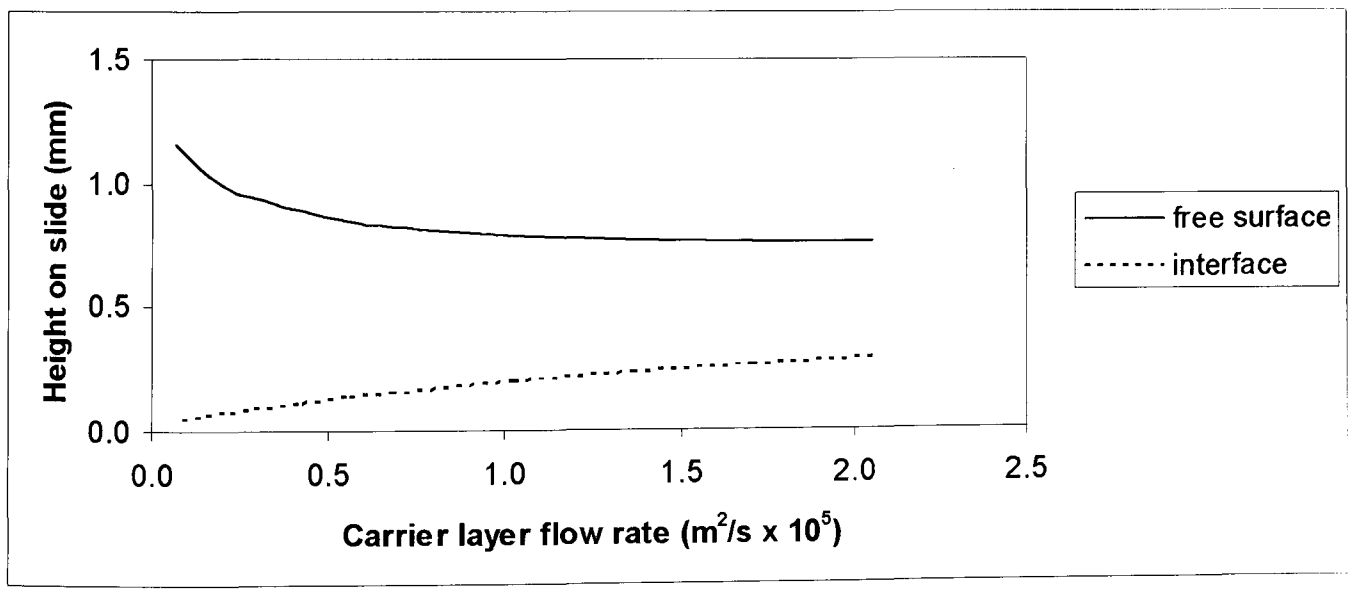

Figure 4.11: Effect of reducing the carrier layer flow rate on slide film thicknesses

Figures 4.13a–c show a sequence of images depicting the invasion of the fluid normally forming the upper layer into the slot and down into the corresponding cavity formed by the upper distribution chamber. The sequence is also appended as a video

clip – see Appendix II – sequence #2. It will be clear that once this condition has been reached and the solutions become mixed within the chamber, it then becomes difficult to re-establish uniform merging flow on the slide even after restoring the carrier flow rate well above the critical threshold value – compare Figures 4.8b and 4.14.

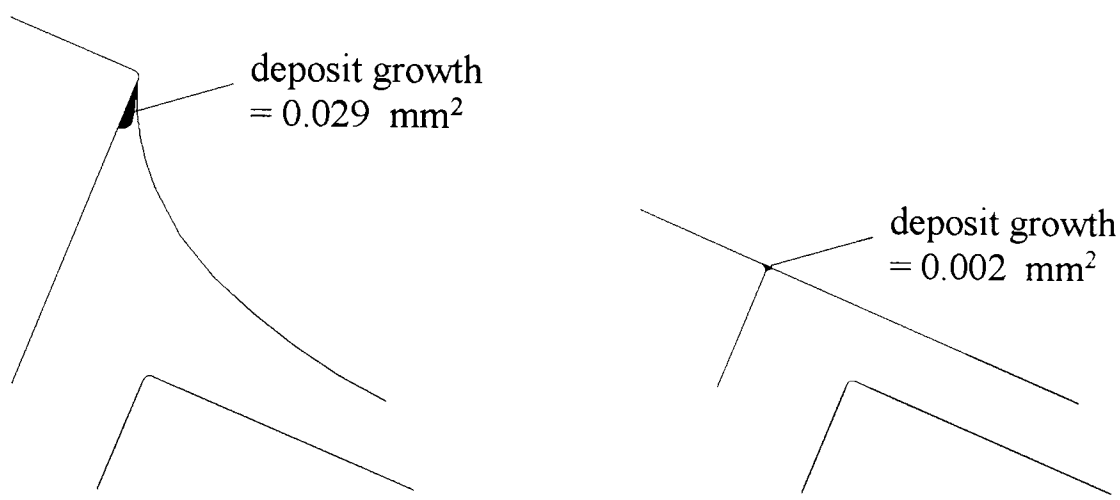

Figure 4.12: Effect of vortices on the generation of deposits for unstable chemistry

This is because the wall shear stress generated by the low viscosity carrier layer is insufficient to purge out the upper layer solution from the walls of the chamber. The coating operator then has no other recourse but to drain down the entire cascade, wash up and recommence the pumping up procedure. It is also evident that any transient undershooting of the carrier layer flow rate when switching set-point in a conventional control loop must be minimised in order to avoid premature failure due to layer mixing within the slot.

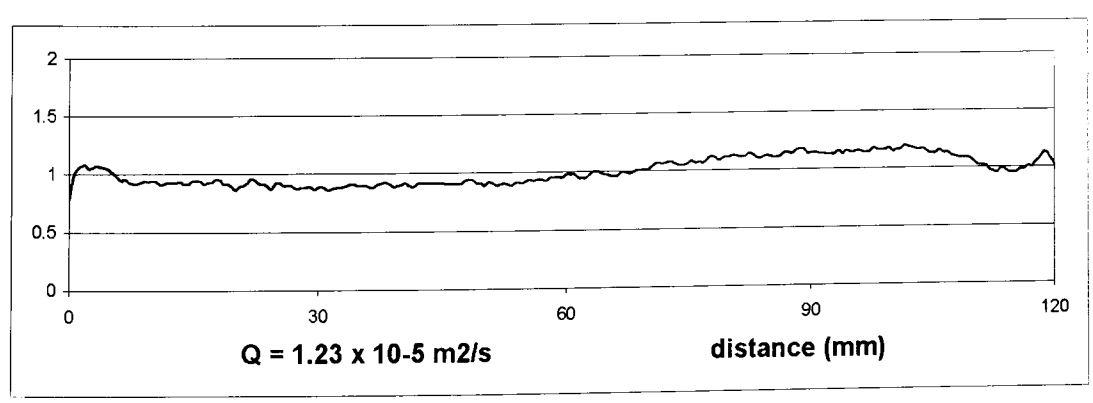

Figure 4.14: Cross-width film thickness uniformity on restoring Q_1 to 1.23 x 10^{-5} m^2 s

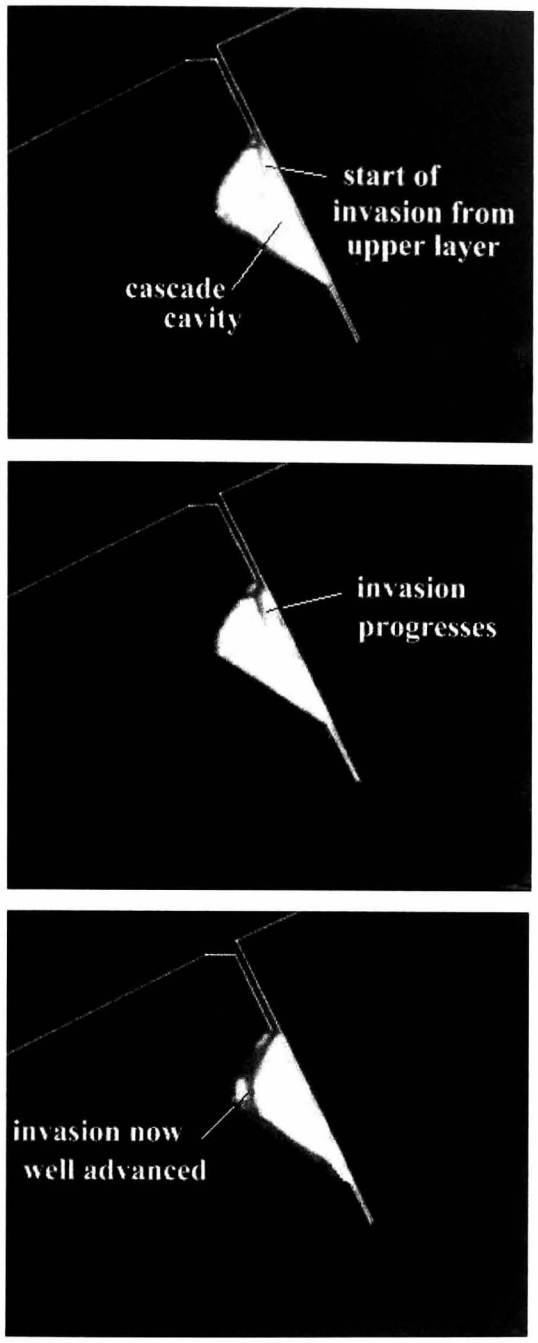

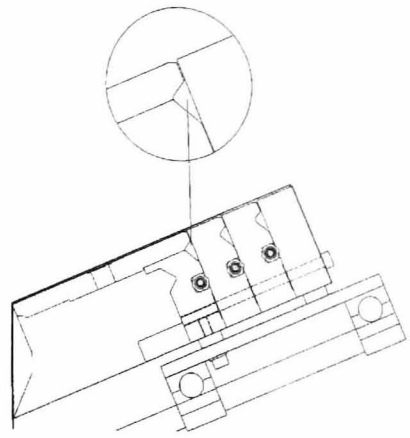

Figure 4.13: Invasion of the upper layer into the carrier layer distribution chamber

4.2.3.2 Trials using a Parallel Slot Exit

It was found that the critical carrier layer flow rate was decreased from 0.82×10^{-5} m^2/s to 0.34×10^{-5} m^2/s on replacing the chamfered slot exit with a parallel slot of the same width. The critical threshold was further reduced to the order of 0.07×10^{-5} m^2/s on decreasing the width to 0.52 mm. This is about the lowest practical limit owing to the impact of finite machining tolerances and pressure induced elastic distortions on the uniformity of the slot width. Figures 4.15a-d and 4.16a-d show the corresponding profiles of the free surface and interface for these two sets of trials for the flow rates

investigated. In addition to enhancing the robustness against invasion of the upper layer, the static contact angle is also significantly increased to the order of 90° or more.

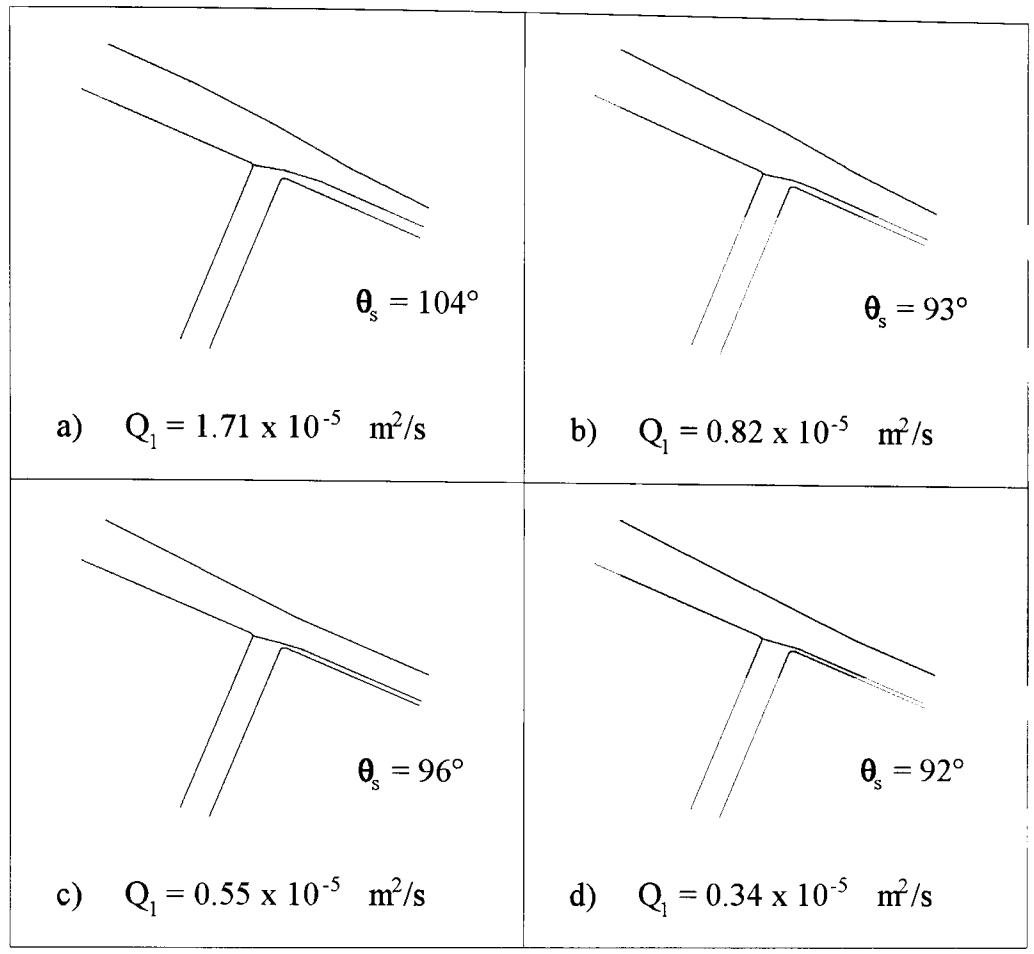

Figure 4.15: Experimental free surface and interface profiles for a 0.8 mm wide slot

Recovery of two layer flow on the slide is shown in Figure 4.17 for a slot of width 0.52 mm after increasing the carrier layer flow rate to 1.71 x 10^{-5} m^2/s from the critical value of 0.07 x 10^{-5} m^2/s. In this case, the upper layer solution had receded part way down the slot without contaminating the supply cavity.

The high viscosity solution is then slowly swept back up to the exit region as a film like flow under the shearing action of the carrier flow and uniform merging of the two layers ultimately restored. The recovery sequence is also appended as a video clip – see Appendix II – sequence #3.

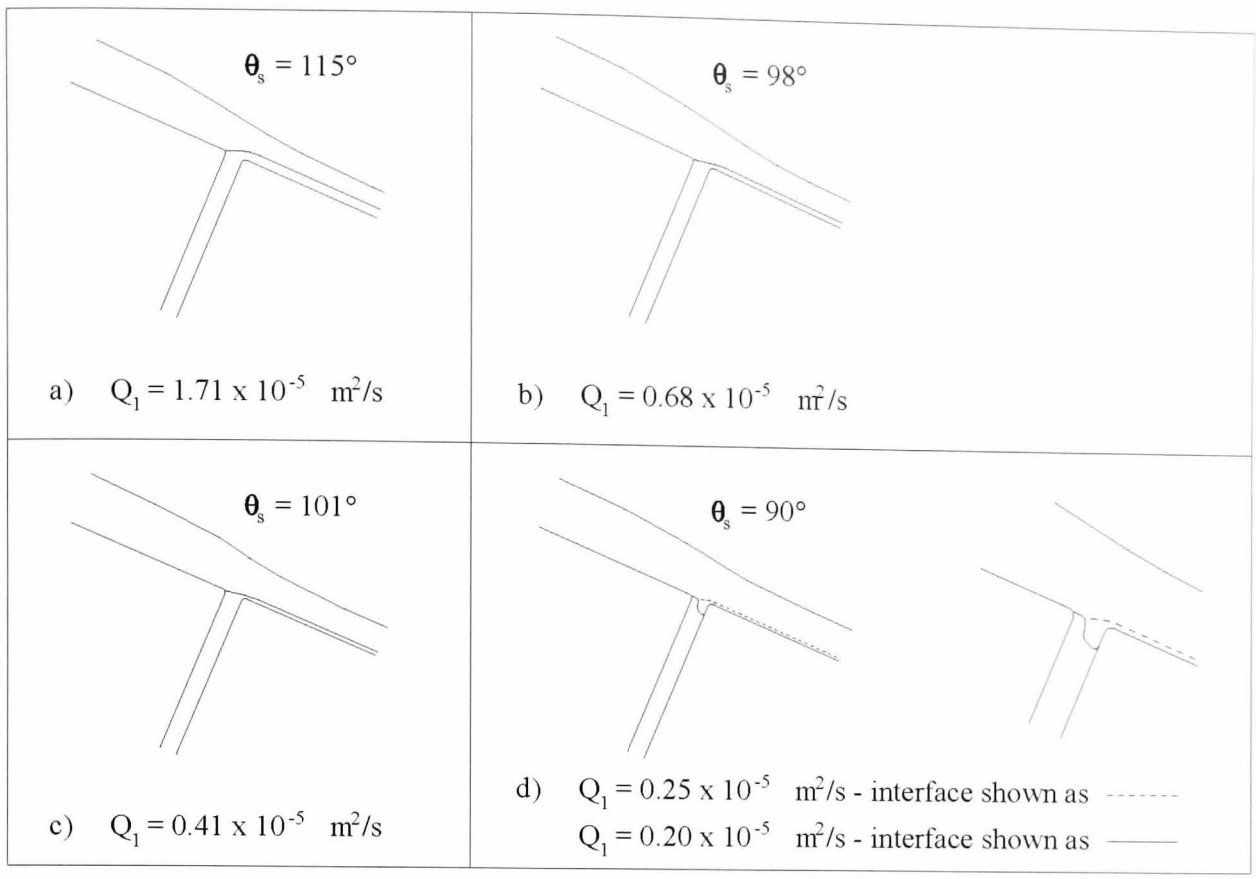

Figure 4.16: Experimental free surface and interface profiles for a 0.52 mm wide slot

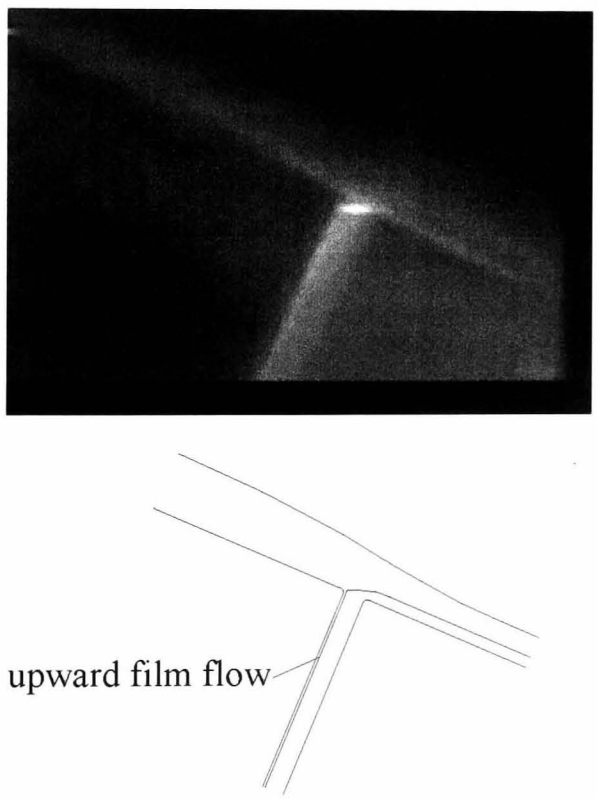

Figure 4.17: Recovery of two layer flow after restoring Q_1 to 1.71 x 10^{-5} m^2/s

4.2.4 Mechanism for Carrier Layer Starvation Bands

Figure 4.16d shows evidence that the upper layer initially invades the carrier layer slot near to the downstream wall. The deformation of the apparent interface strengthens the

argument put forward by Apps [2000] that local mixing occurs within a vortex as predicted by the computational model – see Figure 4.3d. The results suggest a possible mechanism explaining the onset of the broad diffuse bands of varying coating weight affecting full scale multilayer coating as the carrier layer flow rate approaches the critical limit. It is initially assumed that the vortex forms a rolling bank whose strength varies in the cross-machine direction – as shown in Figure 4.18. The vortex dissipates energy carried by the flux entering the slot exit region and results in an increased pressure drop. The pressure upstream of the rolling bank thus also varies between maxima and minima in the cross-machine direction. The result is that the fluid tends to flow sideways in response to local pressure gradients to augment the flux at the weak recirculations at the expense of the strong ones. The strong vortices thus grow while the weak recirculations diminish. The variations in carrier layer flux impact on the shearing action seen by the upper layer to cause this to also vary in thickness in the cross-machine direction in accordance with the predictions shown in Figure 4.11.

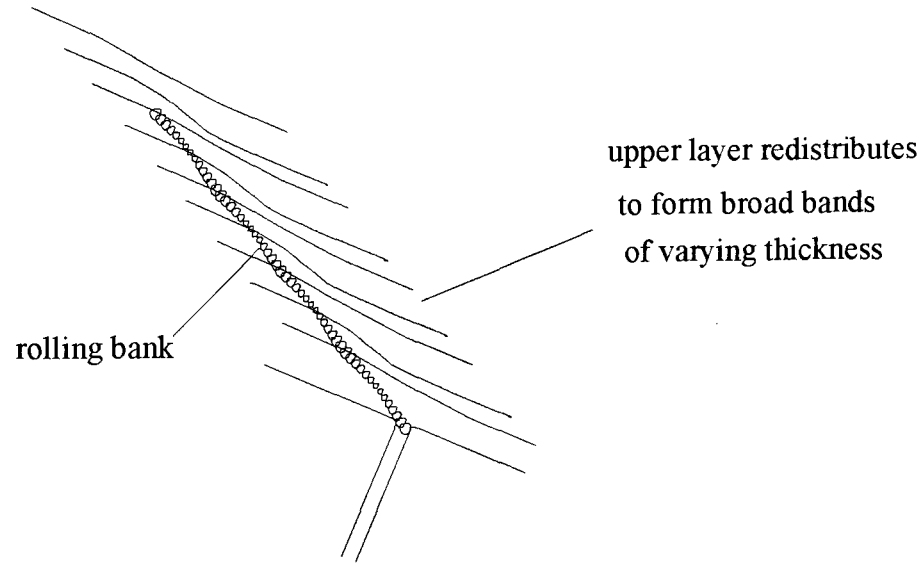

Figure 4.18: A possible mechanism for carrier layer starvation bands

4.2.5 Comparison of Results with Experiments using Low Surface Energy Walls

It is of interest to compare the predictions from this study with those of Leonard [1996], who established criteria for calculating the maximum permissible width of the

exit slot when forming a single layer on a slide. He allowed for the effects of contamination within a coating process by smearing the slot walls and slide with oil. In a second study, he precoated the surfaces with polytetrafluoroethylene as a means of reducing the surface energy and thus the tendency for contaminants to adhere. The advancing contact angle of water on Perspex is typically 71° - Wolfram & Faust [1978] - whereas the value for polytetrafluoroethylene is typically 118° - Padday [1978]. Leonard showed from his experiments that the fluid will flow uniformly from a slot and down the slide without pulling in at the edges or breaking up into rivulets provided that:

$$B < \frac{6.25\mu^2 N_{re}{}^a}{\rho\sigma} \tag{4.2}$$

based on the use of cm., gm. and seconds as units and where:

$$N_{re} = \frac{4Q\rho}{\mu} \tag{4.3}$$

and

$$a = 0.981 + 0.3406.\log(N_{re}{}^{0.3406}) \tag{4.4}$$

Applying Leonard's criteria to the values for Q, ρ, σ and μ used in this case study, the critical maximum allowable slot widths B_L are as in Table 4.4 – for comparison with the actual experimental widths B_H.

Trial	Q (m^2/s)	ρ ($kg.m^{-3}$)	μ (mPa.s)	σ mN/m	N_{re}	a	B_L mm	B_H mm
1	$0.83x10^{-5}$	1005	5.4	34.3	6.10	1.072	0.037	0.80 chamfered
2	$0.34x10^{-5}$	1005	5.4	34.3	2.53	1.028	0.014	0.80
3	$0.07x10^{-5}$	1005	5.4	34.3	0.506	0.947	0.003	0.52

Table 4.4: Comparison with Leonard's criteria for slot exit flow

The results from this work show that a much wider slot is permissible when merging a low viscosity carrier layer with the adjacent upper layers than can be tolerated for establishing a single layer alone. In this case study, the solution providing the carrier layer was initially pumped through the lower slot at a flow rate much greater than the

critical threshold value and the flow established on the slide before introducing the upper layer. Having attained stable flow, the carrier layer flow rate was then reduced to just above the point of instability leading to invasion of the upper layer into the bottom slot. It is therefore evident that this start-up procedure used in combination with the stabilising effect of the high viscosity upper layer very significantly enhances the robustness against instabilities when compared with the conditions and start-up procedure used by Leonard.

4.2.6 Summary

Experimental trials, while limited to the study of the behaviour of one set of coating solutions, confirm that there is a critical flow rate below which a carrier layer ceases to merge uniformly with an upper layer. The results show that the interface remains pinned to the upstream corner provided that the contact angle exceeds 65°, thus giving credence to the work of Apps [2000] who, when solving for various conditions, discarded all solutions for which the static contact angle was less than this value. The results also appear to confirm the presence of a vortex at the top of the downstream slot wall as the critical flow rate is approached. A mechanism for explaining the onset of the bands of diffuse streaks seen on an industrial scale is suggested. The design of the slot exit is important, a parallel slot being significantly more robust against carrier layer starvation effects than a chamfered slot as the flow rate is reduced. Reducing the slot width is similarly advantageous. The ultimate limit to width is then largely dictated by machining errors and reliability when assembling the parts forming the cascade – Ruschak et al. [2002]. The interfacial contact angle increases dramatically on changing from a chamfered to parallel slot but further work is required to extend Moffatt's analysis to cater for an interface between two fluids in order to draw firm conclusions as to whether this also eliminates eddy formation at the interfacial contact line and hence increases robustness against streaks. Vortices associated with the downstream corner are nevertheless unavoidable as the flow rate approaches the critical threshold value.

4.3 Instabilities on the Slide Downstream from the Lower Slot

4.3.1 Sensitivity to Pump Induced Perturbations

When running the trials described in Section 4.2.3.2, where the slide was configured to present a parallel lower slot of width 0.52 mm, it was observed that the flow on the slide downstream of this slot became increasingly disturbed by waves as the carrier layer flow rate approached the critical threshold value. It was also noted that the frequency of the waves corresponded with those of the pulsations derived from the meshing of the teeth within the gear pump used for supplying the carrier layer. A method was devised for estimating the variation in thickness of the upper layer by replaying the video recordings and collecting light emitted from the monitor screen by a fibre optic terminating at the photocathode of a sensitive photomultiplier tube. The fibre optic was positioned at the point on the screen corresponding to the flow cross-section profiled by the laser based technique described in Section 2.7. The output signals were recorded on a Thurlby DSA 524 digital storage adaptor as described in Section 2.8.2 and analysed using Mathcad. Figure 4.19 show the results expressed in terms of percentage variation in the thickness of the upper layer.

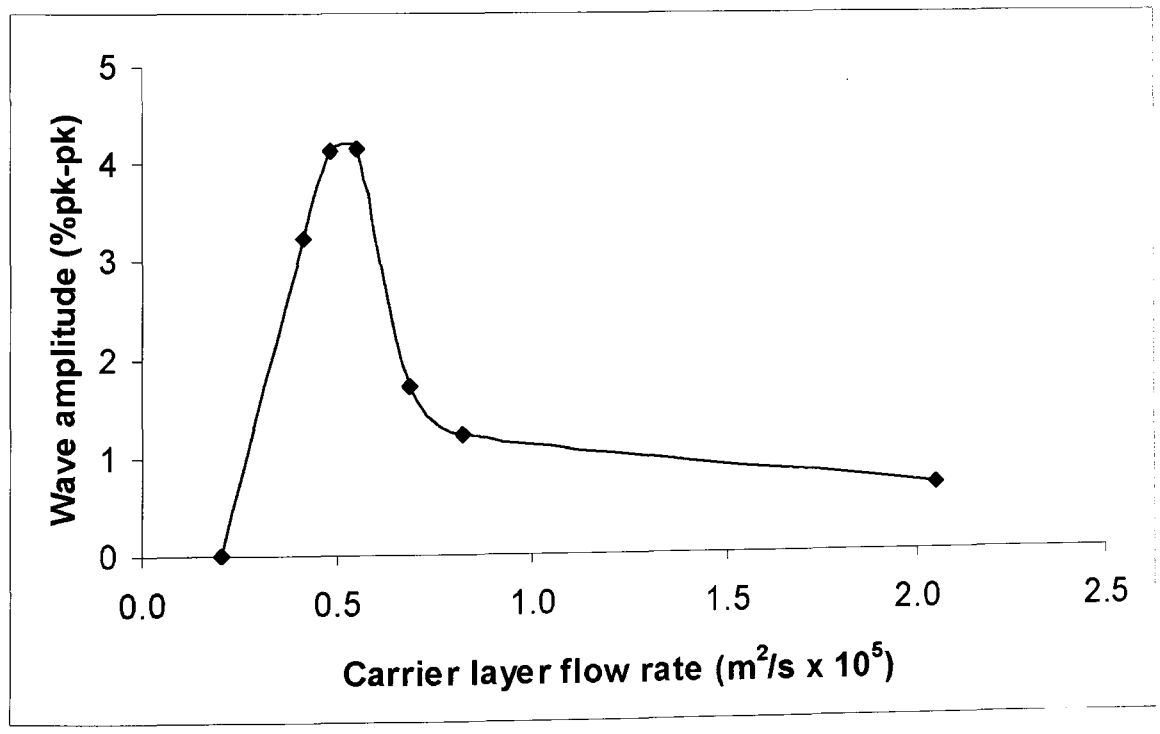

Figure 4.19: Wave amplitude of pump induced perturbations in upper layer thickness

It will be seen that the waves increase rapidly in severity as the carrier layer flow rate is decreased to the critical threshold of 0.56 x 10^{-5} m^2/s applicable to the conditions tested in this experiment. On reducing the flow rate further, the disturbances decrease as the upper layer thickens until a point is reached when the depth equates to that upstream of the lower slot and ceases to be influenced by the fluid hitherto forming the carrier layer.

Close inspection of the recorded images shows that the interface and free surface were oscillating up and down as the critical limit was approached. As the pressure exerted by the carrier layer pump approaches a minimum, the carrier layer thins and causes the upper layer to decelerate and thicken in accordance with Figure 4.11. Figure 4.20 shows the profiles of the interface and free surface at peaks and troughs when close to the critical limit, for which the pulsation frequency was of the order of 1 Hz.

The responses of the interface to pump induced pulsations is shown on a video clip in four separate short sequences as the carrier layer flow is reduced down towards the critical value. This also serves to indicate the presence of the recirculation near the top of the downstream slot wall – see Appendix II – sequences #4a - #4d.

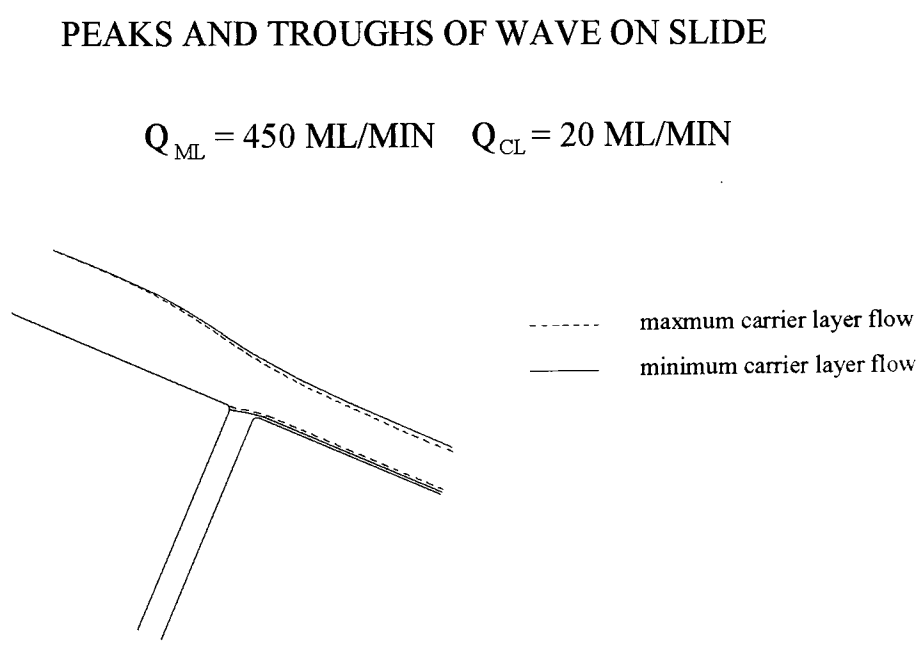

Figure 4.20: Pump induced oscillations of the interface and free surface

Case study # 1 as described in Section 4.2.2 was extended to further explore these effects as part of a general investigation to improve the quality of an inkjet product

being developed by ILFORD Imaging UK Limited. The formulation and operating parameters were specifically selected as known to result in patterns as typically shown in Figure 4.21. Here, the wavelength down the sample is of the order of 12 mm. The defect is a form of barring as described in Section 1.3.6 or pump induced slidewaves as depicted in Figure 1.14. The lower layer was of viscosity 15mPa.s. The properties of the upper layer and the operating conditions were otherwise as in Figure 4.4 and Table 4.2. The upper layer, being highly scattering, allowed the Keyance LC-2220 laser displacement meter described in Section 2.8.2 – see Figure 2.31 - to be used for monitoring the surface displacement. This unit was mounted above the cascade on the pilot coating machine – firstly 10 mm upstream of the lower slot and secondly, 10 mm downstream of the slot. The resulting responses are shown in Figures 4.22 and 4.23 and indicate how the free surface becomes severely disturbed by waves as soon as the layers merge at the lower slot exit.

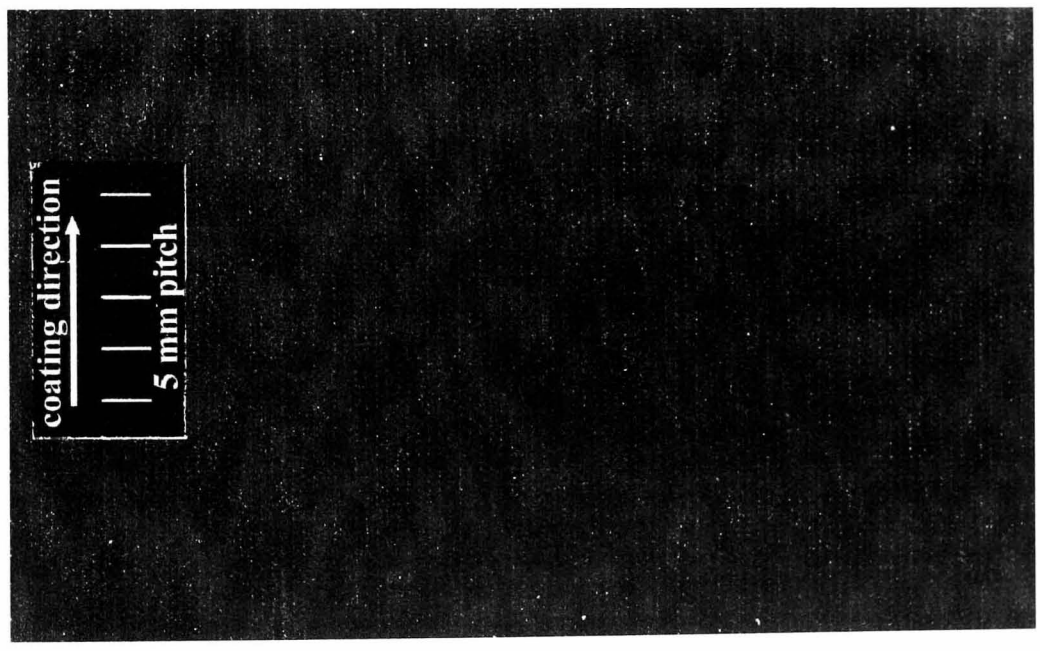

Figure 4.21: Effect of slide waves on the ultimate coating quality

The highly periodic nature of the waves shown in Figure 4.23 suggested that the cause of the perturbations was pulsations arising from the gear pump supplying the lower layer. Measurement of the rotational speed of the pump shaft showed the pulsation frequency to be 0.50 Hz – in good agreement with the 0.53 Hz frequency characteristic of the surface waves. In order to isolate these forced perturbations from inherent instability associated with the flow down an inclined plane, a decision was then taken to extend the case study by running trials on the off-line Perspex cascade as described in Section 2.6.

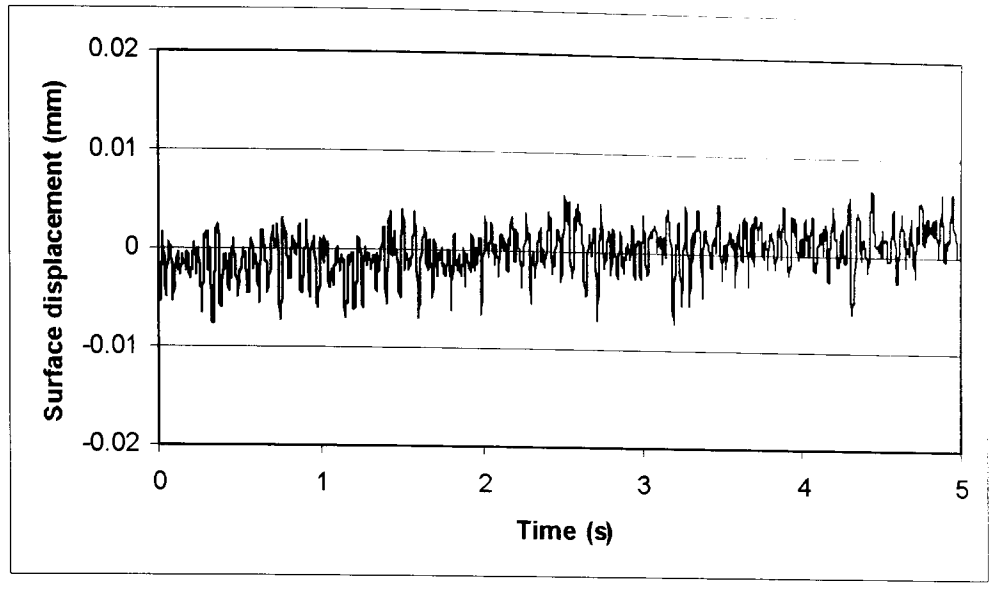

Figure 4.22: Response to surface waves 10 mm upstream of lower exit slot

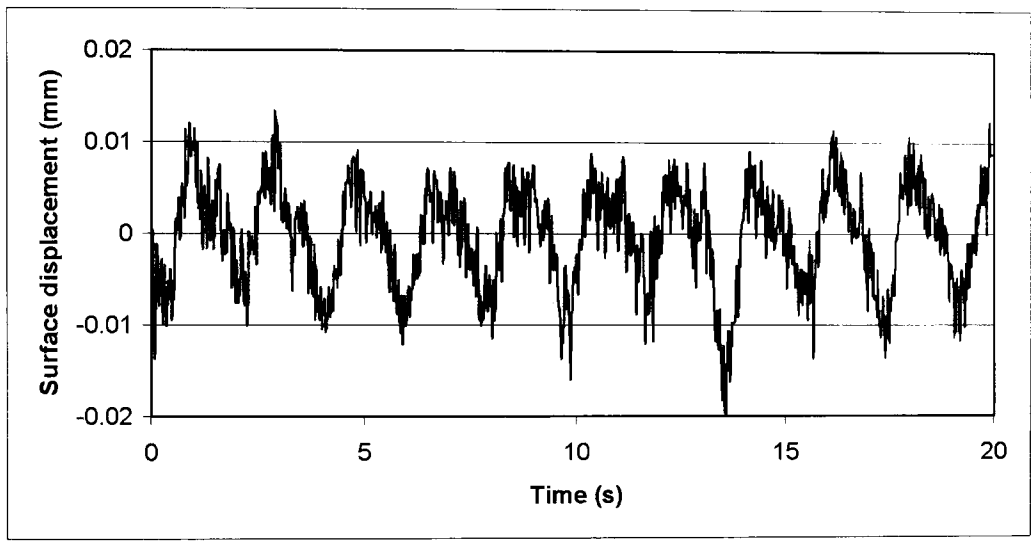

Figure 4.23: Response to surface waves 10 mm downstream of lower exit slot

4.3.2 Inherent Instabilities due to Slidewaves

The method and equipment described in Section 2.8 were used to quantify both surface and interfacial disturbances for the fluids and operational conditions applicable to case study #1 and summarised in Table 4.5. The slide inclination angle was set at 23°.

	Solution Clarity	Flow Rate (m^2/s)	Viscosity at $100s^{-1}$ (mPa.s)	Density (kg/m^3)	Surface Tension (mN/m)
Upper layer	Opaque/scattering	4.0×10^{-5}	400	900	28
Lower layer	Clear	0.5×10^{-5}	15	1000	30

Table 4.5: Solution properties and flow rates used for studying slide waves

Disturbances to the free surface and interface were measured at a point 99.6 mm downstream of the exit slot at which the two flows merged. Results from analysing the signals from the two laser displacement meters mounted above and below the extended Perspex slide are shown in Figure 4.24. The waveforms shown in the lower part of the figure depict results after applying digital filtering to remove unwanted higher frequencies from the data. This was achieved by computing the fast fourier transform using Mathcad, discarding all frequencies above a threshold value and transforming back to the space domain by determining the inverse fast fourier transform. Figure 4.25 shows the power spectra for the surface and interface resulting from the fourier analysis.

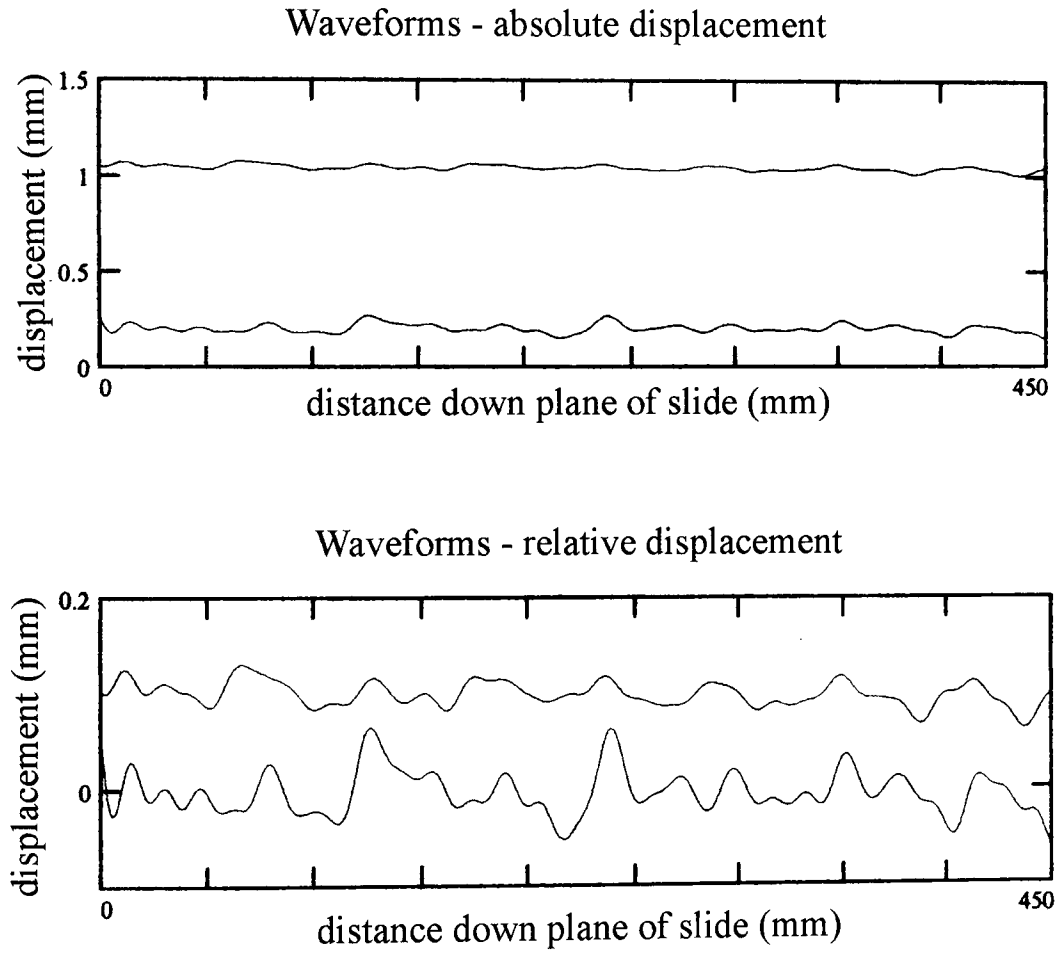

Figure 4.24: Waveforms for the surface and interface

Kobayashi [1992] pointed out that when quantifying the stability of layers flowing down a slide, neutral stability curves calculated using conventional stability analysis for the interface do not have much meaning when applied to the slide bead coating process. This is because such flows would become unstable given sufficient time were

the slide sufficiently long. This is due to the absence of interfacial surface tension. In practice, the length of the slide is kept to a minimum of the order of a few tens of millimetres as dictated by the need to establish a mean equilibrium thickness profile while reducing the bulk of the coating applicator as much as possible. He showed that what matters is the rate of growth of such an instability. He performed a stability analysis in which he computed the dimensionless growth distance $L_{e,min}/H_1$ by solving the Orr-Sommerfeld equations for a range of solution properties and flow rates. Figure 4.26 shows Kobayashi's numerical results for a specific set of conditions given by $Re_1 = 10$ and a slide inclination angle 30° where:

$$Re_1 = \frac{\rho_1 U_a H_1}{\mu_1} \tag{4.5}$$

U_a being the average velocity down the slide.

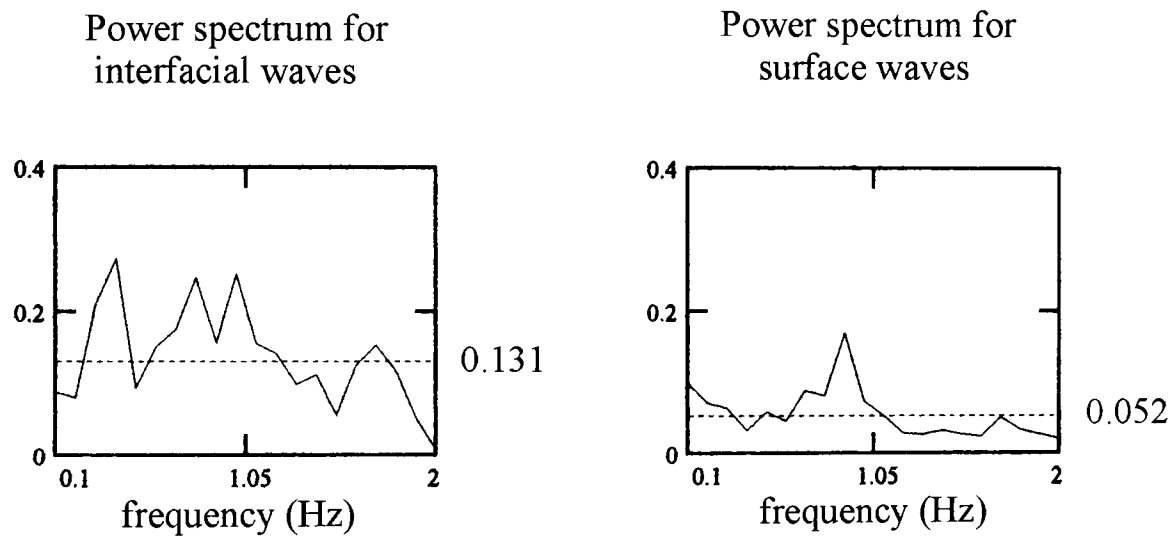

Figure 4.25: Power spectra for the waves at the surface and interface

It will be seen from Figure 4.26 that the rate of growth of the interfacial mode exceeds that for surface waves as the viscosity ratio m departs significantly either side of unity. Here m is given by:

$$m = \frac{\mu_2}{\mu_1} \tag{4.6}$$

It is not possible to directly compare the preliminary results from this work with the predictions of Figure 4.26 as the value of Re_1 was significantly different being of the order of 0.58 and the slide angle 23°. The results nevertheless qualitatively agree with Kobayashi's numerical findings in that the interface becomes significantly more disturbed than the free surface at a finite distance downstream of the slot exit.

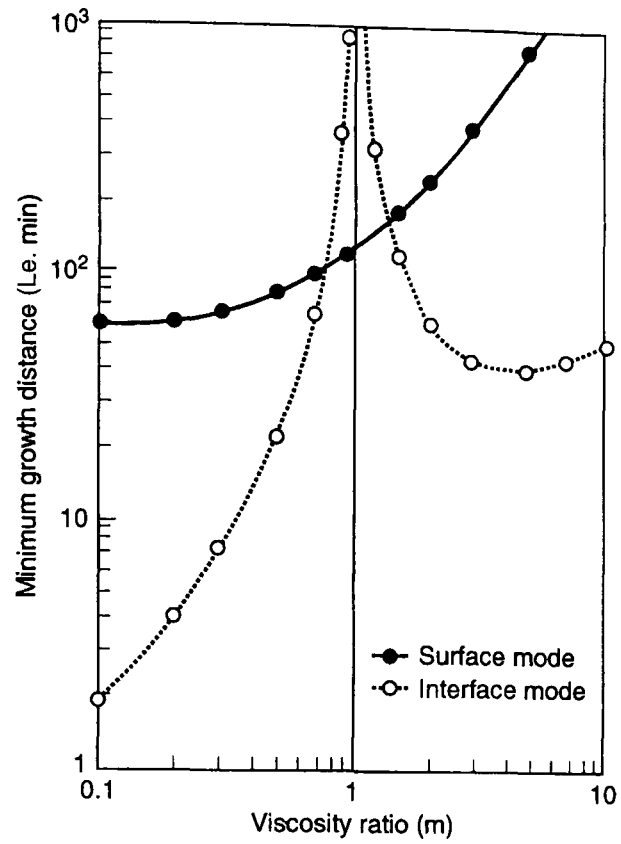

Figure 4.26: Numerical predictions for two layer flow due to Kobayashi [1992] for $Re_1 = 10$ and $\beta = 30°$

Koboyashi [1992], in seeking to validate his theoretical analysis, experienced difficulties in observing what was happening on the slide owing to the opacity of the coloured dyes used and the small wave amplitudes. He therefore had to resort to making subjective assessment of the quality of resulting coatings and measure the pitch of any observed waviness. These limitations are overcome in the techniques described in this work. There was unfortunately insufficient time to enable further work to be carried out but the results are sufficiently encouraging to suggest the experimental techniques be exploited to allow a full validation of the numerical analysis initiated by Kobayashi [1992].

Weinstein [1990], showed from numerical solutions for shear thinning fluids that the surface mode is governed by the mean value of the viscosity, while, for the interface mode, sensitivity increases with the size of the jump in local viscosity. As part of this preliminary study, the velocity distribution within the merged layers was calculated using the equations governing equilibrium two layer flow – see Appendix I. The results show that the velocity gradient is indeed characterised by an abrupt change at the interface – Figure 4.27. This jump arises from the fact that shear is continuous at

the interface requiring that the velocity gradient must be proportional to the local viscosity.

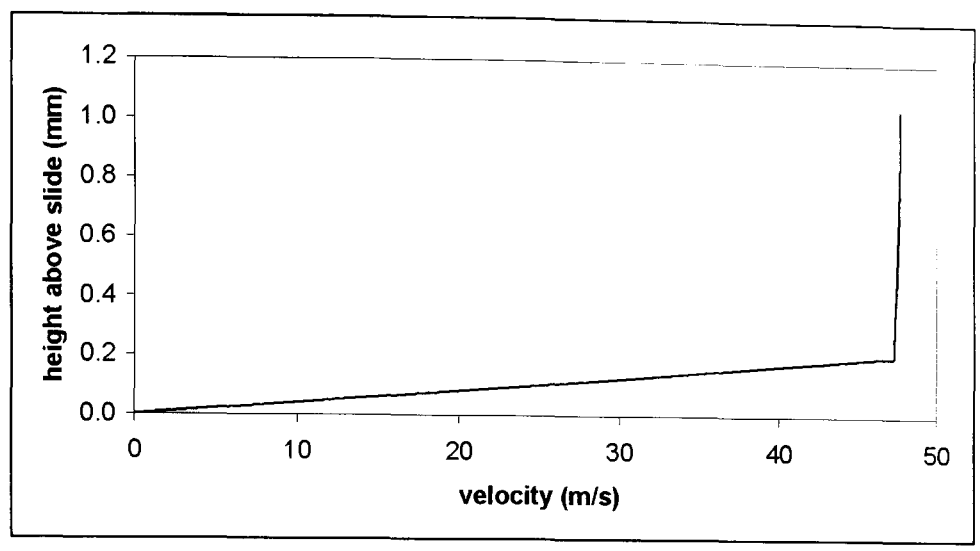

Figure 4.27: Velocity profile for conditions generating slide waves

4.3.3 Summary

The experimental results presented here have shown that the flow of layers merging at the lower slot becomes increasingly sensitive to perturbations in the flow rate of the carrier layer as the flux approaches the critical minimum threshold value. This is not entirely unexpected. Conroy and Weinstein [1994] have shown, when studying the response of two layer flows to forced perturbations generated by vibration or pulsations in the flow, that the interface becomes increasingly sensitive as the bottom layer wet thickness is reduced. Figure 4.28 shows an example from their work where the computed wave amplitude gain per cm slide length at the most dangerous frequency is plotted as a function of bottom layer thickness, expressed as a percentage of the total wet laydown. Here the viscosities of the lower and upper layers were 5.5 mPa.s and 33.8 mPa.s respectively and the total flow rate fixed at 1.14 cm^2s^{-1}. The perturbation response reported here is nevertheless unique. This is because it is associated with the recirculation generated at the downstream slot wall as the carrier layer flow approaches starvation rather than derived from the inherent instabilities at the interface between two flows on the slide itself.

The preliminary experiments reported here serve to confirm the findings of Kobayashi [1992] that the interfacial mode predominates over surface waves as the ratio of the viscosities of two layers departs above or below unity. As pointed out by Hens and Abbenyen [1997], despite the abundant work carried out on the study of instabilities on an inclined plane, much yet needs to be done to gain a complete understanding when related to multi-layer coating. The techniques reported here by which it is now possible to directly quantify interfacial disturbances can readily be exploited to this end. Another avenue of exploration is to follow up a suggestion made by Blake [2001] in which he proposed looking at the effect of interlayer diffusion by inhibiting such effects through adding salt to the lower layer.

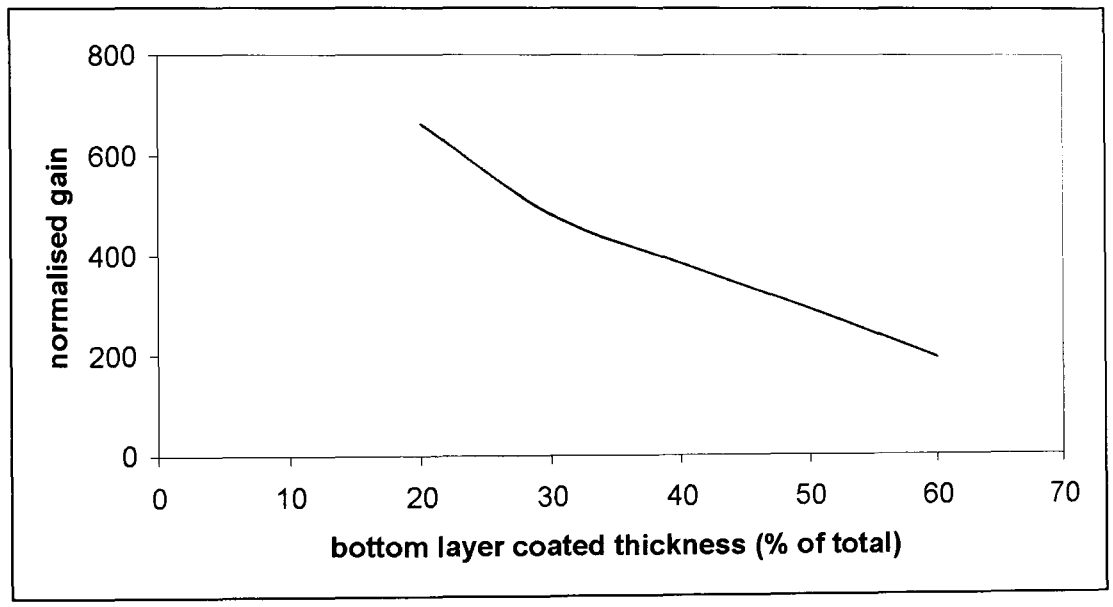

Figure 4.28: Computed interfacial wave amplitude gain factor for a two layer coating for μ_1 = 5.5 mPa.s and μ_2 = 33.8 mPa.s after Conroy and Weinstein [1994]

4.4 Instabilities in the Wet Coating incurred during Drying

4.4.1 Introduction

The justification for developing equipment to monitor air induced disturbances to the wet coating during the early part of drying was described in Section 2.14.1. Much work has been reported on theoretical and experimental studies relating to the effect of dryer design on the efficiency of heat transfer – for example Martin [1977], Petros

[1988], Polat [1993] and Noakes et al. [2002(2)], but only little on the effect on air induced surface perturbations. It is recognised that wet low viscosity coatings are especially prone to becoming disturbed (Cohen and Gutoff [1992]). Ruschak [1987] has developed a theoretical analysis relating to the flow of a thin liquid layer when subjected to a sinusoidal pressure disturbance. He calculated growth rate in terms of the characteristic time τ required for deformation to take place and showed that:

$$\tau = \frac{\mu}{\alpha^2 H_\infty{}^3(\rho g + \sigma\alpha^2)} \qquad (4.7)$$

where $\alpha = 2\pi/\lambda$, λ being the wavelength of the forced perturbation. This work is useful as being applicable to the response of a wet coating to the impingement of air issuing from holes in a plate that are equispaced by a distance λ. It is thus predicted that the growth rate will increase with wet thickness and decrease with viscosity.

In this study, work is carried out to establish the response of a thin wet coating as it moves continuously beneath jets of air issuing from equispaced slots aligned perpendicular to the machine direction – rather than from an array of holes. Perturbations are thus not forced by a pressure distribution varying periodically across the web path but are the result of inherent instabilities arising from the shearing action of air moving over the free surface of the liquid. Equation (4.7) is thus not directly applicable.

Initial trials using the rotary dryer mounted on the pilot coating machine reproduced a wavelike disturbance in a coating held stationary beneath the moving jets. The pattern – Figure 2.78 – is remarkably similar to that seen on the windscreen of a car when in motion after the application of de-icing fluid. Similar patterns are seen on thin horizontal wind-blown water films (Craik [1966]) and on aircraft wings after the application of deicing and anti-icing fluids (Özgen et al. [1999] and Özgen et al. [2002]). Air jet wiping applied to the removal of excess molten zinc in a wire coating process produces similar effects – Buchlin et al. [1997], Gosset and Buchlin [2003].

The objectives for the work described in this study were as follows:

- To establish the mechanism for the wavelike pattern

- To quantify the dependence of wave amplitude on viscosity and wet thickness
- To determine any additional benefits accruing from optimising the water distribution within a multi-layer coating assembly

4.4.2 Wave Growth due to Air Jets issuing from an Array of Slot Nozzles

The work described in Section 2.14.3 showed that the air induced disturbance pattern was essentially the same irrespective of whether generated by the rotary dryer, where the relative speed difference was high (typically 200 m/min.), or whether the sample was moved at a speed of only 7 m/min beneath a linear array of air jets. In order to establish the mechanism for the disturbance, a trial was run using the method described in section 2.14.3.1. The carriage carrying a CCD camera was set in motion to track a freshly coated sample as it entered beneath the dryer. The drying speed was controlled to 7 m/min. by reverting to open loop control in order to minimise instabilities and thus reduce the risk of distorting the response to waves induced in the liquid. The recording of the camera response is reproduced as a video clip appended to this thesis – see Appendix II – sequence # 7. The temperature of the coating solution and of the air supplied to the dryer were controlled to that of the ambient room conditions – namely 23°C. The coating comprised a single layer of PVOH solution with the addition of green dye to enable visual contrast and was laid down at a wet thickness of 75 μm at a coating speed of 15 m/minute. The viscosity was 9.9 mPa.s and the surface tension 34.7 mN/m when measured at 23 °C. Air was supplied to the nozzles at 250 Pa resulting in a maximum air impingement speed of 19.4 m/s as calculated from equation (2.70) – Section 2.14.2. The nozzles were equi-spaced at intervals of 73.5 mm and at a height of 9 mm above the web. Figure 4.29 shows how the waveform captured by the 50 mm field of view of the camera developed with time.

The four waveforms were sampled as the camera passed midway between pairs of adjacent jets and analysed by the digital filtering method described in section 2.14.3.1. It will be seen that the disturbances are initially random but grow by displacement of the liquid generally parallel to the machine direction away from thinner areas and

towards thicker areas until a wavelike pattern emerges. The phase of the waveform then remains stationary relative to the web.

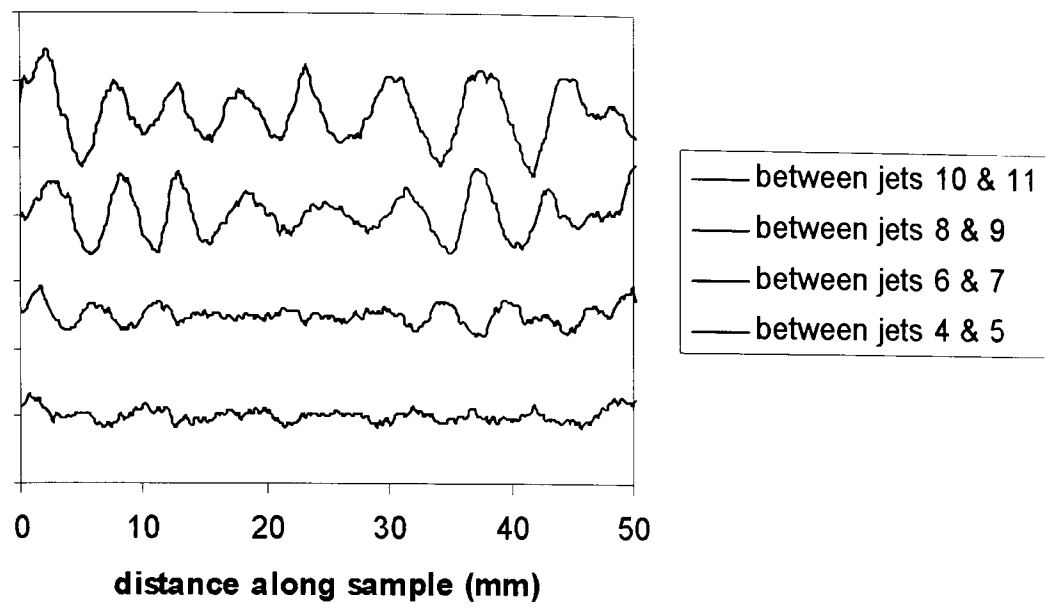

Figure 4.29: Recordings of a given surface wave pattern at four points down the dryer

The wavelength was typically 6.1 mm for this experiment. This finding is in agreement with the work of Gosset and Buchlin [2003] when quantifying waves on a liquid entrained by a rotating cylinder and disturbed by a gas jet. They found that the wave velocity determined by 2-D cross-correlation of successive images recorded by a high speed camera always equalled the substrate velocity for a speed range of 120 to 400 mm/s. The rate of wave growth is shown in Figure 4.30 and found to approximate well to Rt^2 for the time range 0 - 6 seconds, where t is the time in seconds and R is a constant.

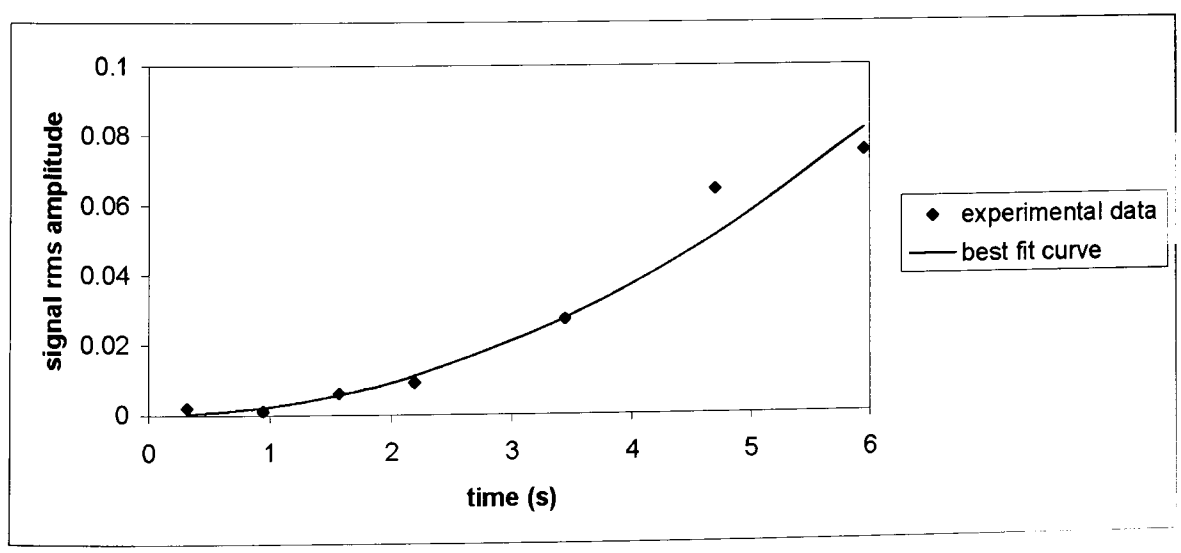

Figure 4.30: Rate of wave growth

The time taken for the fluid to begin to respond to air movement was about 1.2 seconds. It was therefore considered important in these studies to ensure the interval between successive air impingements was less than 1.2 seconds. The lowest acceptable speed for analysing the surface waves was thus of the order of 3.5 m/minute. This explains why the pattern seen when subjecting a wet coating to the rotary dryer operating at a peripheral speed of 200 m/min. was very similar to that generated by passing a coating beneath the stationary linear array at 7 m/min.

4.4.3 The Dependence of Wave Amplitude on Viscosity and Wet Thickness

Having established confidence that the web speed selected for the study gave representative effects, trials were carried out using the equipment and method described in Section 2.14.3.2 for profiling the film thickness at a fixed point beneath the dryer. This was selected to be as far from the entrance zone as possible to allow waves to become well developed. Two coating assemblies were initially studied, both comprising green dyed PVOH solution, the first diluted to achieve a viscosity of 10 mPa.s and the second 20 mPa.s when measured at 23 °C. Three wet thicknesses were evaluated for each viscosity, the lower limit being dictated by coating constraints and the upper limit by excess movement under the dryer when operating at the minimum achievable air pressure. The results are shown in Figure 4.31 for the 10 mPa.s coatings and in Figure 4.32 for 20 mPa.s. It will be seen that the amplitude of the surface waves increases with both air speed and wet thickness and decreases with viscosity.

4.4.4 The Benefit of Optimising Water Distribution using a Carrier Layer

A coating trial was run as part of this study in which a gelatin / cellose mixture of viscosity 43.9 mPa.s and wet thickness 96.6 μm was subjected to air impingement using the linear nozzle array. The pressure and temperature of the air were both increased at any given point during the drying period to a limit as dictated by the onset of disturbances becoming visible beneath the experimental nozzle array.

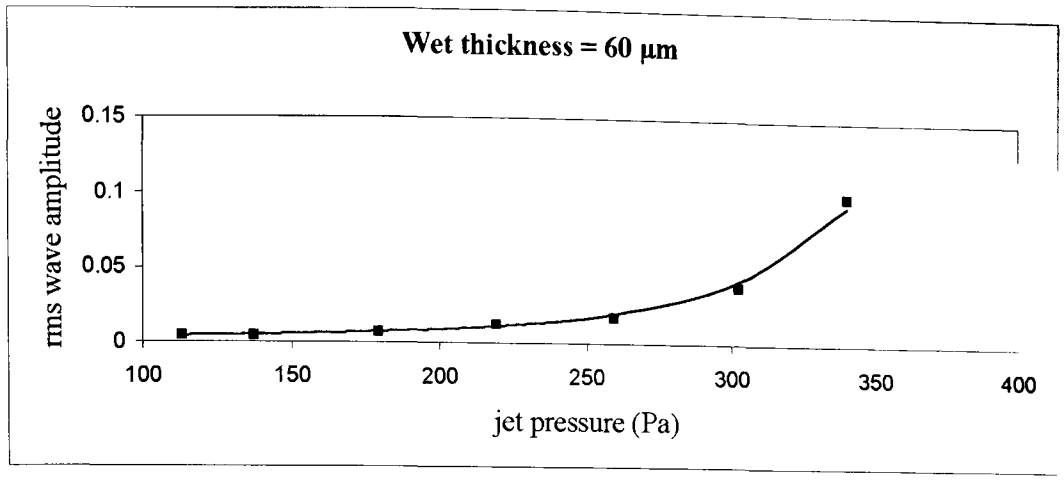

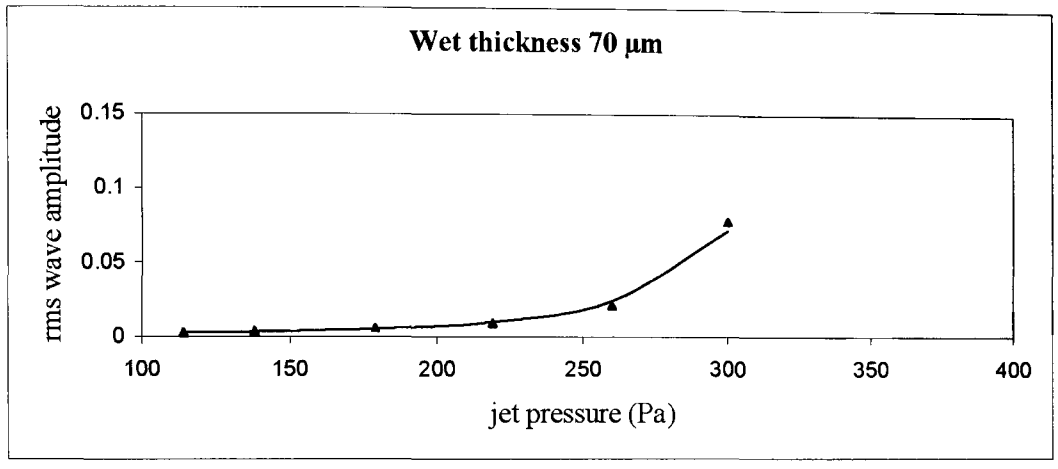

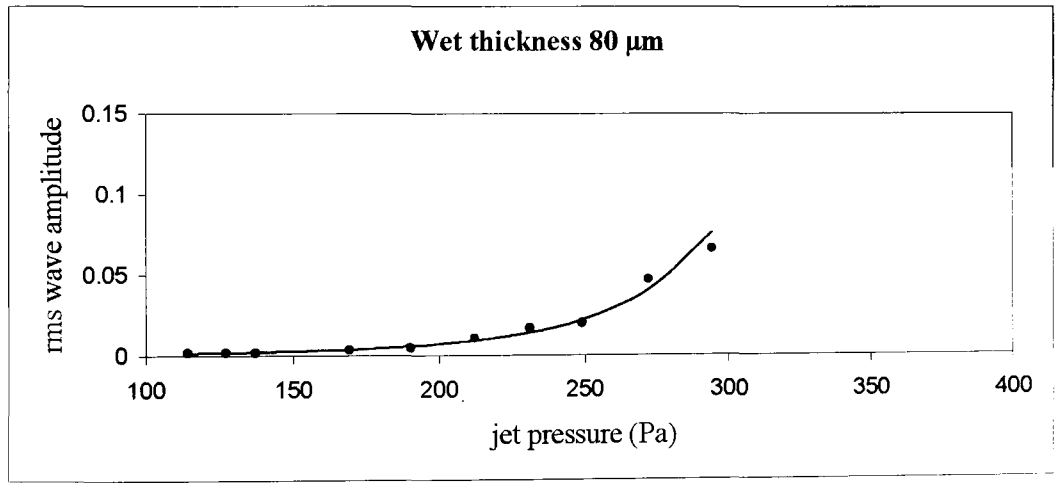

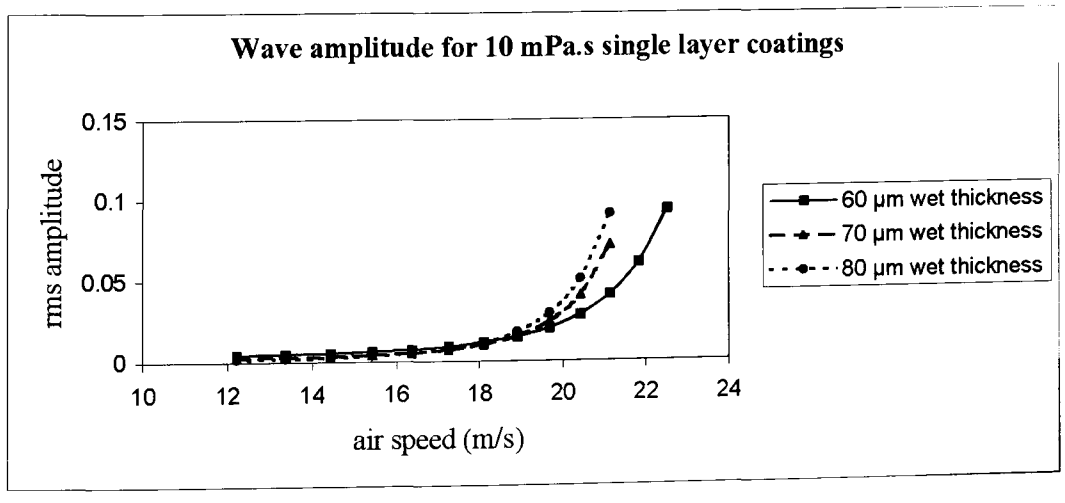

Figure 4.31: Surface wave instability for single layer 10 mPa.s coatings

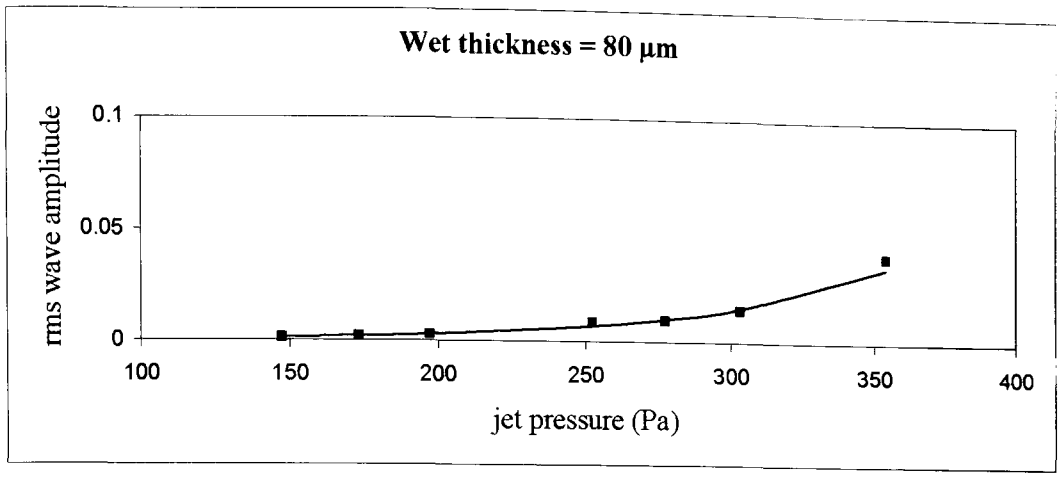

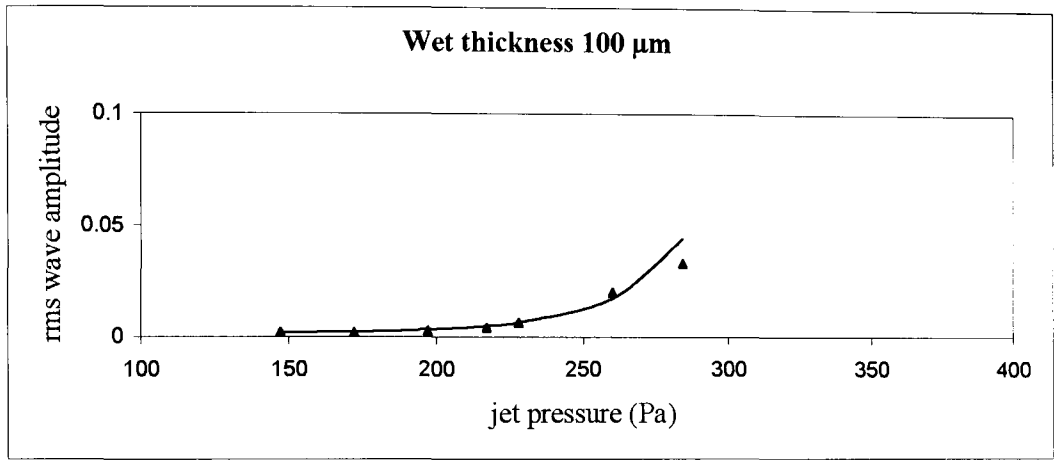

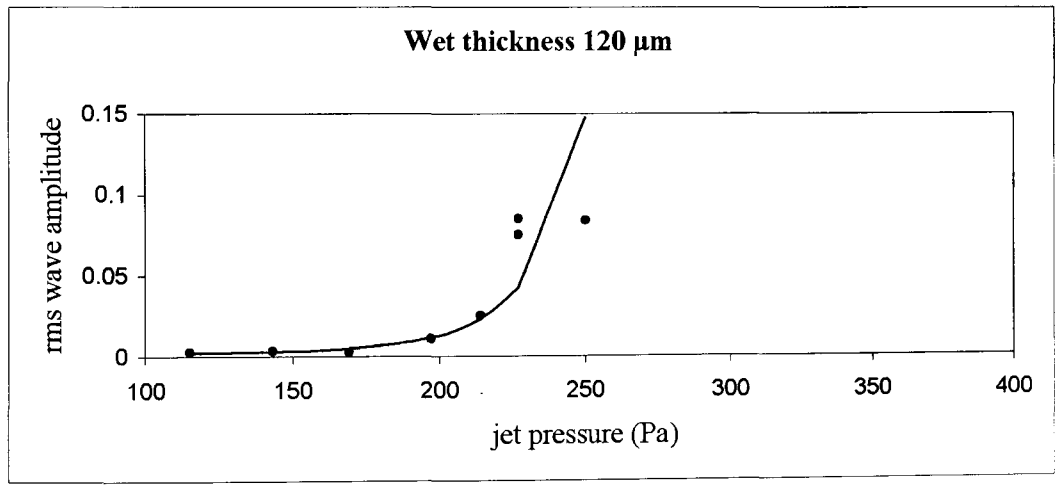

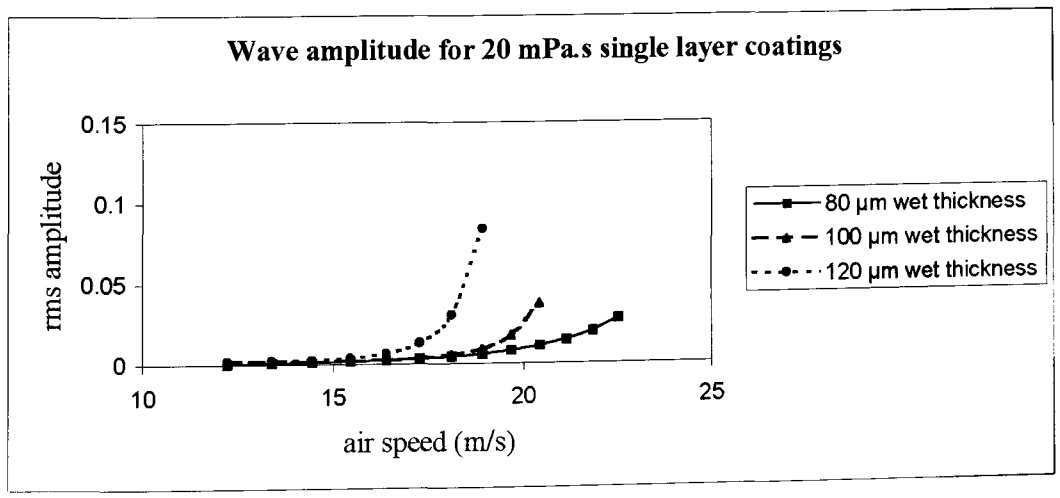

4.32: Surface wave instability for single layer 20 mPa.s coatings

In practice, several runs were attempted using a number of pressure and temperature profiles preset by means of the control system installed on the machine. Figure 4.33 shows the end result and indicates how it was found necessary to limit the air speed to 35 m/s at the first part of drying to prevent visible disturbances to the coating. As drying proceeds, the air pressure can be increased without risk of damage. This is because water is being driven off thereby causing the wet thickness to decrease and the viscosity to increase, both changes being conducive to increasing robustness against surface waves.

EVAPORATION RATE FOR 9 MM NOZZLE-TO-WEB GAP FOR GEL/CELLOSE CASE STUDY DRIED AT 122 M/MIN

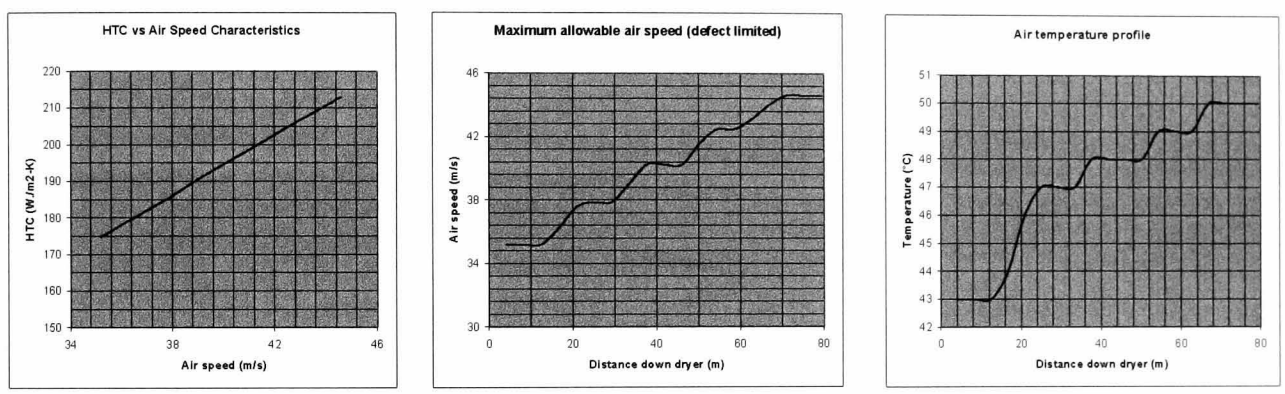

Figure 4.33: Optimisation of Pressure and Temperature Profiles taking into account Disturbances due to Surface Waves

A further set of experiments was run to quantify what benefit could be gained by redistributing the water in the coated assembly in terms of increased robustness against air induced disturbances. Two formulations were examined. Formulation A is similar to the G-C Mix #1 used as single layer test solution for comparing the coating performances of various bases – Section 3.4. The carrier layer based formulation B was similar to that found (Section 3.4.4.6 and Table 3.14) to yield optimum

performance when attempting to coat the worst case scenario presented by subbed base type #3S.

	Single layer formulation A	Carrier layer formulation B
Upper layer	64.4 µm x 43.9 mPa.s	47.0 µm x 108.2 mPa.s
Lower layer	32.2 µm x 43.9 mPa.s	36.3 µm x 35.3 mPa.s
Total layer thickness	96.6 µm	83.3 µm
Total solids content	6.76 gsm	6.74 gsm
Total water load	91.4 gsm	78.2 gsm

Table: 4.6: Formulations used to evaluate the benefit of using a carrier layer

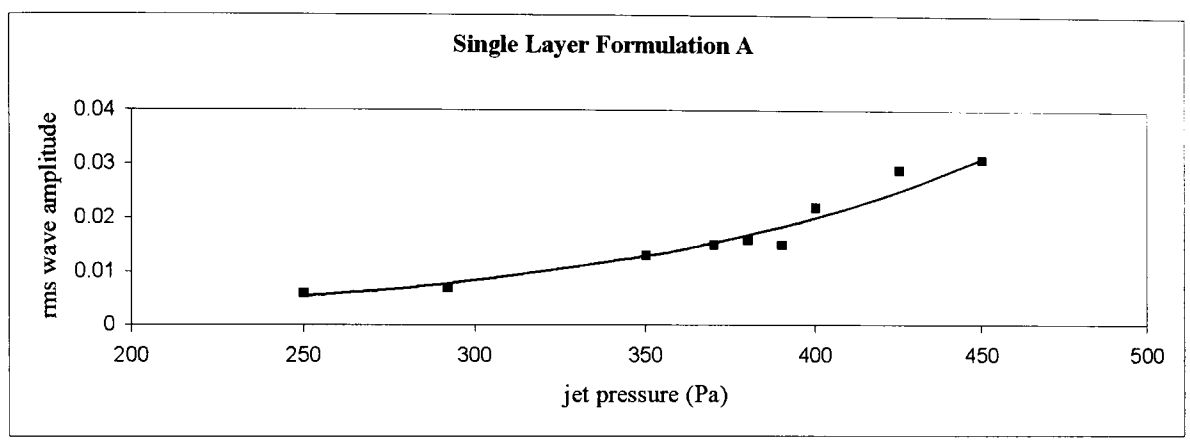

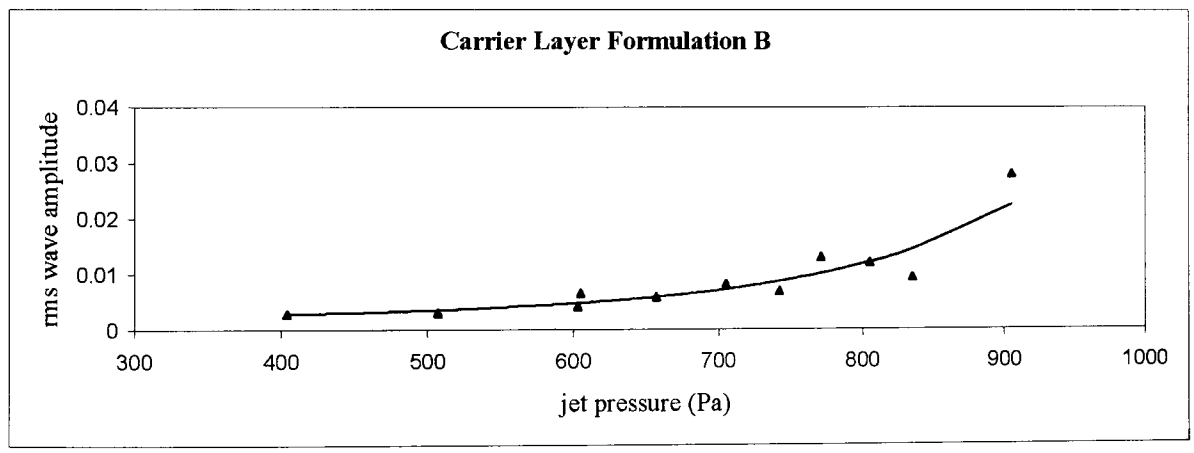

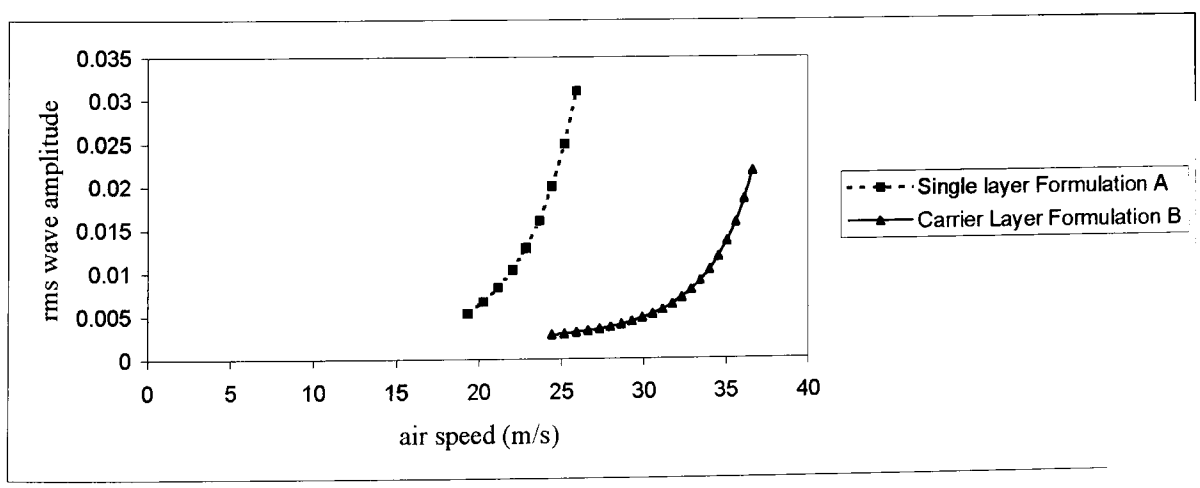

Figure 4.34: Surface wave instability for formulations shown in Table 4.6

Figure 4.34 shows the results from wave amplitude measurements for a range of applicable air pressures for the two formulations A and B. The use of the carrier layer, while allowing higher coating speeds, also enables a significant increase in drying speed for two reasons:

1. The water load has been decreased from 91.4 gsm to 78.2 gsm
2. The pressure can be optimally increased to higher values down the dryer to secure maximum evaporation rate without endangering end quality due to surface waves

The heat transfer coefficient was determined using the method described in Section 2.14.4 for the array of nozzles when set at a gap of 9 mm above the web. The value at a working pressure of 250 Pa was found to be 170 ± 15 $W.m^{-2}K^{-1}$. Taking an arbitrary value of 0.007 for the rms wave amplitude as being just visible on the scale of measurement used in the method described in Section 2.14.3, the results shown in Figure 4.34 indicate that it is allowable to increase the working pressure from 281 Pa to 697 Pa to limit the waviness to this constant level.

Cary and Gutoff [1991] conclude from their studies on the drying of aqueous coatings that the heat transfer coefficient varies according to the expression:

$$h = h_0\left(\frac{\Delta P^{0.39}}{\Delta P_0{}^{0.39}}\right) \tag{4.8}$$

where h_0 is the heat transfer coefficient measured at pressure P_0. The evaporation rate during the early part of drying is proportional to the given heat transfer coefficient while water molecules within the coating are free to migrate to the surface. This is true during the early part of drying, in contrast to later stages where water migration is controlled by diffusion. Hence it can be concluded that the evaporation rate obtained when using the carrier layer formulation is enhanced by a factor of $(697/281)^{0.39}$ or an increase of 47 %. This is a very significant benefit in addition to that obtained from the overall 15 % reduction in water load. Drying rate is often the most significant limit to overall process line speed when taking into account the high costs associated with providing the plant and the energy required to achieve the necessary evaporation.

4.4.5 Summary

The work has shown that surface waves induced from air issuing from an array of equispaced parallel slots aligned perpendicular to the machine direction can be accurately quantified and related to the viscosity and the wet thickness of single layer coatings. Random disturbances produced by the shearing action of the air grow with time, the liquid flowing from thinner areas to thicker areas until a wavelike pattern is fully established which travels at the same velocity as the web.

Measurements show that the amplitude of the established wave increases rapidly with wet thickness and decreases with viscosity much in the same way as predicted by Ruschak [1987] when considering the forced disturbances arising from air issuing from parallel rows of holes.

The work is novel and hitherto unreported as extending to the consideration of multi-layer coatings. It has been demonstrated that redistributing water within a coating to form a carrier layer while increasing solids concentration elsewhere is not only beneficial to coating but can be significantly more advantageous to drying than generally realised.

Chapter V

Conclusions

5.1 General Discussion

This thesis investigates the role of carrier layer flows in determining the effectiveness of an industrial slide multilayer coating process as typically used within industry manufacturing photographic products and ink-jet media. The study is essentially experimental and the scope broad in that issues concerning both the coating and drying of multilayer assemblies are addressed. The study is unusual in that the role played by the surface properties of the substrate has been examined in some detail. The development and exploitation of the extensive pilot facilities initially available at HARMAN technology Limited (formerly ILFORD Imaging UK Limited) formed a major part of this work along with the design and manufacture of specialist equipment for monitoring the flows. Special emphasis has been placed on establishing methods for monitoring flows when:

- establishing the layers on the slide
- making the bead
- continuously coating
- overcoating splices used for joining consecutive rolls of web
- subjecting the wet coating to air from an impingement dryer

Novel methods have been developed for profiling the interface and free surface at both the exit region of the slot and as the merged layers flow down the slide. The work required to develop, design and build a monitoring system for profiling the lower meniscus at the bead forming zone presented a major challenge and extended over a large part of the time devoted to the preparation of this thesis. The unique ability to visualise the free surface when coating substrates that are opaque and characterised by roughness and surface texture as well as porosity and variable surface electric charge offers considerable scope for furthering the understanding of process limitations of

interest to industry. Other significant developments include the setting up of a method to record disturbances to the surface of wet coatings during the early part of exposure to an air impingement dryer. A procedure has been established for determining the coating window for defining the upper and lower limits to the stabilising suction dictated by ribbing flow, break up into rivulets and air entrainment.

Key conclusions arising from the application of these techniques are as follows:

1. The surface energy of the substrate when determined from the measurement of advancing contact angles for pure water, while useful for predicting the ultimate adhesion of a fully dried coating, bears no correlation with the ease of coating. On the other hand, the method of Owens and Wendt to decompose the surface energy into polar and dispersive components using two test fluids, one polar and the other non-polar, shows a strong correlation with coatability using the slide process – as previously reported by Blake and Morley [1997]. Coating experiments show that gelatin "subbed" surfaces, being highly polar, present more difficulty when attempting to make the bead than corona treated "unsubbed" surfaces.

2. Coating window trials show that, for given polar and dispersive surface energy components, a rougher surface is generally detrimental to coating by the slide bead process – in contrast to dip coating (Buonopane [1986]) and curtain coating (Hartman [1989]), where the opposite effect is found.

3. Metastable conditions can exist for the slide bead process where air entrainment is either present or absent, depending on start-up. Under such conditions, defect-free coating can be achieved by temporarily opening up the gap and then restoring back to a value for ensuring a wide coating window – an effect hitherto unreported.

4. A stippled web surface showing a high surface area ratio has been found to coat more easily than one having similar surface energy components and a similar Rz value but of lower surface area ratio. It is suggested that the composite wetting mechanism is responsible for this improvement where the bottom layer viscosity is at least of the order of 40 mPa.s. It would

appear from these limited findings that the coatability of appropriately designed formulations increases with surface area ratio in the same way as resistance to a sliding water drop decreases (Miwa et al. [2000]).

5. A thin low viscosity carrier layer as advocated by Dittman and Rozzi [1977], Choinski [1978], Ishizuka [1989(1)] and Ishizuka [1989(2)] does not consistently broaden the coating window for rough substrates. A more generally successful approach is to ensure the wet thickness of the bottom layer equals or exceeds the value of Rz – a fact hitherto ignored in published work. It would appear from limited measurements on bead profile when coating a rough substrate that the stability of the bead is enhanced as the dynamic wetting line is moved slightly downstream of the projection of the slide surface onto the web. Dynamic contact angle alone does not appear to correlate with robustness against rivulets and air entrainment.

6. The coating window for roughened substrates showing a high degree of resistance to wetting can be significantly broadened by increasing the inclination angle of the slide, the limit being dictated by slide waves.

7. Unbound electric charge has an adverse effect on coatability while not significantly affecting the average dynamic contact angle measured using a needle coater.

8. Bound polar charges orientated to yield a net positive voltage at the surface of the substrate causes a reduction in the dynamic contact angle and results in a decrease in the minimum suction pressure required for resisting air entrainment. The forces acting on the lower meniscus predominate at the dynamic wetting line in contrast to the effect of applying suction which acts uniformly over the entire meniscus. It is thus possible to achieve stable coating while ensuring the static wetting line remains firmly locked to the corner with consequential improved robustness against the generation of streaks. The experiments give credence to the claim by Vandaele et al. [1999] that the increased risk of ribbing from this mode of operation is likely to be sourced in an increase

in curvature of the upper meniscus in the presence of orientated polar charge at the substrate surface.

9. Measurements of the edge retraction rate as a test sample surface replaces a reference web surface during join-withdrawal show that the maximum speed at which a porous substrate can be coated can be significantly enhanced by using a thin low viscosity carrier layer. The tendency for blow hole defects caused by air penetration into holes formed in a porous surface is also significantly reduced by this means.

10. The limit to forming a thin carrier layer flow on the slide is determined by the point of invasion of the upper layer or layers into the slot exit. The threshold flow rate is significantly reduced when replacing a chamfered slot exit with a non-chamfered design and further reduced as the slot width is decreased. The final limit is then largely dictated by machining errors and reliability when assembling the parts forming the cascade. The interface is shown to be locked to the upstream slot wall corner provided that the contact angle exceeds 65°, thus giving credence to the work of Apps [2000] who, when solving for various conditions, discarded all numerical solutions for which the static contact angle was less than this value. The results also appear to confirm the presence of a vortex just beneath the downstream slot corner and a mechanism is suggested for explaining the starvation lines previously observed by Ikin.

11. An unreported effect was observed in that the flow of layers merging at the lower slot exit become increasingly sensitive to forced perturbations in the flow rate of the carrier layer as the flux approaches the critical threshold value. Recordings of the interface profile show this to oscillate up and down out of phase with similar movements in the free surface.

12. The special methods developed to visualise the interface midway down the slide reveal that the severity of interfacial slide waves is of the order of 2.5 times that at the free surface – thus confirming the predictions of Kobayashi [1992] that interfacial disturbances predominate as the viscosity ratio for two merging layers significantly departs from unity.

13. Surface waves induced from air issuing from an array of equispaced parallel slots aligned perpendicular to the machine direction have been accurately quantified and related to the viscosity and the wet thickness of single layer coatings. The amplitude of the established wave increases rapidly with wet thickness and decreases with viscosity. It has been shown that random disturbances produced by the shearing action of the air grow with time, the liquid flowing from thinner areas to thicker areas until a wavelike pattern is fully established which travels at the same velocity as the web.

14. The application of the carrier layer concept through redistributing the water in an aqueous multilayer coating for optimum coating performance has the added benefit of showing a very significant enhancement in the robustness against air induced surface waves. This effect has not been hitherto reported.

5.2 Future Work

The provision of the powerful method for visualising the lower free surface in the bead making zone provides considerable scope for further investigation into a number of areas. These include:

1. The interaction between rough substrate surfaces and the coating bead. This is an area which has received only very little attention up to the publishing of Clarke's results on the curtain coating of rough surfaces. The behaviour of the flow when attempting to coat a stippled base surface is as yet unexplained and calls for further study with the benefit of a robust numerical method for modelling flows over structured surfaces. It is suggested that correlation be made with surface area ratio for a wider range of surfaces.
2. The interaction of the coating bead with other surface properties including bound electric charge and surface energy.

3. The validation of numerical models aimed at the simulation of thin carrier layer flows. This remains a major challenge despite considerable recent advances made by Thompson et al.

It is suggested that the measurement of critical tilt angle (Wolfram and Faust [1978] and Miwa et al. [2000]) for a pure water drop of controlled size could provide a possible indicator for the ease of coating. Alternatively the method of Menchaca-Rocha [1992] for determining the stopping distance for fast moving mercury drops could possibly be developed for water drops to advantage. Such tests, once applied, may well show trends leading to further understanding on why coatability can vary over time when coating nominally consistent substrates.

The close correlation found between experiment and the prediction of the Apps computer model for slot exit flows calls for further exploitation in order to gain more insight into flow behaviour under the extreme conditions met when attempting to supply a thin low viscosity carrier layer. There is a clear case for extending the work of Moffatt [1964] to solve the flow near a static contact line between two fluids both having non-negligible viscosity.

Another avenue of exploration is to follow up a suggestion made by Blake [2001] in which he proposed looking at the effect of interlayer diffusion on the propagation of slide waves by inhibiting such effects through adding salt to the lower layer. This can now readily be undertaken using the method for monitoring the interface as well as the surface when studying two layer flows.

Appendix I

The flow of two layers down an inclined plane

The equations applicable to the fully established flow of two immiscible liquids down an inclined plane are well known. The following derivation is taken from Panton [1984].

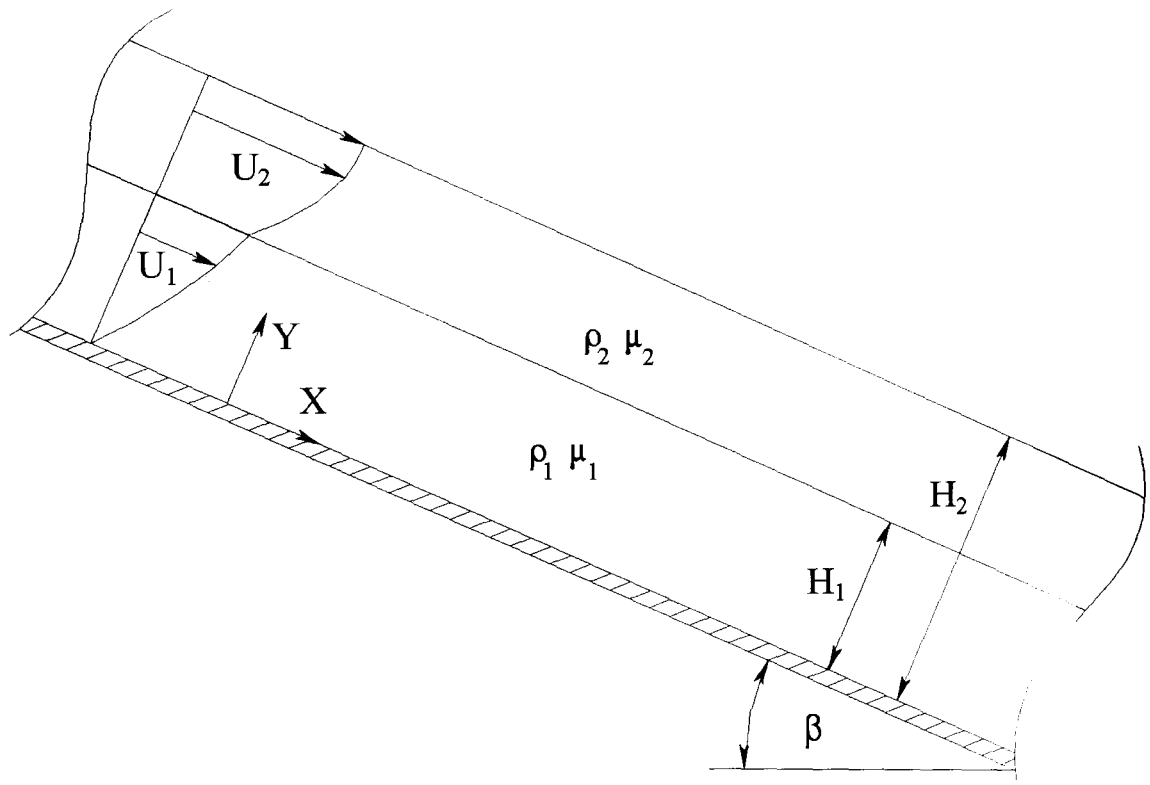

Figure A.1 Two layer flow on an inclined plane

The values of H_1 and H_2 shown in Figure A.1 are unknown *a priori* but are assumed constant once the flows are fully established. The slide is inclined to the horizontal by an angle β and the densities and viscosities are as shown in Figure A.1.

A rectangular coordinate system is taken aligned with the flow with the X axis on the slide. It is assumed that all stream lines are parallel with the slide and that velocity in the cross-machine direction is everywhere zero. Hence U, the velocity in the X direction, is a function of Y alone. This also ensures that continuity is satisfied.

Applying the Navier Stokes equation of motion in the Y direction:

$$0 = \frac{-\delta P}{\delta Y} - \rho g \cos\beta \qquad (A.1)$$

where ρ is either ρ_1 or ρ_2 as needed. A partial integral of this equation gives:

$$P = -\rho g Y \cos\beta + f(X) \qquad (A.2)$$

Assigning P_0 as the atmospheric pressure on the top of the upper layer:

$$P = \rho_2 g(H_2 - Y)\cos\beta + P_0 \qquad \text{for } H_1 \leq Y \leq H_2 \qquad (A.3)$$

Assigning P_1 as the pressure at the interface and substituting for P_1 in (A.3):

$$P_1 = \rho_2 g(H_2 - H_1)\cos\beta + P_0 \qquad (A.4)$$

The pressure in the lower layer is given from (A.1) on substituting P_1 for P when $Y = H_1$:

$$P = \rho_1 g(H_1 - Y)\cos\beta + P_1 \qquad \text{for } 0 \leq Y \leq H_1 \qquad (A.5)$$

Applying the Navier Stokes equation of motion in the X direction:

$$0 = \mu\frac{d^2U}{dY^2} + \rho g \sin\beta \qquad (A.6)$$

The boundary conditions are firstly applied as knowing that slip cannot be sustained at the inclined plane and velocity is continuous at the interface:

$$U_1 = 0 \qquad \text{when } Y = 0 \qquad (A.7)$$

and

$$U_1 = U_2 \qquad \text{when } Y = H_1 \qquad (A.8)$$

Also it is assumed that shear stress is the same on each side of the interface – giving:

$$\mu_1\frac{dU_1}{dY} = \mu_2\frac{dU_2}{dY} \qquad \text{when } Y = H_1 \qquad (A.9)$$

The shear stress at the free surface must necessarily be very small when equated to that due to the air boundary layer. Hence to a first of order of approximation:

$$\mu_2\frac{dU_2}{dY} = 0 \qquad \text{when } Y = H_2 \qquad (A.9)$$

or μ_2 being finite,

$$\frac{dU_2}{dY} = 0 \qquad \text{when } Y = H_2 \qquad (A.10)$$

Integrating (A.6):

$$U_1 = \frac{-\rho_1 g Y^2 \sin\beta}{2\mu_1} + C_1 Y + C_2 \qquad \text{when } Y \leq H_1 \qquad (A.11)$$

and:

$$U_2 = \frac{-\rho_2 g Y^2 \sin\beta}{2\mu_2} + C_3 Y + C_4 \qquad \text{when } H_1 \leq Y \leq H_2 \tag{A.12}$$

where C_1, C_2, C_3 and C_4 are constants.

Applying the no-slip condition at the slide surface from(A.7), in (A11):

$$C_2 = 0 \tag{A.13}$$

and the zero shear at the free surface:

$$C_3 = \frac{\rho_2 g H_2 \sin\beta}{\mu_2} \tag{A.14}$$

Applying the condition expressed by (A.9) for the continuity of stress at the interface in (A.11):

$$C_1 = \frac{\rho_1 g H_1 \sin\beta}{\mu_1} \left\{ 1 + \frac{\rho_2}{\rho_1} \left[\frac{H_2}{H_1} - 1 \right] \right\} \tag{A.15}$$

Applying the condition expressed by (A.8) for no slip at the interface in (A.11) and (A.12) and substituting for C_1 from (A.15) and C_3 from (A.14):

$$C_4 = \frac{\rho_1 g H_1^2 \sin\beta}{\mu_1} \left\{ 1/2 + \frac{\mu_1 \rho_2}{2\mu_2 \rho_1} - \frac{\rho_2}{\rho_1} + \frac{H_2 \rho_2}{H_1 \rho_1} \left[1 - \frac{\mu_1}{\mu_2} \right] \right\} \tag{A.16}$$

Substituting for C_1, C_2 and C_3 in (A.11) and (A.12):

$$U_1 = \frac{\rho_1 g H_1^2 \sin\beta}{\mu_1} \left\{ \left(1 + \frac{\rho_2}{\rho_1} \left[\frac{H_2}{H_1} - 1 \right] \right) \frac{Y}{H_1} - \frac{Y^2}{2H_1^2} \right\} \tag{A.17}$$

and

$$U_2 = \frac{\rho_1 g H_1^2 \sin\beta}{\mu_1} \left\{ 1/2 + \frac{\mu_1 \rho_2}{2\mu_2 \rho_1} - \frac{\rho_2}{\rho_1} + \frac{H_2 \rho_2}{H_1 \rho_1} \left[1 - \frac{\mu_1}{\mu_2} \right] + \frac{\mu_1 \rho_2 H_2}{\mu_2 \rho_1 H_1} \frac{Y}{H_1} - \frac{\mu_1 \rho_2}{2\mu_2 \rho_1} \frac{Y^2}{H_1^2} \right\} \tag{A.18}$$

The values for U_1 and U_2 obtained on solving (A.17) and (A.18) are now used to determined the respective values for the flow rates per unit width Q_1 and Q_2.

The flow of the lower layer down the slide is given by:

$$Q_1 = \int_0^{H_1} U_1 . dy \tag{A.19}$$

to give:

$$Q_1 = \frac{g \rho_1 H_1^3 \sin\beta}{\mu_1} \left[\frac{1}{3} + \frac{1}{2} \frac{\rho_2}{\rho_1} \left(\frac{H_2}{H_1} - 1 \right) \right] \tag{A.20}$$

Similarly, the flow of the upper layer down the slide is given by:

$$Q_2 = \int_{H_1}^{H_2} U_2.dy \qquad (A.21)$$

to give:

$$Q_2 = \frac{g\rho_1 H_1^2 \sin\beta}{\mu_1}\left\{(H_2 - H_1)\left[\frac{1}{2} + \frac{1}{2}\frac{\mu_1\rho_2}{\mu_2\rho_1} - \frac{\rho_2}{\rho_1} + \frac{H_2\rho_2}{H_1\rho_1}\left(1 - \frac{\mu_1}{\mu_2}\right)\right]\right.$$

$$\left. + \frac{\mu_1\rho_2 H_2}{\mu_2\rho_1 H_1^2}\left(\frac{H_2^2 - H_1^2}{2}\right) - \frac{\mu_1\rho_2}{2\mu_2\rho_1}\left(\frac{H_2^3 - H_1^3}{3H_1^2}\right)\right\} \qquad (A.22)$$

The calculated values of Q_1 and Q_2 based on an initial assumption of values for H_1 and H_2 are designated Q_1' and Q_2' respectively. Q_1' and Q_2' are then compared with the known values Q_1 and Q_2 and corrections made to H_1 and H_2. The procedure is repeated iteratively until errors between the calculated and actual values of Q1 and Q2 converge to an acceptably low value enabling the final velocity distribution to be derived from equations (A.17) and (A.18) – see Figure A.2.

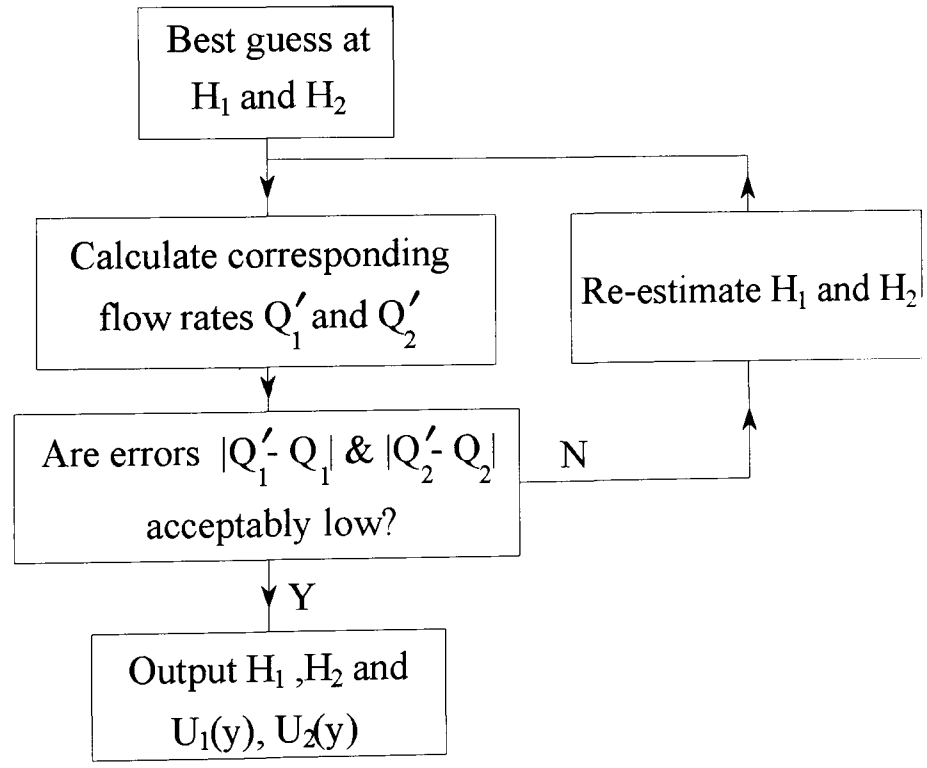

Figure A.2: Iterative process for calculating velocity distribution

Appendix II

A CD-ROM is appended with this thesis and shows video clips relating to experiments on slot exit flows, slide waves, the response of the coating bead to varying surface polar charge and surface waves on a wet coating seen during drying.

SLOT EXIT FLOWS

Video Sequence #1 - slotexitflow1.mpg – ref. Thesis Section 4.2.3.1

Run time ~ 15 s

This clip shows two flows merging at the exit of a chamfered slot machined in a Perspex cascade as described in Section 2.6 using the method detailed in Section 2.7. The lower layer is transparent and the upper layer is opaque and scattering. The properties of the two layers are given in Table A.1. The flow rate of the upper layer is fixed at 6.14×10^{-5} m^2/s.

	Flow rate	Viscosity	Density	Surface Tension
Upper layer	6.14×10^{-5} m^2/s	74.5 mPa.s	1014 kg/m^3	34.3 mN/m
Lower layer	Step change	5.4 mPa.s	1005 kg/m^3	34.3 mN/m

Table A.1: Properties and flow rates used for studying flow at chamfered slot exit

The sequence shows the response to a step change in flow rate of the lower layer down from 1.00×10^{-5} m^2/s to 0.82×10^{-5} m^2/s. The interface moves down through the slot exit to enter the slot itself just prior to the main layer invading the upper distribution chamber.

Video Sequence #2 – slotexitflow2.mpg – ref. Thesis Section 4.2.3.1

Run time ~ 20 s

This clip follows on from sequence #1 after having reduced the flow rate of the bottom layer from 0.82×10^{-5} m^2/s to 0.68×10^{-5} m^2/s, thereby allowing the upper layer to invade the distribution chamber.

The camera has been lowered to focus on the cross-section of the lower end of the exit slot where it connects with the distribution chamber.

Video Sequence #3 – slotexitflow3.mpg – ref. Thesis Section 4.2.3.2

Run time ~ 25 s

This clip is similar to sequences # 1 and #2 except here the slot is parallel instead of chamfered and the flow has been increased from a value below the critical carrier layer flow rate to allow the interface to be slowly swept back up towards the slot exit.

PUMP INDUCED SLIDE WAVES

Video Sequences #4a - #4d – slidewaves.mpg – ref. Thesis Section 4.3.1

Run time 4 x10 s sequences

These clips show the response of the interface and free surface to pump-induced disturbances as the carrier layer flow is reduced down towards the critical flow rate. The slot is parallel and of width 0.52 mm. The properties and flow rates of the two layers are given in Table A.2

	Flow rate	Viscosity	Density	Surface Tension
Upper layer	6.14×10^{-5} m^2/s	74.5 mPa.s	1014 kg/m^3	34.3 mN/m
Lower layer	See below	5.4 mPa.s	1005 kg/m^3	34.3 mN/m

Table A.2: Properties and flow rates used for studying pump induced slidewaves at non-chamfered slot exit

The images are shown in quadrature. The left hand image shows the slide waves viewed normal to the transparent slide – the one on the right shows the cross-sections of the free surface and the interface.

Video sequence # 4a – carrier layer flow rate = 1.71×10^{-5} m^2/s
Video sequence # 4b – carrier layer flow rate = 0.68×10^{-5} m^2/s
Video sequence # 4c – carrier layer flow rate = 0.48×10^{-5} m^2/s

Video sequence # 4d – carrier layer flow rate = 0.34 x 10^{-5} m^2/s – note the relative movements of the upper free surface and interface and an indication of the presence of a recirculation at the top of the downstream slot wall.

CHARGE ASSISTED COATING

Video Sequences #5a & #5b – chargeassist.mpg – ref. Thesis Section 3.6.2

These two video sequences each run for about 30 seconds and show the dynamic response of the lower meniscus to varying polar charge when coating a single layer of viscosity 24.2 mPa.s and surface tension 28 mN/m at 1 s. surface age. The wet laydown was 65 μm and the coating speed 50 m/min.

The images are shown in quadrature, the one on the left indicating charge level varying between + 5v and +507 v and the other the response of the lower meniscus. The vee-shaped image is due to glancing reflection from the surface of the uncoated web.

Video sequence # 5a corresponds to where the coating gap is set at 165 μm for which the stabilisation suction is controlled at 275 Pa.

Video sequence # 5b corresponds to where the gap is opened out to 508 μm to allow through a passing inter-roll join and for which the stabilisation suction fell to 165 Pa due to increased leakage at the sides of the suction box.

Video Sequences #5c & #5d – chargeassist.mpg – ref. Thesis Section 3.6.2

These two video sequences also each run for about 30 seconds and show the dynamic response of the upper meniscus to the same varying polar charge as for sequences # 5a and # 5b.

AIR INDUCED SURFACE WAVES USING ROTARY DRYER

Video Sequence #6 – surfacewaves1.mpg – ref. Thesis Section 2.14.2

Run time ~ 15 s - Note video dated 30 Jul 1993 instead of 30 Jul 2003 in error

This clip shows the development of air induced surface waves on a wet coating being dried under the rotary dryer. The view is by glancing reflection – see Figure 2.77. A zebra stripe mask superimposed over the diffusing light source helps the eye to recognise the waves in the surface. These start to become visible at about 5 to 7 seconds after starting the sequence – that is where the recording time is 15 08 38.

The rotary dryer is operating at a peripheral speed of 200 m/min (3.3 m/s) and nozzle-to-web gap of 10 mm. The air is delivered at a pressure of 885 Pa and a temperature of 40 °C. The air speed is calculated to be 36.7 m/s.

The coating comprises a gelatin cellulose mixture of viscosity 45.2 mPa.s and surface tension 47.7 mN/m at 1 s. surface age. The wet laydown is 96.6 μm.

AIR INDUCED SURFACE WAVES USING LINEAR ARRAY OF AIR IMPINGEMENT NOZZLES

Video Sequence #7 – surfacewaves2.mpg – ref. Thesis Section 4.4.2

Run time ~ 10 s

This clip shows the development of air induced surface waves on a wet coating being dried under a linear array of ten air impingement nozzles. The camera is travelling at the same speed as the web. The vertical stripes moving rapidly from left to right are the jet nozzles as they are being passed by the camera. First one and then two vertical black lines appear on the image – these are reference markers pre-written onto the web. The web is travelling at 7 m/min = 0.117 m/s. The nozzle pitch is 73.5 mm and the gap between the nozzles and web 9 mm. The air is delivered at a pressure of 250 Pa and a temperature of 23°C. The air speed is calculated to be 19.4 m/s.

The coating comprises a solution of PVOH plus green dye. The viscosity is 9.9 mPa.s and the surface tension 34.7 mN/m at 1 sec. surface age. The wet laydown is 75 μm.

Bibliography

Adamson, A.W. *Physical Chemistry of Surfaces*: Wiley-Interscience: New York, pp 2 - 23 [1982]

Ade, F. *US Patent 4,041,897* [1978]

Akhtaruzzaman, A.F.M., Wang,C.K. & Lin,S.P. 'Wave Motion in Multilayered Liquid Films' J.Appl. Mech-T ASME **45** (1) pp25-31 [1978]

Apps, C.J., Ikin, J.B. and Thompson. H.M. 'Minimisation of streak-line defects in slot exit flow in multi-layer coating systems.' *Proc. 3rd Eur. Coat. Symp.* pp 291-296 [1999]

Apps, C. J. 'Slot Exit Phenomena in Industrial Slide-Fed Coating Systems' *PhD. Thesis*, University of Leeds [2000]

Aydore, S. 'High Efficiency Heat Transfer using Asymmetric Impinging Jet' *US Patent 6,564,473*

Batchelor, G.K. 'An Introduction to Fluid Dynamics' Cambridge University Press [1979]

Baumlin,J.M. 'Surfactant effects on surface waves of flowing liquid.' AIChE Spring Meeting March 18-22, Orlando, FL. Paper 19h [1990]

Barstow, F.C. 'Cascade coating apparatus for applying plural layers of coating material to a moving web' *US Patent 3,289,632* [1966]

Bauer, C.L., Shaw-Klein, L. & Reczek, J. 'Method for providing a high viscosity coating on a moving web and articles made thereby' *EP 1,111,452* [2001]

Beguin, A.E. 'Method of coating strip material.' *US Patent 2,681,234.* [1954]

Behan, P.H. and Ikin, J.B. 'The importance of controlling rheology when coating a carrier layer.' *ILFORD Cascade Technology Group Meeting 13 July 1998.*

Bell, B.C., Cline, G.M. & Klasner, C.J. 'Effect of air baffle design on mottle in solvent coatings' *US Patent 6,018,886* [2000]

Bermel, M.S., McKeown, S.P. & Ruschak, K.J 'Slide Bead Coating with a Low Viscosity Carrier Layer' *US Patent 6,579,569* [2003]

Bico, J., Marzolin, C. & Quéré, D. 'Pearl drops' *Europhysics Letters* **47** (2) pp 220 – 226 [1999]

Bird, R.B., Armstrong, R.C. & Hassager, O. 'Dynamics of Polymeric Liquids: Vol.1' *John Wiley & Sons* pp 171 - 172 [1987]

Bird, R.B., Stewart, W.E. & Lightfoot, E.N. 'Transport Phenomena' *John Wiley & Sons* pp 34 - 41 [1960]

Blake, T. D. & Ruschak, K. J. 'A maximum speed of wetting.' *Nature (London)* **282**: pp 489-491 [1979]

Blake,T.D. 'Dynamic Contact Angles and Wetting Kinetics' in J.C.Berg (Ed), *Wettability*, New York: Marcel Dekker pp 251-309 [1993]

Blake, T.D., Clarke, A & Ruschak, K.J. 'Hydrodynamic Assist of Dynamic Wetting.' *AIChE Journal* **40** No.2 pp 229- 242 [1994]

Blake, T.D., Dobson, R., Batts, G.N & Harrison, W.J. 'Coating Processes' *US Patent 5,391,401* [1995]

Blake, T.D. & Morley, S.D. 'Method for increasing the coating speed' *EP 0,769,717* [1997]

Blake, T.D. & Ruschak, K.J 'Wetting: static and dynamic contact lines' in S.F.Kistler and P.M.Schweizer,(Eds), *Liquid Film Coating*, London: Chapman and Hall, Chap 3, pp 63 - 97 [1997]

Blake,T.D. & Clarke, A. 'An Investigation of Electrostatic Assist in Coating' *Proc. 3rd Eur. Coat. Symp.* pp 279-280 [1999]

Blake,T.D., Clarke, A & Stattersfield, E.H. 'An Investigation of Electrostatic Assist in Dynamic Wetting' *Langmuir* **16** No. 6 pp 2928-2935 [2000]

Blake, T.D. Private communication [2001]

Blake, T.D. & De Coninck, J. "The influence of pore wettability on the dynamics of imbibition and drainage" *Colloids and Surfaces A: Physiochem. Eng. Aspects 250* pp 395-402 [2004]

Blake, T.D. Private communication [2005]

Brace, R. Private communication [2002]

Bria, M.P. & Quass, J.D. 'Combination air bar and hole bar flotation *dryer' US Patent 5,647,144* [1997]

Bristow, J.A. 'Liquid Absorption into Paper during Short Time Intervals' *Sven Papperstidn* **70** (19) pp 623-629 [1967]

Booth, G.L. 'Coating Equipment and Processes' New York : Lockwood Publishing [1970]

Bower,C.L., Blake,T.D. & Carruthers,K. 'Dynamic wetting in solvent systems' *Proc. 4th Eur. Coat. Symp.* pp 47-52 [2001]

Buchlin, J-M., Parellada, N. & Anthoine, J. 'Theoretical and Experimental Investigation of Annular Jet Wiping' *Proc. 2nd Eur. Coat. Symp.* pp 204 - 211 [1997]

Buonopane, R.A., Gutoff, E.B. & Rimore, M.M.T. 'Effect of Plunging Tape Surface Properties on Air Entrainment Velocity' *AIChE Journal* **32** No.4 pp 682- 683 [1986]

Burket, R.S., Conaghan, B.F. & Hirshburg, R.I. 'Coating Method' *US Patent 4,443,504* [1984]

Carreau, P.J. Ph.D. Thesis, University of Wisconsin, Madison [1968]

Cary, J.D. & Gutoff, E.B. 'Analyze the Drying of Aqueous Coatings' *Chemical Engineering Progress February 1991* – pp73 -79 [1991]

Cassie, A.B.D. & Baxter, S. 'Wettability of Porous Surfaces' Trans. Faraday Soc. **40**, pp 546 – 551 [1944]

Chen, K.S.A. & Scriven, L.E. 'Liquid penetration into a deformable porous substrate' *TAPPI Journal* Jan. 1990 pp 151 - 161

Chen, K.S.A. 'Studies of multi-layer slide coating and related processes' *PhD. Thesis*, University of Minnesota [1992]

Chen, K.S.A & Scriven, L.E. 'Two views of multilayer coating beads.' *Ind. Coat.Res.* **2** pp 59-64 [1992]

Cheng, D.C-H. 'A review of the role of rheology in coating processes' *Proc.of First European Coating Symposium, Leeds University* pp 301-347 [1995]

Choinski, E.J. 'Method of multi-layer coating.' *US Patent 4,113,903* [1978]

Clarke, A., Blake, T.D. & Ruschak, K.J. 'Method for Curtain Coating at High Speeds' *USP 6,099,913* [2000(1)]

Clarke, A., Blake, T.D. & Ruschak, K.J. 'Method for Electrostatically Assisted Curtain Coating at High Speeds' *USP 6,103,313* [2000(2)]

Clarke, A. 'Coating on a Rough Surface' *AIChE Journal* **48** (10) pp 2149-2156 [2002]

Clarke, A., Blake, T.D., Carruthers, K. & Woodward, A. 'Spreading and Imbibition of Liquid Droplets on Porous Surfaces' *Langmuir* **18** pp 2980 – 2984 [2002]

Clarke, A., Bower, C.L. & Goppert, K.M. 'Apparatus and Method of Coating a Web' *US Patent 6,638,576* [2003]

Clarke, A., Bower, C.L. & Goppert, K.M. 'Method of Creating and Coating a Material' *US Patent 6,780,455* [2004]

Cohen, E.D. & Gutoff, E.B. 'Modern Coating and Drying Technology' New York: VCH Publishers [1992]

Cohu, O. 'Air Entrainment in MultiLayer Curtain Coating'. *Proc. of Third European Coating Symposium, University of Erlangen-Nurnberg* pp 53-58 [1999]

Cohu, O. 'On the Correlation Between Air Entrainment Velocity and (High Shear) Viscosity in Coating Operations' *Proc. of Fourth European Coating Symposium, Brussels* pp 87-92 [2001]

Connelly, R.W., Contestable, B.A. & Greener, J. Unpublished data. [1984]

Connelly, R.W. & Greener, J. 'High-Shear Viscometry with a Rotational Parallel-Disk Device' *Journal of Rheology* **29** (2) pp 209 - 226 [1985]

Conroy, J.E. & Weinstein, S.J. 'Minimization of Slide Instabilities by Variations in Layer Placement, Fluid Properties and Flow Conditions' *US Patent 5,376,401* [1994]

Coyle, D.J., Macosko, C.W. & Scriven, L.E. 'Stability of symmetric film-splitting between counter-rotating cylinders' *J.Fluid Mech.* **216** pp 437 – 458 [1990]

Craik, A.D.D. 'Wind-generated waves in thin liquid films' *J.Fluid Mech.* **26** (2) pp 369 – 392 [1966]

Cunha, F. & Carbonaro, M. 'Surface Wave Instability on Aircraft De/Anti-Icing Fluid Films' *Proc. of First European Coating Symposium, Leeds* pp 189 - 188 [2001]

Dettre, R.H. & Johnson, R.E. 'Contact Angle Hysteresis – II Contact Angle Measurements on Rough Surfaces' in *Contact Angle Wettability and Adhesion* F.M.Fowkes (Ed) Advances in Chemistry Series No.43, ACS, Washington, DC pp 136 – 144 [1964]

Devine, W.D. 'Coating by means of a coating hopper with coating slots where the coating composition has a low slot Reynolds number' *US Patent 5,143,758* [1991]

Ditchburn, R.W. 'Light'. Academic Press. p 565 [1976]

Dittman, D.A. and Rozzi, A. 'Method of multi-layer coating.' *US Patent 4,001,024* [1977]

Dragomirescu, Sünderhauf, G., Raszillier, H. & Durst, F. 'Curtain Coating at High Speed – Fluid Dynamical Limitations' *Proc. of Fourth European Coating Symposium, Brussels* pp 185 - 191 [2001]

Durst, F. and Wagner, H-G. 'Slot Coating' in S.F.Kistler and P.M.Schweizer (Eds). *Liquid Film Coating* London: Chapman and Hall, Chap 11a, pp 401 – 426, [1997]

Endoh, A. & Morikawa, M. 'Process for Preparing Color Light-Sensitive Material by Multi-Layer Co-Coating' *US Patent 5,656,417* [1997]

Enomae, T., Kataoka, H. & Onabe, F. 'In-Plane Distribution of Paper Absorbency Measured by Liquid Absorption Profilometer' *Sen-i Gakkaishi* **55** (2) pp 65 – 72 [1999]

Farhni, F. & Zimmermann, A. 'Coating device' *US Patent 4,109,611* [1978]

Faust, H.L. 'Menisci studies in bead coating' M.S.thesis, Drexel University [1975]

Ferguson, J. & Kemblowski, Z. *Applied Fluid Rheology*, London & New York: Elsevier Applied Science pp 51 – 71, pp 86 – 94 and p 245 [1991]

Fermin, R.J. & Scriven, L.E. 'Electrostatically Assisted Coating Flows" *Proc. of 3rd European Coating Symposium, University of Erlangen-Nürnberg* pp 91-95 [1999]

Francis, J.R.D. 'Wave Motions and the Aerodynamic Drag on a Free Oil Surface' *Philos. Mag. Ser. 7* **45** (366) pp 695 – 702 [1954]

Fossdyke, G.R. Private communication [2004]

Fox, R.W. & McDonald, A.T. 'Introduction to Fluid Mechanics' John Wiley & sons – New York, pp 426 - 428 [1973]

Fowkes, F.M. 'Determination of Interfacial Tensions, Contact Angles and Dispersion Forces in Surfaces by assuming Additivity of Intermolecular Interactions in Surfaces' *J. Phys . Chem – US* **66** (2) p382 [1962]

Garin, R.I. & Vachagin, K.D. 'Minimum thickness of a photo emulsion during extrusion [slide] coating of cine films' *Trudy Khim. Teknol. Inst.* **48** p 125 [1972]

Gaskell, P.H., Savage, M.D., Summers, J.L. & Thompson, H.M. *EPSRC LINK / DTI Grant GR/K39721, Final Report (Leeds University)* [1998]

Gaskell, P.H., Thompson, H.M., Savage, M.D. & Ikin, J.B. 'Steady recirculating flow near contact lines' *Chem. Eng. Sci.*, **54**, pp 819-828 [1999]

Gibbons, C.B., Kerr, W.C. & Maddocks, R.H. 'Web treatment method.' *US Patent 3,702,258* [1972]

Girifalco, L.A. & Good, R.J. *J.Phys.Chem.* **61,** p904 [1957]

Glass, J.E. & Prud'homme, R.K. 'Coating Rheology: Component Influence on the Rheological Response and Performance of Water-Borne Coatings in Roll Applications' in S.F.Kistler & P.M.Schweizer (Eds), *Liquid Film Coating*, London: Chapman and Hall, pp 137 – 182 [1997]

Good, R.J. 'Theory for the Estimation of Surface and Interfacial Energies' in R.F.Gould (Ed) *Contact Angle, Wettability and Adhesion*, Advances in Chemistry Series 43 – American Chemical Society, pp 74 - 87 [1964]

Goppert-Berarducci, K.E. & Higgins, E.P. 'Method for Predicting Coatability' *US Patent 6,177,128* [2001]

Gosset, A. & Buchlin, J.M. 'Comparison of experimental techniques for the measurement of unstable film flow' *Proc. of Fifth European Coating Symposium, Fribourg, Switzerland* pp 47 - 52 [2003]

Greiller, J. E. 'Method of Making Photographic Elements.' *US Patent 3,632,374* [1972]

Greiller, J. E. 'Curtain coating apparatus.' *US Patent 3,968,772* [1976]

Gutoff, E.B. & Kendrick, C.E. 'Dynamic contact angles' *AIChE J* **28** pp 459 – 466 [1982]

Gutoff, E.B. 'Premetered Coating' in E.D. Cohen and E.B. Gutoff, (Eds), *Modern Coating and Drying Technology,* New York: VCH Publishers pp 117 – 167 [1992]

Gutoff, E.B. & Cohen E.D., *Coating and Drying Defects - Troubleshooting Operating Problems*, New York: John Wiley [1995]

Hackler, M.A. et al. 'Frequency response of coating flows to small three-dimensional disturbances by supercomputer aided analysis' Paper read at AIChE Spring Meeting, March 30 – April 2, New Orleans, LA, paper 43d [1992]

Hansen, R.S. 'The theory of diffusion-controlled adsorption kinetics with accompanying evaporation' *J.Phys. Chem.* **64** 637 [1960]

Hartman, R.L. 'High Speed Curtain Coating Process and Apparatus' *International Patent Application WO 89 / 05477* [1989]

Hens, J. 'History of Coating' presented at the 8th International Coating Process Science and Technology Symposium, February 25-29, New-Orleans, LA, Pap 1a [1996]

Hens, J. & Boiy, L. 'Operation of the bead of a pre-metred coating device' *Chem. Eng. Sci.* **41** (7) pp 1827 – 1831 [1986].

Hens, J and Van Abbenyen, W., 'Slide coating' in S.F.Kistler and P.M.Schweizer, (Eds), *Liquid Film Coating* London: Chapman and Hall, Chap 11b pp 427 - 462, [1997]

Herminghaus, S. 'Roughness-induced non-wetting' *Europhysics Letters* **52** (2) pp 165 – 170 [2000]

Hirschburg, R.I. & Christodoulou, K.N. 'Dual Geometry for Slide-Bead Coating' *US Patent 5,458,925* [1995]

Hoffman, R.L. 'A study of the advancing interface. I. Interface shape in liquid-gas systems.' *J. Colloid Interface Sci.* **50** (2) pp 228-241 [1975]

Howe, A.M., Harrison, W.J. & Blake,T.D. 'Method for increasing the coating speed' *European Patent 0,773,472* [1997]

Hua, X.Y. & Rosen, M.J. 'Dynamic surface tension of aqueous surfactant solutions I. Basic parameters.' *J. Coll. Interf. Sci.* **124**: pp652-659 [1988]

Hughes, D. J. 'Method for simultaneously applying a plurality of coated layers by forming a stable multilayer free falling vertical curtain. ' US Patent 3,508,947 [1970]

Ikin, J. B. 'Flow visualisation studies of a slide bead coating process.' Paper 41c read at *6th International Coating Process and Technology Symposium*, AIChE Spring National Meeting, 29 March – 2 April 1992, New Orleans, LA. [1992]

Ikin, J.B., Summers, J.L. & Thompson, H.M. 'An experimental and numerical investigation of double-layer slide bead coating' *Proc. 2nd Eur. Coat. Symp.* pp 320-328 [1997(1)]

Ikin, J.B. 'Coating apparatus' *GB Patent 2,352,990* [2001(1)]

Ikin, J.B., Gaskell, P.H., Noakes, C.J. & Thompson, H.M. 'An Experimental Study of Instability Phenomena and Coating Limits in Industrial Carrier Layer Flows' *Proc. 4th Eur. Coat. Symp.* pp 277 – 282 [2001(2)]

Ikin, J.B. 'Preliminary User Requirement Specification – Two Stage Drying System – M22' –12 June 2003

Isayama, S. & Takehara, N. 'Coating Apparatus' *US Patent 4,299,188* [1981]

Ishizaki, K and Fuchigami, S. 'Method of simultaneously applying multiple layers to web.' *US Patent 4,525,392* [1985]

Ishizuka, S. 'Method of multi-layer coating.' *US Patent 4,863,765* [1989(1)]

Ishizuka, S. 'Method of simultaneous multilayer application.' *European Patent Application 0 313 043* [1989(2)]

Iwado, J. 'Method for drying coating film in manufacture of thermal-developable light-sensitive material' *US Patent 6,586,171* [2003]

Jackson, B.W. 'Apparatus for Coating a Substrate' *US Patent 3,993,019* [1976]

Jiang, T.S., Lee, H.O., Liu, Y. Yen, S.C., Valentini, J.E., Thomas,W.R. and Sevenhuysen, P. 'The essence of surface dilational modulus in thin film coating' AIChE Spring Meeting, Orlando Florida, March 18-22 [1990]

Johnson, R.E. & Dettre, R.H. 'Contact Angle Hysteresis - I Study of an Idealized Rough Surface' in *Contact Angle Wettability and Adhesion* F.M.Fowkes (Ed) Advances in Chemistry Series No.43, ACS, Washington, DC pp 112 – 135 [1964]

Joos, F.M. 'Leveling of a Film with Stratified Viscosity and Insoluble Surfactant' *AIChE Journal* **42** (3) pp 623- 637 [1996]

Kao, T.W. 'Stability of two-layer stratified flow down and inclined plane' *Phys. Fluids*, **8** (5) p 812-820 [1965]

Kao, T.W. 'Role of viscosity stratification in the stability of two-layer flow down an incline' *J.Fluid Mech.* **33** . p 561-572 [1968]

Katagiri,Y, Oki,K. & Tokimasa,Y. 'Coating method' *European Patent 1,116,992* [2001]

Katagiri, Y, Tokimasa, Y., Suga, Y & Noguchi,Y. 'Method of Curtain Coating' *US Patent 6,607,786* [2003]

Kerker,M. 'The Scattering of Light and other electromagnetic radiation' New York, Academic Press [1969]

Kisler, S., Chirokas, E.A. & Foster,D.A. 'Precharged web coating apparatus' *US Patent 4,457,256* [1984]

Knight, D.E., Tsao, Y-H., Burch, E.L., Bi, Y., Niu, B-J, Zahrobsky, P.C. & Kumpf, B.A. 'Process for Applying a Topcoat to a Porous Basecoat' *US Patent 6,475,612* [2002]

Kobayashi, C. et al. 'Stability of two-layer Stratified Flow on Inclined Plane – Comparison of Theoretical Analysis with Experimental Results' AIChE Spring Meeting - Paper 86a [1986]

Kobayashi, C. 'Stability analysis of film flow on an inclined plane. I. One layer, two layer flow' *Ind. Coat. Res.* **2**: pp 65-88 [1992]

Koepke, G., Frenken, H., Bussmann, H. & Browatzki, K. 'Process for the Multiple Coating of Moving Webs' *US Patent 4,572,849* [1986]

Kogelnik,H. in 'Advances in Lasers – A.K.Levine (Ed)' Dekker,New York [1965]

Larkin, K.G. 'Efficient nonlinear algorithm for envelope detection in white light interferometry' *J. Opt. Soc. Am. A* **13** (4) pp 832-843 [1996]

Leonard, W.K. 'Slot Coating Method and Apparatus' *US Patent 5,506,000* [1996]

Levarlet, C.G.C., Finnicum, D.S. & Quiel,R.R. 'Device and Method for Optimizing a Given Parameter in a Process of Coating a Support with a Liquid Composition' *US Patent 5,646,737* [1997]

Longhurst , R.S. 'Geometrical and Physical Optics' Second impression - Longmans p 411-412 [1960]

Martin, H. 'Heat and Mass Transfer between Impinging Gas Jets and Solid Surfaces' *Advances in Heat Transfer* **13** pp 1-60 [1977]

Massey, B.S. 'Mechanics of Fluids – 4th edition' Van Nostrand - New York [1979]

Menchaca-Rocha, A. 'The Mobility of Mercury Drops on Rough Glass Surfaces' *J.Coll. Intf. Sci.* **149,** p 472 [1992]

Mercier, J.A., Torpey, W.A and Russell, T.A 'Multiple coating apparatus'. *US Patent 2,761,419* [1956]

Miller, C.A. & Neogi, P. 'Interfacial Phenomena – Equilibrium and Dynamic Effects' Marcel Dekker,Inc. - New York [1995]

Miwa, M., Nakajima, A., Fujishima, A., Hashimoto, K. & Watanabe,T. 'Effects of the Surface Roughness on Sliding Angles of Water Droplets on Superhydrophobic Surfaces ' *Langmuir* **16** p 5754 [2000]

Miyamoto, K, & Katagiri, Y. 'Curtain Coating' in S.F.Kistler and P.M.Schweizer, (Eds), *Liquid Film Coating* London: Chapman and Hall, Chap 11c pp 463 - 494, [1997]

Moffatt, H.K. 'Viscous and Resistive Eddies near a Sharp Corner' *J.Fluid Mech.*, **18**, pp 1-18 [1964]

Mori, F., Toda, Y, Bouwstra, J.B. & van der Pluym, A. 'Method of coating a continuously moving web' *European Patent 1,186,951* [2002]

Muës, W., Hens, J. & Boiy, L. 'Observation of a dynamic wetting process using laser-Doppler velocimetry.' *AIChE.* **35** (9) pp 1521-1526 [1989]

Nadeau, G.F. 'Method of coating a liquid photographic emulsion on the surface of a support.' *US Patent 2,952,559* [1960]

Nakajima, A. Private communication [2005]

Nakajima, K. & Miyamoto, K. 'Coating method.' *European Patent Application 0,530,752* [1993]

Nakajima, K. 'Coating method and apparatus for heat-development photo-sensitive material' *European Patent 1,184,087* [2002]

Newman, F.H. & Searl, V.H.L. 'The General Properties of Matter' 5th edition – Edward Arnold (Publishers) Ltd. – London – p255 – [1957]

Noakes, C.J., Gaskell, P.H., Thompson, H.M. & Ikin, J.B. 'Streak-Line Defect Minimization in Multi-Layer Slide Coating Systems' *Trans IchemE* **80** Part A pp 449 – 463 [2002(1)]

Noakes, C.J., Thompson, H.M., Gaskell, P.H., Lowe, D.C., Lowe, S. & Osborn, M.J. 'Heat transfer characteristics of air flotation dryers' *Paper Technology* **43** (10) pp 46 –50 [2002(2)]

Du Nouÿ, P. *Journal General Physiology,* **1,** p 521 DIN-Blatt 53914 [1919]

Olszak, A.G., Schmit, J & Heaton, M.G. 'Interferometery: Technology and Applications' published by Veeco Metrology Group, Tucson, AZ. [2001].

Orchard, S. E. 'On surface levelling in viscous liquids and gels.' *Appl. Sci. Res.* **11**: p 451-464 [1962]

Owens, D.K. & Wendt, R.C. 'Estimation of the Surface Free Energy of Polymers' *J. of Applied Polymer Science* **13** pp.1741-1747 [1969]

Özgen, S., Degrez, G. & Sarma, G.S.R. 'Two-fluid-layer flow stability' *Proc. 3rd Eur. Coat. Symp.* pp 239 - 244 [1999]

Özgen, S., Cabonaro, M. & Sarma, G.S.R. 'Experimental study of wave characteristics on a thin layer of de/anti-icing fluid' *Physics of Fluids* **14** (10) pp 3391 – 3402 [2002]

Padday, J.F. 'Multiple coating apparatus' *US Patent 3,005,440* [1961]

Padday, J.F. 'Wetting, Spreading and Adhesion' Academic Press – London [1978]

Panton R.L. 'Incompressible Flow' John Wiley & Sons – New York [1984]

Petros, K.W. 'Efficient dryer and drying process' *US Patent 4,779,355* [1988]

Polat, S. 'Heat and Mass Transfer in Impingement Drying' *Drying Technology* **11** (6) pp 1147 – 1176 [1993]

Pourier, C.C. 'Curtain coating of corrugated paper board' *TAPPI* **49** (10) pp 66A-67A [1966].

Quiel, R.R.; Gros, A.E.; Finnicum, D.S.& Joos, F.M. 'Slide Bead Coating Method' *US 2002/0081390* [2002]

Rayner,R. Private communication. [2001]

Rolley, E.; Guthmann, C.; Gombrowicz, R. & Repain, V. 'Roughness of the Contact Line on a Disordered Substrate' *Phys. Rev. Lett.* **80** (13) p 2865 [1998]

Ruschak, K.J. 'Coating Flows' *Ann. Rev. Fluid Mech.* **17** pp 65 – 89 [1985]

Ruschak, K.J. 'Flow of a Thin Liquid Layer Due to Ambient Disturbances' ' *AIChEJ.* **33** (5) pp 801-807 [1987]

Ruschak, K.J., Suter, D.J. & Weinstein, S.J. 'Optimized versatile coating hopper' *US Patent* 6,350,318 [2002]

Russell, T.A. 'Method of Multiple Coating' *US Patent 2,761,791* [1956]

Sakiadis, B.C. 'Boundary-layer behavior on continuous solid surfaces.' *AIChEJ.* 7 (2) pp 21-25 [1961]

Schunk, P.R. 'Surfactant and polymer additives in coating and related flows' *Ph.D. Thesis, University of Minnesota.* [1989].

Schunk, P.R. & Scriven, L.E. 'Constitutive equation for modeling mixed extension and shear in polymer solution processing.' *J.Rheol.* **34**: pp. 1085 – 1119 [1990]

Schunk, P.R. & Scriven, L.E. 'Surfactant effects in coating processes' in S.F.Kistler and P.M.Schweizer, (Eds), *Liquid Film Coating*, London: Chapman and Hall, pp 495 - 536, [1997]

Schweizer, P.M. 'Visualisation of coating flows', *J.Fluid Mech.*, **193**, pp 285-302 [1988]

Schweizer, P.M. 'Fluid handling and preparation' in E.D. Cohen and E.B. Gutoff, (Eds). *Modern Coating and Drying Technology,* New York: VCH Publishers pp 23 – 61 [1992]

Schweizer, P.M. 'Experimental methods' in S.F.Kistler and P.M.Schweizer, (Eds), *Liquid Film Coating*, London: Chapman and Hall, pp 209-250 [1997(1)]

Schweizer, P.M. 'Control and optimisation of coating processes' in S.F.Kistler and P.M.Schweizer, (Eds), *Liquid Film Coating*, London: Chapman and Hall, pp 735-768 [1997(2)]

Schweizer, P.M. & Rossier, P.-A. 'The Operating Window of Slide Coating.' *Proc. 4th Eur. Coat. Symp.* - Brussels – 1-4 Oct. pp 263 – 276 [2001]

Schweizer, P.M. & Rossier, P.-A. 'High Speed Operating Range for Slide Coating' *Proc. 5th Eur. Coat. Symp.* – Fribourg, Switzerland – 17-19 Sept. pp 182 – 189 [2003]

Scriven, L.E. & Suszynski, W.J. 'Coating and Drying Porous Sheets' in *Coating Process Fundamentals – Basic Phenomena, Principles, Illustrations, Challenges* Antwerp, Belgium, March 15-17 1993.

Sisko, A.W. 'The Flow of Lubricating Greases' *Ind.Eng.Chem.* **50** (12) pp 1789-1792 [1958]

Smith, M.K. 'The mechanism for the long-wave instability in thin liquid *films' J. Fluid Mech.* **217** pp 469-485 [1990]

Suga, Y., Nakajima, K., Kobayashi, K. & Miyamoto, K. 'Curtain Coating Method for Eliminating Sagging at High Flow Rates' *US Patent 5,393,571* [1993]

Tallmadge,J.S., Weinberger, C.B. & Faust, H.L. 'Bead coating instability: A comparison of speed limit data with theory' *AIChE J.* **25** pp 1065 – 1072 [1979]

Tobari, J. & Kishido, T. 'Coating Apparatus' *US Patent 5,827,369* [1998]

Tricot, Y-M. 'Surfactants: static and dynamic surface tension' in S.F.Kistler and P.M.Schweizer, (Eds), *Liquid Film Coating*, London: Chapman and Hall, pp 99 - 136 [1997]

Valentini, J.E., Thomas, W.R., Sevenhuysen, P., Jiang, T.S., Lee, H.O., Liu,Y. and Yen, S.C. 'Role of Dynamic Surface Tension in a Slide Coating' . *Ind.Eng.Chem. Res.* **30**: pp 453 – 461 [1991]

Valentini, J.E., Chandler, J.T., Jiang, Q., Chiew,Y.C. & Fina, L.J. ' Surface Elastic Effects in Premetered Coating Techniques' *Ind.Eng.Chem. Res.* **35**: pp 434 – 449 [1996]

Van Abbenyen, W., Christodoulou, K. & Scriven, L.E 'Frequency response of a coating flow: Predictions for slide coating'. Paper read at AIChE Spring Meeting, March 6-10, New Orleans, LA, paper 2d [1988]

Van Abbenyen, W. and Muës, W. 'Comments on "Stability of multilayer stratified flow on an inclined plane"' *Ind.Coat.Res.* **2** pp 89-93 [1992]

Vandaele, F. & Vancoppenolle, G. 'The influence of electrostatic assist on the coating window of slide and slot coating' *Proc. 3rd Eur. Coat. Symp.* pp 247-252 [1999]

Von Bahr, M., Seppänen, R., Tiberg, F. & Zhmud, B. 'Dynamic Wetting of AKD-sized papers' *J. Pulp. Pap. Sci.* **30** (3) pp 74-81 [2004]

Vyverberg, R.G. 'Charging Photoconductive Surfaces.' in J.H.Dessauer & H.E.Clark (Eds.) *Xerography and Related Processes*, London, The Focal Press, pp 201-216 [1965]

Walkup, L.E. *US Patent 2,777,957* [1957]

de Waard, H. & Lazarus, D. 'Modern Electronics' Addison-Wesley Publishing Company – Reading MA pp 182 – 185 [1966]

Wang, C.K., Seaborg, J.J. & Lin, S.P. 'Instability of multi-layered liquid films.' *Phys. Fluids* **21** pp 1669 – 1673 [1978]

Watanabe, K. 'Fluid frictions of shark skin and lotus leaf – How does the drag reduction occur?' *J. Jpn Soc. Tribologis* **45** (5) pp 354 – 359 [2000]

Weinstein, S.J. 'Wave propagation in the flow of shear-thinning fluids down an incline.' *AIChEJ* **36** (12) pp 1873-1889 [1990]

Weinstein, S.J & Kurz, M.R 'Longwavelength instabilities in three-layer flow down an incline.' *Phys.Fluids.* **A3**(11) pp 2680-2687 [1991]

Weinstein, S.J. & Palmer, H.J. 'Capillary hydrodynamics and interfacial phenomena' in S.F.Kistler and P.M.Schweizer, (Eds), *Liquid Film Coating*, London: Chapman and Hall. pp 19-62 [1997]

Wolfram, E. & Faust, R. 'Liquid Drops on a Tilted Plate, Contact Angle Hysterisis and the Young Contact Angle' in J.F.Padday (Ed) *Wetting, Spreading and Adhesion*, London: Academic Press, pp 213 – 222 [1978]

Woodward, R.P. 'FTÅ200 Measurement Capabilities' First Ten Ångstroms, 465 Dinwiddie Street, Portsmouth, VA 23704 [2001]

Wraith, M.A., King. J.R. and Garvey, J.I.M. Private communication [2003]

Yapel, R.A., Edman, T.M., Scheller, B.A., Wallace, L.B. & Warren, J.L 'Web coating method with continuous coating over splices' *International Patent Application, Publication Number WO 99/46640* [1999]

Yih, C-S. 'Stability of Liquid Flow down an Inclined Plane' *The Physics of Fluids* **6** (3) pp 321 – 334 [1963]

Young, T. *Phil.Trans.Roy.Soc.(London)* **95** p65 [1805]

Zaretsky, M.C.; Billow, S.A. & Whitney, R.A. 'Coating method using electrostatic assist' *EP 1,088,596* [2001]

Zeldes, M.D. 'Coating Process Employs Surfactants' *US Patent 4,508,764* [1985]

Zhou, X.B. & Th.M.,J. 'Influence of Surface Roughness on the Wetting Angle' *J.Mater.Res.*, **10** p 1984 [1995]

Zisman, W.A. 'Relation of Equilibrium Contact Angle to Liquid and Solid Constitution' in *Contact Angle Wettability and Adhesion* F.M.Fowkes (Ed) Advances in Chemistry Series No.43, ACS, Washington, DC pp 1 – 51 [1964]

Zuccher, S. & Buchlin, J-M. 'Liquid Film Instabilities in Die Coating Processes' *Proc. 4th Eur. Coat. Symp.* pp 171 - 176 [2001]

Zvan, G.R., Douglas,L.J. & Kistler, S.F. 'A Novel Method for Dynamic Contact Angle Measurement' *International symposium on Coating Process Science & Technology. Spring National Meeting, New Orleans, LA* [1992]